University of Minnesota

This is to certify that I have examined this copy of a doctoral thesis by

Jian Zhao

and have found that it is complete and satisfactory in all respects,
and that any and all revisions required by the final
examining committee have been made.

Catherine E. French Carol K. Shield

Faculty Advisors

_____ _____

Signature of Faculty Advisors

_____ _____

Date

Graduate School

Development of EFT for Nonlinear SDOF Systems

A Thesis
Submitted to the Faculty of the Graduate School
of the University of Minnesota
by

Jian Zhao

In Partial Fulfillment of the Requirements
for the Degree of
Doctor of Philosophy

October 2003

Dedicated to

my parents

Zhao, Minghou & Cao, Yunmei

and specially my wife

Fei Xu

ABSTRACT

Effective force testing (EFT) is a test procedure that can be used to apply real-time seismic simulations to large-scale structures that can be represented by lumped-mass systems. In an EFT test, hydraulic actuators are used to applied dynamic forces through the mass center of the test structure anchored to a stationary base. The force to be imposed (effective force) is the product of the structure mass and the ground acceleration record, thus a known priori. Motions measured relative to the ground are equivalent to those of the structure in a shake table test or an earthquake event. This research extended the development and implementation of the EFT method to fully utilizing test equipment and testing nonlinear SDOF structural systems undergoing large deformation in real time.

Velocity feedback compensation is required for the actuator control to ensure that forces are applied to the test structure accurately. Nonlinearities in the servo-system could have a significant impact on the implementation of velocity feedback compensation when an EFT test requires large flow demands, which could be caused by large structural velocity responses and/or large forces applied to the structure. Detailed mathematical models were proposed for a test system at the University of Minnesota, which accurately described the servo-system behavior over a wide range of frequencies and across the major operation range of the servovalve.

Based on the nonlinear servo-system model, a nonlinear velocity feedback compensation scheme was proposed and verified through computer simulation and experimental tests on a mass-spring-dashpot structural system. Results showed that with

the nonlinear velocity feedback compensation, dynamic forces could be applied to the nonlinear structure at all frequencies of interest. In addition, the effects of system uncertainties on the performance of the test system including stability were investigated through linear system analyses, computer simulation, and experiments.

The viability of the EFT method was further validated by a proof-of-concept test, in which a one-story steel structure was tested using a shake table and the EFT method. The comparison of the test results indicated that the EFT method can be used to apply real-time seismic simulation to structures undergoing large nonlinear deformation.

ACKNOWLEDGMENTS

My deepest appreciation is extended to my advisors Dr. Catherine French and Dr. Carol Shield for their guidance on this research project as well as for the guidance and support they have provided during my graduate study at the University of Minnesota. I sincerely appreciate the help Dr. Thomas Posbergh has provided throughout the research. I would like to thank Paul Bergson from the University of Minnesota and Dr. Greg Banas from the University of Illinois at Urbana-Champaign for providing valuable technical advice and assistance with the equipment used for this project. Acknowledgment is also given to many of my fellow students at the University of Minnesota for their assistance in making the research a success. This research was funded in part by the National Science Foundation under grant number NSF/CMS-9821076. Acknowledgment is also given to the Doctoral Dissertation Fellowship support (2002-2003) provided by the 3M Corporation through the Graduate School at the University of Minnesota.

TABLE OF CONTENT

LIST OF TABLES

LIST OF FIGURES

NOMENCLATURE

Roman Symbols

A	Actuator piston area
A, B, C, D	Coefficients of the total solution of single-degree-of-freedom system
A_0	Orifice area
A_1, A_2	Sectional areas of orifice flow
A_{eft}	Relative acceleration of structure in EFT test
a_i	Coefficients of the denominator of a linear system
A_M	Absolute acceleration of structure in shake table test
A_N, A_S	Acceleration reading in EFT test
A_{stt}	Relative acceleration of structure in shake table test
A_T	Table acceleration in shake table test
A_v	Main-stage valve spool area
c	Viscous damping coefficient of single-degree-of-freedom system
C_c	ratio of Vena contracta area and orifice area
C_d	Discharge coefficient of orifice
C_{ep}	Actuator external leakage
C_F	Conversion factor from kips to volts
C_F	Conversion factor from inches to volts
C_l	Total servo-system leakage coefficient (proportional)
C_{lv}	Main-stage valve leakage
C_{ip}	Actuator internal (cross-port) leakage
D_a	Actuator displacement readings in EFT test
D_{eft}	Relative displacement in EFT test
$D_{N,}\ D_{M,}\ D_{S,}$	Displacement readings in shake table test
D_{stt}	Relative displacement in shake table test
D_T	Table displacement in shake table test

$D_{U,}\ D_D$	Displacement readings in EFT test
$den(s)$	Denominator of transfer function
e	Experiential base
e	DC error (outer loop)
e_i	DC error (inner loop)
F_c	Coulomb friction of single-degree-of-freedom system
f_D	Damping force of single-degree-of-freedom system
F_{Deft}	Total damper force in EFT test
F_{Dstt}	Total damper force in shake table test
f_S	Resistance force of single-degree-of-freedom system
g	Acceleration due to gravity
G_{Fu}	Transfer function of system from command to force output
G_{di}, G_{pi}	Inner-loop controller D gain and P gain
G_d, G_p	Controller D gain and P gain
$H(s)$	Transfer function
$H(z)$	Transfer function in discrete form
H_s	Transfer function of servovalve
H_{sp}	Transfer function of pilot-stage servovalve
H_{sm}	Transfer function of main-stage servovalve
H_{st}	Transfer function of structure
j	Complex number
k	Stiffness of single-degree-of-freedom system
K_3	Sensitivity factor of internal LVDT
K_a	Compressibility coefficient of fluid inside actiator
K_c	Velocity feedback compensation gain
K_v	Main-stage valve flow gain
K_s	Servovalve gain
K_{vp}	Pilot-stage valve flow gain
L	Length of leakage orifice
$L_{W,}\ L_E$	Load cell readings

M_{in}, M_{out}	Fluid mass in/out of control volume
M	Amplitude response of a linear system
M_c	Section moment of column
m	Mass of single-degree-of-freedom system
$num(s)$	Numerator of transfer function
P_0	External time-dependent force
p_{eff}	Effective force
p_i	Poles of a system
P_L	Pressure difference across the actuator piston
P_1, P_2	Pressure inside actuator chambers
P_s	Pressure supply
Q	Flow rate through orifice
Q_1~Q_4	Orifice flow through main-stage servovalve
Q_{in}, Q_{out}	Flow rate in/out of control volume
Q_{vp}	Pilot-stage valve flow
Q_L	Load flow (flow to actuator)
Q_{lv}	Leakage flow of servovalve
R	Reynolds number
r, c, e	Geometric coefficients of the leakage orifice
RF	Reduction factor due to leakage
s	Complex variable defined as $\sigma \pm j\omega$
S_v	Sensitivity factor of velocity transducer
t	Time
T	Temperature in Fahrenheit
T_d	Time delay to be compensated
T_l	Lead time provided by phase-lead network
T_{ld}	Time constant of phase-lead network
u_1, u_2	Velocity of orifice flow
u	Force command
u	Average flow velocity

u, w	Velocity components of flow
V_0	Control volume of fluid
V_t	Volume of actuator piston chambers
$x, \dot{x}, \ddot{x}$	Displacement, velocity, and acceleration
$x_g, \ddot{x}_g$	Ground displacement and acceleration
$x_t, \ddot{x}_t$	Total displacement of structure on shake table
x_v	Spool opening (-1 ~ 1)
$\widetilde{x}_v$	Spool position of the main-stage valve
$x_{v\max}$	Maximum spool stroke of the main-stage valve
X, Z	Body forces on control volume of fluid
x, z	Cartesian coordinates
z_i	Zeros of a system

Greek Symbols

α	Constant of phase-lead network
β	Bulk modulus of fluid
β_e	Effective bulk modulus of fluid
γ	Weight density of fluid
ρ	Mass density of fluid
ν	Viscosity of fluid
μ	Absolute viscosity of fluid
ϕ	Phase response of a linear system
τ	Time constant of a first-order system
ω	Loading frequency
ω_n	Natural frequency of second-order system
ω_{ns}	Equivalent frequency of pilot-stage valve
ζ	System damping ratio
ζ_s	Equivalent damping ratio of pilot-stage valve

CHAPTER ONE

INTRODUCTION

1.1 General

Experimental research remains important in earthquake engineering though nonlinear dynamic analysis of structures has advanced much in recent years. This is especially true when the behavior of structural components, required by analytical studies, is difficult to model due to nonlinearities and strain-rate dependencies. In addition, the analysis of a full-scale structural system based on individually proven component models needs to be validated experimentally before the results can be extended in practice. Hence, experimental procedures that can be used to subject large-scale structures and structural components to seismic loading are essential to further our understanding of the effects of earthquakes. When the behavior under investigation is velocity or strain-rate dependent, such as in cases where structures incorporate active, semi-active, or passive control devices, real-time dynamic testing is necessary.

Shake table testing can simulate real-time dynamic loading on structural models. However, structures tested on shake tables typically have to be scaled down, and very few shake tables have the capacity as shown in Ogawa et al. (2001) to apply earthquake loads to full-scale structures. At smaller scales, it is difficult to investigate structural details such as anchorage of reinforcements in concrete and resistance mechanisms such as shear. Tests with small-scale models also may not accurately demonstrate the effect of structural control devices. In addition to the scaling limit, table outputs may not replicate

the required ground motion due to the interaction between the table and the test structure, especially when the test structure behaves nonlinearly (Shield et al., 2001). Shake tables tests are also economically constrained due to the high cost of table construction.

Effective force testing (EFT) is a real-time dynamic testing technique that overcomes many of the limitations of shake tables, while using common laboratory equipment (i.e., servo-hydraulic actuators). EFT is applicable to structures that can be represented by lumped-mass systems as in a shake table test. With the EFT method, hydraulic actuators apply dynamic forces through the center of mass of the test structure attached to a fixed base. Motions measured relative to the ground would be equivalent to the responses that the structure would develop relative to a moving base as in a shake table test or an earthquake event (Dimig et al., 1999; Shield et al., 2001).

1.2 Effective Force Testing

EFT is based on a transformation of coordinates (Murcek, 1996). Consider a single-degree-of-freedom (SDOF) system subjected to ground acceleration shown in Fig. 1.1 (a), the structural response relative to the global reference x_t is the summation of the relative response to the shake table x and the table motion x_g. The governing differential equation of the structure can be obtained by applying D'Alembert's principle of dynamic equilibrium to the free-body diagram of the structure shown in Fig. 1.1 (a),

$$m\ddot{x}_t + c\dot{x} + kx = 0\,, \tag{1.1}$$

where m is the mass of the system, c is the equivalent viscous damping coefficient, and k is the system stiffness (Chopra, 1995). Because the total structural acceleration $\ddot{x}_t$, is

defined as $\ddot{x}_t = \ddot{x} + \ddot{x}_g$, Eq. (1.1) can be rewritten as

$$m\ddot{x} + c\dot{x} + kx = -m\ddot{x}_g = P_{eff} . \quad (1.2)$$

The structure subjected to effective force testing is illustrated in Fig. 1.1 (b), in which hydraulic actuators are used to apply "effective forces" (P_{eff}) to the center of the structure mass. The effective forces are the product of the ground acceleration and the structure mass. Hence, they are known a priori and are independent of the structural properties (i.e., stiffness and damping) and the changes in structural properties during a test. If the actuator could apply effective forces accurately to the test structure, the responses of the structure in an EFT test would be same as those in the shake table test.

1.3 Literature Review

1.3.1 Effective Force Testing

The concept of EFT was first described in papers discussing the pseudodynamic testing method (Mahin and Shing, 1985; Mahin et al., 1989). These papers presented the possibility of conducting real-time tests using a pseudodynamic test setup with explicit time-varying forces imposed at the center of the lumped mass. It was pointed out that this technique would eliminate the need for computing required displacements as in pseudodynamic testing while it would require high-quality controllers and servovalves.

Murcek (1996) first experimentally evaluated the effective force testing method using a linear elastic SDOF system, which consisted of a cart and a pretensioned (to 15 kip to prevent possible buckling) rod that served as a spring. The structural stiffness, natural frequency, and damping were found to be 67.1 kips/in., 6.2 Hz, and 2% critical damping, respectively. A 77-kip actuator with a three-stage 90-gpm servovalve was used to apply

the required effective forces. Both sinusoidal forces and earthquake effective forces were tested. It was found that when controlled only by the feedback control coming with the test equipment, the actuator was unable to apply forces accurately near the natural frequency of the test structure. The inability of the actuator to apply force accurately was attributed to the interaction between the actuator control and the structure through an intrinsic "natural velocity feedback" loop (Dyke et al., 1995).

After identifying the problem and confirming it through computer simulations, Murcek proposed a solution: a velocity feedback correction loop added to the control of the actuator to negate the effect of the natural velocity feedback. The natural velocity feedback was compensated by modifying the command signal to the servovalve based on the measured structure/piston velocity. The solution was tested through simulations, based on which, Murcek further noted that the performance of the compensated system would depend on the accuracy of the servo-system modeling.

This experimental verification of the solution using precorrected command signals is summarized in Dimig et al. (1999). The correction to the command signals was made using the anticipated velocity of the test structure instead of the measured velocity in real time. The expected velocity was calculated by solving the equation of motion of the linear elastic SDOF structure, and the modified command was generated before testing. Test results showed that with the precorrected command signals, the actuator was able to apply effective forces at all frequencies (0-10 Hz).

Timm (1999) implemented the velocity feedback correction using the same test setup with a measured velocity. It was found that when the compensation was made in real time instead of using the precorrection, the expected resonance at the natural frequency of

the structure was not excited. This was attributed to an inevitable response delay in the servo-system because the implementation of EFT with the precorrected command signals was successful, and yet a time offset in the measured response was evident compared to the expected response. Timm modified the analytical model of the servo-system to include a phase delay of the servovalve and proposed a phase adjustment for the velocity feedback compensation to negate the response delay. Computer simulation incorporating the phase delay confirmed the findings and the proposed solution. Tests with phase adjusted velocity feedback correction demonstrated success in applying forces near the natural frequency of the structure.

Shield et al. (2001) summarized this work and pointed out that the effective force testing method enabled real-time dynamic tests for the linear elastic system and the implementation of EFT was independent of the properties of the test structure. On the other hand, several mismatches in the comparison of the Fourier amplitude of the measured forces and the command forces were evident, such as a sharp drop at the natural frequency (6 Hz), a spike around 12 Hz, and a discontinuity near 4 Hz. The discontinuity near 4 Hz was likely caused by an additional vibration mode of the system associated with a bouncing motion of the cart. The other two mismatches were attributed to the 15-kip offset of the actuator force command (to keep the bar pretension) because simulations without the pretension did not show the drop and the spike, and simulations with the pretension showed the drop and the spike.

The previous implementations of velocity feedback compensation and the validation of the EFT method were limited by the test setups in that the test structure needed to be its linear range of behavior. In addition, the relatively large stiffness and the large natural

frequency prevented large velocity responses of the structure; hence the concept of the velocity feedback compensation could only be tested within a limited operating range of the servovalve. The bar pretension also caused the servovalve to have nonlinear behaviors, which were not considered in the previous investigations due to the limitation of the analog circuits used in the studies. A new test setup and digital implementation were necessary to investigate the natural velocity feedback and its compensation techniques at large flow demands.

1.3.2 Natural Velocity Feedback

The natural velocity feedback describes the interaction between the actuator control and actuator piston motion. The principles for the interaction were described by Merritt (1967) through a continuity analysis of fluid volumes in actuator chambers. However, the applications of the principles documented in Merritt (1967) were in displacement-controlled systems; hence, the effect of the natural velocity feedback on the force tracking ability of actuators was not demonstrated.

Dyke et al. (1995) studied the effect of the control-structure interaction in the design of active structure control strategies. It was shown using pole-zero mapping that the poles of the structure attached to the actuator were also the zeros of the transfer function from the command to the actuator force. Therefore, the actuator attached to a lightly damped structure would be greatly limited in its ability to apply forces near the natural frequency of the structure. Actuators would be unable to apply a force at the natural frequency of undamped structures. As part of the study, the interaction between the actuator control and the structure was demonstrated by a feedback loop from the structure velocity to the load flow of the servovalve, and the feedback loop was named "natural

velocity feedback."

Alleyne et al. (1999) explained a similar force-tracking problem in the control of active suspension of automobiles using hydraulic actuation. It was discussed that due to the intrinsic piston velocity feedback, the force tracking ability of a hydraulic actuator could be greatly limited near the natural frequency of the attached system. It was further pointed out that simple control strategies, such as a Proportional-Integral-Derivative (PID) control, are not sufficient for a system in force control using servo-hydraulic actuation, and more advanced control algorithms are necessary.

The interaction between the actuator and the attached structure can be found in other applications of hydraulic actuation under force control, such as in Niksefat et al. (2001). It is evident in their derivation of the transfer function of the controlled system that the poles of the structure attached to the actuator are also the zeros of the overall transfer function. However, the dynamics of the attached structure was stiffness-dominant (the system mass and damping were negligible), therefore the natural frequency of the system was very large, and the effect of the natural velocity feedback were neglected.

1.3.3 Velocity Feedback Compensation

The detrimental effect of the natural velocity feedback on a force-controlled test system was observed during the development of the EFT method. As discussed previously, a solution, velocity feedback correction, was proposed by Murcek (1996) and implemented by Timm (1999) to compensate for the effect. The experimental results showed success of the solution under limited conditions. In the solution, a positive velocity feedback loop was added to the control of the servo-system to eliminate the interaction between the actuator control and the structure attached to the actuator.

Similar concepts can be found in other applications of servo-hydraulic actuation. Heintze (1997) discussed a "cascade ΔP inner-loop control" of a servo-hydraulic actuator, which combined with a displacement controlled outer loop, improved the position tracking ability of a brick-laying robot. In the inner-loop control, a velocity feedback compensation, which was conceptually similar to the velocity feedback compensation, was used to decouple the dynamics of the actuator load (i.e., the structure attached to the actuator) from the actuator control. Schothorst (1997) further explained the concept of the "cascade ΔP inner-loop control", and pointed out that the inner-loop control would make the actuator act as a force generator (i.e., the actuator would follow a force command). The inner-loop control combined with a multi-fold outer-loop control (displacement, velocity, and acceleration) was used to control a flight simulator.

In both applications, the structures were mass-dominant systems, thus the natural frequency of the structure was very small. In addition, force tracking was not the control objectives, and velocity feedback compensation was treated as a means for improving the performance of the outer-loop control. The compensated was based on the desired velocity of the flight simulator or the estimated velocity of the robot arm, resulting in feedforward compensation. Consequently, the importance of the response delay of the servo-system was not noticed. To avoid potential instability, undercompensation by using a larger servovalve flow gain in the compensation was recommended (Heintze et al., 1995).

Alleyne (1996) proposed a Lyapunov-based control algorithm for force tracking of a servo-hydraulic actuator in applications of a machine tool axis. The control algorithm was later applied to the control of an active automobile suspension system (a structure

with mass, damping, and stiffness) (Alleyne et al., 2000). In the experimental study, the excitation frequency (1 Hz) was not close to the natural frequency of the test setup (4 Hz), and the system damping was large (25% of critical damping). Therefore, the effect of the natural velocity feedback was not clearly demonstrated. The Lyapunov-based algorithm was further simplified such that the determination of the system input (desired valve command) included a velocity feedback compensation term. It was further pointed out that if the dynamics of the actuator load were well known, the velocity feedback compensation could actually be replaced by a feedforward compensation as indicated by Heintze et al. (1995). However, the coefficient of the velocity feedback compensation term was not explicitly given.

Although aforementioned studies have provided some information regarding the natural velocity feedback and the velocity feedback compensation, their effects on an EFT system (a force-controlled system) have not been fully understood. The EFT system is unique because force tracking of the actuator is the control objective, and the behavior and the dynamics of the test structure are typically not known before testing. Therefore, it is necessary to systematically investigate the natural velocity feedback and its compensation. For this purpose, detailed mathematical models of the system including system nonlinearities are necessary.

1.3.4 Servo-system Modeling

Modern servo-hydraulic control dates from World War II, when Mr. Moog invented the servovalve (Maskrey et al., 1978). Ever since then, servovalves have seen numerous applications in transportation, machinery, missile, and robot control. The great demand for this highly efficient means of power transmission has fostered the rapid development

of modern hydraulic control engineering. The text by Merritt (1967) covers the fundamentals, operating principles, modeling, and analysis of hydraulic control components and systems. Nonlinearities in control systems briefly mentioned at the end of the text have been further studied by others for various applications. In addition, the specification standards for servovalves (Thayer, 1965) and specifications for individual products, such as Moog specifications and MTS specifications have been helpful for people to understand and model the behavior of servovalves and actuators.

Based on the well-documented operating principles of servovalves, various models with different complexity levels have been derived for individual applications. Nikiforuk et al. (1969) presented a detailed analysis of a two-stage servovalve, which considered the dynamics and interaction of major valve components, such as a nozzle-flapper and spool. Wang et al. (1995) developed a detailed nonlinear model for a two-stage MTS servovalve, in which the component dynamics and interactions, such as jet flow forces on the pilot-stage spool were considered. Theyer (1965) provided a "simplified" model for two-stage Moog valves, which included armature-flapper dynamics of the first-stage valve. Schothorst (1997) and Heintze (1997) considered the flapper-nozzle dynamics for the pilot-stage in their modeling of a three-stage servovalve. The dynamics of the main-stage spool was omitted; instead the main-stage spool velocity was directly related to the pilot-stage flow by a constant. A nonlinear main-stage flow property was observed during their system identification though a single flow gain was used in the controller design. A problem with these complex models is that it is difficult to accurately determine the model parameters.

On the other hand, simple models have been developed and used in many engineering

applications of servovalves. Newell et al. (1995) presented a model for a two-stage servovalve used in a small-size sliding shake table. The dynamics of the servovalve was represented by a first-order transfer function, and the actuator piston friction and the load pressure influence on the servovalve flow property were considered. Conte et al. (2000) derived a linear model for a three-stage servovalve used in controlling a uni-axial shake table. The servovalve dynamics were represented by a gain and a response delay term. The valve flow was assumed proportional to the servovalve spool opening. Gavin (2001) described a two-stage servovalve model, in which the servovalve dynamics were approximated by a first-order term, and the nonlinear servovalve flow property (i.e., load pressure influence) was linearized using Taylor's expansion as described in Merritt (1967). These simple models are helpful for linear system analysis and linear controller design; however, simple models can be insufficient to capture the significant nonlinear dynamics of a servo-system.

To implement the effective force testing method, large size servovalves are necessary for testing large size structural systems undergoing large velocities. Hence, there is a need for accurate yet uncomplicated servo-system models that can capture the major dynamics and nonlinearities of a three-stage servovalve. In the mean time, the model parameters should be identifiable with typical structural laboratory equipment.

1.4 Objectives and Research Scope

The purpose of the research was to extend the development and implementation of the EFT method to fully utilizing the capacity of test equipment and to testing nonlinear SDOF structural systems undergoing large deformations in real time. The objective of

the research was to control the actuator to follow effective force commands accurately and robustly even when the servo-system was taken into its nonlinear range of behavior as the test required large hydraulic power (flow). The feasibility of the EFT method was examined by comparing the forces applied to the test structures (measured by a load cell) with respect to the command forces (effective forces). Comparison of structural responses provided a secondary validation of the compensation scheme designs.

The objective of this research was accomplished in two phases. In the first phase, detailed mathematical models for a test system were derived to better understand the system behavior and to facilitate the development of the velocity feedback compensation schemes. Numerical simulations and linear system analysis were conducted to investigate potential stability problems. Experimental tests on a simple SDOF (mass-spring-damper) structure were used to validate the analytical results. The structure was designed to have repeatable nonlinear structural behaviors such that the effect of structural nonlinearities on the test system performance could be studied.

In the second phase of the study, a one-story steel structure was tested on a shake table at the University of Illinois and using EFT at the University of Minnesota. Results obtained using two earthquake simulation techniques were compared to validate the EFT method, and to verify the feasibility of the proposed nonlinear velocity feedback compensation scheme. The comparison included both global responses (effective forces, structure accelerations, velocities, and displacements) and local responses (damper forces, and column base shears).

The dissertation is organized as follows. Chapter 2 presents fundamentals and background knowledge in structural engineering, hydraulics, and control engineering,

which are essential to understanding and modeling the test system. Chapter 3 contains a derivation of a servo-system model for the simulation of the system behavior and for the design of velocity feedback compensation schemes. Chapter 4 describes the system identification, in which the parameters used in the models developed in Chapter 3 were determined with available resources and designed experiments.

Chapter 5 presents an analysis of the natural velocity feedback and the concept of velocity feedback compensation. A nonlinear velocity feedback compensation scheme was designed and validated analytically. Chapter 5 also summarizes an investigation of the effects of three critical parameters on the performance of the velocity feedback compensation. Chapter 6 presents the experimental validation of the proposed nonlinear velocity feedback compensation and the conclusions drawn in Chapter 5 regarding the critical parameters.

Chapter 7 presents a discussion of important factors that can affect the performance of the EFT method and related stability problems. Chapter 8 summarizes a proof-of concept test for the EFT method, in which a one-story steel structure was tested using a shake table and the EFT method, and test results were compared. Finally, Chapter 9 summarizes the conclusions drawn from the research at the University of Minnesota on the implementation of nonlinear velocity feedback compensation for effective force testing.

CHAPTER TWO

BACKGROUND AND FUNDAMENTALS

When testing structures using the EFT method, servo-hydraulic actuators are powered by hydraulic fluid under pressure and in force control (i.e., the command and feedback signals are forces). The multidisciplinary research requires knowledge in structural dynamics, hydraulics, and modern feedback control. This chapter provides some basic engineering concepts and methods in these fields to facilitate the understanding of the physical system operation, test system modeling, and control algorithm design.

2.1 Dynamic Analysis of SDOF Structures

Structures, such as highway bridges and one-story buildings can be modeled as single-degree-of-freedom (SDOF) systems when subjected to earthquake loadings. The equation of motion for a SDOF system in Eq. (1.1) can be derived from D'Alembert's principle of dynamic equilibrium. The equation in a more general form is

$$m\ddot{x} + f_D + f_S = -m\ddot{x}_g \tag{2.1}$$

where f_D is the damping force and f_S is the resistance force.

The damping component models the energy dissipation of the structural system. Although many mechanisms contribute to the energy dissipation, damping in structural systems is usually idealized as viscous damping (causing an exponentially decaying free vibration response) and Coulomb friction (causing a linearly decaying free vibration

response) (Chopra, 1995). The damping can be further idealized by an equivalent viscous damping (i.e., $f_D = c\dot{x}$) to simplify system analyses.

Force f_S represents the force-deformation relation of a structural system, and is usually determined by structural analysis or through static loading tests. This relationship is of interest because it describes the ability of the structure to resist external forces. Typically, the initial structural response is linear elastic (i.e., the resisting force is proportional to the structural deformation, $f_S = kx$). Beyond the linear elastic range, the structure can be either nonlinear elastic, such as the one shown in Chapter 3 through Chapter 7 or nonlinear (i.e., the resisting force is a function of the structural deformation history), such as the one shown in the proof-of-concept test in Chapter 8.

The governing differential equation of a linear elastic structure subjected to sinusoidal force is

$$m\ddot{x} + c\dot{x} + kx = p_0 \sin \omega t \,. \tag{2.2}$$

The solution of Eq. (2.2) with zero initial conditions (i.e., $x(0) = 0$ and $\dot{x}(0) = 0$) is (Chopra, 1995)

$$x(t) = \underbrace{e^{-\xi\omega_n t}(A\cos\omega_D t + B\sin\omega_D t)}_{\text{transient}} + \underbrace{C\sin\omega t + D\cos\omega t}_{\text{steady state}} \tag{2.3}$$

where

$$\begin{aligned} C &= \frac{p_0}{k}\frac{1-(\omega/\omega_n)^2}{\left[1-(\omega/\omega_n)^2\right]^2 + \left[2\zeta(\omega/\omega_n)\right]^2} \\ D &= \frac{p_0}{k}\frac{-2\zeta(\omega/\omega_n)}{\left[1-(\omega/\omega_n)^2\right]^2 + \left[2\zeta(\omega/\omega_n)\right]^2} \end{aligned} \tag{2.4}$$

and

$$A = -D$$
$$B = -\frac{\zeta}{\sqrt{1-\zeta^2}} D - \frac{\omega/\omega_n}{\sqrt{1-\zeta^2}} C \tag{2.5}$$

where $\omega_n = \sqrt{k/m}$ is the natural frequency, $\omega_D = \sqrt{1-\zeta^2}\omega_n$, is the damped natural frequency, and $\zeta = c/(2\sqrt{mk})$ is the damping coefficient of the structure. The vibration at the forcing frequency persists (thus called steady-state response) while the transient response decays with time due to structural damping. The decaying rate and pattern depend on the structural damping.

If the forcing function is an earthquake ground acceleration input, numerical methods, such as the Newmark-β method (with γ = 1/2 and β = 1/4), were used to solve the equation of motion. When the structure went into the nonlinear range of behavior, Newton-Raphson iteration was applied to each incremental time step to minimize computational errors. The calculated structural responses (referred to as expected responses) were compared to measured responses.

The effective forces were applied to the structure through an actuator, which was powered by hydraulic fluid under pressure. Hence, knowledge of hydraulics is essential for understanding and modeling the servo-system behavior.

2.2 Fluid Mechanics

A petroleum-based fluid, Mobil DTE 25, was used in the servo-system of this study (MTS, 1994). Some physical properties of hydraulic fluids such as density, viscosity, and bulk modulus and fluid flow such as Bernoulli's equation and Reynolds number are introduced in this section. In addition, the properties of hydraulic flows through orifices

are discussed in detail because flow through orifices enables the hydraulic power transmission from the supply (hydraulic pumps) to applications.

2.2.1 Hydraulic Fluid Properties

Density

The weight density, γ (in terms of lb/in^3), of a Mobil DTE 25 fluid is 0.0319 lb/in^3 at 0°F (Exxonmobil, 1996). The variation of the weight density with the temperature of the fluid is

$$\gamma_{@T} = 0.0319 - 0.144 \times 10^{-4}(T - 60^{\circ}\text{F}) \tag{2.6}$$

where T is the temperature in Fahrenheit. The fluid temperature in the operation of the servo-system was typically around 120°F; therefore, the weight density of the Mobil DTE 25 fluid under the operating condition was approximately 0.031 lb/in^3.

The mass density of the fluid ρ, in units of lb-sec^2/in^4, can be calculated using

$$\rho = \frac{\gamma}{g} \tag{2.7}$$

where g is the acceleration due to gravity, 386.1 in/s^2. For the Mobil DTE 25 fluid in the test system in operation, the mass density is 0.8×10^{-4} lb-sec^2/in^4.

Viscosity

Viscosity of the fluid represents the friction between fluid layers when relative motion between layers occurs (resembles the damping of a fluid in motion). The absolute viscosity of a fluid μ, in units of lb-sec/in^2, is directly defined as the ratio of the friction force to the velocity gradient. In terms of μ the kinematic viscosity is defined by

$$\nu = \frac{\mu}{\rho}, \tag{2.8}$$

and appears in many equations and definitions of fluid properties.

The fluid viscosity varies with the fluid temperature. For a Mobil DTE 25 fluid, the kinematic viscosity was typically 0.066 in^2/sec at 104°F and 0.01 in^2/sec at 212°F (Exxonmobil, 1996). Through linear interpolation, the kinematic viscosity was 0.058 in^2/sec at the common operation temperature (120°F).

Bulk Modulus

The bulk modulus β of a fluid describes the change in the fluid volume along with the change in fluid pressure at a constant temperature T, and is defined as

$$\frac{1}{\beta} = -\frac{1}{V_0}\left(\frac{\partial V}{\partial P}\right)_T \tag{2.9}$$

where V is the volume of the fluid, V_0 is the initial total volume of the fluid, and P is the pressure to which the fluid is subjected.

The bulk modulus of a fluid represents the "stiffness" of the fluid. The bulk modulus for Mobil DTE 25 under 3000 psi pressure was 253.7 ksi at 120°F. However, a value as high as this is rare in practice because entrapped air can significantly reduce the bulk modulus. Because an accurate measurement of the bulk modulus is difficult to obtain, experience is essential in estimating the bulk modulus of the fluid in the servo-system. According to Merritt (1967), an effective bulk modulus (β_e) of 100 ksi can yield reliable results for petroleum base hydraulic fluids. The effective bulk modulus value was used throughout this study.

2.2.2 Hydraulic Flow

The analysis of a general compressible flow is not necessary for most applications of hydraulic actuation in structural/material testing because the typical operation pressure (3

ksi) of a hydraulic fluid is small compared to the bulk modulus of the fluid (β_e, 100 ksi). In addition, the pressure variation that affects the volume of the fluid is negligible (typically less than 1 ksi). Therefore, incompressible flow is a good approximation of the hydraulic flow in the test system, and an analysis of flow of an incompressible fluid with a constant density and viscosity is discussed next.

Navier-Stokes Equations

The equation of motion of a flow can be derived by applying Newton's second law to an infinitesimal control volume (Street, 1993). The resulting Navier-Stokes equations is given here for a two-dimensional incompressible flow with a constant mass density of ρ and an absolute viscosity of μ,

$$\begin{aligned}\rho\left(\frac{\partial u}{\partial t}+u\frac{\partial u}{\partial x}+w\frac{\partial u}{\partial z}\right)&=\rho X-\frac{\partial P}{\partial x}+\mu\left(\frac{\partial^2 u}{\partial x^2}+\frac{\partial^2 u}{\partial z^2}\right)\\ \rho\left(\frac{\partial w}{\partial t}+u\frac{\partial w}{\partial x}+w\frac{\partial w}{\partial z}\right)&=\rho Z-\frac{\partial P}{\partial z}+\mu\left(\frac{\partial^2 w}{\partial x^2}+\frac{\partial^2 w}{\partial z^2}\right)\end{aligned} \tag{2.10}$$

where u and w are the velocity components of the flow in the x and z direction of Cartesian coordinates, respectively, t is time, X and Z are the body forces per unit volume in the x and z directions, respectively, and P is pressure acting on the fluid.

Fluid motion (flow) is generally dominated by either inertia forces (mass) or friction forces (viscosity). Flows dominated by inertia forces are referred to as turbulent, and are characterized by irregular motion of fluid particles while flows dominated by viscosity are referred to as laminar, and are characterized by orderly motion of fluid. The different regimes of a flow can be distinguished by its Reynolds number.

Reynolds Number

The Reynolds number, a dimensionless quantity, is used to describe the transition

from inertia-dominated flows to viscosity-dominated flows (Street, 1993). The Reynolds number is defined as the ratio of the inertial forces to the friction forces of a flow,

$$R = \frac{\rho u d}{\mu} = \frac{u d}{\nu} \tag{2.11}$$

where u is the average velocity of the flow and d is a characteristic length of the flow. The flow velocity can be approximated by the total flow rate divided by the cross-sectional area of the flow while the characteristic length is different from one case to another, and is typically related to the geometry of the flow passage.

The behavior of laminar flows could be obtained by solving the Navier-Stokes equation, while obtaining the behavior of turbulent flows is typically empirical (Merritt, 1967). On the other hand, solving the Navier-Stokes equations for general flow relationships is neither practical nor necessary for engineering practices. In many cases, such as flows in pipes or through orifices, simplified analyses can be used to generate accurate and useful results.

Potential Flow and Bernoulli's Equation

For a flow in a cylindrical pipe or through an orifice, friction forces are important only on boundaries, such that the flow away from the boundary is dominated by inertial forces, but behaves like a laminar flow. If the boundary can be neglected, the resulting orderly flow dominated by inertial forces is termed potential flow (Merritt, 1967).

Consider an incompressible potential flow subjected to a negligible body force. In its steady state, the following assumptions can be made: $\partial u/\partial t = 0$ (steady state), $X = 0$ (no body forces), and $\mu = 0$ (no friction forces in main body of flow). The general Navier-Stokes equation (2.10) reduces to

$$u\frac{\partial u}{\partial x} = -\frac{1}{\rho}\frac{\partial P}{\partial x}, \tag{2.12}$$

and after integration to

$$\frac{u^2}{2g} + \frac{P}{\gamma} = constant\ . \tag{2.13}$$

Eq. (2.13) is called Bernoulli's equation. Note that an average velocity across the flow section is used in Bernoulli's equation to simplify the analysis. Bernoulli's equation can be used to describe flow through orifices, which is the basic means of controlling hydraulic power in a servo-system.

Flow through Orifices

An orifice is a sudden change in a flow passage or a sharp-edged opening. The flow through an orifice inside a cylindrical pipe shown in Fig. 2.1 is comparable to the flow in a servovalve. Referring to Fig. 2.1, the application of Bernoulli's equation at a point upstream (point 1) and a point a distance away from the orifice downstream (point 2, termed vena contracta) yields

$$\frac{u_2^2}{2g} + \frac{P_2}{\gamma} = \frac{u_1^2}{2g} + \frac{P_1}{\gamma} = constant \tag{2.14}$$

where P_1 and P_2 represent the pressure upstream and downstream, and u_1 and u_2 are the average velocities of the flow at the two points, respectively.

For an incompressible flow, the conservation of mass requires

$$Q = A_1 u_1 = A_2 u_2 \tag{2.15}$$

where Q is the flow rate in in^3/s, and A_1 and A_2 are the cross-sectional area of the flow at the two points under consideration. The cross-sectional area of the pipe A_1 is readily known while the vena contracta area A_2 is usually difficult to obtain. To facilitate the

analysis, the vena contracta area is replaced by the modified orifice area C_cA_0. Substituting (2.15) into (2.14) gives

$$Q = C_d A_0 \sqrt{\frac{2}{\rho}(P_1 - P_2)} \tag{2.16}$$

where $C_d = C_c \Big/ \sqrt{1 - C_c^2 (A_0 / A_1)^2}$ is the discharge coefficient of the orifice flow. The discharge coefficient is a function of orifice geometry and the flow properties, and is difficult to obtain analytically except for a few ideal cases.

Discharge Coefficient

The discharge coefficient of a flow is usually expressed as a function of its Reynolds number. Because the Reynolds number is linked back to the flow rate to be determined, discharge coefficients are often estimated experimentally. Figure 2.2 shows a discharge vs. Reynolds number plot for a pipe orifice flow that is closer to a laminar flow than a turbulent flow (Merritt, 1967). The discharge coefficient increases rapidly with an increase of Reynolds number for a low Reynolds number range. Beyond that region, the discharge coefficient decreases asymptotically to a constant value as the Reynolds number increases.

The submerged orifice shown in Fig. 2.3 can be characterized in a similar way. In this case, the upstream pressure keeps constant, and the downstream pressure varies, which are similar to a valve orifice with a constant pressure supply, and variable load pressure. As can be demonstrated, the relationship between the flow rate Q and the pressure drop across the orifice (P_1-P_2) is similar to Eq. (2.16). Again, the discharge coefficient can be treated as a function of the Reynolds number. A typical plot of the discharge coefficient vs. Reynolds number for this flow case is shown in Fig. 2.4 (Street,

1993). Similar observations can be made: the flow discharge increases rapidly with an increase in the Reynolds number at the low Reynolds number region. After the peak, the flow discharge decreases asymptotically.

Therefore, the nature of the discharge of an orifice flow is nonlinear with respect to the Reynolds number, which is a function of the fluid properties and orifice geometry. However, experience has shown that a discharge coefficient of C_d = 0.6 may be a good approximation for flows through small orifices (i.e., $A_0 << A_1$) (Merritt, 1967).

The flow through servovalve orifices enters actuator chambers to cause differential pressures and generate mechanical forces that are applied to test structures. The relation between hydraulic flows and the resulted mechanical forces is described by the law of conservation of mass.

2.2.3 Continuity Equation

Consider a fluid with a mass density ρ in a controlled volume V_0 (e.g., an actuator chamber), the law of the conservation of mass states that the rate of the mass change in the volume must be equal to the incoming flow rate minus the outgoing flow rate (Merritt, 1967). Therefore,

$$\sum M_{in} - \sum M_{out} = \frac{d\left(\rho V_0\right)}{dt} = \rho \frac{dV_0}{dt} + V_0 \frac{d\rho}{dt} \tag{2.17}$$

where $M=\rho Q$, and Q is the flow rate. The mass density ρ is a function of pressure and temperature of the fluid inside the control volume. The first-order terms Taylor's series expansion may be used to approximate the small variation of ρ (Merritt, 1967),

$$d\rho = \left(\frac{\partial \rho}{\partial P}\right)_T dP + \left(\frac{\partial \rho}{\partial T}\right)_P dT \,. \tag{2.18}$$

Because the temperature of hydraulic fluids in operation is approximately constant, the rate of change in density of the controlled fluid volume (i.e., ρV=constant) as a function of pressure is

$$\frac{d\rho}{dt} = \rho \frac{dP}{dt} \frac{1}{\rho} \left(\frac{\partial \rho}{\partial P} \right)_T = \rho \frac{dP}{dt} \left[-\frac{1}{V} \left(\frac{\partial V}{\partial P} \right)_T \right] = \frac{\rho}{\beta} \frac{dP}{dt}. \tag{2.19}$$

Substituting Eq. (2.19) into Eq. (2.17) and dividing both sides by ρ gives

$$\sum Q_{in} - \sum Q_{out} = \frac{dV_0}{dt} + \frac{V_0}{\beta} \frac{dP}{dt}. \tag{2.20}$$

The law of the conservation of mass shown in Eq (2.20) indicates that the net flow into a controlled volume (such as an actuator chamber) is consumed by the expansion of the volume and the compression of the fluid inside the volume due to increased pressure. Note that the compressibility of hydraulic fluids is small enough that the mass densities of the incoming fluid, the outgoing fluid, and the fluid inside the volume are assumed identical.

Hydraulic power is transmitted from supply sources (e.g., a hydraulic pump) to test structures through controlled orifice flows described using Eqs. (2.16) and (2.20). Such control of the power transmission is made in real-time automatically through actuators, servovalves, and their controllers. Therefore, knowledge of general dynamic systems and feedback control is essential in understanding the behavior of a test system.

2.3 Feedback Control of Dynamic Systems

Dynamic systems are usually modeled by differential equations. The response of the systems to an input can be obtained by solving the governing differential equations for

the input. Similar to the dynamic analysis of a SDOF structure, numerical simulations are required to calculate the response of dynamic systems when inputs are arbitrary or when the system has significant nonlinearities. On the other hand, analyzing system performances in general, such as stability, is essential in control engineering. Although stability can be analyzed for nonlinear systems, linearization of the system about an equilibrium point (e.g., the system null position in this study) can greatly facilitate the analysis and controller design. For a linearized system with single input and single output, frequency domain methods of control system design can be applied.

2.3.1 Transfer Function

The response of the one-story structure shown in Fig. 1.1 (a) to an earthquake input can be determined by solving the equations of motion ($m\ddot{x} + c\dot{x} + kx = u(t)$) in the time domain as shown in Eq. (2.1) through Eq. (2.5). Specifically, if the input function takes the form of a complex exponential, $u(t) = e^{st}$, where s is complex (i.e., $s = \sigma + j\omega$), the particular solution (steady-state response) of the system can be assumed as

$$x(t) = H(s)u(t) = H(s)e^{st} \tag{2.21}$$

Substituting Eq. (2.21) into the differential equation of the system gives

$$ms^2H(s)e^{st} + csH(s)e^{st} + kH(s)e^{st} = e^{st} \tag{2.22}$$

and solving Eq. (2.22) for $H(s)$ yields

$$H(s) = \frac{1}{ms^2 + cs + k} = \frac{x(t)}{u(t)} \tag{2.23}$$

Function $H(s)$ is called the transfer function of the linear system, which directly relates the system output to the input e^{st}. For a general linear system, the transfer function is defined as the ratio of the Laplace transform of the system output to the

Laplace transform of the system input, and can be formulated using Laplace transform theorems with zero-initial-condition assumptions (Ogata, 1997).

A dynamic system may include multiple sub-systems, which are connected in such a manner that the input of one sub-system is the output of another sub-system. The transfer function of each component can be placed in a box, and the input-output relationships between components can be represented by lines with arrow ends. With the resulting block diagram, the transfer function of the overall system can be obtained following the rules of block diagram algebra (Franklin, 1999).

The transfer function of a linear system provides an algebraic representation of the system because it is an operational expression of the governing differential equations of the system. Once the transfer function of a linear dynamic system is established, analytical tools of modern control engineering, such as the pole-zero map, root locus, and frequency response method, can be used to obtain the characteristics of the system.

2.3.2 Pole-Zero Map

If the behavior of a dynamic system is modeled as a group of ordinary differential equations, its overall transfer function is a ratio of polynomials,

$$H(s) = \frac{num(s)}{den(s)} = K\frac{(s-z_1)(s-z_2)\cdots}{(s-p_1)(s-p_2)\cdots}. \tag{2.24}$$

where z_i (roots of $num(s) = 0$) are zeros of the system and p_i (roots of $den(s) = 0$) are poles of the system, respectively. The poles and zeros of a system can be plotted in the s-plane (σ-axis vs. ω-axis), and the resulting plot is called a pole-zero map of the system. The positions of poles and zeros of a dynamic system in the s-plane indicate the system characteristics. For example, vibration modes and the frequency and damping of the

vibration, can be obtained directly from the plot.

Response of systems to a unit impulse input $\delta(t)$ is usually used to explain the correspondence between system responses and pole positions (Franklin, 1999). The correspondence is summarized in Fig. 2.5. Poles of a dynamic system decide the shape of the impulse response (exponential or sinusoidal function). Poles in the left half-plane correspond to stable responses of the system while right half-plane poles correspond to unstable responses. The stability criteria can be extended to a system subjected to other inputs because any input can be viewed as a sequence of impulses. Zeros of a system affect the system response by limiting the magnitude of the response corresponding to adjacent poles. Specifically, a zero on top of a stable pole cancels the contribution of the corresponding response to the total response of the system (Franklin, 1999).

System parameters may change, thus affecting the pole and zero locations and system characteristics, such as the system stability. The root locus method can be used to study the changing positions of the poles of a system in the *s*-plane with respect to the changing system parameters. In some cases, especially when the coefficients are in a symbolic form, it is necessary to analyze the stability of a system without solving for the roots of the denominator of the system transfer function.

2.3.3 Routh's Stability Criterion

The denominator of a system transfer function, $den(s)$ as shown in Eq. (2.24), is called the characteristic equation of the system. For an nth-order linear system, the characteristic equation is an nth-order polynomial:

$$den(s) = a_0 s^n + a_1 s^{n-1} + a_2 s^{n-2} + \ldots + a_{n-1} s + a_n \tag{2.25}$$

where the coefficients a_0 through a_n are real quantities. The previous discussion indicates

that the system is stable if all the roots of this equation have negative real parts. Routh's stability criterion provides a necessary and sufficient condition for stability without solving for the roots of the characteristic equation. A detailed procedure for applying Routh's stability criterion can be found in many control engineering texts, such as the ones by Franklin et al. (1999). An example is shown in Appendix 3 to investigate the stability of the test system.

Routh's stability criterion is a useful method for determining the ranges of parameters from the perspective of stability. On the other hand, such analysis needs an accurate model of the system while in some cases, an accurate model of the system is not available due to lack of knowledge and/or unknown system parameters. The system responses to a series of sinusoidal inputs with various frequencies can be measured to identify the system model. The response of a linear dynamic system subjected to sinusoidal inputs is referred to as the system's frequency response.

2.3.4 Frequency Response

For a stable system such as a damped second-order system subjected to a sinusoidal input, the transient response vanishes after awhile. At the steady-state, the frequency response of a system can be directly related to its transfer function. For example, given an input, $u(t) = p_0 \sin(\omega_0 t)$, the steady-state response of system shown in Eq. (2.2) is $x(t) = p_0 M \sin(\omega_0 t + \varphi)$ (Chopra, 1995). It can be shown that the amplitude ratio M is the magnitude of the transfer function of the system shown in Eq. (2.23) evaluated at the input frequency,

$$M = \frac{1}{\sqrt{\left(k - m\omega_0^2\right)^2 + \left(c\omega_0\right)^2}} = \left|H(j\omega_0)\right|, \tag{2.26a}$$

and the phase difference between the output and input is the phase angle of the transfer function evaluated at the input frequency,

$$\varphi = \tan^{-1}\left(\frac{c\omega_0}{k - m\omega_0^2}\right) = \angle H(j\omega_0)\,. \tag{2.26b}$$

The magnitude and phase angle of the transfer function of a system can be calculated for a range of frequencies, and plotted against the input frequencies. The resulting plots (i.e., magnitude and phase versus frequency) are called Bode plots. Magnitude plots are usually in logarithmic scale and the standard unit for magnitude is dB, which is equal to $20\log\left|H(j\omega)\right|$, where the base of the logarithm is 10. The frequency responses of simple first and second-order systems are discussed as follows.

First-order Term

For a system with $H(s) = (\tau s + 1)^{-1}$, where τ is a positive real number, the magnitude and phase are,

$$\left|H(j\omega)\right| = 1\Big/\sqrt{(\omega\tau)^2 + 1} \tag{2.27a}$$

$$\angle H(j\omega) = -\tan^{-1}(\omega\tau)\,, \tag{2.27b}$$

as shown in Fig. 2.6. The system output copies inputs with low frequencies while the response magnitude rolls off at high frequencies. At the frequency ω=1/τ, the magnitude of the system output reduces to about 70 percent of the input ($1/\sqrt{2}$, or -3dB) and the phase angle is -45°. The output always lags behind the input, and when the product of $\omega\tau$ is small, the phase lag can be approximated as,

$$\angle H(j\omega) = -\tan^{-1}(\omega\tau) \approx -\omega\tau \tag{2.28}$$

Similarly, for a system with $H(s) = (\tau s + 1)^{+1}$, the magnitude is the inverse of the

magnitude shown in Eq. (2.27a) and Fig. 2.6. The output has a phase lead ($\tan^{-1}(\omega\tau)$). When the product of $\omega\tau$ is small, the phase lead can be approximated as $\omega\tau$.

Second-order Term

For systems with $H(s)=\left[\left(s/\omega_n\right)^2+2\zeta\left(s/\omega_n\right)+1\right]^{-1}$, such as the one in Eq. (2.2), the magnitude and phase,

$$\left|H(j\omega)\right|=1\Big/\sqrt{\left(1-\left(\omega/\omega_n\right)^2\right)^2+\left(2\zeta\,\omega/\omega_n\right)^2} \tag{2.29a}$$

$$\angle H(j\omega)=-\tan^{-1}\left[\frac{2\zeta\,\omega/\omega_n}{1-\left(\omega/\omega_n\right)^2}\right], \tag{2.29b}$$

are shown in Fig. 2.7. The system output follows inputs with low frequencies while the response magnitude rolls off at a greater rate than that in a first-order system at high frequencies. For systems with low damping, inputs with frequencies around the natural frequency of the system are amplified.

At the system natural frequency, resonance happens and the magnitude is

$$\left|H(j\omega_n)\right|=\frac{1}{2\zeta}. \tag{2.30}$$

The response of a system with very small damping does not have a phase lag; rather the phase has a sudden change around the natural frequency of the system. However, if the system damping is large, the phase delay of the system response is not negligible. When $\frac{2\zeta}{\omega_n}\omega$ is small, the phase lag can be approximated by

$$\angle H(j\omega)=-\frac{2\zeta}{\omega_n}\omega \quad \text{for } \omega<<\omega_n. \tag{2.31}$$

For a system with $H(s) = (s/\omega_n)^2 + 2\zeta(s/\omega_n) + 1$, the frequency response is the inverse of the curve plotted in Fig. 2.7. Around the natural frequency of the system, the response magnitude will reduce depending on the system damping. Specifically, at the natural frequency of the system, the magnitude becomes

$$|H(j\omega_n)| = 2\zeta, \tag{2.32}$$

which indicates that a system with a pair of conjugate zeros will not respond well to sinusoidal inputs with a frequency close to its natural frequency. When the system damping is zero, the magnitude of the system response to inputs with the system natural frequency becomes zero.

Any system of the form (2.24) can be expanded in partial fractions with each term a 1st or 2nd order system. These basic terms can be used to generate frequency responses for the overall system (Franklin, 1999). Fig. 2.8 presents the frequency response of a third-order system made of a second-order term with a natural frequency of 1.6 Hz and a first-order term with a time constant of 0.05s. It can be observed that the slope of the magnitude response after the peak is larger than that in Fig. 2.7 though the basic shape does not change much. In addition, the phase lag is evident at all frequencies.

2.3.5 Applications of Frequency Response

Many complicated dynamic systems or system components behave in such a way that they can be approximately modeled using a first-order or second-order transfer function. Frequency response plots are sometimes given in product specifications for small amplitude inputs (to keep the system in the linear range of behavior). The frequency response of an unknown system can also be obtained experimentally using a series of

sinusoidal inputs or a sinesweep input (sine waves with linearly increased frequencies). An equivalent system model and the related parameters can be obtained from the obtained frequency responses.

On the other hand, the applicability of the theories always needs check. For example, in the study of an EFT system, transient responses are significant in total responses. Hence, the frequency response method might not be fully applicable in explaining the system behavior with an earthquake input. On the other hand, transient responses of a dynamic system are related to their steady-state responses as revealed in Section 2.1. Specifically, the coefficients of complementary solution of the governing differential equation are algebraic functions of the coefficients of its particular solution, from which the frequency response is derived. Therefore, the frequency response method combined with computer simulation, which includes both transient and steady-state responses, were used in the study.

First-order model identification

If a system is represented using a first-order transfer function, the required time constant τ can be determined by

$$\tau = 1/\omega \tag{2.33}$$

where ω is the frequency in rad/s, at which the magnitude response reduces to $1/\sqrt{2}$ (or roughly 70%) of input.

Second-order model identification

For a second-order approximation, two parameters are to be determined (ζ and ω_n). When the frequency response of a system is obtained experimentally with sinusoidal inputs, the system damping can be estimated by

$$\zeta = \frac{1}{2\left|H(j\omega_n)\right|}. \tag{2.34}$$

The natural frequency of the system is the frequency, at which the phase of the system is 90° (π/2).

Phase-lead network

Another example of a first-order system can be found in a phase-lead network,

$$H(s) = \frac{T_{ld}s + 1}{\alpha T_{ld}s + 1} \tag{2.35}$$

where T_{ld} is the time constant to be designated, and α is a constant smaller than unity. The frequency responses,

$$\left|H(j\omega)\right| = \sqrt{1 + \left(\omega T_{ld}\right)^2} \Big/ \sqrt{1 + \left(\alpha\omega T_{ld}\right)^2} \tag{2.36a}$$

$$\angle H(j\omega) = \tan^{-1}\left(\omega T_{ld}\right) - \tan^{-1}\left(\alpha\omega T_{ld}\right) \tag{2.36b}$$

are shown in Fig. 2.9 for two time constants (50 ms and 10 ms) and α equal to 0.1. When ωT_{ld} is small, the resulting phase lead can be approximated by

$$\angle H(j\omega) = \left(1 - \alpha\right)T_{ld}\omega\,. \tag{2.37}$$

Figure 2.10 shows the phase responses in regular scale. A frequency range exists for both given systems depending on the time constant T_{ld}, in which the phase angle is approximately proportional to input frequency. Within the linear range, the phase lead can be represented by the slope of the curve, T_l, determined by

$$T_l = \left(1 - \alpha\right)T_{ld}\,. \tag{2.38}$$

The slope has a unit of time, thus called lead-time, which represents the phase lead the network can provide.

The effectiveness of a phase-lead network can be affected by the constant α for a given time constant T_{ld}. On the other hand, a phase-lead network also amplifies signals as shown in the amplitude response in Fig. 2.9. The amplification is determined by the constant α because the magnitude of the frequency response becomes $1/\alpha$ as the input frequency goes to infinity. A range of values for the constant α may be appropriate for an application, and a value of 0.1 was chosen for this study.

2.4 Summary

This chapter presents a brief review of fundamentals in structural dynamics, hydraulics and control engineering, applications of which can be found throughout the thesis, from system identification/analysis to controller design. The next chapter presents the system modeling.

CHAPTER THREE

MODELING OF TEST SYSTEM

It is necessary to establish mathematical models for the test system before system analysis and control design. The derivation of mathematical models may take many paths depending on particular situations. Some equations can be obtained by applying physical principles while others may be approximated from analyzing experimental data. Both of these techniques were employed in this chapter.

3.1 Description of the Test System

A schematic of the test system is presented in Fig. 3.1, in which a 35 kip MTS 244.52 actuator is attached to a SDOF structure model. The actuator was controlled by a 90 gpm MTS 256.09 servovalve, which was in turn controlled by an MTS 407 analog controller. During a test, force command signals were sent from a personal computer to the servovalve controller, which compared the command signal to a feedback signal and sent a current proportional to the difference between these two signals to the servovalve to drive the valve spool. The spool regulated the hydraulic flow entering the actuator, causing differential fluid pressure across the actuator piston. The pressure difference multiplied by the piston area was approximately the force applied to the test structure. The force was sensed by a load cell on the actuator piston, and was fed back to the servovalve controller to close the control loop.

The servovalve is the key component of the servo-system because it converts

electronic command signals into physical motion of valve spools, which makes the regulation of hydraulic flow possible. As schematically shown in Fig. 3.2, the servovalve contains three stages. The first stage is a torque motor armature, and the second stage is a spool-type valve. The first two stages form a two-stage servovalve that can be used as a functional unit. In a three-stage servovalve, a larger size spool-type valve is used to increase the ability of the servovalve to control flows. In this case, the two-stage valve is called the pilot-stage valve, and the larger valve is called the main-stage valve.

3.2 Mathematical Models

3.2.1 Servovalve Controller

The control of the system starts from a command signal, which can be generated by the internal function generator of the MTS 407 controller or an external program input, such as the effective force inputs in this study. The external input was converted into a voltage signal by a factor (C_F), which is same as the sensitivity factor of the feedback sensor (i.e., the load cell for the actuator). The command signal was adjusted by a dither signal (i.e., a small sine wave with a high frequency (500 Hz)), and then compared with a feedback signal. The difference between these two voltage signals is called the DC error (e). The error signal was modified by a Proportional-Integral-Derivative (PID) controller, and then sent to the valve driver module inside the controller as a valve command (v). The process is schematically shown in the block diagram of Fig. 3.3, in which the limit check block represents the ±10 volts limit of the electrical signals.

The valve command signal was expressed as

$$v = C_F \left(G_p e + G_d \dot{e} \right), \tag{3.1}$$

where G_p and G_d are the proportional and derivative gain setting of the PID controller, respectively (Note that the integral gain was always set as zero in this study). The DC error and its derivative are

$$e = u - F \ , \ \dot{e} = \dot{u} - \dot{F} \tag{3.2}$$

where u is the command signal (effective force), F is the force feedback measured by the actuator load cell, and $\dot{u}$ and $\dot{F}$ are the time derivatives of these signals.

The valve command signal is the input to the inner feedback control loop shown by the dashed lines of Fig. 3.1. The inner loop controls the position of the main-stage valve spool, which is measured by an internal Linear Variable Differential Transformer (LVDT), and is fed back to the valve driver to close the inner control loop.

3.2.2 Valve Driver Module

The valve driver module inside the servovalve controller functioned similarly to the outer loop controller except that the valve command signal indicated the desired spool position, and the feedback signal measured by an LVDT indicated the actual spool position. A block diagram is presented in Fig. 3.4 to illustrate the inner control loop. The the DC error of the inner loop, e_i is

$$e_i = v - K_3 \tilde{x}_v \, , \tag{3.3}$$

where K_3 is the equivalent sensitivity factor of the LVDT and $\tilde{x}_v$ is the main-stage spool position.

A PD controller was built into the valve control module to adjust the inner loop error signal before sending it to the pilot-stage valve. Following the tuning procedure of the servovalve by the manufacturer, a unity proportional gain and a zero derivative gain were found suitable for the control of the servovalve; therefore, the dynamics of the inner PD

controller was neglected (i.e., the pilot-stage valve command equals the inner loop error $v_i = e_i$). The dynamics of other components of the servovalve shown in Fig. 3.4 are described individually in the following sections.

3.2.3 Servovalve (Pilot-Stage)

The pilot-stage valve was a 1 gpm MTS 252.21 servovalve custom manufactured by Moog, Inc. The first stage was a torque motor armature. Electrical current applied to coils wound around the armature generated torque, causing the rotation of the armature and a flapper connected with the armature. The offset of the flapper from its neutral position caused differential flow/pressure acting on the ends of the spool of the second-stage valve. The position of the spool was sensed by a center spring, which was an extension of the flapper. The position of the second-stage spool, in turn, controlled hydraulic flows to the main-stage valve.

Although it is possible to derive high-order models for the pilot-stage valve including the dynamics of individual valve components, such as in Nikiforuk (1969), simple models can be enough to capture the behavioral characteristics of Moog valves (Thayer, 1965). Because the frequency range of interest is typically limited for seismic applications (e.g., 0-10 Hz in this study), it is only necessary for a model to represent the servovalve response up to a certain frequency (e.g., 20 Hz). Therefore, a first-order differential equation is usually sufficient to approximate the flow (Q_{vp}) controlled by the pilot-stage valve corresponding to an inner-loop command signal (v_i). The pilot-stage valve dynamics was described as

$$\tau \dot{Q}_{vp} + Q_{vp} = K_{vp} v_i \,, \tag{3.4}$$

where K_{vp} is the flow gain of the pilot-stage valve and τ is the equivalent time constant of

the pilot-stage valve. The subscription $_{vp}$ stands for "pilot-stage valve."

If the response at high frequencies is under investigation, a second-order model can be necessary (Thayer, 1965)

$$\frac{1}{\omega_{ns}^2}\ddot{Q}_{vp} + \frac{2\zeta_s}{\omega_{ns}}\dot{Q}_{vp} + Q_{vp} = K_{vp}v_i\,, \tag{3.5}$$

where ω_{ns} and ζ_s are the apparent natural frequency and the equivalent damping ratio of the pilot-stage valve, respectively. The second-order model was used to validate the parameter identification of the first-order model in the next chapter. Note that an assumption has been embedded in these models that the pilot-stage flow is proportional to the position of the pilot-stage spool position. This assumption will also be validated in the next chapter.

3.2.4 Servovalve (Main-Stage)

The pilot-stage flow controls the movement of the main-stage spool by causing differential pressures acting on the spool ends. It can be shown that the forces acting on the main-stage spool, such as the force required to move the spool (the load pressure) is typically small compared with the available driving force (the pressure supply), and the motion of the spool is small (on the order of a tenth of an inch) (Chen, 2003). Therefore, the effects of spool mass, friction, and other forces acting on the spool as well as the compressibility of hydraulic fluid are negligible (Thayer, 1965). These assumptions resulted in the following relationship between the pilot-stage flow (Q_{vp}) and the main-stage spool position ($\tilde{x}_v$)

$$A_v\dot{\tilde{x}}_v = Q_{vp}\,, \tag{3.6}$$

where A_v is the main-stage spool area, and $\dot{\tilde{x}}_v$ is the time derivative of the main-stage

spool position (velocity of the spool).

The relationship between the valve command signal (v) and the main-stage spool position ($\tilde{x}_v$) can now be formulated by combining Eqs. (3.3), (3.4), and (3.6) and regrouping

$$\tau A_v \dddot{\tilde{x}}_v + A_v \ddot{\tilde{x}}_v + K_{vp} K_3 \dot{\tilde{x}}_v = K_{vp} v \,. \tag{3.7}$$

Note that the spool position of the main-stage valve ($\tilde{x}_v$) has a unit of length. It is often convenient to normalize the spool position by the maximum spool stroke $x_{v\max}$, as shown in Fig. 3.4. The normalized spool position is named spool opening (x_v, $-1 < x_v < 1$), and used throughout the thesis. The main-stage spool regulates the direction and flow of hydraulic fluid to an actuator.

3.2.5 Main-stage flow

The actuator piston is driven by hydraulic flow under pressure. As the actuator applies variable loads to the test structure, the pressure inside the two chambers of the actuator may vary significantly. The pressure change in turn affects the behavior of the flow through the main-stage valve, thus a detailed analysis is necessary to formulate the relationship between the main-stage spool opening and the flow to the actuator.

As shown schematically in Fig. 3.5, the main-stage valve is a symmetric spool-type valve. When the spool is at its null position, there is no flow through the valve because both load ports are closed to both the supply line and return lines though leakage flows exist due to the matching tolerance between the spool and its sleeve. When the spool moves away from its null position (to the right as shown in Fig. 3.5), two similar sharp-edged orifices are formed, as shown in Fig. 3.6 (a), to allow hydraulic flow into the right

load port (Q_1) and hydraulic flow out of the left load port (Q_2). Two other flow passages are formed as shown in Fig. 3.6 (b) to allow leakage flows into the return lines. The pressure (P_1) inside the right load port rises because of the incoming flow, while the pressure (P_2) inside the left load port drops because of the outgoing flow. The resulting differential pressure across the actuator piston is defined as the load pressure (P_L),

$$P_L = P_1 - P_2 . \tag{3.8}$$

Flows through the load flow orifices can be described by Eq. (2.16). Therefore

$$Q_1 = C_d A_{vs} \sqrt{\frac{2}{\rho}\left(P_s - P_1\right)} \tag{3.9}$$

$$Q_2 = C_d A_{vs} \sqrt{\frac{2}{\rho} P_2} \tag{3.10}$$

where C_d is the orifice discharge coefficient, A_{vs} is the orifice area, P_s is the hydraulic pressure supply, and ρ is the mass density of the hydraulic fluid. Note that the return pressure was assumed zero in the above derivation. The orifice area is related to the spool opening by

$$A_{vs} = w\left|\tilde{x}_v\right| = w\left|x_v\right| x_{v\max} , \tag{3.11}$$

where w is the area gradient (perimeter) of the valve spool.

When the spool moves away from its null position, the resulting leakage orifices are small annular orifices, which are greatly different from the load flow orifices. Therefore, instead of using Eq. (2.16), the leakage flows was approximated by (Merritt, 1967)

$$Q_3 = \frac{\pi r c^3}{6\mu L}\left[1 + \frac{3}{2}\left(\frac{e}{c}\right)^2\right]\left(P_s - P_2\right) \tag{3.12}$$

$$Q_4 = \frac{\pi r c^3}{6\mu L}\left[1 + \frac{3}{2}\left(\frac{e}{c}\right)^2\right] P_1 \tag{3.13}$$

where r, c, and e are servovalve geometric coefficients as illustrated in Fig. 3.6 (b), μ is the fluid viscosity, and L is flow passage length ($\tilde{x}_v$ in this case). Again, the return pressure was assumed zero. As can be seen, leakage flows are proportional to $1/x_v$ for a given valve (i.e., fixed geometric coefficients); therefore, the valve leakage reduces as the spool opening increases (Merritt, 1967).

For a symmetrical critically centered valve,

$$Q_1 = Q_2 \tag{3.14}$$

$$Q_3 = Q_4 \tag{3.15}$$

Substituting Eqs. (3.9) and (3.10) into Eq. (3.14) yields

$$P_s = P_1 + P_2 . \tag{3.16}$$

Note that the same result can be obtained by substituting Eqs. (3.12) and (3.13) into Eq. (3.15). Solving Eq. (3.8) and Eq. (3.16) simultaneously gives

$$P_1 = \frac{P_s + P_L}{2} \tag{3.17}$$

$$P_2 = \frac{P_s - P_L}{2} \tag{3.18}$$

Finally, the load flow (Q_L) (the flow into/out of the actuator chambers) can be determined by

$$Q_L = Q_1 - Q_4 \tag{3.19}$$

$$Q_L = Q_2 - Q_3 \tag{3.20}$$

By substituting Eqs. (3.9), (3.13), and (3.17), into Eq. (3.19), the load flow equation

becomes

$$Q_L = C_d A_{vs} \sqrt{\frac{1}{\rho}(P_s - P_L)} - \frac{\pi r c^3}{6\mu \tilde{x}_v}\left[1 + \frac{3}{2}\left(\frac{e}{c}\right)^2\right]\frac{P_s + P_L}{2} \tag{3.21}$$

Because the leakage flow can be viewed as part of the flow leaving a control volume (i.e., an actuator chamber), it is neglected in determining the flow property of the valve to simplify the system analysis. Its effect is considered in the analysis of the actuator dynamics in the next section. Therefore

$$Q_L = C_d A_{vs} \sqrt{\frac{1}{\rho}\left(P_s - P_L\right)} \tag{3.22}$$

When the spool moves in the opposite direction (to the left), the resulting load pressure would be $-P_L$, and the load flow can be determined by

$$Q_L = -C_d A_{vs} \sqrt{\frac{1}{\rho}\left(P_s + P_L\right)} \tag{3.23}$$

where the minus sign indicates the direction of the flow is opposite to that of the previous case. Combining Eqs. (3.22) and (3.23) and applying Eq. (3.11) gives

$$Q_L = K_v x_v \sqrt{1 - \frac{x_v}{|x_v|}\frac{P_L}{P_s}} \tag{3.24}$$

where $K_v = \left(C_d w x_{v\max} \sqrt{1/\rho}\right)\sqrt{P_s}$ is called the flow gain of the servovalve. Note that the flow gain is proportional to $\sqrt{P_s}$. This relation is used to calculate the flow gain of the main-stage valve in the next chapter.

Hydraulic fluid flows into one actuator chamber and out of the other chamber, thus raising the pressure on one side of the actuator piston while reducing the pressure on the other side by roughly the same amount. It is now necessary to formulate the relationship

between the load flow (Q_L) and the resulting load pressure (P_L).

3.2.6 Actuator

The actuator piston for a double acting actuator is schematically shown in Fig. 3.6. The servovalve spool opening is assumed positive as shown in Fig. 3.5, which causes hydraulic fluid flow into the right chamber of the actuator. The resulting pressure difference causes a tension force of the actuator piston, which is defined as a positive force herein. The law of conservation of mass shown in Eq. (2.20) can be used to relate the load pressure to the load flow.

It is necessary to first define the leakage flows shown in Fig. 3.6. The clearance between circular actuator piston rings and their sleeves forms an annular flow passage that allows a leakage flow. Similar to Eq. (3.12), the cross-port leakage (i.e., leakage from one chamber of the actuator to the other) is

$$Q_{ip} = C_{ip}\left(P_1 - P_2\right) \tag{3.25}$$

where $C_{ip} = \dfrac{\pi r c^3}{6\mu L}\left[1 + \dfrac{3}{2}\left(\dfrac{e}{c}\right)^2\right]$ is the internal leakage coefficient. The external leakage flows (i.e., leakage from actuator chambers to the drain ports) are approximated by

$$Q_{epi} = C_{ep}P_i\,,\ i = 1,2 \tag{3.26}$$

where C_{ep} (similar to C_{ip}) is the external leakage coefficient and P_i is the pressure inside the actuator chambers.

Applying the continuity equation (2.20) to both chambers yields

$$Q_1 - C_{ip}(P_1 - P_2) - C_{ep}P_1 = \frac{dV_1}{dt} + \frac{V_1}{\beta_e}\frac{dP_1}{dt} \tag{3.27}$$

$$C_{ip}(P_1 - P_2) - C_{ep}P_2 - Q_2 = \frac{dV_2}{dt} + \frac{V_2}{\beta_e}\frac{dP_2}{dt} \tag{3.28}$$

where Q_1 and Q_2 are flows into/out of the actuator chambers, V_1 and V_2 are the chamber volumes, P_1 and P_2 are the chamber pressures, respectively, and t is time.

It is appropriate to assume that the volume of the pressure side chamber increases while the volume of the return side chamber decreases simultaneously. The volume change equals the piston area times the piston stroke, therefore

$$V_1 = V_{01} + Ax\,,\ \frac{dV_1}{dt} = A\dot{x} \tag{3.29}$$

$$V_2 = V_{02} - Ax\,,\ \frac{dV_2}{dt} = -A\dot{x} \tag{3.30}$$

where V_{01} and V_{02} are the initial volumes of the chambers including the connecting lines, A is the actuator piston area, and x is the actuator piston movement. Because the actuator piston is rigidly connected between the test structure and an assumed rigid support, x is also the structural displacement response. Similarly, the actuator piston velocity $\dot{x}$ is also the structural velocity response.

Differentiating Eq. (3.17) and Eq. (3.18) once with respect to time gives (assuming that the variation of the pressure supply is negligible)

$$\frac{dP_1}{dt} = \frac{1}{2}\frac{dP_L}{dt} \tag{3.31}$$

$$\frac{dP_2}{dt} = -\frac{1}{2}\frac{dP_L}{dt} \tag{3.32}$$

Substituting Eqs. (3.29) through (3.32) into Eq. (3.27) and Eq. (3.28) and subtracting Eq. (3.28) from Eq. (3.27) yields

$$\left(Q_1+Q_2\right)-2C_{ip}\left(P_1-P_2\right)-C_{ep}\left(P_1-P_2\right)=2A\dot{x}+\frac{V_t}{2\beta_e}\frac{dP_L}{dt} \tag{3.33}$$

where $V_t=V_1+V_2$ is the total contained volume of both chambers.

Recall that Q_1 and Q_2 are slightly different from the load flow Q_L determined by Eq. (3.22) due to the neglected servovalve leakage. The leakage flow is now considered in determining the flow (Q_1 and Q_2) to the actuator chambers,

$$Q_1,Q_2=Q_L-Q_{lv}\,. \tag{3.34}$$

The valve leakage flow Q_{lv} is

$$Q_{lv}=\frac{\pi rc^3}{6\mu\widetilde{x}_v}\left[1+\frac{3}{2}\left(\frac{e}{c}\right)^2\right]\frac{P_s+P_L}{2} \tag{3.35}$$

It can be seen that the leakage flow can be treated as two parts: a "constant leakage" (related to P_s) and a "proportional leakage" (related to P_L). The proportional leakage is considered here while the effect of the constant leakage will be investigated in Chapter 7 through computer simulations. In order to the facilitate the system analysis, the complicated servovalve leakage was further approximated by

$$Q_{lv}=C_{lv}P_L\,, \tag{3.36}$$

Substituting Eqs. (3.8), (3.34), and (3.36) into Eq. (3.33) yields

$$Q_L=K_a\dot{P}_L+C_lP_L+A\dot{x} \tag{3.37}$$

where $K_a=V_t/4\beta_e$ is the compressibility coefficient of the hydraulic fluid inside both actuator chambers, and $C_l=C_{lv}+C_{ip}+C_{ep}/2$ is the total leakage coefficient of the servovalve/actuator combination.

Eq. (3.37) indicates that the load pressure is affected by the velocity of the actuator

piston/test structure. The load pressure multiplied by the piston area ($P_L A$) gives the force (F) applied to the test structure; therefore, the applied force is affected by the structural velocity response. The effect will be discussed in detail later in the system analysis.

3.2.7 Test Structure

The test structure was modeled as a SDOF system. Both viscous damping and Coulomb friction were considered in the following equation of motion,

$$F - F_c = m\ddot{x} + c\dot{x} + kx, \tag{3.38}$$

where F_c is the Coulomb friction of the test structure, m, c, and k are the structural mass, damping, and stiffness, respectively. When implementing the structural model in computer simulations, a situation must be considered where a total driving force is smaller than the designated Coulomb friction. In the block diagram model shown in Fig. 3.8, the total driving force $F - (m\ddot{x} + c\dot{x} + kx)$ is compared with the designated friction force; then, the real friction takes the smaller value between these two forces.

If the friction is small enough such that the structure is able to move smoothly, the friction effect can be approximated using an equivalent viscous damping (Chopra, 1995). The dynamics of the test structure can then be described by

$$F = m\ddot{x} + c\dot{x} + kx, \tag{3.39}$$

where the same notation c is used to represent the total equivalent viscous damping.

In summary, the major function of the servovalve controller (a PID controller) is described by Eq. (3.1). The dynamics of the three-stage servovalve within a certain range of frequencies (0-10 Hz) can be represented by Eq. (3.7). The flow property of the servovalve is defined by Eq. (3.24). The dynamics of the actuator described by Eq.

(3.37) relates the hydraulic flow to the actuator to the force acting on the test structure. These equations along with structural models given in Eq. (3.38) or (3.39) can be solved simultaneously to simulate the dynamic response of the test structure subjected to effective forces applied by a servo-hydraulic actuator. Computer simulations can be used to obtain the system responses.

3.3 Computer Simulation Models

Block diagrams are often more convenient for revealing relationships between individual components, such as the effect of the piston/structure velocity on the actuator dynamics shown in Eq. (3.37). To construct a block diagram, the dynamics of the system components in terms of transfer functions are formulated as follows.

In the frequency domain, the transfer function corresponding to Eq. (3.1) is

$$H_c = C_F \left(G_p + G_d s \right). \tag{3.40}$$

The first-order model of the pilot-stage valve, Eq. (3.4) is

$$H_{sp} = \frac{K_{vp}}{\tau s + 1}, \tag{3.41}$$

and the dynamics of the main-stage spool, Eq. (3.6) is

$$H_{sm} = \frac{1}{A_v s}. \tag{3.42}$$

By applying principles of operational algebra to the block diagram model of the inner loop control shown in Fig. 3.4, the transfer function for the three-stage servovalve can be derived as

$$H_s = \frac{H_{sp}H_{sm}}{1 + H_{sp}H_{sm}K_3}\left(\frac{1}{x_{v\max}}\right) = \frac{K_{vp}}{\tau A_v s^2 + A_v s + K_3 K_{vp}}\left(\frac{1}{x_{v\max}}\right). \tag{3.43}$$

The flow property of the main-stage valve remains the same as Eq. (3.24). The transfer function for the actuator dynamics is cross-linked with the dynamics of the test structure, for which the transfer function is formulated by

$$H_{st} = \frac{A}{ms^2 + cs + k}. \tag{3.44}$$

The block diagram model portion shown in Fig. 3.9 was used to demonstrate the interaction between the piston (structure) velocity and actuator dynamics. The summing point represents the law of the conversation of mass: the flow driven into the actuator chamber needs to counteract the compressibility of the hydraulic fluid, the leakage flow, and the chamber volume variation represented by $A\dot{x}$. The corresponding loop from the structural velocity to the summing point is the *natural velocity feedback* loop discussed in Dyke et al. (1995).

The block diagram model of the overall test system is shown in Fig. 3.10, in which masked blocks are used to represent the dynamics of the analog controller, servovalve, and the SDOF structure. Computer simulations were conducted with SIMULINK® 3.0, a dynamic system simulation package for MATLAB® version 5.3. In addition to computer simulations using the nonlinear high-order models, linear system analysis was used to provide closed form derivations and solutions for the linearized systems within a limited range of system parameters. Linear system analysis was also used to study the stability of the test system.

3.4 Models for Linear System Analysis

Nonlinear models were approximated within a useful, though limited, range as linear systems, and high-order transfer functions were approximated using low-order transfer functions within a certain range of frequency. For example, the nonlinearity, ***load pressure influence*** in the servovalve flow property, states that the load flow is proportional to the square root of the supply pressure minus the load pressure. When the load pressure is small, such that the square root term is close to unity, the nonlinear flow model shown in Eq. (3.24) can be simplified to a linearized approximation,

$$Q = K_v x_v . \tag{3.45}$$

The derivative gain of the servovalve controller is usually very small (on the order of a tenth of millisecond), thus for low frequencies, the PID controller was approximated by

$$v = G_p e . \tag{3.46}$$

In addition, for low frequencies (i.e., well below the roll-off frequency of the servovalve), such as frequencies below 10 Hz in this study, the servovalve dynamics shown in Eq. (3.7) were represented by the linear relation,

$$x_v = K_s v , \tag{3.47}$$

where $K_s = \dfrac{1}{K_3 x_{v\max}}$ is the valve gain.

With the linearized system models, control engineering techniques such as pole-zero mapping and the frequency response method shown in Chapter 2 was used to provide insight to the system behavior including system stability. Preliminary system analysis was conducted to study the interaction between system components and to form the transfer function of the test system.

3.5 Linear System Analysis

With the linearized component models shown in Eq. (3.45) through (3.47), the block diagram model of the test system shown in Fig. 3.10 was used to formulate a transfer function (G_{Fu}) from the force command to the force output,

$$G_{Fu}(s) = \frac{AK_vC_FK_sG_p(ms^2 + cs + k)}{A^2s + (K_as + C_l)(ms^2 + cs + k) + AK_vC_FK_sG_p(ms^2 + cs + k)}. \tag{3.48}$$

The numerator polynomial includes the denominator of the structure transfer function ($ms^2 + cs + k$); therefore, the poles of the structure are also zeros of the overall transfer function. The second-order term in the numerator indicates that the force output of the system will not respond well to command forces that have frequencies near the natural frequency of the second-order term (i.e., the natural frequency of the test structure).

Note that the natural velocity feedback exists in every test system using servo-hydraulic actuation. However, it causes control problems when a test system is in force control while it does not affect the performance of a test system in displacement control (see Appendix 1 for detailed derivation).

3.6 Summary

Mathematical models for a test system using servo-hydraulic actuation were derived in this chapter. Preliminary system analysis was conducted to derive an overall system model, from which general characteristics of the test system (natural velocity feedback problem) was obtained. Parameters for the proposed models need to be identified to facilitate the detailed analysis and computer simulation.

CHAPTER FOUR

SYSTEM IDENTIFICATION

The parameters of the system models to be determined are listed in Table 4.1. Among these parameters, the servovalve response delay and servovalve flow property were critical because they have a significant impact on the performance of the test system. Other servo-system parameters and structural properties are important to the understanding of the system behavior through computer simulations. The parameter identification roughly follows the order in which they were introduced in the last chapter.

4.1 Pilot-Stage Servovalve

4.1.1 Valve Dynamics

The performance curve of the MTS 252.21 valve indicated that its frequency response (magnitude) was constant for frequencies below 30 Hz, and rolled off as the command frequency increased. To approximate the valve performance at low frequencies using the first-order model shown in Eq. (3.4) and Eq. (3.41), a time constant (τ) was needed. It was estimated from the performance curve that the response reached 70% of its full capacity at a frequency of 115 Hz, hence the time constant was

$$\tau = \frac{1}{2\pi(115)} = 0.0014 \text{ s}. \tag{4.1}$$

This estimation is very close to the suggested value (0.0013 s) for a Moog series 30 servovalve (Thayer, 1965), which roughly has the same capacity as an MTS 252.21

servovalve.

The product specification also states that the frequency corresponding to the 90°-phase point for the servovalve is 230 Hz. This indicated that the servovalve dynamics over a wider range of frequency could be represented by the second-order model shown in Eq. (3.5), in which two parameters, the apparent natural frequency (ω_n) and the equivalent damping ratio (ζ), were needed. By the definition of the 90°-phase point of a second-order system, the apparent natural frequency was 230 Hz, at which the magnitude was found to be 45% of the full capacity from the performance curve. Hence, the equivalent damping ratio was estimated following Eq. (2.30)

$$\zeta = \frac{1}{2(0.45)} \approx 1.11 . \tag{4.2}$$

As indicated in the last chapter, both the first-order and second-order model should provide similar frequency response for low frequencies. The frequency responses of the two models are compared in Fig. 4.1. Both magnitude and phase responses are well matched in the low frequency range (< 10 Hz), and a close match can be observed at higher frequencies (< 30 Hz) with reasonable accuracy. At a frequency around the apparent natural frequency of the valve, the magnitude responses are still close though the phase responses have deviated. Hence, the first-order model with a time constant of 0.0014 s was adequate and used for representing the dynamics of the pilot-stage valve for frequencies up to 30 Hz.

4.1.2 Valve Flow Property

The hydraulic flow through the pilot-stage valve was controlled by a spool-type valve, thus the flow property of the valve could be described using Eq. (3.24). Similar to

the main-stage spool, the force acting on the pilot-stage valve was negligible compared to the pressure supply. Therefore, a similar linear relation as Eq. (3.45) was used for the pilot-stage valve.

The rated flow capacity of the MTS 252.21 servovalve is 1 gpm (3.85 $in.^3/s$) under 1000 psi pressure drop across the valve. Meanwhile, the supply pressure was roughly 2800 psi, and the return pressure was negligible. Thus, after considering the real pressure drop as shown in Eq. (3.24), the flow gain of the pilot-stage valve was approximately

$$K_{vp} = \frac{3.85 \text{ in.}^3/\text{s}\sqrt{2.8}}{10 \text{ volt}} = 0.644 \text{ in.}^3/\text{s}/\text{volt}. \tag{4.3}$$

Note that the pilot-stage flow gain was defined as the flow per volt referring to Eq. (3.4).

4.2 Main-Stage Servovalve

4.2.1 Valve Dynamics

The main-stage spool position is related to the pilot-stage flow by Eq. (3.6), in which the spool area A_v needs to be determined. The resulting spool position is normalized by the maximum spool stroke $x_{v\max}$, such that the main-stage spool opening is expressed in terms of percentage of spool opening ($-1 < x_v < +1$) as shown in Fig. 3.4. These two parameters may be measured, and yet are proprietary to the servovalve manufacture. The sensitivity factor of the spool LVDT was estimated as

$$K_3 = 10/x_{v\max}, \tag{4.4}$$

such that a 10-volt LVDT signal indicates the maximum spool stroke.

An experimental procedure was used to validate the valve model and the parameters. The actuator was in displacement control, and the actuator piston was kept in its neutral

position by shutting of the hydraulic supply to the main-stage valve. Therefore, the DC error signal was equal to the command signal. In addition, the proportional gain of the servovalve controller was set to unity and the derivative gain set to zero, such that the valve command signal was equal to the DC error signal. With this procedure, the command signal to the servovalve could be controlled without additional equipment. A sinesweep input (0-100 Hz in 100 seconds) with constant amplitude of 2 volt was chosen as the command signal.

The MTS 407 controller allowed the monitoring of the valve command signal and inner loop feedback signal that represented the spool position. By plotting the magnitude ratio and the phase difference of these two signals in the frequency domain, the frequency response of the servovalve was obtained. The measured frequency response is compared in Fig. 4.2 to simulation results. The proposed servovalve model with a first-order pilot-stage model matched well with the experimental results at low frequencies (below 10 Hz), while it deviated from the measured response at higher frequencies. The fast descending pattern of the phase response shown in Fig. 4.2 at high frequencies indicates that the servovalve might have higher-order dynamics. This was explained by a better match of the calculated response with the second-order pilot-stage model shown in dashed lines.

The discrepancy of the magnitude response at high frequencies was attributed to an underestimation of the pilot-stage flow gain (K_{vp}). The flow gain was determined as the slope of a straight line connecting the maximum spool opening point and the origin while the flow property of a spool-type valve (i.e., a curve of flow vs. spool opening) can be nonlinear. During the above test, the spool opening was kept small (within 10%), at

which the flow gain is typically higher. Simulation results with a larger flow gain (arbitrarily 10% greater than the identified flow gain) better matched the experimental results as shown in Fig. 4.3. Especially, the phase responses matched the experimental results well up to 50 Hz.

The flow gain typically reduces as the spool moves away from its neutral position (can be smaller than the secant flow gain). Therefore, the identified flow gain was deemed as a better representation of the servovalve flow property on an average base across the whole operating range of the pilot-stage valve. In addition, frequencies below 10 Hz were of interest; hence the first-order pilot-stage model was chosen for the rest of the study.

4.2.2 Simplified Valve Dynamics (Valve gain)

Experimental results shown in Figs. 4.2 and 4.3 also indicated that the magnitude response was constant for low frequencies (below 10 Hz); therefore, it was appropriate to further simplify the servovalve dynamics to a gain shown in Eq. (3.47), and the valve gain was

$$K_s = 0.1 \tag{4.5}$$

To further validate this parameter for large amplitude and low frequency inputs, the same experimental procedure was followed with another sinesweep input (0-10 Hz). A phase-lead network shown in Eq. (2.35) was used to amplify the command signal such that a larger command signal was obtained and tested. A plot of the spool opening versus the valve command is presented in Fig. 4.4, in which the thick dashed line represents the linear curve fit of the experimental result. The servovalve gain was roughly 0.1 across almost the whole operating range of the servovalve. In addition, a hysteretic behavior

was evident as shown in Fig. 4.4.

4.2.3 Servovalve Response Delay

The hysteresis was due to the response delay of the servovalve, which is elucidated in Fig. 4.5 that the spool position lags behind the valve command. With the second-order servovalve model shown in Eq. (3.7) and the parameters identified above, the servovalve phase delay was estimated using Eq. (2.31) for low frequencies as

$$T_d = \frac{2\zeta}{\omega_n} = \frac{A_v}{K_3 K_{vp}}. \tag{4.6}$$

The apparent natural frequency of the system was calculated as 59 Hz, the equivalent damping was determined to be 96.4% of critical damping, and the time delay was 5.2 ms. Note that the inner-loop controller P gain setting can have an impact on the servovalve response delay if it not unity as in this study.

The calculated response delay was verified using the measured phase response of the system shown in Fig. 4.6. A linear regression was made to approximate the phase delay as a linear function of input frequency (Hz). The response delay was the slope of the regression line divided by 2π, resulting a response delay of 4.7 ms.

The small inconstancy in these estimations is inevitable due to uncertainties in the servo-system and modeling errors. Fine tuning of the parameter was made based on observations in Chapter 7, and a response delay of 5 ms was used in the implementation. The servovalve flow property was another parameter that was affected by servo-system nonlinearities and uncertainties.

4.2.4 Initial Flow Gain

A servovalve flow curve relates the flow into the actuator to the main-stage spool

opening. The initial flow gain K_v is defined as the slope of the flow curve at the origin. According to the product specification, the initial flow gain for the servovalve is 1.6 gpm (6.16 in.^{3}/s) per percentage of spool opening with a pressure drop of 1000 psi across the servovalve. Because the spool opening in this study was defined between -1 and 1, the flow gain was determined as 160 gpm (6.16 in.^{3}/s) with a pressure drop of 1000 psi. The real pressure drop needs to be considered to determine the flow gain of the servovalve in operation.

Although the pressure supply of the test system is about 2800 psi as indicated by a pressure gage on the hydraulic service manifold, and the pressure in the return line is usually negligible, a smaller pressure drop was more realistic because of supply pressure variations during a test. Therefore, a pressure drop of 2650 psi, as to be shown in Section 7.1.2, was used to consider the real pressure drop across the servovalve. According to Eq. (3.24), the initial no-load flow gain was determined as

$$K_v = 616 \text{ in.}^3/\text{s}\sqrt{2.65} = 1003 \text{ in.}^3/\text{s}. \tag{4.7}$$

If the servovalve flow property were linear, the maximum flow through the valve would be 260 gpm (1003 in.^{3}/s). However, an MTS 256.09 servovalve is capable of regulating 90 gpm with a fully opened spool and 1000 psi pressure drop across the servovalve. After taking the effect of the pressure drop into account, the maximum flow rate through the servovalve was calculated as 147 gpm (564 in.^{3}/s). The difference between the linearly predicted maximum flow and the maximum flow capacity indicates a nonlinear relationship between the spool opening and the regulated flow. A hydraulics explanation of the nonlinear no-load flow property of the servovalve can be found in Appendix 2.

A typical flow curve of an MTS 256.09 servovalve with a pressure drop of 1000 psi and zero load pressure is shown in Fig. 4.7 (Chen, 2001). It can be seen that the flow gain decreases with an increase in spool opening. Because the testing condition (e.g., hydraulic supply) was different from the one, under which the typical flow curve was constructed, an experimental procedure was necessary for the flow property identification of the servovalve.

4.2.5 Nonlinear Servovalve Flow Property

In the designed test procedure, the actuator was under displacement control with a sinusoidal input, the frequency and amplitude of which could be determined according to Appendix 3. The test was conducted under no load condition (without a structure connected to the actuator) such that the pressure difference across the actuator piston (load pressure) was negligible. The spool opening was obtained directly by measuring the inner-loop feedback while the corresponding flow was calculated using Eq. (3.37). Because the load pressure was negligible and its derivative was deemed (and proved during the test) negligible, the flow calculation was further simplified as the piston velocity multiplied by the piston area. The piston velocity was calculated using the central difference method from the measured piston displacement.

The result of a typical test is presented by dots in Fig. 4.8. Although a curve fitting can be used to determine a flow curve that best represent the flow property, it was not used the error of the resulting curve, especially near the origin, can be large enough to deteriorate the performance of EFT. In addition, the difference between the obtained flow curve and the inverse flow curve (another curve fitting) was large enough to ruin computer simulations. Therefore, as shown by the solid lines in Fig. 4.8, a piecewise

linear curve that connected 21 control points at an interval of 10% spool opening was constructed to represent the flow property of the servovalve. The flow values at the control points were calculated as the mean of the experimental results. The values of a typical flow curve are listed in Table 4.2, in which a linear extrapolation was used to generate the points beyond the 80% spool opening.

Within a certain range of spool opening (10 % in this study), the measured servovalve vs. spool opening curve is linear as shown in Figure 4.8; hence, the linear velocity feedback compensation might be viable. On the other hand, the slope of the flow curve decreases significantly at 80% spool opening, indicating reduced controllability of the servovalve. A spool opening of 60% was deemed a good upper limit for practice because the corresponding flow gain would not be significantly reduced.

4.3 Actuator Dynamics

Actuator dynamics include the fluid compressibility and leakage of the system. To estimate the compressibility coefficient of the actuator, the total chamber volume was determined by the piston area multiplied by the total stroke of the actuator (10 in.). According to the product specification, the piston area was 12.73 in.^{2}. Therefore,

$$K_a = \frac{V_t}{4\beta_e} = 0.3182 \text{ in.}^3/\text{ksi} \tag{4.7}$$

It was difficult to determine the leakage coefficient C_l of the servo-system in practice because the leakage was related to the level of wornness of the equipment such as the piston sealing. The product specification indicated that the null flow (mainly leakage when the spools are at their neutral position) of the three-stage valve was 3.5 gpm and the

null flow of the pilot-stage valve was 0.29 gpm under a 3000 psi pressure drop across the servovalve. Hence, the leakage coefficient was estimated to be 1.1 gpm (4.2 $in.^3/s$) per ksi pressure drop for the valve ((3.5-0.29) gpm/(3 ksi)). Significant uncertainties exist in the above estimation such that a leakage coefficient within the following range

$$4 \text{ in.}^3/\text{s}/\text{ksi} \le C_l \le 8 \text{ in.}^3/\text{s}/\text{ksi} \tag{4.8}$$

could be a good estimation for the whole servo-system. Fortunately, the system leakage does not affect the implementation of the velocity feedback compensation though it may affect the system stability (i.e., the determination of the maximum allowable controller P gain (G_p) as shown in Section 4.5, in which a leakage coefficient of 5.5 $in.^3/s/ksi$ was used.

4.4 Test Structure

Two structures were used in this study to validate the EFT method: A simplified structure that could be modeled as an SDOF system was used in the development of various velocity feedback compensation algorithms for EFT, and a one-story building structure was used in the proof-of-concept tests discussed in Chapter 8. The simplified structure described by Eq. (3.48) is considered in this section.

The structural model consisted of a concrete mass atop four caster wheels with two springs on each side of the structure in the direction of motion as shown in Fig. 4.9. The springs, which had a rated stiffness of 1 kip/in. each, were designed to have one-inch precompression. The springs on either side of the mass were designed to lose contact with the mass at displacements exceeding the precompression, resulting in a reduced stiffness. Thus, the structure was a linear elastic structure when the displacement

response was within the precompression, while it acted as a nonlinear elastic structure when the displacement response exceeded the precompression.

A measured force-displacement relation for the experimental setup is shown in Fig. 4.10. The initial stiffness was found to be 3.96 kip/in., and the stiffness reduced to 2.0 kip/in. beyond precompression based on a linear curve fit. The concrete mass weighed approximately 15.5 kips. A fluid viscous damper provided damping to the structure.

To determine the damping and the friction force of the structure, a free vibration test was conducted, and results are presented in Fig. 4.11. Simulations (dashed lines) based on Eq. (3.38) and the block diagram model shown in Fig. 3.7 were made to determine the combination of viscous damping and friction force that minimized the error between the measured displacements and simulation results based on a least square technique. The resulting damping ratio and friction force were 3.0% of critical damping and 6 lbs, respectively.

4.5 Controller Gains

The major function of the servovalve controller was a PID controller. A large P gain typically improves the system performance while it may cause instability. A proper amount of D gain reduces overshoot caused by a high P gain in a feedback-controlled system. However, the derivative term would amplify signals with high frequencies, such as noise signals. The integral gain reduces the steady-state tracking error while it may cause a wind-up problem when a constant offset exists in feedback signals or command signals. Appropriate gain settings were found such that the system would be the most responsive yet with enough margins for stability.

It was appropriate to consider the system stability at the null operating point of the servovalve because system operation usually occurred near this region, and the valve flow gain took its maximum value at this position. In addition, the load pressure was typically small when the servovalve spool was at its null position such that the load pressure influence was negligible, and the linear analysis was valid. As shown in Appendix 3, Routh's stability criterion was applied to a linearized system model to determine the maximum allowable P-gain as

$$G_p \leq 0.71 . \tag{4.9}$$

A slightly larger proportional gain (e.g., 0.8) was used in practice without causing serious instability because the leakage flow might have taken the upper limit of the range shown in Eq. (4.8) instead of 5.5 $in^3/s/ksi$ as used in the derivation of Eq. (4.9).

With a P gain 0f 0.8, a small D gain (e.g., 0.2 ms) was found to be appropriate for the system through trial and error. In addition, controller I gain is to reduce steady-state tracking errors while the purpose of this study was to investigate time-dependent responses of structural systems. Hence, the controller I gain was set as zero.

4.6 Parameter Verification

In order to verify the identified system parameters and the system models proposed in Chapter 3, computer simulations of the test system were conducted, and the results were compared to the experimental results. A frequency range of 0 to 10 Hz was of interest to this study because the frequency contents of typical earthquake ground accelerations corresponding to larger frequencies are small. A sine wave sweep (i.e., a sine wave function with a constant amplitude and a linearly increasing frequency generated by

$\sin\left(2\pi\frac{\omega}{T}\frac{1}{2}t^2\right)$, where ω = 10 Hz, T = 32 s, and $0 \le t \le T$) for frequencies between 0 and 10 Hz enables the investigation of the system response at every frequency within the sweep. Fig. 4.12 presents the experimental and the simulation results of the system with a 0.5-kip sinesweep input. The close match between the test results and the simulation indicates the accuracy of the proposed models and identified parameters.

4.7 Summary

System parameters in the mathematical models developed in Chapter 3 were identified in this chapter, and listed in Table 4.1. The system model and the identified parameters were used to analyze the test system and its response. Various velocity feedback compensation schemes for the implementation of the EFT method are investigated in the next chapter.

CHAPTER FIVE

VELOCITY FEEDBACK COMPENSATION

This chapter presents an analysis of the ***natural velocity feedback*** in detail, and then extends the implementation of ***velocity feedback compensation*** to consider servo-system nonlinearities. In addition, critical parameters in the implementation of the proposed compensation scheme are discussed, including controller P gain, the servovalve flow gain, and the response delay of the servovalve. Classical control engineering methods, such as pole-zero map, root locus, and frequency response were the major tools used for both analysis and design of the velocity feedback compensation. Computer simulations were used for the analysis of the test system with nonlinear compensation schemes.

5.1 Natural Velocity Feedback

The implementation of the EFT method without any velocity feedback compensation was shown to be unsuccessful with a simplified SDOF structural model (Murcek, 1996). A similar phenomenon was observed in both the experiment and simulation of a different test system (including the test structure) shown in Fig. 4.12. The magnitude of the measured force was below that of the command force across the whole frequency range (0-10 Hz). At the natural frequency of the test structure (1.56 Hz), the force amplitude approached zero. The actuator could not accurately apply forces near the natural frequency of the test structure due to the interaction between the actuator control and actuator piston velocity.

5.1.1 Control-Structure Interaction

Referring to the test system models shown in Figs. 3.9 and 3.10, the objective of actuator control is to minimize the error between the command signal (effective force) and the feedback signal (applied force to the test structure). The control is realized through the control of the fluid pressures inside the actuator chambers, which are regulated by the hydraulic flow into/out of the chambers. When the system is in operation, hydraulic flow is driven into one actuator chamber (roughly the same amount of flow is driven out of the other chamber) to generate forces applied to the test structure. Meanwhile, the structure moves under the applied forces, as does the actuator piston, which is rigidly attached to the structure. The resulting motion (i.e., the velocity) of the piston changes the volume of both chambers, thus affecting the fluid pressures inside the chambers.

Mathematically, the phenomenon is described by the principle of conservation of mass shown in Eq. 3.37, where the chamber volume change is represented by the piston velocity multiplied by the piston area ($A\dot{x}$). The natural velocity feedback loop is indicated in Fig. 3.9, and its effect is represented by a flow "deduction" from the load flow regulated by the servovalve.

5.1.2 Effect of the Natural Velocity Feedback

For a system in force control, a force feedback loop incorporated in the servovalve controller helps the actuator track force commands. The natural velocity feedback affects the actuator in applying forces accurately because the aforementioned chamber volume variation could not be directly sensed by the servovalve controller.

For the linearized system shown in Fig. 3.11 but with the second-order servovalve

model, the transfer function from force command (u) to the applied force (F) is

$$G_{Fu}(s) = \frac{AK_vC_FK_{vp}G_p(ms^2 + cs + k)}{[A^2s + (K_as + C_l)(ms^2 + cs + k)](\tau A_v s^2 + A_v s + K_3K_{vp})x_{v\max} + AK_vC_FK_{vp}G_p(ms^2 + cs + k)}. \quad (5.1)$$

Because the dynamics of the servovalve are unlikely the same as those of the test structure, the numerator and the denominator of the transfer function do not have components in common. Therefore, the numerator includes the denominator of the test structure, and the transfer function has zeros that are the poles of the structure as shown in the pole-zero map of the test system in Fig. 5.1.

The frequency response of the system is shown in Fig. 5.2. Corresponding to the conjugate zeros shown in Fig. 5.1, there is a dip in magnitude at the natural frequency of the test structure, for which the frequency response is shown by the dashed line in Fig. 5.2. The dip indicates that at steady state the ability of the actuator to apply forces with a frequency near the natural frequency of the test structure is greatly limited. As indicated in Section 2.3.4, the amplitude of the force output of the test system with a sinusoidal input can be estimated by the norm of the transfer function evaluated at the natural frequency of the test structure. Because the norm of a second-order term is 2ζ, the amplitude of the force output would be proportional to the damping of the test structure. When the structure damping is zero, the actuator is unable to apply any force at the natural frequency of the test structure.

The test system had two pairs of conjugate poles as shown in Fig. 5.1, corresponding to two vibration modes. The low frequency poles should represent the dynamics of the test structure. However, the poles were displaced due the natural velocity feedback. In addition, the damping of the vibration mode was large, indicating that force inputs at that

frequency would not be amplified. The poles with a higher frequency (61 Hz) were related to the dynamics of the servovalve because they would disappear if the system were represented by Eq. (3.48), in which the servovalve dynamics was simplified as a valve gain.

The high-frequency poles correspond to the amplitude spike in solid line as shown in Fig. 5.2. This vibration mode can be excited when the system becomes instantaneously unstable due to uncertainties in the system. In this case, electrical noise, which usually has a frequency of 60 Hz, would be amplified, and the force output would be noisy. In addition, this lightly damped vibration mode also amplifies forces with frequencies above 20 Hz as shown in the frequency response. This amplification may be a potential problem for tests with high-frequency excitations.

5.2 Direct Velocity Feedback Compensation

Understanding the natural velocity feedback leads to a direct solution shown in Fig. 5.3. In this solution, the chamber volume variation to be compensated was determined by the product of the piston area and the piston/structure velocity, and the compensation was made directly to the actuator to cancel the effect of natural velocity feedback. The solution was not readily viable because the ports to the actuator were usually not accessible, and the implementation required a special valve and its controller that were not available. Nevertheless, the concept was used to explore the potential of velocity feedback compensation and the properties of the compensated system.

With the direct velocity feedback compensation, the transfer function G_{Fu} becomes

$$G_{Fu}(s) = \frac{AK_v C_F K_{vp} G_p}{(K_a s + C_l)(\tau A_v s^2 + A_v s + K_3 K_{vp}) x_{v\max} + AK_v C_F K_{vp} G_p}, \tag{5.2}$$

or

$$G_{Fu}(s) = \frac{AK_v C_F K_s G_p}{K_a s + C_l + AK_v C_F K_s G_p}, \tag{5.3}$$

if the servovalve dynamics is simplified as a servovalve gain (K_s). Comparison of the transfer functions to Eq. (5.1) or Eq. (3.51) shows that poles of the test structure are no longer zeros of the overall system. A stable pole-zero cancellation removes the conjugate zeros from the transfer functions such that the system output (force) would not be affected by the dynamics of the test structure.

The roots of the system are plotted relative to the various levels of velocity feedback compensation in Fig. 5.4. The motion of the roots with increasing compensation level (from zero compensation to full compensation) is shown by arrows. As the conjugate poles approach the zeros, the effect of the zeros is reduced as shown in the frequency response of the system in Fig. 5.5 (i.e., the affected frequency range decreases, and the depth of the dip at the natural frequency of the test structure reduces). With a full compensation, the poles are on top of the zeros, indicating a total cancellation of the effect of the natural velocity feedback.

On the other hand, when the natural velocity feedback is over compensated, the poles that cancel the zeros move towards the right-hand side of the s-plane, indicating a reduced stability margin or even instability. In addition, with the velocity feedback compensation, the conjugate poles corresponding to the high-frequency vibration mode (lightly damped as discussed previously) move to the left, indicating a more stable vibration with a smaller frequency and a faster decaying rate once the vibration mode is

excited.

The frequency responses with different compensation levels shown in Fig. 5.5 indicate that a slight undercompensation can significantly deviate the effect of the compensation. For example, the response magnitude at the natural frequency of the test structure corresponding to 95% compensation is about -10 dB or the amplitude of the force output is about 32% of the force command. Therefore, the acceptable range of compensation is very narrow.

The compensated system behaves as a first-order system at low frequencies as shown in Eq. (5.3) with a high roll-off frequency, hence the actuator should be able to follow the command closely within the frequency range of interest. However, the numerator and denominator of the transfer function do not have the same zero-order coefficient, indicating an amplitude reduction in the force output for low frequency inputs. The tracking error is due to the leakage of the servo-system, and the amplitude reduction (*RF*) can be estimated by

$$RF = 1 - \frac{AK_v C_F K_s G_p}{C_l + AK_v C_F K_s G_p}. \tag{5.4}$$

With the parameters identified in Chapter 4 (listed in Table 4.1), *RF* was calculated as 2%.

Therefore, the velocity feedback compensation can improve the ability of the actuator to track force commands. In practice, the velocity feedback compensation was made by modifying the command signal to the servovalve (Murcek, 1996).

5.3 Velocity Feedback Compensation

The velocity feedback compensation is schematically shown in Fig. 5.6. Instead of a positive feedback loop (a)-(b)-(c) as in the direct compensation, a positive feedback loop (a)-(d)-(e)-(f) was added to the actuator control to cancel the effect of the natural velocity feedback (a negative loop (a)-(b)-(c)). Comparing to the direct compensation, the chamber volume variation to be compensated ($A\dot{x}$) must be multiplied by the inverse dynamics of the servovalve and its controller before the compensation signal is added to the command signal. In addition, it is only necessary to consider the dynamics of the servovalve and its controller in the velocity feedback compensation loop. Therefore, the success of the velocity feedback compensation depends on how accurate the servovalve model defines the real system performance and how well the compensation scheme is implemented.

5.4 Linear Velocity Feedback Compensation

5.4.1 Linear Compensation Design

The design of the velocity feedback compensation is presented in Fig. 5.7. The path from point (f) to point (c) shows the forward dynamics formed by three components: the dynamics of the servovalve controller described by Eqs. (3.1) and (3.40), the servovalve dynamics by Eqs. (3.7) and (3.43), and the servovalve flow property by Eq. (3.24). In order to implement the velocity feedback compensation, the inverse of the dynamics of these components is needed.

The inverse flow relationship determines the required spool opening that allows a certain amount of flow (i.e., a compensation flow for $A\dot{x}$) to the actuator. The

servovalve flow model shown in Eq. (3.24) contains two major nonlinearities of the servo-hydraulic system: nonlinear flow gain and load pressure influence. If the spool opening and the applied forces are within a limited range (i.e., $|x_v| \le 0.1$ and $|P_L| \le 0.05P_s$) such that the nonlinearities are negligible, the servovalve flow can be simplified to be proportional to the spool opening as shown in Eq. (3.45). Therefore within a limited range, the inverse flow relationship is

$$x_v = \frac{Q_c}{K_v}. \tag{5.5}$$

where K_v is the initial no-load flow gain determined by Eq. (4.6).

The inverse servovalve dynamics relate the required spool opening determined by Eq. (5.5) to a valve command. The direct inverse of the servovalve dynamics results in a transfer function with a second-order term in the numerator, which is inherently unstable because it can greatly amplify signals with high frequencies, such as an electrical noise. On the other hand, the inverse of the simplified relation shown in Eq. (3.47) ($1/K_s$) is not good enough because it omits the response delay of the servovalve included in Eq. (3.43), while the response delay of the servo system is significant to the performance of the velocity feedback compensation (Timm, 1999). Hence in the compensation design, a first-order term ($K_s \frac{1}{T_d s + 1}$) with a time constant (T_d) of 5 ms was used to represent the servovalve dynamics for frequencies of interest (0-10 Hz), and the first-order phase-lead network shown in Eq. (2.34) multiplied by $1/K_s$ was used to invert the valve dynamics. The required time constant was determined by

$$T_{ld} = \frac{T_d}{1-\alpha}. \tag{5.6}$$

where the constant α was taken as 0.1 because it could provide both good phase-lead performance (the performance would be reduced if α is too large) and acceptable noise amplification (noises would be greatly amplified if α is too small). Fig. 5.8 presents the frequency response of the second-order servovalve model, the simplified first-order model, and the phase-lead network (inverse dynamics). The responses (amplitude and phase) of the combined dynamics (i.e., the second-order servovalve model followed by the phase-lead network divided by K_s) shown in dark solid lines are flat up to 20 Hz, indicating effective inverse dynamics for a wide range of frequencies.

PID controls with a zero I gain introduce some phase lead into the DC error signal if the derivative gain (controller D gain) is not zero. The derivative gain was usually set to a small value (a few tenths of a millisecond such as 0.2 ms) in this study; hence, the controller dynamics was simplified as a gain. To inverse the dynamics, the resultant phase lead (the lead-time G_d/G_p) was considered by reducing the time delay determined by Eq. (5.6), and the inverse relation was simply $1/G_p$.

5.4.2 Analysis of the linearized compensation scheme

The test system with linearized velocity feedback compensation is shown in Fig. 5.9, in which the velocity feedback compensation is represented by shaded blocks. Because the transfer function of the system is cumbersome to present, the pole-zero map of the compensated system shown in Fig. 5.10 is instead used to demonstrate the system performance. A stable pole-zero cancellation is evident near the imaginary axis, indicating that the actuator would be able to apply force at the natural frequency of the

test structure. Correspondingly, in the frequency response of the compensated system shown in Fig. 5.11, the amplitude dip around the natural frequency has been removed. In addition, compared to the pole-zero map of the uncompensated system in Fig. 5.1, the high-frequency mode in the compensated system has higher damping (from 0.4% to 1.6%).

However, the poles and zeros are not exactly the same as in the directly compensated system. This is because the phase-lead network is not an exact inverse of the dynamics of the servovalve and its controller. Consequently, both magnitude and phase responses of the compensated system are not perfectly smooth around the natural frequency of the test structure due to the close but incomplete pole-zero compensation, as indicated by two pointers in Fig. 5.11. The frequency response near the structural natural frequency is enlarged in Fig. 5.12. Although the bump can be reduced (not removed) through fine-tuning of the time constant of the phase-lead network, it is not practical because it is impossible to determine the exact response delay of the servovalve in practice.

Similar to the directly compensated system, the linearly compensated system has a steady-state tracking error at low frequencies as shown in Fig. 5.12. The close match between the responses of the linearly compensated system and the directly compensated system indicates that the error can be estimated using Eq. (5.4). With the parameters identified in Chapter 4, the tracking error was found to be 2%. In addition, the system output (applied forces) approaches the command as the frequency increases, and the output is roughly equal to the command at 10 Hz. Beyond 20 Hz, the system output is significantly affected by the lightly damped vibration mode of the system such that the force output grows rapidly with an increase of the forcing frequency.

A computer simulation of the system subjected to a 0.5 kip sine wave sweep was conducted and the result is presented in Fig. 5.13. A portion of the simulation result (from 4s to 8s) is shown in the time domain to make the plot more readable. The force tracking of the actuator is greatly improved compared to the case without compensation. On the other hand, the following problems can be identified: the force output does not match the force command between 5s and 7s in the time domain. Correspondingly, the FFT amplitude of the force output does not match very well that of the command forces from 1.5 Hz to 2.5 Hz. The reason is that the maximum spool opening in the simulation was about 13%, which slightly exceeded the linear range of the servovalve flow property when the forcing frequency was between 1.5 and 2.5 Hz (between 5s and 7s in the time domain). In addition, the load pressure influence was not considered in the linear velocity feedback compensation. Hence, A nonlinear compensation scheme is necessary in order to remove these discrepancies.

5.5 Nonlinear Velocity Feedback Compensation

In the linear compensation design, the servovalve was assumed to perform near its null position, and the applied force was assumed much smaller than the capacity of the actuator. However, it is likely that the limit would be breached during the application of the EFT method. In tests that require large flow demands (represented by large spool openings), caused by either large force command or large structural velocity response, nonlinearities in the servo-system become significant and must be addressed in the velocity feedback compensation.

5.5.1 Nonlinearities in Servovalve

Equation (3.24) describes the servovalve flow property, which contains two major nonlinearities, *load pressure influence* and *nonlinear flow gain*. The load pressure influence is explicitly represented by the square root term in Eq. (3.24). It reflects the nonlinear relation between the flow through an orifice and the pressure drop across the orifice: the larger the chamber inside pressure, the smaller the pressure drop across the load flow orifice, and the harder it is for the servovalve to drive hydraulic fluid into the actuator chamber.

The nonlinear flow gain is typically not obvious because servovalves are typically deemed proportional, meaning the controlled flow is proportional to valve commands if the load pressure is negligible. As discussed in Appendix 2, the nonlinearity is caused by the nature of hydraulic flow through a variable sharp-edged orifice: the flow discharge rate decreases with an increase of the orifice area (spool opening). Other factors that affect the flow property of a servovalve are the variation of supply pressure and return pressure. This factor was lumped into the nonlinear flow gain because the flow curve was determined under the working conditions of the servovalve. A piecewise linear curve based on test (identification) results was used to represent the nonlinear no-load flow gain of the servovalve.

5.5.2 Nonlinear Compensation Design

The design of the nonlinear velocity feedback compensation is presented in Fig. 5.14. The objective of the design was to incorporate in the compensation path (from point (d) to point (e)) the inverse of the dynamics including nonlinear relations in the forward path (from point (f) to point (c)). Because the controller remains the same, and the servovalve

dynamics model has been proven accurate for frequencies up to 20 Hz and throughout the operation range of the servovalve, the inverse dynamics of the servovalve and its controller remained the same in the nonlinear compensation design.

The inverse of the nonlinear servovalve flow property was based on the nonlinear characteristic of the servovalve identified in Chapter 4. Once the nonlinear flow model was verified through simulation and experiment, the nonlinear velocity feedback compensation was straightforward. The compensation signal ($A\dot{x}$) was first multiplied by $1\Big/\sqrt{1-\frac{x_v}{|x_v|}\frac{P_L}{P_s}}$ to consider the effect of large forces being applied to the structure. Then a linear interpolation based on the piece-wise linear flow curve was used to find the required spool opening to provide the compensation flow to the actuator. The inverse of the load pressure influence requires two more inputs, the spool opening and the load pressure. The spool opening was obtained directly from the servovalve controller, and the load pressure was approximated by the measured force divided by the piston area.

5.5.3 Evaluation of Nonlinear Compensation Scheme

The test system with the nonlinear velocity feedback compensation is shown in Fig. 5.15. To evaluate the efficiency of the nonlinear velocity feedback compensation design, a computer simulation was conducted for the system subjected to a 0.5-kip sine wave sweep. Figure 5.16 compares the simulation forces to the command forces in both the time domain and the frequency domain. Again only a portion of the response in the time domain (from 4s to 8s) is presented to facilitate the comparison. With the nonlinear compensation, which incorporated the exact inverse of the nonlinear flow relation of the servovalve, the discrepancies shown in Fig. 5.16 (with linear compensation) were almost

completely removed.

The effect of the nonlinear compensation is further demonstrated in the response of the system subjected to a 2-kip sine wave sweep shown in Fig. 5.17. In this simulation, the maximum required spool opening was around 55%, which was way beyond the linear range of the servovalve flow property (10%). No obvious difference between force output and command can be identified in the time domain. In the frequency domain, the force output follows the command throughout the whole frequency range (0-10 Hz). A small spike exists at the natural frequency of the test structure, reflecting the incomplete pole-zero compensation. As predicted by Eq. (5.4), the amplitude of the force output is a bit less than that of the command at low frequencies.

The simulation results of the test system with linear compensation and without compensation are also shown in Fig. 5.17 for comparison. A sharp drop of the FFT amplitude of the force output around 1.6 Hz is evident for the linearly compensated system in the frequency domain. This can be explained as follows: because the initial flow gain used in the linear compensation scheme is the largest slope of a typical flow curve, using the reciprocal of the initial flow gain in the compensation loop causes undercompensation when the spool opening is large. Meanwhile the force tracking ability of the actuator can be greatly affected by a slight undercompensation (e.g., 5%) as indicated in Fig. 5.5.

In summary, to negate the effect of the natural velocity feedback, the compensation was made by modifying the command signal to the servovalve controller. The proposed compensation scheme requires an accurate knowledge (model) of the dynamics and the flow property of the servovalve. The physical system may have uncertainties such that

the identified models may deviate from the physical properties of the system. Therefore, it is necessary to investigate the ability of the compensation scheme and the compensated system to accommodate variation in system parameters.

5.6 Critical Parameters in Velocity Feedback Compensation

The design of velocity feedback compensation schemes require the determination of the following parameters: controller P gain (G_p), controller D gain (G_d), servovalve gain (K_s), servovalve response delay (T_d), and servovalve flow property including the initial no-load flow gain (K_v). Among these parameters, the controller D gain was considered with the overall response delay of the servovalve, and the servovalve gain identified in Chapter 4 was deemed accurate. The remaining three parameters are discussed in this section, and the discussion includes their effects on the overall system stability.

5.6.1 Controller P Gain

As indicated in Figs. 5.4 and 5.10, a compensated test system has two second-order components: one represents the vibration of the test structure, and the other represents the dynamics of the servovalve (typically with a high frequency). With the velocity feedback compensation, the dynamics of the first component approaches that of the test structure, which is the goal of the test system. Meanwhile, the damping of the high-frequency mode increases. Therefore, any P gain below the maximum P gain determined in Chapter 4 for the purpose of the stability of the uncompensated system should be appropriate for use in the compensated system.

Generally, relatively larger P gains should be used in a test system because they usually improve the overall performance of a stable system. Figure 5.18 compares the

frequency response of the compensated system with various controller P gains. A higher P gain corresponds to smaller distortion caused by the incomplete pole-zero cancellation in both amplitude and phase responses around the natural frequency of the test structure. In the last case shown in Figure 5.18, a P gain of 0.8 was used while the maximum allowable P gain for the uncompensated system was 0.71 according to Routh's stability analysis because a larger P gain would usually cause an unstable high-frequency vibration. A larger P gain than the predicted limit would be expected in general in practice due to a larger system leakage than the assumed leakage as to be discussed in Section 7.1.1.

Increasing the controller P gain may slightly increase the damping of the vibration of the test structure as shown in Fig. 5.19, the root loci of the test system. On the other hand, larger controller P gains (e.g., 1.0 for this test system, which is way beyond the maximum allowable value) may cause instability as indicated by the two poles at the right-hand side of the *s*-plane in Fig. 5.19. It should be noted that the resulting unstable poles correspond to a component of the force output at a frequency around 65 Hz, which usually does not cause damage of the test structure because the structure does not respond to excitations at such high frequencies.

Based on these observations, the laboratory implementation of the EFT method, which will be discussed in the next chapter, started with a P gain that could keep the uncompensated system stable (0.7), and proceeded with larger P gains (0.8 and 1.0 with an additional leakage path) to improve the overall system performance.

5.6.2 Servovalve Flow Gain

The velocity feedback compensation is based on an estimation of the flow property

including the initial flow gain, which may vary during a test due to uncertainties of the test system and test environment (i.e., hydraulic supply, etc.). Therefore, the natural velocity feedback may be instantly either under- or over-compensated when the compensation is based on a predetermined flow curve.

The initial flow gain (K_v) is an important representative property of the servovalve flow. The root loci of the linearly compensated system with respect to various initial flow gains are shown in Fig. 5.20. Two conjugate poles that represent the SDOF test structure shown in larger crosses are expected if there is no problem in applying forces to the structure. Slight over- or under-compensation may change the damping of the vibration mode that represents the test structure. Although overcompensation appears helpful in stabilizing the high-frequency vibration, an overcompensated system may become unstable. Unlike the instability caused by a large controller P gain, the unstable vibration at a frequency close to the structural resonant frequency can cause unwanted damage to the test structure. The stability margin of the system, indicating the maximum tolerable overcompensation, was related to the structural damping. A high structural damping helps the system tolerate system identification errors.

Compared to the rest of the flow curve, a relatively accurate initial flow gain may be readily obtained because tests with small amplitude excitations can be conducted to optimize the estimation. The effect of the whole flow curve of the servovalve is shown in Fig 5.21, which compares the simulation results of a nonlinear system subjected to a 2-kip sine wave sweep (0-10 Hz) with different compensation levels. The flow curve was modified by a factor of 1 or 2 percent while the initial flow gain was kept the same. As can be seen, 2% undercompensation resulted in large reduction in force amplitude at the

natural frequency while 1% overcompensation might cause unpredictable force output such as the spikes in the time domain.

It should be noted that the spike at the natural frequency in the frequency domain does not necessarily correspond to the spikes in the time domain. Instead, the spike at the natural frequency was attributed to the fact that the overcompensation contaminated the valve command signal with small signals at the resonant frequencies of the structure (from the structural velocity response). The accumulating process of the FFT calculation builds up a spike at the frequency.

It can be anticipated that the results of a real test would lie in between these two cases because both under- and over-compensation may happen in a single test at different instances. Noisy force output is likely to happen when the required spool opening is large because the system uncertainties usually increase with flow demands.

5.6.3 Servovalve Response Delay

Another system parameter that cannot be determined exactly prior to testing is the response delay of the servovalve. Similar to the main-stage valve flow property, the pilot-stage valve can be affected by the variation of the hydraulic supply, which in turn may affect the response delay of the three-stage servovalve. Therefore, slight under- or over-compensation of the servovalve response delay is likely to happen when the delay compensation is based on a predetermined delay time.

The effect of the delay compensation to the root loci of the compensated system is illustrated in Fig. 5.22. The system with more delay compensation has larger damping for both vibration modes than that of a less compensated system. Specifically, the high-frequency mode can be unstable if the response delay is not compensated. In addition,

incorrect delay compensation alters both the frequency and the damping of the mode that represents the test structure, which is unwanted. Compared to the case of the flow gain, the system has a wider stability margin with respect to the response delay compensation.

The frequency responses of the system with various delay compensation schemes are shown in Fig. 5.23. As identified in Chapter 4, 5 ms is a good estimate of the total response delay of the servovalve and its controller in this study. If the response delay is undercompensated, the amplitude response shows a peak at a frequency smaller than the natural frequency and a valley at a frequency larger than the natural frequency. The system response with overcompensation shows a reversed pattern, a valley before a peak. For the test system with the nonlinear velocity feedback compensation, a series of simulations were conducted, and the results are presented in Fig. 5.24. Similar observations can be made regarding the correspondence between the delay compensation and the pattern of the force amplitude in the frequency domain. This information is useful when searching for the optimal time constant for the phase-lead network.

5.7 Summary

In this chapter, the natural velocity feedback loop intrinsic to the servo-system was discussed along with a solution, velocity feedback compensation. Linear velocity feedback compensation is limited because significant nonlinearities exist in the servovalve when large flow demands are required during a test. The servo-system nonlinearities must be considered in the velocity feedback compensation to assure the force tracking ability of the actuator. A nonlinear compensation scheme was designed and discussed using computer simulations along with three critical parameters (i.e., the

controller P gain, the servovalve flow property, and the servovalve response delay). These compensation schemes were experimentally investigated using a SDOF structural model.

CHAPTER SIX

EXPERIMENTAL IMPLEMENTATION OF EFT

The feasibility of EFT with velocity feedback compensation is experimentally evaluated using a SDOF structure. Details of the experimental program are first described. Test results with both sinesweep inputs and earthquake effective forces are then presented to evaluate the performance of the test system with the velocity feedback compensation schemes. Experimental studies are also used to verify the conclusions drawn in Chapter 5 regarding the effect of the critical parameters.

6.1 Experimental Program

6.1.1 Test Setup

A schematic of the test system is shown in Fig. 6.1, in which the velocity feedback compensation was applied using an additional controller shown as the dashed block. The investigation was conducted using an SDOF mass-spring-damper structural model. A schematic of the test setup is illustrated in Fig. 6.2, and the laboratory realization of the test setup is shown in Fig. 4.12. The structural properties (i.e., m, c, and k) are listed in Table 4.1, and details of the test structure are given in Section 4.4 and Appendix 4.

Six linear variable differential transformers (LVDTs) were used to monitor the displacement response of the cart in the beginning. After concerns about possible torsion of the cart and slip between layers of the concrete mass were cleared, the LVDT housed within the actuator was the only displacement sensor used. The range of the internal

LVDT was ±5 inch. A positive displacement corresponded to a displacement of the actuator piston towards the actuator reaction frame, which is also the positive force direction.

The velocity response of the structure was monitored with a P510 series tachometer-type velocity transducer by Unimeasure Inc. The velocity transducer was placed on the side of the mass opposite the actuator, and aligned with the center of the mass. The velocity sensor had a sensitivity factor of 0.196 volt/in/s, and a travel length of 10 inch. A positive velocity corresponded to an extension of the sensor cable (a motion towards the actuator reaction frame), thus a displacement increase would cause a positive velocity signal.

Actuator forces were measured using a load cell mounted on the actuator piston. The load cell signal as well as the actuator LVDT signal was conditioned by two conditioning modules installed in the servovalve controller. The outputs were available through two BNC connectors on the rear panel of the controller. The servovalve spool opening (spool position) was measured by an LVDT inside the main-stage servovalve house. The signal along with other internal control signals, such as the valve command signal and DC error signal were available through two BNC connectors on the front panel of the servovalve controller.

Data was collected by an Optim MEGADAC 3008AC data acquisition system. A sample rate of 200 samples per second was chosen for most of the experimental program. Four channels of data were typically read, including the actuator position, the actuator force, the structural velocity, and the spool opening of the servovalve. The Optim data acquisition system had a sample-and-hold mechanism, which locked the voltage signals

in all channels simultaneously before they were sampled and converted into digital signals.

The velocity feedback compensation schemes were implemented using a dSpace DS1102 DSP controller. The hardware consisted of a DSP Controller Board based on a Texas Instruments TMS320C31 floating-point digital signal processor (DSP) built as a standard PC/AT card. The DS1102 contained two 16-bit 250KHz sampling A/D converters (ADCs) and two 12-bit 800KHz sampling A/D converters. Each ADC had a sample/hold circuit (i.e., no delay between signals). All ADCs take single-ended bipolar inputs with ±10 volt input span. The DS1102 also contained four 12-bit D/A converters (DACs). All DACs had single-ended voltage outputs with ±10 volt span. The DS1102 hardware was managed by ControlDesk®, software installed in the host computer of the DS1102.

6.1.2 Ground Accelerations

Command signals were sent to the servovalve controller from a National Instruments digital-to-analog (D/A) card, which was installed in a Windows NT workstation. A computer program read the values from a user-defined data file, and sent the digital signal to the D/A card, which produced an output voltage that was proportional to the data values. The scale factor was the conversion factor (*CF*) pre-determined for the program according to the type of input units (control variable) chosen in the servovalve controller. An example data file is shown in Appendix 5 to demonstrate the format of the data file. Earthquake ground acceleration records are typically defined at 0.02-second intervals while in this study, the data was refined by linearly interpolating nine points between each data point such that the signals sent to the servovalve controller were

updated every 0.002 seconds.

The input functions used in the experimental investigations included sinesweep (0-10 Hz) and earthquake effective forces. The ground acceleration records chosen for the experimental program were the Imperial Valley earthquake of May 18, 1940, recorded at El Centro at 270 degrees, with a peak ground acceleration of 0.34 g and the Northridge earthquake of January 17, 1994, recorded at Santa Monica City Hall ground at 90 degrees, with a peak ground acceleration of 0.84 g. These earthquake records were obtained from the strong motion database of the Pacific Earthquake Engineering Research Center (PEER) at http://peer.berkeley.edu/smcat/search.html.

The ground acceleration records for these earthquakes are shown in Figs. 6.3 and 6.4 along with their FFT amplitudes. In order to reduce the amount of data to be collected, segments of these earthquake records were used that represented the most demanding portion of the records and had frequency content similar to the entire records. These ground acceleration records and their FFT amplitudes are shown in Figs. 6.5 and 6.6, respectively.

The earthquake records were chosen based on their frequency contents. Fig. 6.7 shows a force-velocity curve for the servovalve-actuator combination generated based on Eq. (3.24) and Eq. (3.37). The fluid compressibility and leakage were omitted, thus the piston velocity was directly related to the load flow of the servovalve by

$$A\dot{x} = Q_L = Q\left(x_v\right)\sqrt{1-\frac{x_v}{\left|x_v\right|}\frac{P_L A}{P_s A}}\,. \tag{6.1}$$

For a given spool opening (from -1 to 1 with an interval of 0.2 in the plot), the maximum achievable velocity can be calculated using Eq. (6.1) for any given load

pressure (applied force divided by the piston area). The nonlinear no-load flow property of the servovalve was included in the calculation of $Q(x_v)$.

With sine wave sweep inputs, the structure would be excited with small amplitude forces. Therefore, the horizontal shaded area in the force-velocity plot in Fig. 6.7 would be tested for the system. The Northridge earthquake ground acceleration record has small frequency content around the resonant frequency of the structure, but has large acceleration peaks at 9s as shown in Fig. 6.5. Therefore, the vertical shaded region in Fig. 6.7, which represents conditions with large forces and small velocities, could be tested. Tests with El Centro earthquake effective force inputs could demonstrate the system performance for the blank regions inside the ±60% spool opening curve because large force and large velocity might happen at the same time during the tests.

In the following sections, the performances of the system are demonstrated through comparing test results (i.e., force output and structural responses). In the comparison of forces, "commands" are effective force commands ($-m\ddot{x}_g$) sent to the servovalve controller. "Measurements" are the forces measured by the actuator load cell, that is, the forces physically applied to the structure. "Simulations" are the simulated forces to the structure. When comparing structural responses. "Expected responses" are the results of the numerical integration of the governing differential equation shown in Eq. (3.38) with the effective force inputs. "Measured responses" are the structural displacements and velocities measured by the actuator LVDT and the velocity transducer. "Simulation responses" are the results of the numerical simulation of the whole test system with the effective force inputs.

6.2 Direct Implementation of EFT

The first objective of the experimental study was to demonstrate the natural velocity feedback problem using a different test system than that of previous studies at the University of Minnesota (Murcek, 1996 and Timm, 1999). The system response was first evaluated over a range of frequencies (0-10 Hz) of interest by applying sinesweep input functions, and then by applying effective force input functions to the test system without velocity feedback compensation.

Sinusoidal Input Function

Figure 6.8 compares command forces, simulation forces, and measured forces and the FFT amplitude of these forces using a 0.5 kip sine wave sweep input function. The actuator had difficulties applying forces throughout the test. Correspondingly, in the frequency domain, the ability of the system to apply forces around the natural frequency of the structure (1.6 Hz) was greatly limited due to the effect of the natural velocity feedback. The comparison of the expected, simulation, and measured structural responses is shown in Fig. 6.9. The resonant frequency of the structure was not excited because of the missing forcing content around the natural frequency, and the structural responses were significantly smaller than the desired responses. Computer simulations correctly predicted the performance of the test system.

The applied force was noisy, especially at the beginning of the test. This was due in part to the static friction, which the actuator had to overcome to move the structure. The noisy system response (force) was also due to a lightly damped vibration mode of the system with a frequency around 61 Hz as shown in Fig. 5.3. On the other hand, the force content at this frequency (61 Hz) could not excite the structure, and the structural

responses were smooth as shown in Fig. 6.9.

Earthquake Effective Force Inputs

Tests were also performed in which effective forces based on the ground acceleration of the earthquakes described in the previous section were input to the system. Figs. 6.10 and 6.11 present the test results using the El Centro earthquake record, and Figs. 6.12 and 6.13 present the test results using the Northridge earthquake record. The El Centro earthquake contained significant frequency content around the natural frequency of the test structure, thus the actuator had difficult in following the command signal, especially in catching the force peak at 2s. On the contrary, the Northridge earthquake contained little frequency content at the structural resonant frequency, and the actuator seemed to be able to better follow the force command and catch the force peak around 9s.

In the frequency domain, there was a range of frequencies for both tests around the natural frequency of the structure, where the amplitude of the force outputs was significantly below that of the force commands. Due to the missing frequency content in the applied forces, the resonant frequency of the structure was not excited as shown in the displacement and velocity responses of the structure in Figs. 6.11 and 6.13. Toward the end of the tests with zero force commands, aftershock free vibrations were expected as shown in grey lines, while they were not obtained during the tests or in the simulation.

These test results indicated that with the direct application of the EFT method, the hydraulic actuator could not apply forces accurately around the resonant frequency of the structure, which was rigidly connected to the actuator piston. This confirmed the observations made in previous studies by Murcek (1996) and Timm (1999). The effect can be compensated by modifying the command signal to the servovalve controller based

on measured piston velocities.

6.3 Linear Velocity Feedback Compensation

In the laboratory implementation of the velocity feedback compensation, the chamber volume change due to the piston motion was determined by the measured structural velocity multiplied by the piston area. The compensation signal was modified by the inverse of the forward dynamics and then added to the command signal. The linear compensation scheme had been implemented using analog circuits (Timm 1999). A digital implementation of the linear compensation is presented in this section to illustrate some conclusions drawn in Chapter 5.

Laboratory Implementation

In the digital implementation, analog signals (e.g., command signals from the National Instruments D/A card, and voltage signals from the velocity transducer, etc.) were converted into digital signals by the A/D converter of the DSP board. The digital signals were then processed by the control algorithm to generate the modified command signals. The new command signals were converted back to voltage signals and sent to the servovalve controller. The control algorithms were coded in C language with functions provided by dSpace and compiled by the C language compiler for TMS320C31 DSP hardware provided by Texas Instruments. An example of the compensation schemes in C language can be found in Appendix 6.

The velocity transducers used in this study did not have signal conditioning, hence, a unit buffer (a unity-gain circuit) was closely coupled to the transducer to avoid signal attenuation over a long distance of the signal transmit. A buffer circuit can be found in

texts such as the one by Horowitz and Hill (1990). Note that the voltage signal generated by the velocity transducer should be divided by the sensitivity factor to get the velocity signal shown in the compensation schemes in terms of simulation models.

Figure 5.9 shows the test system with the linear velocity feedback compensation. In the laboratory implementation, all constants in the compensation loop were combined into a single factor determined by,

$$K_c = \frac{A}{S_v K_v K_s G_p}, \tag{6.2}$$

where S_v is the sensitivity factor of the velocity transducer. For example, when the solution was first tried, a Trans-Tek Model 0114-0000 velocity transducer was used with a range of ±2 in., and a sensitivity factor of 0.582 volt/in./s. The gain was calculated as 0.271 with the parameters identified in Chapter 4 (K_v=1003 in.^{3}/s. K_s=0.1, and G_p=0.81).

A discrete equivalent of the phase-lead network shown in Eq. (2.35) was used in the digital implementation. By applying the trapezoid-rule substitution for the frequency variable *s* (Franklin 1994), the phase-lead network can be rewritten as

$$H(z) = \frac{X(z)}{U(z)} = \frac{(T + 2T_{ld})z + (T - 2T_{ld})}{(T + 2\alpha T_{ld})z + (T - 2\alpha T_{ld})}. \tag{6.3}$$

In the time domain, the current output was calculated using the current input and past input and output by

$$x(t) = \frac{1}{T + 2aT_{ld}}\left[(T + 2T_{ld})u(t) + (T - 2T_{ld})u(t - T) - (T - 2aT_{ld})x(t - T)\right] \tag{6.4}$$

where $u(t)$ and $x(t)$ are the current input and output signal samples, $u(t-T)$ and $x(t-T)$ are the last input and output signal samples, T_{ld} is the lead time (T_{ld}=T_d/(1-α),

where T_d is the response delay to be compensated) and α is 0.1 as in the simulation studies, and $t=kT$, where k is an integer and T is the sampling period. With a sampling rate of 2 kHz in this study, T was 0.5ms.

Sinusoidal Input Functions

The system response (i.e., force output) to a 0.5k sinesweep input function is shown in Fig. 6.14 along with the FFT amplitudes of the forces. The measured force followed the command force in the time domain except the noisy force peaks and valleys between 5s and 7s, which could have been due to the lightly damped high-frequency vibration in the system. Comparison in the frequency domain indicates that the actuator was able to apply forces at all frequencies within 10 Hz. A small amplitude spike at 1.6 Hz is evident in the frequency domain due to the aforementioned accumulative process of the FFT amplitude calculation.

The amplitude of the applied force was slightly below that of the command force over the whole frequency range in Fig. 6.14. It was in part attributed to the proportional leakage of the servo-system shown in Eq. (5.8). The force tracking error should be reduced at high frequencies as indicated by the simulation results shown by the dashed lines in Fig. 6.14. However, the servovalve leakage was not constant throughout the whole range of its operation. When the actuator tried to track the high frequency signals, the spool was near its null position, where the leakage coefficient was larger. The increased leakage flow at small spool openings in turn affected the tracking ability of the actuator at high frequencies. Another factor was the constant leakage in the system to be discussed in Chapter 7.

Figure 6.15 compares the measured structural responses with the expected and

simulation results. The displacement and velocity responses show that the measured response generally matched the expected response but did not achieve the magnitude of the expected response. The reason that the structure was not fully excited might have been that the applied force was low at frequencies near the natural frequency of the structure due to incomplete velocity feedback compensation.

The simulation was generally able to predict the force output and the structural responses, indicating that the analysis of the system model in Chapter 5 was applicable to the physical test system. On the other hand, because the simulation could not capture the real-time variation of the servovalve flow property, the amplitude spike at the natural frequency and the shallow drop around 2 Hz were not captured by the simulation. In addition, the simulation did not match well the experimental responses after 15s when the structural responses were small in Fig. 6.15. The reason may have been that the mechanism of the energy dissipation could not be modeled well with a combination of viscous damping and friction when the structure moved within a small range as shown in the analysis of the free vibration results in Fig. 4.12.

The system response to a 2.0 kip sinesweep input function is shown in Fig. 6.16. The applied force was able to follow the sinesweep input except over the time range from 4s to 7s, when the desired velocity was large (as shown in Fig. 6.17). The large velocity caused a large hydraulic demand (55% spool opening should have been required if the actuator had had no problem in tracking forces) because the modified command signal to the servovalve was dominated by the velocity compensation signal, which was based on the structural velocity. The servovalve exhibited nonlinear flow properties at large spool openings; hence, the linear velocity feedback compensation was not sufficient. In the

frequency domain, the FFT of the applied force shows a sharp drop around the natural frequency of the test structure.

Due the lack of the frequency content in the force applied to the structure, the structural responses were significantly below the expected responses as shown in Fig. 6.17. Again, the simulation accurately predicted both the force output of the test system and the structural response under the incorrect excitation, indicating that the models developed in Chapters 3 and 4 could accurately represent the physical test system. Both the experimental and simulation results demonstrated that the linear velocity feedback compensation was not able to negate the natural velocity feedback when large hydraulic power was required (expressed as large spool openings).

Earthquake Effective Force Inputs

The digital implementation of the linear velocity feedback compensation was also tested with earthquake effective force inputs. The system response to the El Centro earthquake (0.17g) shown in Fig. 6.18 indicates that the actuator was generally able to follow the command force. The comparison in the frequency domain shows a good match over the entire frequency range of interest. However, the force peak at 2s was not fully reached, and the FFT amplitude of the applied force around the natural frequency of the structure (1.6 Hz) was slightly less than that of the effective force input.

The required spool opening in the first 4s of the test was larger than 10% (16% around 2s), thus the system was under-compensated with the linear compensation. As a result, the measured displacement and velocity response shown in Fig. 6.19 were smaller than the expected responses during the first 8s. The influence of the under-compensation near 2s was spread out because the structure went into the nonlinear range of its behavior,

and the structural responses after the peak at 2s were dependent on the response history. Around 8s, both the effective force and the structural responses were small, which resembled a new test starting point; hence during the rest of the test, the linear compensation was adequate, and the experimental results matched the expected responses well.

The system response for the Northridge earthquake (0.42g) in Fig. 6.20 closely matched the effective force input in both the time domain and the frequency domain, and the structural responses in Fig. 6.21 closely matched the expected responses. This was because the Northridge effective force input contained only a small amount of frequency content around the natural frequency of the structure, thus the velocity response and the required spool opening were small (< 10%), and the linear velocity feedback compensation worked well in this case. Especially, when the effective force peak hit the structure at 9s, the structural velocity was around 5 in./s, and the required spool opening was small; hence, the force peak was reached in the test. In addition, the free vibration after 15s when the force command stopped was realized though the experimental response decayed slightly faster.

Therefore, the linear velocity feedback compensation can be used to negate the effect of natural velocity feedback under limited conditions: the structural velocity and the applied force remain small, corresponding to a small hydraulic demand (the maximum spool opening remains below 10%) during a test. Beyond this limit, nonlinear velocity feedback compensation is necessary.

6.4 Nonlinear Velocity Feedback Compensation

Laboratory Implementation

According to the nonlinear velocity feedback compensation design shown in section 5.5.2, the compensation flow ($A\dot{x}$) needs to be multiplied by $1\Big/\sqrt{1-\frac{x_v}{|x_v|}\frac{P_L}{P_s}}$ to consider the load pressure influence. Three new measurements were required for this process, the current spool opening (x_v), load pressure (P_L), and pressure supply (P_s). Because the instant pressure measurements were difficult to obtain, the pressure supply was assumed constant (2.65 ksi), and the load pressure was approximated by the measured force divided by the piston area. The spool opening was read directly from the servovalve controller, which always contained offsets. In order to remove the effect of the initial offset on the determination of the sign of the spool opening ($x_v/|x_v|$), the average of the inputs during the first ten-second operation of the DSP controller (with zero force input) were calculated and subtracted from spool opening signals. The same process was used for other measurements, such as the piston velocity and the measured force, to remove their initial offsets.

The modified compensation flow was then used to determine the required spool opening based on the identified piece-wise linear flow curve. The curve was defined by flow values at 21 control points within the whole servovalve operation range (-1 ~ 1) with an interval of 0.1; hence linear interpolation was used between control points in the process. The required spool-opening signal was then multiplied by the inverse servovalve gain to obtain the corresponding valve command signal (voltage), and was modified in phase using the same phase-lead network as in the linear compensation.

After being divided by the controller P gain, the phase-adjusted voltage signal was finally added to the effective force command signal.

Sinusoidal Input Functions

With the flow curve identified in Chapter 4, tests were conducted with sinesweep input functions. Fig. 6.22 presents the system response to a 0.5 kip sine sweep input. Compared to the test with the linear velocity feedback compensation, the amplitude drop around 2 Hz in Fig. 6.14 was removed, indicating an improved ability of the actuator to follow force commands within the frequency range. With an improved force input near the resonant frequency, the structural responses shown in Fig. 6.23 better matched the expected responses. In addition, the expected peaks in both the displacement and velocity response were reached. The noisy force output from 5s to 8s and the discrepancy in the displacement and velocity responses after 10s were attributed to uncertainties in the system (i.e., hydraulic supply variation) that the nonlinear compensation was not able to model and include.

Figure 6.24 presents the test results for a 2.0 kip sine sweep input. The FFT of the measured force does not show any obvious drop across the whole frequency range, indicating that the actuator was able to apply forces correctly at all frequencies. Compared to the test with the linear velocity feedback compensation, the ability of the actuator to follow force commands was greatly improved. Small discrepancies can be seen in the frequency domain from 1.5 Hz to 2.5 Hz, which corresponds to 4s to 8s in the time domain, where the force output was noisy. As shown in Fig. 6.25, the structural velocity response between 4s to 8s was large, which indicates large required spool openings (55% maximum) during the test. At large spool openings, the system

uncertainties become significant as indicated by the larger variation in the servovalve flow property as shown in Fig. 4.9. Hence, the velocity feedback compensation based on the piece-wise linear flow curve might instantly incomplete. The inaccurate force applied to the structure might have been responsible for the discrepancy in the structural responses in Fig. 6.25. The structural responses after their peaks were also affected because nonlinear structural responses are dependent on the loading history.

Earthquake Effective Force Input

The responses of the system to the same earthquake effective force input functions as in the linearly compensated tests are shown in Figs. 6.26 - 6.29. The measured displacement and velocity response generally followed and were in phase with the expected responses. Compared to Figs. 6.18 - 6.21, both the system response (force output of the actuator) and the structural responses were improved. In the test with the El Centro earthquake, the force peak at 2s was better reached as shown in Fig 6.26, and the structural responses were better matched between 1s and 8s as evident in Fig 6.27. In the test with the Northridge earthquake, a better match between the measured force and command force can be observed in the frequency domain from 1 Hz to 2 Hz, and the velocity peak around 9s was better reached.

The test results with increased effective force input functions (from 50% of the full scale to 80% of the full scale) are presented in Figs. 6.30 - 6.33. The actuator had no problem in following force commands that contained relatively small frequency content at the structural resonant frequency such that the structural velocity was small when the force peak was applied to the structure, as in the case with the Northridge earthquake effective force input. On the other hand, the actuator showed some difficulties in

catching force peaks when a large velocity occurred at the same time as in the case of the El Centro earthquake effective force input.

In the test with the 0.27 g El Centro earthquake effective force input, the structural responses showed some large discrepancies from the expected responses. The measured responses were smaller than the expected responses before 12s and larger after 17s. This was attributed to the fact that the incomplete velocity feedback compensation might have changed the loading history to some extent, which in turn resulted in a different response history because the nonlinear structural response depended on the loading history.

Simulation results match the effective forces and expected structural responses better than the measured responses because the exact inverse of the forward dynamics including servovalve nonlinearities were incorporated in the compensation loop of the simulation. The simulation results indicate that the performance of the proposed nonlinear velocity feedback compensation depends on the accuracy of the model of the servovalve and its controller.

6.5 Comparison of Compensation Schemes

To further demonstrate the nonlinear velocity feedback compensation, tests were conducted with the full-scale El Centro earthquake (0.34g) and the full-scale Northridge earthquake (0.84g). The test results are compared to those of the tests with the linear velocity feedback compensation scheme and without velocity feedback compensation in Figs. 6.34 - 6.37.

The tests with the El Centro earthquake are shown in Figs. 6.34 and 6.35. With the nonlinear compensation, the measured force in general better followed the command

force than that of the test with the linear compensation. For example, the force peak at 2s was better (yet not fully) reached with the nonlinear compensation. The measured structural responses generally follow the expected responses though there is some phase shift between 6s and 11s. On the other hand, with the linear compensation, the structural responses were significantly smaller than the expected responses.

In the tests with the Northridge earthquake shown in Figs. 6.36 and 6.37, the measured forces showed a good match with the command force in both cases. However, the structure in the test with the linear compensation developed a very different deformation pattern after 11s, and the response amplitudes were significantly smaller than the expected response and that of the test with the nonlinear compensation.

These comparisons demonstrate the superiority of the nonlinear compensation scheme over the linear compensation scheme. Meanwhile, the comparisons also reveal the limitation of the current nonlinear compensation scheme: the natural velocity feedback compensation is based on a predetermined servovalve flow curve while at large spool openings, the variations in the servovalve flow property become important, and may deteriorate the system performance. The ability of the test system to tolerate uncertainties is explored in the following section.

6.6 Effect of Critical Parameters

Tests with a 0.5 kip sine sweep input function and the linear velocity feedback compensation were conducted to demonstrate the effect of three parameters on the performance of the compensated system discussed in Chapter 5. These parameters were the controller P gain (G_p), servovalve flow gain (K_v), and servovalve response delay (T_{ld}).

It should be noted that although it was intended to consider these parameters individually, their effects are usually combined.

6.6.1 Controller P Gain

Large controller P gain generally improves the overall system performance; however, the increase of the controller P gain is limited due to potential stability problems. Linear analysis by applying Routh's stability criterion indicates that the maximum allowable P gain is closely related to the servo-system leakage, which was hardly a fixed value. A P gain of 0.81 was initially used though the predicted maximum P gain was 0.71 as shown in Appendix 3.

During the course of the study, the actuator developed problems and required new seals and a recharge of the piston. This repair significantly reduced the actuator leakage; consequently, a P gain of 0.68 had to be applied to keep the uncompensated system stable. The small P gain caused large force tracking errors of the actuator across the whole frequency range of interest. Therefore, a needle valve was connected to the actuator ports to create additional "cross-port leakage". With the increased proportional leakage, the maximum allowable P gain was increased to 1.0.

Figure 6.38 compares the performance of the linearly compensated system with three controller P gains. The additional "cross-port leakage" was engaged in all the tests. The force tracking error of the test with the smaller P gain (0.61) was significantly greater than that of the other cases (i.e., G_p of 0.81 and 1.0). Although the system performance with a P gain of 1.0 looked similar to that of the test with a P gain of 0.81, the structural response was indeed improved with a larger P gain because of the improved force tracking ability of the actuator.

On the other hand, a large P gain may drive the high-frequency mode of the test system into the unstable range as shown in Fig. 5.22. This situation (i.e., unstable high-frequency mode) happened many times when tests were conducted to determine the maximum allowable P gain beyond the predicted one in Appendix 3 before the additional leakage flow passage was installed. An example of the unstable high frequency vibration is shown in Section 6.6.3, where a P gain of 1.0 was used, and the servovalve response delay compensation was purposely set incorrectly.

6.6.2 Servovalve Flow Gain

Because of the uncertainties in the servo-system, such as hydraulic supply variation, the predetermined flow property is unlikely able to reflect the physical condition all of the time, thus causing under- or over-compensation during a test. Fig. 6.39 compares the system response with linear velocity feedback compensation based on various initial flow gains. Similar to the simulation results shown in Fig. 5.24, under-compensation weakened the ability of the actuator to track forces around the natural frequency of the structure while over-compensation contaminated the command signal with a signal at the structural resonant frequency.

The conclusion can be extended to tests that required the nonlinear velocity feedback compensation. The actuator in an under-compensated system would have problems in tracking force commands, such as reaching force peaks, while an over-compensated system would cause incorrect structural responses and even instability. Both situations were observed experimentally during the process of the development of the nonlinear velocity feedback compensation scheme.

6.6.3 Servovalve Response Delay

Uncertainties in the determination of the servovalve response delay may affect the system response as shown in Figs. 5.26 and 5.27. The simulation results were confirmed by experiments shown in Fig. 6.40. As indicated in Chapter 4, a time delay of 5 ms was optimal for the servovalve in this study while tests with 3-ms and 7-ms compensation were conducted to investigate the effect of the variation of the compensated time delay. With insufficient delay compensation, a peak before a valley appeared in the FFT of the measured force while a peak after a valley appeared in the frequency domain when the delay was over-compensated.

As indicated in Section 5.6, a combination of high P gain and insufficient delay compensation might cause an unstable high-frequency vibration of the actuator piston. On the other hand, the unstable vibration would not grow unbounded due to physical limits of the test system. An example of the system response with a P gain of 1.0 and the compensated delay of 2ms is shown in Fig. 6.41. Towards the end of the test when the force command was zero, the actuator applied a force with 1-kip amplitude and 64 Hz frequency to the structure. The force vibration might have started by some random input (i.e., noise), and would go on until the hydraulics were shut down or the controller P gain was turned down such that the high-frequency mode moved back to the stable range. Meanwhile, the disturbance in the applied force was not able to excite the structure because the forcing frequency was far away from the resonant frequency of the structure.

6.7 Summary

In the direct implementation of the EFT method, the interaction between the actuator

control and the actuator piston velocity, termed "natural velocity feedback", affected the actuator's ability to apply forces accurately around the natural frequency of the test structure. The concept of velocity feedback correction proposed by Murcek, termed "velocity feedback compensation" herein, was implemented using a physical SDOF structural model and a digital controller. The effect of the natural velocity feedback was compensated by modifying the command signal to the servovalve controller. This process required that the compensation loop incorporate the inverse of the dynamics of the servovalve and its controller.

Servovalves have high-order dynamics and nonlinear flow properties. In the laboratory implementation of the velocity feedback compensation, the servovalve dynamics were simplified as a first-order delay with a valve gain; the servovalve flow property was first linearized around the null position of the servovalve spool. The above linearization resulted in a linear compensation scheme, which can be implemented using either analog circuits (Timm, 1999) or a digital signal processor. Test results showed that within a certain operating range of the servovalve (±10% spool opening as indicated in Section 4.2.5), the linear compensation could be used to negate the effect of the natural velocity feedback. Beyond the linear range, caused by a large hydraulic demand (large spool opening), nonlinearities in the servovalve must be considered in the velocity feedback compensation.

Two major nonlinearities, nonlinear flow gain and load pressure influence, were identified in Chapter 4. The identified piece-wise linear flow curve was used to invert the servovalve flow relation. An estimation of the supply pressure and two additional inputs, the spool position and the applied force were needed to invert the load pressure influence.

The experimental results showed that with the nonlinear velocity feedback compensation, EFT could be used to apply larger forces at all frequencies to the structure in tests that required large flow demands.

The proposed nonlinear velocity feedback compensation scheme required an accurate model (knowledge) of the servovalve. Critical system parameters affected by servo-system uncertainties were studied experimentally to investigate their effect on the implementation of the EFT method. The test results correlated with those obtained analytically in Chapter 5. Other factors that can affect the performance of the EFT method are discussed in the next chapter.

CHAPTER SEVEN

FACTORS THAT AFFECT THE PERFORMANCE OF EFT

The methodology of velocity feedback compensation has been shown through both experiment and simulation to be able to negate the effect of natural velocity feedback and make the implementation of EFT success. The implementation of velocity feedback compensation requires an accurate knowledge of the servo-system. Uncertainties of the servo-system that could affect the laboratory implementation of the EFT method are discussed in this chapter.

7.1 Uncertainties in Servo-System

The performance of the proposed nonlinear velocity feedback compensation depends on an accurate servovalve flow curve and accurate delay estimation. Uncertainties in the servo-system, such as leakage and pressure supply variation, reduce the accuracy of the system identification. Leakage in the system may affect the system stability and the controllability of the actuator, while variation in the supply pressure affects the flow property and response delay of the servovalve.

7.1.1 Leakage Flow

Servo-system leakage includes the main-stage valve leakage described by Eq. (3.21) and actuator leakages described by Eqs. (3.25) and (3.26). The proportional leakage C_l used in the analytical study represents the actuator cross-port leakage, part of the actuator external leakage, and part of the servovalve leakage. Because leakage passages are

caused by hardware wear and imperfection, which are difficult to evaluate, the leakage coefficient is difficult to determine accurately. Controller gain setting based on incorrect leakage estimation may affect the system performance and stability.

The effect of the proportional leakage is shown in the root loci of a linearly compensated system with respect to various proportional leakages in Fig. 7.1. If the leakage were zero instead of 5.5 in.^{3}/s/ksi, which was used in determining G_p for the design of the linear compensation scheme, the compensated system would have an unstable vibration mode related to the valve dynamics. Large proportional leakage increases the damping of the high-frequency mode, and thus allows a larger controller P gain (G_p). This is shown in Fig. 7.2, in which the maximum achievable P gain calculated following Routh's stability criteria is plotted against the proportional leakage. The observation was the base of the addition of the cross-port leakage passage mentioned in Chapter 6. Meanwhile, it should be noted that large leakage increases the force-tracking error of the actuator as shown in Section 5.2.

The proportional leakage cannot fully represent the total leakage of the system. For example, the servovalve leakage described by $\frac{\pi r c^3}{6\mu\tilde{\alpha}_v}\left[1+\frac{3}{2}\left(\frac{e}{c}\right)^2\right]\frac{P_s+P_L}{2}$ includes a term related to half of the supply pressure. In addition, part of the actuator external leakage shown in Eq. (3.26) is proportional to the supply pressure because $P_i=\frac{P_s \pm P_L}{2}$. This part of the leakage (termed constant leakage) represents a physical phenomenon that the leakage exists whenever the hydraulic pressure is applied to the system. Because of the constant leakage, the force output of the actuator would be below the command force

across the whole frequency range as shown in the simulation results in Fig. 7.3. The simulation with a constant leakage of 0.5 in.^{3}/s matched well the system response to a 0.5 kip sinesweep input function with linear velocity feedback compensation (also shown in Fig. 6.22), indicating that the force tracking error could be in part attributed to the constant leakage of the system. In addition, simulation results indicated that the tracking error of the actuator would increase with an increase of constant leakage. For example, a constant leakage of 2.0 in.^{3}/s would result in an unacceptable system tracking error as shown by the dark dashed lines in Fig. 7.3.

Although a feedforward compensation of the constant leakage was theoretically possible, such compensation was not further explored because the test system was sensitive to incomplete compensation, and the leakage parameter was difficult to accurately identify. Instead, increasing the effective force command signals was used to offset the effect of small constant leakages. If the constant leakage is large, the servo-system should be sent to the factory for repair.

7.1.2 Pressure Supply

Two hydraulic pumps provided 150 gpm oil flow at 3000 psi pressure to the entire laboratory at the University of Minnesota. When an actuator in the laboratory took hydraulic flow from the supply line and drove the same amount of flow into the return line (work was done during the process), the flow consumption caused a pressure drop in the supply line. The pressure reduction in the supply line was sensed and compensated by the hydraulic pumps. Because the hydraulic pumps had their own dynamics and response delay, the pressure supply to the servovalves varied while other tests were underway in the laboratory. The pressure supply variation caused by the other tests was

generally small and dependent on their relative positions to the EFT system on the supply line while the pressure supply variation caused by an EFT test itself was significant.

Figure 7.4 shows the supply pressure variation during a test with a small amplitude sinesweep input, in which the peak spool opening increased from zero to 15% and then decreased at a similar rate to zero. The supply pressure was 2860 psi in the beginning and returned to the same value at the end. During the test, the supply pressure dropped when the spool opened in either direction, and pressure regained roughly its initial value when the spool moved back to its null position. When the pressure drop was large (due to a large spool opening), the regained pressure in the supply line had a small overshoot (i.e., the supply pressure could have been instantaneously greater than the initial value, 2860 psi).

The result of a similar test, in which the maximum spool opening reached 80%, is presented in Fig. 7.5. A similar observation can be made regarding the pressure variation along with the variation of the hydraulic demand (represented by the spool opening). The instantaneous supply pressure overshoot was greater but was capped by an upper limit. In addition, a sudden pressure drop and regain were evident at 18s and 52s respectively, roughly corresponding to a 45% spool opening, indicating some unknown dynamics of the hydraulic system.

The unknown pump dynamics and related response delay were also believed to be responsible for the unsymmetrical supply pressure history corresponding to a symmetrical spool opening history shown in Figs. 7.4 and 7.5. The asymmetrical pressure variation pattern indicates nonlinearity in the hydraulic supply, meaning that the supply pressure variation is dependent on the hydraulic demand history. The nonlinearity

increases the difficulty in determining the servovalve flow property.

The supply pressure variation was not compensated in the laboratory because it was difficult to model the pressure variation and the relation between the supply pressure and the servovalve flow. The modeling error might be significant enough to result in a poor response of the test system. A roughly average value in the second test (2650 psi) was used as the supply pressure in the compensation of the load pressure influence.

An accumulator with a capacity of ¼ gallon closely coupled to the servovalve was used to reduce the uncertainty of the servovalve flow property. The nonlinear flow curve of the servovalve with the accumulator is presented in Fig. 7.6. Compared to a previous flow curve shown in Fig. 4.8, the scattering of the experimental data is reduced. In addition, the slopes of the curve at ±80% spool openings are increased, indicating better controllability of the servovalve.

7.2 Uncertainties in Test Structure and Test Environment

The velocity feedback compensation was based on a measured piston velocity. The velocity measurement might include other vibration components in the test structure such as the rotation of the cart in Timm (2001). Results of both experiment and simulation indicated that the velocity feedback compensation could compensate for the effect of some secondary vibration modes in the test structure. This section explores potential problems in testing structures against a flexible reaction frame, in which the piston velocity would not be the same as the structure velocity.

When the actuator applies forces to the test structure (represented by m, c, and k), the same forces are applied to the reaction frame (represented by m_1, c_1, and k_1). As shown

in Fig. 7.7, the piston velocity with respect to the actuator house, which affects the actuator control, is the summation of the velocity responses of the structure and the reaction frame because the actuator house moves with the reaction frame. Fig. 7.8 presents the root locus of a test system with a flexible reaction system, which was assumed to have a 150 lb equivalent weight and 40 kip/in. stiffness. The system without velocity feedback compensation has two pairs of zeros corresponding to the natural frequency of the test structure and the reaction frame such that the actuator would not be able to apply forces at both frequencies. When the piston velocity is compensated, two conjugate poles move towards the zeros that represent the structure and eventually cancel them. On the other hand, two other conjugate poles that are supposed to cancel the zeros corresponding to the reaction frame instead move into the unstable region. Therefore, if the compensation were based on a piston velocity relative to a light flexible reaction frame (e.g., an A-frame), the system might become unstable.

If the compensation were based on the structure velocity instead, the effect of the zeros corresponding to the structure would be cancelled while the zeros corresponding to the flexible reaction frame would not be affected as shown by simulation in Fig. 7.9. The effect of the remaining zeros on the force tracking ability of the actuator within the frequency range of interest would be reduced if the reaction system had either large damping or a large resonant frequency (a frequency away from the frequency range of interest).

The root locus of another assumed test system with a heavy stiff reaction system, which is represented by a 150 kip equivalent weight and 400 kip/in. stiffness, is shown in Figs. 7.10 and 7.11. It seems that the stable pole-zero cancellation is achieved without

any problem if the velocity feedback compensation is based on the piston velocity. However, the simulation results cannot be extended to other reaction systems blindly. Computer simulations should be conducted for the individual test system to avoid potential stability problems. When the compensation is based on the structural velocity, the effect of the remaining zeros depends on the damping and the resonant frequency of the reaction system. A slightly damped vibration mode close to the natural frequency of the test structure might still significantly affect the ability of the actuator to excite the test structure correctly, and the compensation based on the piston velocity would be required.

7.3 Effect of Servo-system on Test Structure

Effective forces are applied to the test structure by a hydraulic actuator, which is not an exact replacement of the force vector acting on the structure shown in the free body diagram in Fig. 1.1 (b). A close examination of the test system shown in Fig. 7.12 reveals that the piston rod moves with the structure. Hence, friction and viscous damping (caused by the shear of the hydraulic fluid between the piston and actuator house) might affect the test structure though the actuator control is based on load cell reading, which does not include the above friction and damping forces. The effect of the servo-system on the test structure was evaluated by comparing the results of free vibration tests with the actuator attached to those identified in Chapter 4, where the actuator was unattached. In the parametric simulations shown below, a stiffness of 3.96 kips/in. was used though static loading tests shown in Fig. 4.10 indicated some variations (less than 1%) in the structural stiffness.

7.3.1 Damping of Structure

In the free vibration tests with the actuator attached, another actuator on the opposite side of the structure as shown in Fig. 7.13 was used to pull away the structure. The structure was released when a steel coupon attaching the structure to the second actuator fractured. The structure then had an initial offset prior to release. The velocity feedback compensation was applied to the attached actuator, which had a zero force command.

The test result with a -0.69 in. initial offset is shown in Fig. 7.14 along with simulation results that best fit the test results. The simulation result in grey dashed lines indicates that the system had a damping coefficient of 0.008 and a friction force of 35 lbs. Although the damping properties are different from those identified in Chapter 4 (0.024 and 6 lbs), test results normalized by the initial offsets shown in Fig. 7.15 indicate that the vibrations were dampened to similar amplitude at 7s after the same number of cycles. Therefore, the test system with proper velocity feedback compensation would have equivalent energy dissipation to the structure on a shake table though the dissipation mechanism may be different.

The change in the energy dissipation mechanism was attributed to actuator force (energy) input. Because the actuator was controlled with zero force command, it tried to cancel the resistant force (sensed by the actuator load cell) caused by the actuator chamber volume variation and friction and damping forces of the actuator during the free vibration test. Due to inevitable incomplete compensation, the actuator force was not zero as indicated by the load cell readings. The force measurement was plotted versus the structural velocity in Fig. 7.16. A linear curve fitting was made to characterize the relation between the resistant force and the structure velocity (i.e., the slope and the

intercept of the regression line). The slope represents an equivalent viscous damping coefficient and the intercept represents the friction of the actuator. The curve fit indicates that the actuator input was equivalent to a negative viscous damping (-0.022) and a positive friction (38 lbs).

If the actuator force measured by the load cell was used as the input (F) in the simulation based on Eq. (3.38), a damping coefficient of 0.028 and a friction of 2 lbs best fit the test results as shown by the dark dashed lines in Fig. 7.14. This simulation considers only the structure; hence, the identified damping properties are similar to those in Chapter 4. A simple relation can be found between the two identified damping properties: The structure viscous damping (friction force) plus the damping (friction force) provided by the actuator gives the system viscous damping (friction force). The negative viscous damping and positive friction indicate that the actuator did both positive and negative work. With proper velocity feedback compensation, the energy input was similar to the energy takeout such that the structural behavior was not affected significantly though the exponentially decayed response became a linearly decayed response. Two more free vibration tests were conducted, one with slight over-compensation and another with under-compensation, to investigate the effect of velocity feedback compensation on the energy dissipation of the test system.

7.3.2 Effect of Velocity Feedback Compensation

The free vibration test with the over-compensation of the natural velocity feedback is presented in Fig. 7.17. Compared to the case with the roughly correct compensation, more negative damping occurred (a viscous damping of -0.003 and a friction force of 37 lbs) because the actuator was commanded to apply additional forces to the structure due

to the incomplete cancellation of the natural velocity feedback. The additional force was proportional to the structure velocity because the modification of the actuator command was based on the structure velocity. On the other hand, if the actuator force was used as the input (F) in the simulation based on Eq. (3.38), the identified parameters (0.026 and 1 lbs) were very close to those in Chapter 4. The actuator force is plotted against the structure velocity in Fig. 7.18. Again, the structure damping (friction) plus the damping (friction) provided by the actuator is close to the damping (friction) of the test system, indicating that over-compensation caused additional energy input to the test structure.

On the contrary, the free vibration test with under-compensation of the natural velocity feedback shown in Fig. 7.19 indicates high damping in the system (0.026 and 38 lbs). If the actuator force was considered as the input in the simulation, the identified parameters were 0.027 and 3 lbs, respectively, which are again very close to the structure damping properties identified in Chapter 4. The plot of the actuator force vs. structure velocity shown in Fig. 7.20 indicates that the actuator caused a damping of -0.003 and a friction force of 29 lbs. The aforementioned relation between the system damping and the actuator/structure damping holds for this case, indicating that the actuator input less energy than it should to the system if the velocity feedback is under-compensated.

Therefore, the structural behavior related to damping is sensitive to the level of the velocity feedback compensation. The apparent damping properties depend on whether the natural velocity feedback is over- or under- compensated. Generally, the actuator input more energy into the system with over-compensation for the natural velocity feedback, while the actuator dissipated more energy in the under-compensated system. As a result, the test structure would show smaller damping in an over-compensated

system and larger damping in an under-compensated system. This correlates with the conclusions drawn in the root locus analysis of the system in Fig. 5.20.

7.3.3 Mass of Structure

The actuator piston moves with the test structure, thus the system mass includes the mass of the actuator piston. The piston in this study weighed approximately 120 lbs, which represented less than 1% of the mass of the test structure. This would be expected in general for EFT because the actuator would typically be sized according to the structural mass and the peak ground acceleration (Spink 2002). The effect of the addition of the mass on the natural frequency of the test structure was deemed negligible.

7.4 Nonlinear Behavior of Structure

Theoretically, a successful implementation of the EFT method is independent of the nonlinear behavior of a test structure. However, testing a nonlinear structure might require large hydraulic flow demand due to large structural velocity response during the test. In these cases, the implementation (not the methodology) of the velocity feedback compensation would be affected because the current nonlinear compensation scheme requires an accurate knowledge of the servo-system, which is difficult to obtain due to system uncertainties, especially at large spool openings. Consequently, the velocity feedback compensation might be instantaneously incomplete, and the test results would be different from the expected results if the structural response is sensitive to loading histories.

For example, in the test with a 2.0 sine sweep input function and nonlinear velocity feedback compensation shown in Fig. 6.25, the measured structural responses matched

well with the expected responses even though the maximum spool opening was 55%. During the test, the structure was well into the nonlinear range of its behavior (the structural stiffness reduced by half when the displacement was beyond 1 in.). Other examples include the test with full-scale Northridge earthquake effective force input shown in Figs. 6.36 and 6.37 and the nonlinear velocity feedback compensation. The structure was correctly excited such that the nonlinear structural behavior was captured during the test.

On the other hand, in another nonlinear test with 0.27g El Centro earthquake effective force input shown in Figs. 6.30 and 6.31, a smaller response was obtained in the test before 11s while the measured response was larger than the expected response after 18s. The reason might have been that the structural response was sensitive to the force peak around 2s, which the actuator did not fully reach at due to instantaneous under-compensation.

7.5 Summary

Many factors can affect the performance of the proposed nonlinear velocity feedback compensation and the EFT method. The effects may come from uncertainties in the servo-system, such as leakage flow and pressure supply variation, or from uncertainties in the test environment such as a flexible reaction frame and/or large flow demands. Compared with a structure subjected to a shake table test or an earthquake event, the structural response in a test using the EFT method can be slightly affected by the actuator attached to the test structure. The actuator physically adds a small mass to the structure and alters the energy dissipation of the structure through additional energy input to the

test system. The energy input can be positive or negative (dissipation) depending on the performance of the velocity feedback compensation. Nevertheless, with a correct implementation of the velocity feedback compensation, the EFT method can be used to apply real-time seismic simulation to nonlinear structures. This is further validated using a single-story steel structure in the next chapter.

CHAPTER EIGHT

PROOF-OF-CONCEPT TEST

To verify that the EFT method would produce results equivalent to those produced in a shake table study, a proof-of-concept test was conducted by subjecting the same structure to both test methods and comparing the results.

8.1 Experimental Program

A simple one-story structure was selected for the proof-of-concept test. The structure consisted of a rigid diaphragm (two rectangular steel frames filled with reinforced concrete) supported at its corners on four replaceable steel columns as shown in Fig. 8.1. The shake table study was conducted using the shake table at the University of Illinois at Urbana-Champaign, and the EFT study was conducted at the University of Minnesota. The concrete mass weighed approximately 10 kips to fit the load capacity of the table, and the column spacing was 60×72 in. to fit the hole-pattern of the base plate of the table. The column spacing also fit the size of the diaphragm, which was made for the previous SDOF structure. Four plates with tapped holes were welded on the steel frame of the diaphragm to provide connections for the columns.

The columns were made of W10x15 sections with A572 grade 50 steel, which had a measured yield stress of 62.5 ksi. The columns were 72 in. high and oriented in weak-axis bending such that the resonant frequency of the structure was approximately 3 Hz. The structure stiffness in the orthogonal direction was approximately 23 times larger than

that in the direction of motion; hence the out-of-plane motion was prevented without additional diagonal braces. Because the results of the shake table study showed repeatable structural behavior even after major yielding of the columns, the same columns were used in the companion EFT tests. In order to minimize the effects of the connections on the comparison of the dynamic responses of the structure, the column ends were welded to a 1.5-in. thick plate at the bottom and a 1-in. thick plate at the top, and the plates were bolted to the diaphragm and the foundation using four ½-in. diameter A490 bolts.

Two fluid dampers were connected between the middle chevron brace and the foundation. The dampers were used to keep the structure from extensive damage for most of the tests while tests both with the dampers and without the dampers were conducted. The behavior of the dampers was found to be nonlinear; hence, the structural behavior was difficult to predict even when the columns were in the linear elastic range.

Both global and local responses of the structure were monitored. The measured global responses included acceleration (A), velocity (V), and displacement (D) of the mass. In the shake table tests, the structural velocity was measured directly relative to the table while the structural acceleration and displacement were measured relative to the global reference frame. The table displacement and acceleration were subtracted from these measured responses to calculate the relative responses to the table, and the relative responses were compared to the measured responses in the EFT study.

The monitored local responses included column flange strains and damper forces. The column moment and shear (Q) were calculated from strain measurements. Strain gages were placed on each column 8 in. from both column ends as shown in Fig. 8.2 (a).

It was assumed that plane sections remained plane after deformation at the gage sections (i.e., linear strain distribution across the section as shown in Fig. 8.3). Hence, the strains at the flange tips were calculated using a linear extrapolation (strain gages were not right at the flange tips). The moment at a gaged section was calculated by $ES\varepsilon$ before the section yielded ($\varepsilon \leq \varepsilon_y$), where ε was the average strain at the four flange tips of the section. The stress-strain relationship was assumed elastic-perfectly plastic. When yielding occurred at a gaged section, the corresponding moments were approximated by

$$M_c = ES\varepsilon\left[1-\left(1-\frac{\varepsilon_y}{\varepsilon}\right)^2\left(1+\frac{\varepsilon_y}{2\varepsilon}\right)\right], \tag{8.1}$$

where E is the modulus of elasticity of steel (29,000 ksi), S is the section modulus of the column with respect to the weak axis (1.45 in.^{3}) , and ε_y is the yield strain of the steel (σ_y/E=0.0021). The second term in the bracket estimates the contribution of the shaded blocks in Fig. 8.3 that need to be subtracted from a moment calculated by $ES\varepsilon$.

The base shear for each column was calculated by dividing the sum of the two end moments by the distance between the gaged sections. The total base shear was the summation of the base shears of the four columns. The total base shear (kx) was also calculated by subtracting the damper force ($c\dot{x}$), measured by two load cells in line with the dampers, from the total inertial force, $-m\left(\ddot{x}+\ddot{x}_g\right)$, where $\ddot{x}+\ddot{x}_g$ was the measured acceleration relative to the global reference. In the EFT study the total inertial force was replaced by the measured actuator force (should be $-m\ddot{x}_g$, where $\ddot{x}_g$ is the measured shake table acceleration) plus the relative inertial force ($-m\ddot{x}$).

The load cells were made of a 1-in. diameter threaded rod. The gage placement on

the threaded rod is shown in Fig. 8.2 (b), including two gages measuring the axial strain and the other two measuring the Poisson strain. The load cells were calibrated with the signal conditioner, a 2100 system by Measurement Group Inc. The conditioner excitation was 5 volts, and the gain was set such that the output was ±1 volt when using shunt calibration. With the above conditioner setup, the sensitivity factor of the load cells was found to be 2.0 kips/volt by static loading tests.

The input functions used in the shake table study included a sine wave sweep (1-10 Hz), the El Centro earthquake ground acceleration, and the Northridge earthquake ground acceleration. The frequency of the sinesweep inputs started from 1 Hz because the shake table actuator was under displacement control. The ground acceleration signals were transformed into required displacement signals by the actuator controller through double integration. For low frequency accelerations, the above process could cause a large displacement command, which might exceed the table stroke limit (-2in. to 2in.). The maximum peak ground accelerations for the El Centro and Northridge earthquake records used in the shake table study were limited (0.30g and 0.55g, respectively) for this reason.

8.2 Shake-table Test

A schematic of the test structure on the shake table is shown in Fig. 8.4, and the laboratory realization is shown in Fig. 8.5. More details regarding the connections can be found in Appendix 7. The relative responses were calculated using

$$D_{stt} = \left(D_N + 2D_M + D_S\right)/4 - D_T \tag{8.2}$$

$$A_{stt} = A_M - A_T \tag{8.3}$$

$$F_{Dstt} = -\left(L_W - L_E\right) \tag{8.4}$$

where D_{stt}, V_{stt}, and A_{stt} are the displacement, velocity, and acceleration of the structure relative to the table, and F_{Dstt} is the damper force. As labeled in Figs. 8.4 and 8.5, there were four potentiometers, three at the structural mass level (D_N, D_M, D_S) and one on the shake table (D_T), two accelerometers, one on the mass (A_M) and the other on the table (A_T), and two load cells (L_W and L_E), one for each damper. The sign conventions for positive global responses and positive column moment and shear are shown in Fig. 8.4.

The columns were bolted to a ½ in. thick base plate, which was bolted to the table using ½-in. diameter bolts shown as the dots in Fig. 8.6. The bending of the base plate during testing was prevented by one bolt located 5 in. away from the column base plate in the direction of motion. Experimental results have shown that more than 97% of the structural displacement was due to the shear deformation of the columns and the rest of the displacement was from the overturning of the structure due to the bending of the table base plate.

The load displacement relationship for a static loading test of the structure on the shake table is shown in Fig. 8.7, from which the structural stiffness was found to be 8.65 kips/in. using a linear curve fit. Due to the physical limitation of the test equipment, the static loading test was conducted in one direction (positive displacement direction) with a maximum offset of ¼ in. Free vibration tests with and without the fluid dampers were conducted to determine the structural properties, and the test results are shown in Figs. 8.8 and 8.9, respectively. Because the measured table displacement was too noisy to be used in determining the structural displacement relative to the table, the measured structural velocity was used in the parameter identification.

The parametric simulation was based on Eq. (3.38), where the structural stiffness k was obtained through the static loading test, while the structural damping (i.e., viscous damping c and Coulomb friction F_c) and the structural mass were determined based on a least square technique. The structural mass was considered in the process because it may affect the period of the simulation response, which in turn may affect the error evaluation of the process of the parameter identification.

In the test without dampers, the structural velocity relative to the table remained constant after 4s because the shake table could not stay stationary during the tests. Hence, the measured table acceleration multiplied by the structural mass was considered as the input force F in Eq. (3.38). The results of the simulation with 10.1 kip mass, 0.3% viscous damping, and 1 lb. friction force best matched the experimental results.

In the case with the fluid dampers, the dampers were found to have a complicated nonlinear damping characteristic, which slightly affected the natural frequency of the structure. Hence, the structural mass (9.3 kips) obtained in this test was deemed incorrect due to the inaccurate damping characterization (using a combination of viscous damping and Coulomb friction to model the complex behavior). In addition, the structural response would be difficult to predict analytically due to the difference between the modeled and the actual structural damping .

8.3 Effective Force Testing

A schematic of the structure used during the EFT study is shown in Fig. 8.10, and the laboratory realization is shown in Fig. 8.11. The same columns as in the shake table study were used in the EFT study because the shake table tests had good repeatability of

the column behavior even after major yielding. More details regarding the connections are documented in Appendix 7. The structural responses were calculated using

$$D_{eft} = \left(2D_a + D_U + D_D\right)/4 \tag{8.5}$$

$$A_{eft} = \left(A_N + A_S\right)/2 \tag{8.6}$$

$$F_{Deft} = L_W - L_E \tag{8.7}$$

where D_{eft} and A_{eft} are the displacement, velocity, and acceleration of the structure and F_{Deft} is the damper force. As labeled in Figs. 8.10 and 8.11, the sensors used in EFT tests included two potentiometers, one at the structural mass level (D_U) and one at the damper level (D_D) in addition to the actuator LVDT (D_a), two accelerometers (A_N and A_S), one on each side of the mass, and same two load cells (L_W and L_E). The sign conventions for positive global responses and positive column moment and shear are shown in Fig. 8.10.

The columns were bolted to a ¾-in. thick base plate, which was bolted to the strong floor using 1-in. diameter threaded rods (36 in. long) shown as dots in Fig. 8.12. Although the base plate and the anchorage of the base plate were different from those in the shake table study, experimental results have shown that the structural stiffness was close to that in the shake table study. The load displacement relationship for a static loading test of the structure is shown in Fig. 8.13, from which the structural stiffness was found to be 8.77 kips/in. through a linear curve fit.

The structural stiffness of the structure in the EFT test was 1.4% greater than that obtained in the shake table study due to a slight change in column boundary conditions. The structural mass changed by 2%, which was in part due to the addition of a thick plate for connecting the actuator in the EFT test. With the above structural properties, the

natural frequency of the structure changed approximately by 1% between the two tests (from 2.89 Hz in the shake table study to 2.87 Hz in the EFT study).

The measured displacements obtained in free vibration tests with and without the fluid dampers are shown in Figs. 8.14 and 8.15, respectively. The structural damping and mass were determined using the same procedure as in the shake table study, and the structural displacement was used in the process. The structure without the dampers had very small damping (0.2% viscous damping plus 1 lb friction). In addition, the simulation with 8.2% viscous damping best fit the test results with the dampers. The identified structural properties are listed in Table 8.1 along with those in the shake table study.

Compared to the shake table study, the structural damping properties had a greater change than the stiffness. For the case without the dampers, the structural viscous damping in the EFT test reduced by 33% though the damping was very small such that test and/or simulation errors might have been responsible for the difference. For the structure with the dampers, the damping decreased by approximately 10% (from 9.2% in the shake table test to 8.2% in the EFT test) in addition to the disappearance of the friction force in the EFT test. The force velocity curve of the damper shown later indicated that the damper performed differently, which was attributed to an unknown change in the damper fluid and a change in the working environment of the dampers. With a reduced damping, it was anticipated that the structural responses observed in EFT tests would be slightly greater than those in the shake table study.

8.4 Servo-system Parameters for EFT Tests

The procedure in Appendix 3 was followed to identify the parameters required by the EFT tests. The structural mass was limited by the shake table capacity, and the peak ground accelerations for the two selected earthquake records (El Centro earthquake and Northridge earthquake) were limited by the shake table stroke. With the structural properties identified in the last section, the capacity of the servo-system was checked using nonlinear numerical analysis. The servo-system used in this study (a 35-kip actuator controlled by a 90-gpm servovalve) was found to be capable of applying the effective forces to the test structure based on measured table acceleration in the shake table tests.

With the second-order model obtained in Chapter 3 and the parameters identified in Chapter 4, the servovalve response delay was found to be 5.2 ms. In addition, the controller P gain was empirically determined as 1.0 and the controller D gain 0.2 ms in the EFT tests. After considering the 0.2 ms phase lead caused by the PID controller, the response delay T_d to be compensated was found to be 5.0 ms. Similar to the tests on the SDOF structural model, the constant α was empirically chosen as 0.1 for the phase-lead network (Eq. (2.35) and Eq. (6.4)). The valve gain was 0.1 (10 volts command signal corresponds to 100% spool opening) as in the tests discussed in the previous chapters.

The servovalve flow curve was identified following the procedure in Appendix 3. The test results are listed in Table 8.2, and the mean curve defined in the shaded blocks was used in the EFT tests. One noteworthy observation is that the flow values, especially those corresponding to small spool openings, are larger in the tests with smaller amplitude commands (i.e., smaller peak hydraulic demand or spool opening). Hence,

using the average flow curve in the EFT tests that require only small spool openings, would cause slight over-compensation. There was no attempt made to optimize the flow curve for individual tests to get the best correlation between shake table test and EFT test results, and the identified flow curve was used in all EFT tests.

Other required parameters are as follows. The sensitivity factor of the tachometer-type velocity transducer was 0.196 volt/in./s (specified by manufacturer); the actuator piston area was 12.73 $in.^2$ (specified by manufacturer); and the pressure supply was 2650 psi (empirically measured). With these parameters, tests were conducted with both sinusoidal and earthquake effective force inputs. Because the shake table was not able to apply the specific ground acceleration perfectly, the measured table acceleration in the shake table tests multiplied by the identified structural mass was used for the force command signals in the EFT tests.

8.5 Test Results

The EFT tests were conducted with the measured table acceleration of selected shake table tests. In the following comparisons, "Shake table test" represents the measured table acceleration times the estimated structural mass, which is also the effective force command for EFT tests. "EFT test" represents the force applied to the structure measured by the actuator load cell. The forces are compared in both the time domain and the frequency domain. The structural responses (i.e., displacement and velocity) measure relative to the shake table or the strong floor and local responses such as column base shear calculated from strain gage readings are then compared in the time domain. Results obtained in the EFT tests are shown by dashed lines while the shake table results are

shown by gray solid lines.

8.5.1 Tests with Dampers

When the two dampers were attached to the structure, the columns were kept in their linear elastic range of behavior during the shake table study. Hence, the EFT tests corresponding to the shake table tests with large excitations are presented. Figure 8.16 compares the forces of the tests with a 0.13g sinesweep (1-10 Hz) acceleration input. Due to the dynamics of the shake table and its servo-hydraulic system, the table output overshot low frequency signals (≤ 5 Hz) while the table output was smaller than the command at larger frequencies. The effective force command based on the measured table acceleration was followed closely in the EFT test except that the force applied to the structure by the actuator was slightly greater than the force command from 6s to 9s in the time domain. This was attributed to a slight over-compensation of the natural velocity feedback because the maximum spool opening during the test was about 20%, and the identified flow curve slightly underestimated the real flow property of the servovalve in this case. The relatively larger discrepancy near 2.8 Hz (i.e., the natural frequency of the test structure) in the frequency domain was in part attributed to the accumulative nature of the FFT algorithm.

Both the global response and local response of the EFT test agreed well with those of the shake table test as shown in Figs. 8.17 though the structural responses in the EFT test were slightly greater than the shake table results. The difference in the structural responses was attributed to the slight over-compensation of the natural velocity feedback and the aforementioned decrease in structural damping. The damper behavior is

examined by comparing the force-velocity curves in Fig. 8.18. As can be seen, the resistant forces provided by the dampers in the EFT test were smaller that those in the shake table test. The columns in both tests had a slight hysteretic behavior as shown in Fig. 8.19 though the static loading tests shown in Fig. 8.13 indicated that the structure was still linear elastic.

The results of tests with a 0.29g El Centro earthquake input are compared in Figs. 8.20 through 8.21, and the tests with a 0.55g Northridge earthquake input are compared in Figs. 8.22 through 8.23. Close matches in both forces and structural responses are evident indicating that with the nonlinear velocity feedback compensation, the actuator was able to apply forces accurately. On the other hand, the maximum spool opening in the 0.29g El Centro earthquake test was 16%, and the maximum spool opening was about 30% in the 0.55g Northridge earthquake test. As a result, slight force discrepancies in the frequency domain near the natural frequency of the test structure indicate a slight over-compensation of the natural velocity feedback, which correlated to the observations made in the tests with the sinesweep input shown Fig. 8.16.

8.5.2 Tests without Dampers

The EFT tests without dampers were problematic due to the narrow stability margin of the system as a result of the small structural damping. Test results with a 0.3g El Centro earthquake are presented here to illustrate the problem encountered. Figure 8.24 shows a comparison of the measured force in the EFT test with the effective force command (i.e., the measured shake table acceleration times the structural mass). Although the actuator seemed able to apply forces at all frequencies within 10 Hz, large force overshoots around 3s are evident. The force overshoots caused large piston

velocities, which in turn caused large hydraulic demands. As indicated in Section 7.1.2, the uncertainties (i.e., primarily the variation in the servovalve flow property) of the servo-system typically increased with an increase in hydraulic demand. Hence, the implementation of the EFT method based on a predetermined flow curve might have caused under- or over-compensation of the natural velocity feedback.

In this case, the over-compensated system was slightly driven into the unstable region after 3s, and the structural responses were much larger than those in the shake table test as shown in Fig. 8.25. Because the test structure without dampers had little damping (0.25%), the test system could not tolerate the instantaneous instability. In addition, although the command force was zero after 25s, the actuator applied a small amplitude force to the structure due to the incomplete compensation of the piston velocity. The frequency of the force input was identical to the resonant frequency of the test structure, and the force input was in phase with the structural response, thus resulting in a small energy input. The energy input at this frequency maintained a constant amplitude oscillation, which did not die down until the program was shut down.

Tests with under-compensation of the natural velocity feedback were conducted to eliminate the instability. A test with 93% velocity compensation is shown in Figs. 8.26 an 8.27 for the same 0.3g El Centro earthquake input. Although the system was able to maintain stability and the actuator force seemed able to follow the force command, the structural responses were much smaller than those in the shake table study due to the increase in the system damping caused by the under-compensation of the natural velocity feedback (Section 7.3.1).

Because the proposed nonlinear velocity feedback compensation was based on a

predetermined flow curve, which did not consider the uncertainties of the hydraulic supply system, EFT testing with the current velocity compensation should be limited to structures with some damping (e.g., 2% based on experiences from this study) to prevent instantaneous instability.

8.5.3 Tests with One Damper

The two fluid dampers provided roughly 8.2% critical damping to the test structure. Tests with one damper were conducted with EFT to simulate more typical structural damping. The feasibility of the EFT method was examined by comparing the measured actuator force to the effective force command because shake table tests with the single damper were not conducted. Figure 8.28 presents the test results with a 2kip sinesweep input. The actuator closely followed the force command as shown in both the time domain and the frequency domain plots. The maximum spool opening during the test was 55%, which was close to that in the parameter identification tests. Hence, the natural velocity feedback was properly compensated with the identified flow curve shown in Table 8.2. In addition, the force tracking ability was not affected by the hysteretic column behavior (i.e., columns yielded during the test) shown in Fig. 8.29 and the highly nonlinear damper performance shown in Fig. 8.30.

Similar observations can be made for the test with a 0.29g El Centro earthquake input shown in Fig. 8.31, and the test with a 0.55g Northridge earthquake input shown in Fig. 8.32. A better match is evident for the El Centro test because the earthquake effective force had a small frequency content at the resonant frequency of the test structure, hence peak forces were unlikely to happen simultaneously with peak velocities. These results indicate that the EFT method with the nonlinear velocity feedback compensation can be

used to apply real-time seismic simulations to structures. More advanced adaptive velocity compensation is necessary for testing structures with little damping.

8.6 Summary

The feasibility of the EFT method was examined by comparing the test results obtained from shake table studies to those obtained from the companion EFT tests on a single-story steel structure. The comparison of the test results showed that with the nonlinear velocity feedback compensation, forces can be applied to the structure satisfactorily at all frequencies of interest, and the EFT method can be used to apply real-time seismic simulation to structures. On the other hand, with the current nonlinear velocity compensation scheme, there is a structural damping requirement of approximately 2% to avoid possible instantaneous instabilities due to variations in hydraulic supply pressure and uncertainties in the parameters used in the nonlinear velocity feedback compensation scheme.

CHAPTER NINE

CONCLUSIONS AND RECOMMENDATIONS

Real-time dynamic testing is necessary for studying structures with strain-rate critical components and structures utilizing velocity dependent devices (e.g., active or passive damping devices). Effective force testing (EFT) is a dynamic testing procedure to apply real-time simulated earthquake loads to large-scale structures that can be simplified as lumped mass systems. In an EFT test, the test structure is anchored to a stationary base, and dynamic forces are applied by hydraulic actuators to the center of structural mass. The force to be imposed (effective force) is the product of the structural mass and the ground acceleration record, and thus is independent of the structural properties such as stiffness and damping, and their changes during the test. Motions measured relative to the ground are equivalent to the response that a structure would develop relative to a moving base as in a shake table test or an earthquake event.

The development and implementation of EFT has been underway at the University of Minnesota since 1996. The purpose of this research was to extend the development and implementation of the EFT method to fully utilizing the capacity of the test equipment and testing nonlinear SDOF structural systems. The implementation of EFT requires velocity feedback compensation in order for the actuators to apply forces accurately to structures. Nonlinearities of the servo-system become significant to the performance of the EFT method and must be considered when a test requires large hydraulic demands.

9.1 Summary of Research Program

The objective of the research was to control the actuator to follow effective force commands accurately even in the nonlinear range of performance of the servo-system. The feasibility of the EFT method was first examined by comparing the applied forces measured by the actuator load cell with command forces (effective forces) and secondly by comparing the measured structural responses relative to the calculated responses of a simple SDOF structure (mass-spring-damper system). To further verify the EFT method, a one-story steel structure was tested on a shake table and using the EFT method, and the measured responses were compared. The comparison included both global responses (effective force, structural acceleration, velocity, and displacement) and local responses (damper force and column base shear).

The servo-system in this study consisted of a 35 kip actuator, a 90 gpm servovalve and an analog servovalve controller. Detailed mathematical models for the servo-system were derived to better understand the system behavior and to facilitate the velocity feedback compensation design. Computer simulation and linear system analysis were conducted to investigate potential stability problems. The conclusions of analytical studies were validated experimentally using the simple SDOF structure and the one-story steel structure.

The implementation of the EFT method should be independent of the nonlinear behavior of test structures as long as the natural velocity feedback can be properly compensated. To verify the independency, the simple SDOF structure was designed such that nonlinear elastic structural behaviors could be obtained repeatedly. In addition, in the tests of the one-story steel structure, the dampers were highly nonlinear though the

columns were only partly yielded.

9.2 Conclusions

9.2.1 Modeling of Servo-System

A mathematical model of the test system was developed, which describes the relations between the system components (i.e., servovalve, actuator, controller, and test structure). The system model was derived from the fundamental physics and the mathematical formulations by Merritt (1967), while detailed models for the individual components were proposed to better represent the physical system.

The servovalve controller primarily functions as a proportional-integral-derivative (PID) controller. A large P gain usually improves the system performance (i.e., better force tracking of the system); however too large of P gain may cause an unstable high-frequency vibration mode in the test system. A small controller D gain (i.e., a couple of tenths of milliseconds) can help stabilize the aforementioned vibration. The controller I gain was always set to zero to avoid wind-up problems caused by the integration of signals having constant offsets. In this case (i.e., PID control with a zero I gain and a nonzero D gain), the PID controller also causes a small phase lead.

The dynamics of the servovalve were modeled as a second-order system, and the required parameters were determined based on the physical operation of the valve (e.g., the spool area and the flow gain) and verified through experiments. The second-order valve model facilitated the determination of servovalve response delay and the stability analysis of the test system regarding the high-frequency vibration mode. Experimental results indicated that the second-order model could accurately represent the servovalve

dynamics across a wide range of frequencies (0-20 Hz).

The relation between the hydraulic flow through the servovalve and the main-stage spool opening was found to be nonlinear. Two types of nonlinearities were identified for the servovalve: *load pressure influence* and *nonlinear flow gain*. The load pressure influence described the nonlinear flow through a fixed orifice with a variable pressure difference across the orifice. Bernoulli's equation was used to relate the flow to the load pressure, and the nonlinear relation was explicitly expressed by a square root term. On the other hand, the nonlinear flow gain, which was found to reflect the nonlinear flow discharge through a variable orifice, was difficult to describe mathematically. Hence a testing procedure was proposed to determine the no-load flow property of the servovalve.

The actuator dynamics was derived based on the continuity analysis of the hydraulic fluid volumes inside the actuator chambers, in which the leakage flow was further studied. The system leakage flow includes the valve leakage, actuator cross-port leakage, and actuator external leakage. The system leakage was modeled by a combination of a proportional leakage and a constant leakage. The proportional leakage, which represents the leakage related to the load pressure across the actuator piston, was found to stabilize the high-frequency vibration mode. On the other hand, the constant leakage represented the leakage that existed whenever the system was loaded by hydraulic pressure. The constant leakage could significantly deteriorate the force tracking ability of the actuator at all frequencies of interest.

Parameters for the proposed models were identified based on experiments and product specifications. The system was tested with sinesweep force and displacement commands to validate the overall system model and the identified parameters. The close

match between the simulation results and the experimental results indicated the accuracy of the model. Various velocity feedback compensation schemes were then investigated with computer simulation before their laboratory implementation.

9.2.2 Velocity Feedback Compensation

During a test directly implementing the EFT method, the servovalve controls hydraulic fluid into and out of the chambers of the actuator to generate forces applied to the structure. Meanwhile the resultant motion of the structure/piston changes the volume of the chambers. A standard Proportional-Integral-Derivative (PID) controller coming with the servovalve was unable to compensate for the chamber volume variation, thus causing force-tracking errors of the actuator.

The direct compensation for the interaction between the actuator control and the actuator piston velocity requires an access to the ports connecting the actuator chambers and a special servovalve, which are not easily available. Hence, the effect of the natural velocity feedback was compensated by modifying the command signal to the servovalve. Compared to the direct compensation, the proposed velocity feedback compensation (previously the velocity feedback correction) needs to incorporate the inverse of the dynamics of the servovalve and its controller. Furthermore, only the dynamics of the servovalve and its controller needs to be considered in the velocity feedback compensation.

Although servovalves have high-order dynamics, the dynamics could be accurately represented by a first-order delay with a valve gain for the frequency range of interest (0-10 Hz). Hence, a first order phase-lead network with a constant was used to invert the valve dynamics. The dynamics of the PID controller with a zero I gain was simplified as

a constant and a small phase lead, which was considered in determining the response delay of the servovalve.

The servovalve would behave nonlinearly when large flow demands are required during a test. Hence, the nonlinearities must be considered in the velocity feedback compensation if the servovalve capacity is to be fully utilized. Large flow demands could be caused by large structural velocity responses and/or large effective forces. These situations could happen even in linear elastic tests though structural nonlinearities could be a cause of large structural velocities. An estimation of the supply pressure and two additional inputs, the spool position and the applied force were used to compensate for the load pressure influence, and the identified flow curve (i.e., the piecewise linear curve connecting 21 control points across the operating range of the servovalve) was used to invert the nonlinear flow gain of the servovalve.

The velocity feedback compensation schemes were verified experimentally using the simple SDOF structure and the one-story steel structure.

9.2.3 Experimental Study

The velocity feedback correction proposed in the previous studies (linear velocity feedback compensation) was found effective but limited (i.e., the maximum spool opening must be within 10%, the linear range of the servovalve behavior). With the nonlinear velocity feedback compensation, effective forces were applied to the simple SDOF structure at all frequencies in tests with a variety of hydraulic demands (maximum 60% spool opening). In some demanding yet successful tests, the structure was taken well into its nonlinear range of behavior, indicating that the structural nonlinearities would not affect the implementation of the EFT method.

The feasibility of the nonlinear velocity feedback compensation and the EFT method was further evaluated by testing a one-story steel structure with a shake table and EFT and comparing the results. The comparison of the test results with the two test techniques showed that with proper velocity feedback compensation, the EFT method could be used to apply real-time seismic simulation to a structure that has complex damping properties and hysteretic behaviors.

To completely compensate the natural velocity feedback, accurate model of the servo-system is necessary. Uncertainties in the servo-system may affect the performance of velocity feedback compensation because the nonlinear compensation scheme was based on a single flow curve, and a fixed servovalve response delay. The uncertainties in servovalve flow properties may cause instantaneous under- or over-compensation of the natural velocity feedback. The under-compensation might affect reaching force peaks, especially when the effective force command contains large frequency content at the resonant frequency of the test structure. On the other hand, the over-compensation might cause instability in testing a lightly damped structure; hence, it is recommended to use EFT to test structures with at least 2% critical damping to avoid possible instantaneous instability.

An incomplete (either over- or under-) compensation of the natural velocity feedback may slightly change the loads applied to the test structure. Similar to shake table testing, the effect of the slight inaccurate loading may be significant when testing a nonlinear structure because the structural responses could be load-history dependent.

9.3 Future Development of EFT

With the proposed nonlinear velocity feedback compensation and the testing procedure shown in Appendix 3, the EFT method can be used in the laboratory to apply real-time simulated seismic loads to large-scale structures. As the EFT method becomes available to researchers, the testing capability of existing laboratory equipment will expand from quasi-static testing to real-time dynamic testing of large-scale structures. The further development of the EFT method may focus on the following directions:

- A better understanding of the uncertainties in the servo-system including the hydraulic supply and accumulation system. New velocity feedback compensation can be designed based on a better model of the servo-hydraulic system.
- Adaptive velocity feedback compensation algorithms to improve the performance of EFT, especially the stability of a system testing structures with small damping.
- Direct compensation of the natural velocity feedback by directly modifying the flow into/out of the actuator chambers.
- Effective force testing with substructuring techniques for testing structural subassemblages.
- Multi-degree-of-freedom (MDOF) implementation of the EFT method.
- Bi-directional implementation of the EFT method for testing non-planar structures.

REFERENCES

1. Alleyne, A., (1996), Nonlinear force control of an Electro-hydraulic actuator, *Proceedings of the 1996 Japan/USA symposium on flexible automation*, pp. 193-200, Boston, MA, June

2. Alleyne, A., and Liu, R. (1999), On the limitations of force tracking control for hydraulic active suspensions, *ASME Journal of Dynamic Systems Measurement and Control*, Vol. 121, No. 2, pp. 184-190.

3. Alleyne, A., and Liu, R. (2000), A simplified approach to force control for electro-hydraulic systems, *Control Engineering practice*, No. 8, pp. 1347-1356.

4. Burrows, C. R., Mu, C., and Darling, J., (1991), Dynamic analysis of a flapper-nozzle valve, *Journal of dynamic systems, measurement, and control*, Vol. 113, pp. 163-167.

5. Chen, H, (2001, 2003), A typical flow vs. spool opening curve, personal contact.

6. Chopra, A. K. (1995). *Dynamics of structures: Theory and applications to earthquake engineering*. Prentice-Hall, Englewood cliffs, N.J.

7. Conte, J., and Trombetti, T., (2000). Linear dynamic modeling of a uni-axial servo-hydraulic shaking table system. *Earthquake Engineering and Structure Dynamics*, Vol. 29, pp 1375-1404.

8. Dimig, J., Shield, C., French, C., Bailey, F., and Clark, A. (1999). Effective force testing: A method of seismic simulation for structural testing. *Journal of Structural Engineering*. 125(9), 1028-1037.

9. Dyke, S. J., Spencer, B. F., Quast, P., and Sain, M. K. (1995). Role of control-structure interaction in protective system design. *Journal of Engineering Mechanics*, ASCE, 121(2), 322–338.

10. Exxonmobil oil Co. (1996), Material safety data bulletin for Mobil DTE 25. Product and Technical Information: 800-662-4525.

11. Franklin GF, Powell JD, and Emami-Naeini A. (1994). *Feedback control of dynamic systems*. (3rd edition) Addison-Wesley, Boston, MA.

12. Gavin, H.P, 2001, *Servovalve modeling*, unpublished data.

13. Heintze, J. and van der Weiden, A.J.J., (1995), Inner loop design and analysis for hydraulic actuator with application to impedance control. *Control Engineering Practice*, Vol. 3, pp. 1323-2330

14. Heintze, J., (1997), *Design and Control of a Hydraulically Actuated Industrial Brick Laying Robot.* Ph.D thesis, Delft University of Technology, Netherlands.

15. Horowitz, P and Hill, W (1990), *The art of electronics*. Cambridge University Press, New York, NY.

16. Mahin, S. A., and Shing, P. B. (1985). Pseudodynamic method for seismic testing. *Journal of Structural Engineering*, ASCE, 111(7), 1482–1503.

17. Mahin, S. A., Shing, P. B., Thewalt, C. R., and Hanson, R. D. (1989). Pseudodynamic test method - Current status and future directions. *Journal of Structural Engineering*, ASCE, 115(8), 2113–2128.

18. Martin, D. J. and Burrows, C. R., (1976). The dynamic characteristics of an electrohydraulic servovalve, *Journal of dynamic systems, measurement, and control*, Vol. 98, pp. 395-406.

19. Maskrey, R.H. and Thayler W.J., (1978). A brief history of electro-hydraulic servomechanisms, *Technical bulletin 141*, Moog inc. controls division, East Aurora, N.Y. 14052.

20. Merritt, H. E. (1967). *Hydraulic control system*s. Wiley, New York, NY

21. MTS Systems co. (1994), Product specifications for series 256 servovalves.

22. MTS Systems co. (1999), Product specifications for series 244 hydraulic actuators.

23. Murcek, J. A. (1996). *Evaluation of the effective force testing method using a SDOF model, Master's thesis*, Civil Engineering, University of Minnesota, Twin cities.

24. Newell, D., Dai, H., Sain, M., Quast, P., and Spencer, B., (1995). Nonlinear modeling and control of a hydraulic seismic simulator. *Proceedings of American Control Conference*. pp 801-805.

25. Nikiforuk, P. N., Ukrainetz, P. R., and Tsa, S. C., 1969, Detailed analysis of a two-stage four-way electro-hydraulic flow-control valve, *Journal of Mechanical engineering science*, Vol. 11, No. 2, pp. 168-174.

26. Niksefat, N., and Sepehri, N., (2001), Designing robust force control of hydraulic actuators despite system and environmental uncertainties, *IEEE control systems magazine*, April, pp. 66-77.

27. Ogawa, N., Ohtani, K., Katayama, T., and Shibata H., (2001), Construction of a three-dimensional, large-scale shaking table and development of core technology. *Philosophical Transaction of the Royal Society: Theme Issue on Dynamic Testing of Structures*. A 359: 1725-1751.

28. Schothorst, G., (1997), *Modeling of Long-Stroke Hydraulic Servo-Systems for Flight Simulator Motion Control and System Design*. Ph.D thesis, Delft University of Technology, Netherlands.

29. Shield, C, French, C, and Timm, J. (2001). Development and implementation of the Effective force testing method for seismic simulation of large-scale structures. *Philosophical Transaction of the Royal Society: Theme Issue on Dynamic Testing of Structures;* A 359: 1911-1929.

30. Spink MJ. (2002). *MDOF implementation of effective force testing: a method of seismic simulation*, Master's thesis, University of Minnesota, Minneapolis.

31. Thayler W.J., (1958). Transfer functions for Moog servovalves, *Technical bulletin 103*, Moog inc. controls division, East Aurora, N.Y. 14052,

32. Thayler W.J., (1962) Specification standards for electro hydraulic flow control servovalves, *Technical bulletin 117*, Moog inc. controls division, East Aurora, N.Y. 14052.

33. Timm, J. (1999). *Natural velocity feedback correction for effective force testing*. Master's thesis, Civil Engineering, University of Minnesota, Twin cities.

34. Wang, D., Dolid, R., Donath, M., and Albright, J., 1995, Develop and verification of a two-stage flow control servovalve model. *Fluid power systems and technology*, Vol 2, pp. 121-129.

35. Zhao J, French C, Shield C, and Posbergh T. (2002). Development of EFT for nonlinear SDOF systems. *Proc. 7th National Conf. on Earthquake Engineering*. Boston, MA,

36. Zhao J, French C, Shield C, and Posbergh T. (2003). Nonlinear velocity compensation for Effective Force Testing. *Proc. 2003 Structural Congress and Exhibition*. Seattle, WA.

37. Zhao J, French C, Shield C, and Posbergh T. Considerations for the development of real-time dynamic testing using servo-hydraulic actuation. *Earthquake Engineering and Structural Dynamics*. Vol. 32, No. 11. pp. 1773-1794

TABLES

Table 4.1 System parameters for simulation

Parameter	Value	Parameter	Value
A	12.73 in.^{2}	K_a	0.3182 in.^{3}/ksi
A_v	0.3044 in.^{2}	K_s	0.1
c	0.024 kips/in/s	K_v	1003 in.^{3}/s
C_l	5.5in.^{3}/s/ksi	K_{vp}	0.644 in.^{3}/s/volt
C_F	0.25 volt/kip	m	15.5 kips
C_F	2.0 volt/in.	P_s	2.65 ksi
F_c	6 lbs	T_d	5.0 ms
G_p	0.8059 ~1.0	T_{ld}	5.6 ms
G_d	0.002 s	$x_{v\max}$	0.11 in.
k	3.96 kips/in.	α	0.1
K_3	90.91 volt/in.	τ	0.0014 s

Table 4.2 Flow curve of the servovalve (flow value in in^3/s)

x_v	0.1	0.2	0.3	0.4	0.5	0.6	0.7	0.8	0.9	1.0
Q_L +	102.2	187.2	260.4	321.1	369.8	411.2	441.0	468.3	495.7	523.0
Q_L -	-101.0	-188.2	-260.9	-324.2	-377.1	-419.9	-452.3	-480.2	-508.2	-536.2

Table 8.1 Structural Properties of single-story structure

	Shake table study				Effective force testing			
	m kip-s^2/in.	c kip-s/in.	F_c kips	k kips/in.	m kip-s^2/in.	c kip-s/in.	F_c kips	k kips/in.
no damper	0.0262	0.003	0.001	8.62	0.0267	0.002	0.001	8.75
w/ damper	0.0241	0.088	0.008	8.59	0.0249	0.079	0	8.70

Table 8.2 Servovalve Flow Curve for proof-of-concept test (flow value in in^3/s)

Spool	4.5 in.	4.0 in.	3.5 in.	3.0 in.	2.5 in.	2.0 in.	1.5 in.	1.0 in.	**Average**
-1.0	0.0								**-515.9**
-0.9	0.0								**-496.2**
-0.8	-476.4								**-476.4**
-0.7	-455.0	-450.3							**-452.6**
-0.6	-418.5	-420.6	-417.9						**-419.0**
-0.5	-369.7	-374.1	-377.0	-374.7					**-373.9**
-0.4	-315.7	-317.5	-320.8	-323.9	-327.9				**-321.2**
-0.3	-253.2	-254.0	-255.1	-257.9	-264.1	-264.3			**-258.1**
-0.2	-183.1	-183.7	-184.6	-184.6	-189.3	-190.0	-190.7		**-186.6**
-0.1	-98.4	-98.8	-99.1	-99.2	-100.9	-102.3	-102.3	-102.6	**-100.5**
0.0	0.0	0.0	0.0	0.0	0.0	0.0	0.0	0.0	**0.0**
0.1	99.2	99.5	100.0	100.2	102.0	103.2	103.9	104.5	**101.6**
0.2	182.7	182.9	183.5	183.4	188.0	188.7	188.5		**185.4**
0.3	253.3	253.9	254.9	257.0	263.1	262.6			**257.5**
0.4	313.0	314.4	317.2	319.6	322.3				**317.3**
0.5	364.2	367.8	370.0	365.8					**366.9**
0.6	408.7	411.1	405.1						**408.3**
0.7	444.7	438.4							**441.6**
0.8	464.4								**464.4**
0.9	0.0								**481.5**
1.0	0.0								**498.7**

FIGURES

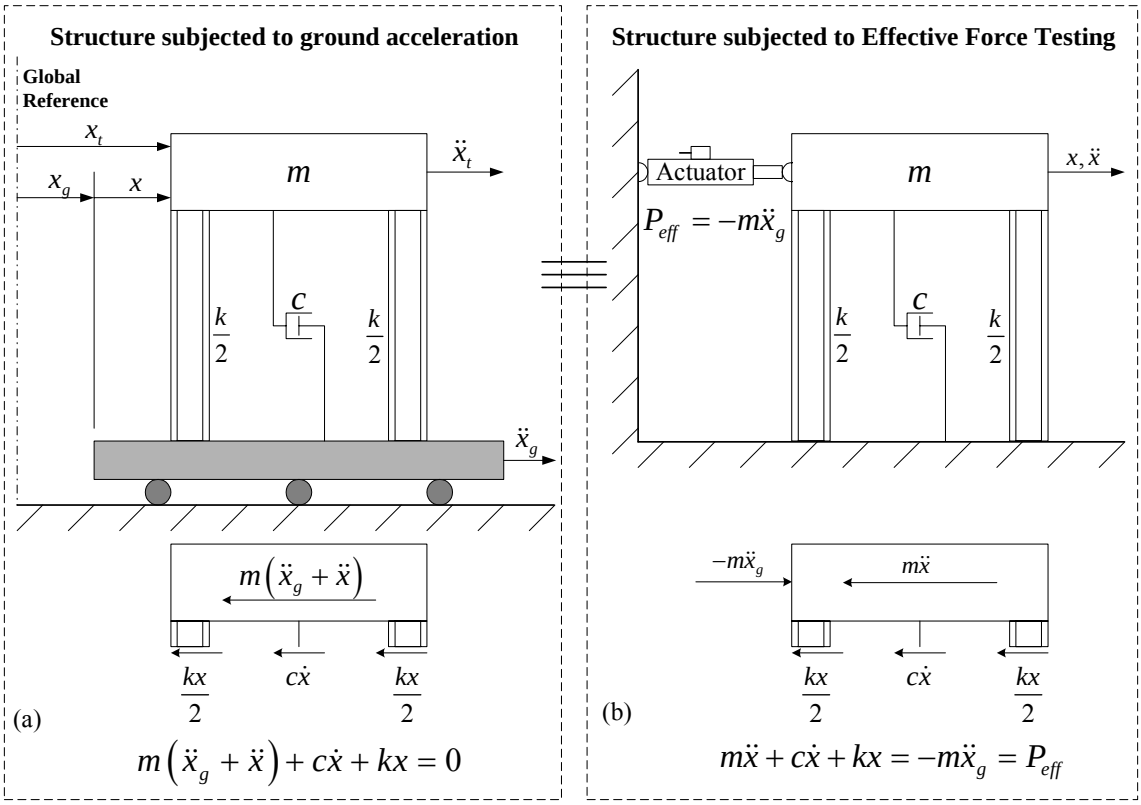

Figure 1.1 Comparison of shake table test to Effective Force Testing

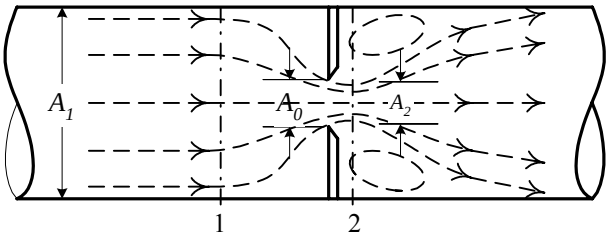

Figure 2.1 An orifice inside a cylindrical pipe

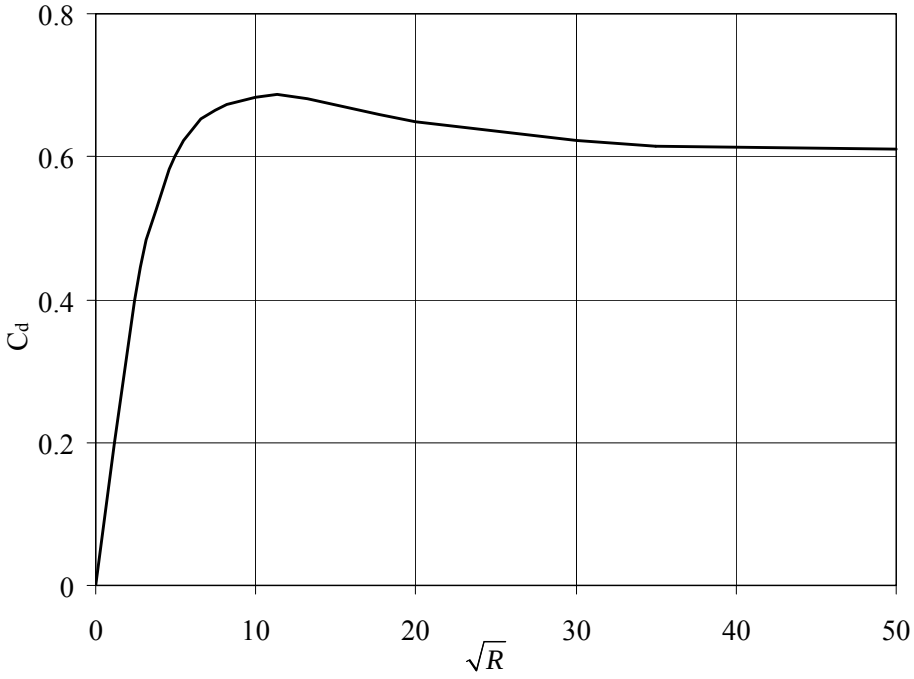

Figure 2.2 Typical plot of discharge coefficient versus Reynolds number for flows through an orifice in a pipe (reproduced after Merritt)

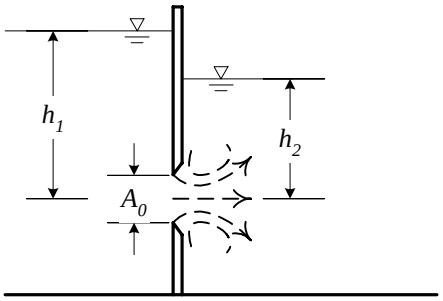

Figure 2.3 A submerged sharp-edged orifice

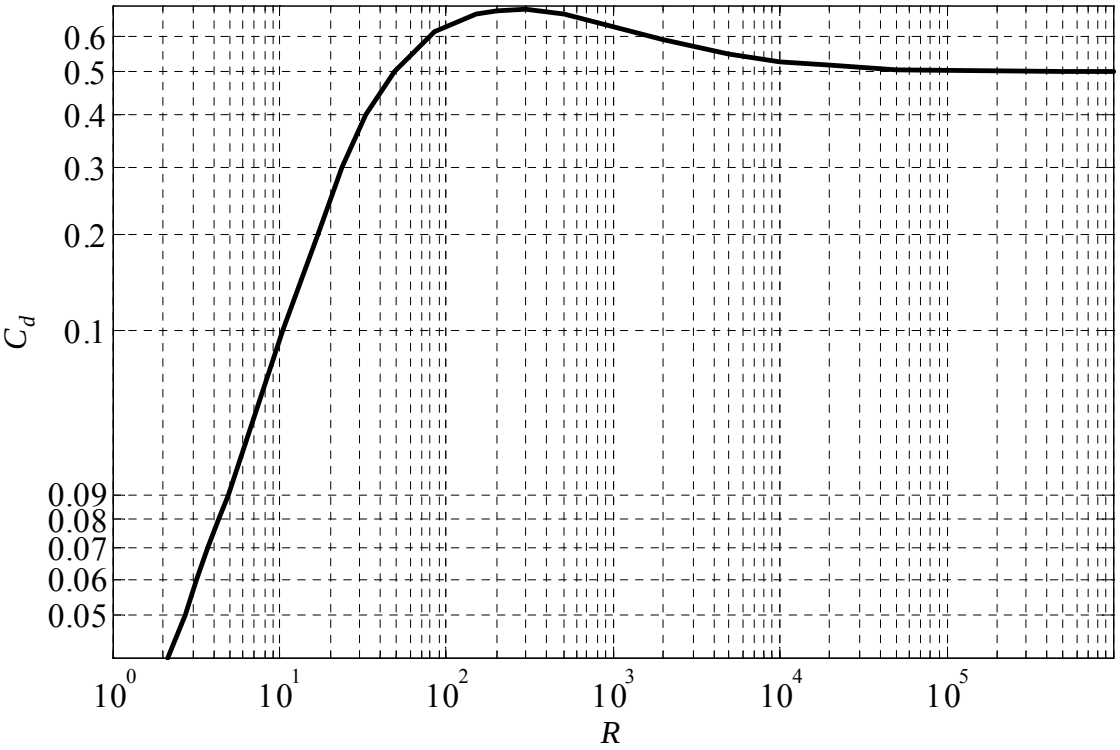

Figure 2.4 Typical plot of discharge coefficient versus Reynolds number for flows through a submerged orifice. (reproduced after Street et. al.)

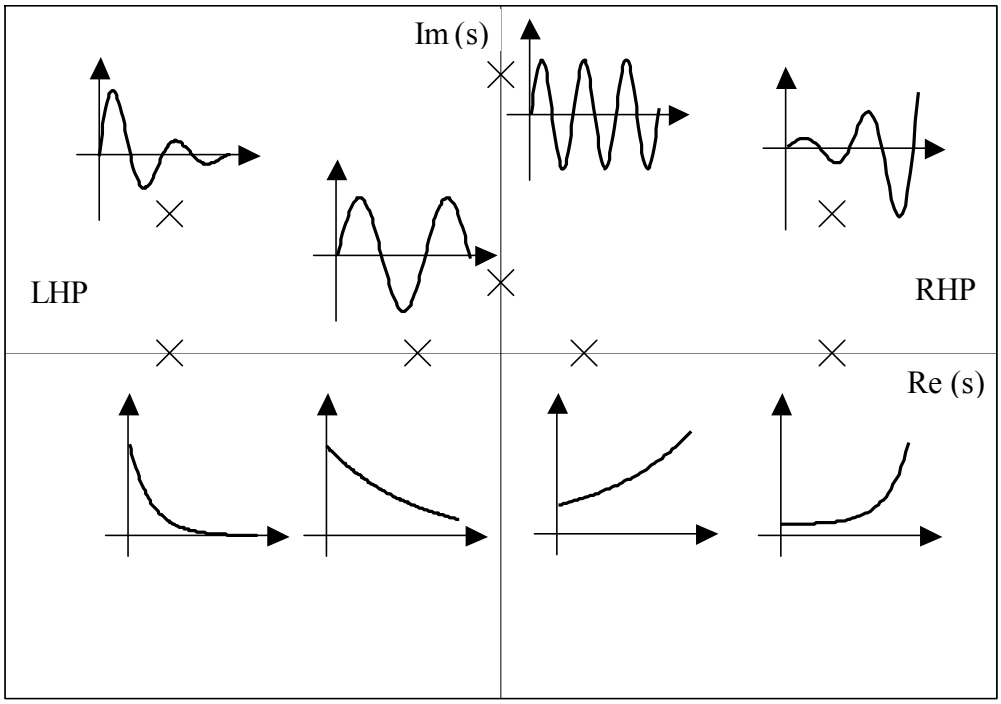

Figure 2.5 Impulse response associated with pole positions in the *s*-plane

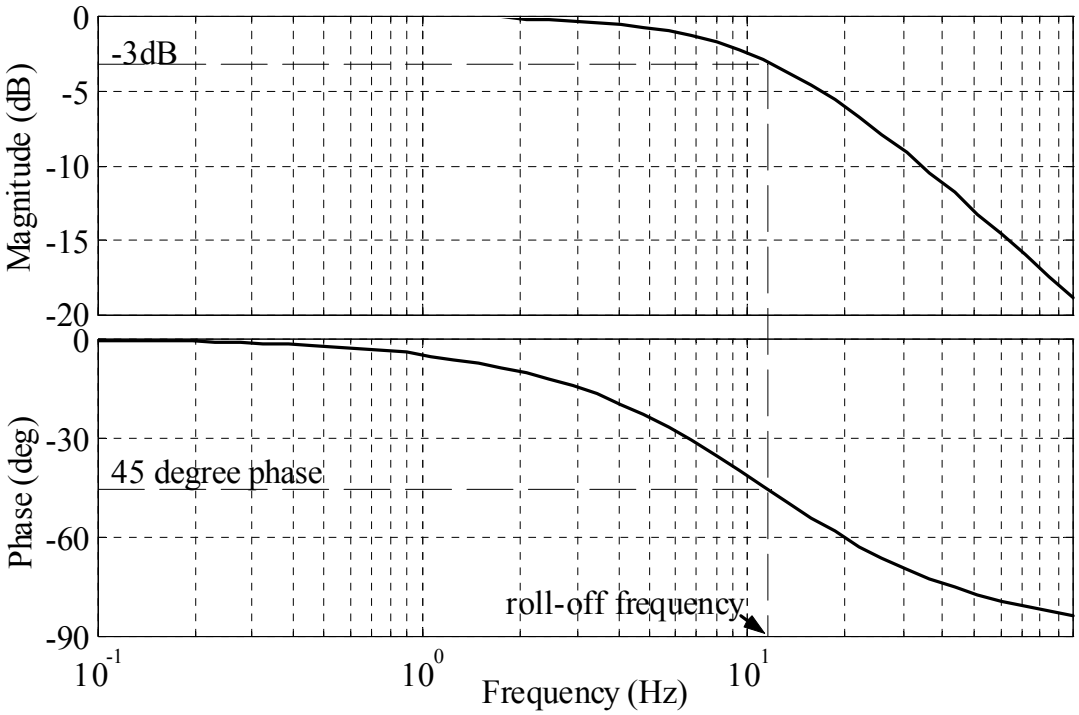

Figure 2.6 Frequency response of a first-order term in denominator ($\tau = 0.0014$ s)

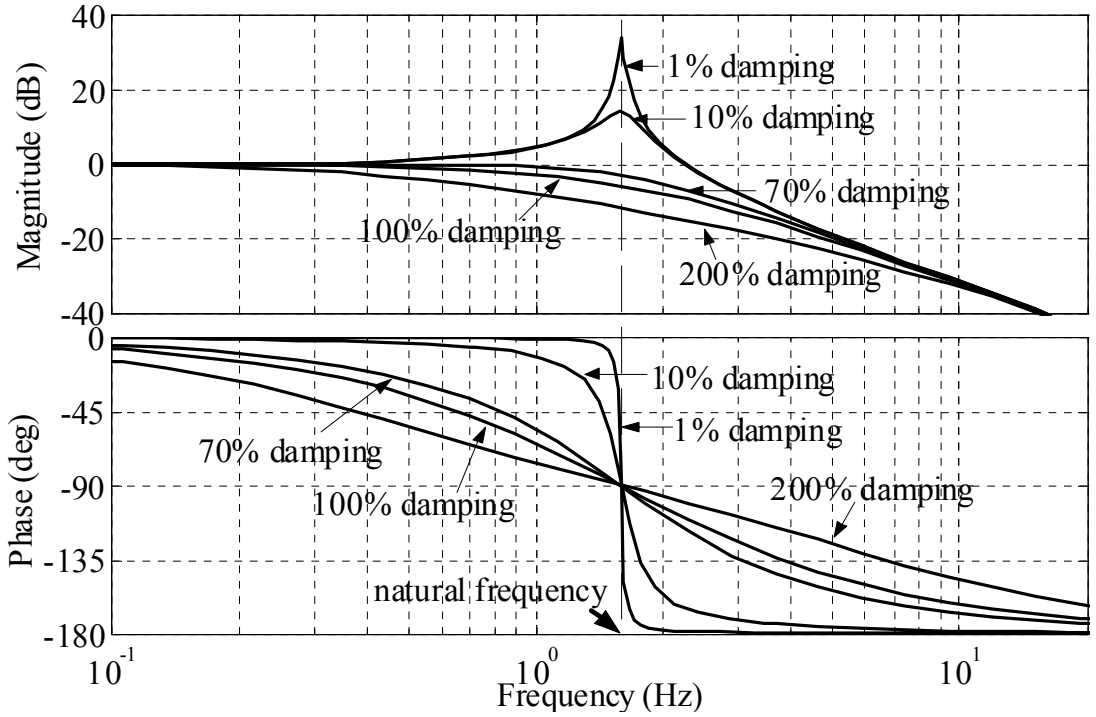

Figure 2.7 Frequency response of a second-order term in denominator (ω_n = 1.6 Hz)

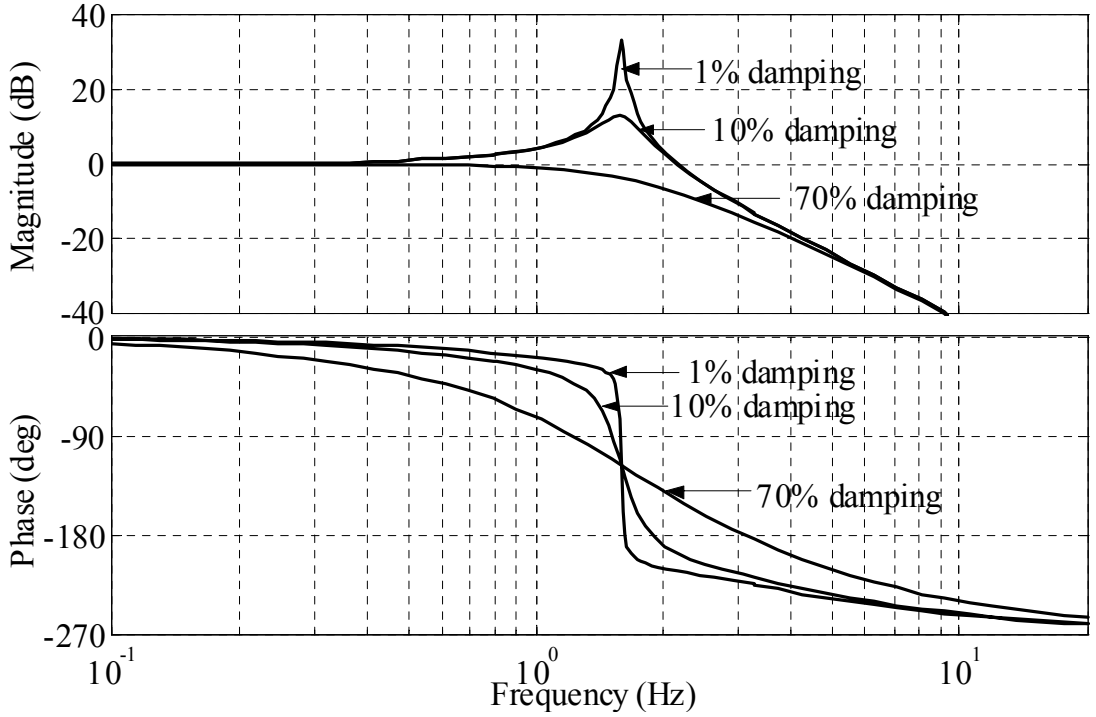

Figure 2.8 Frequency response of a third-order system

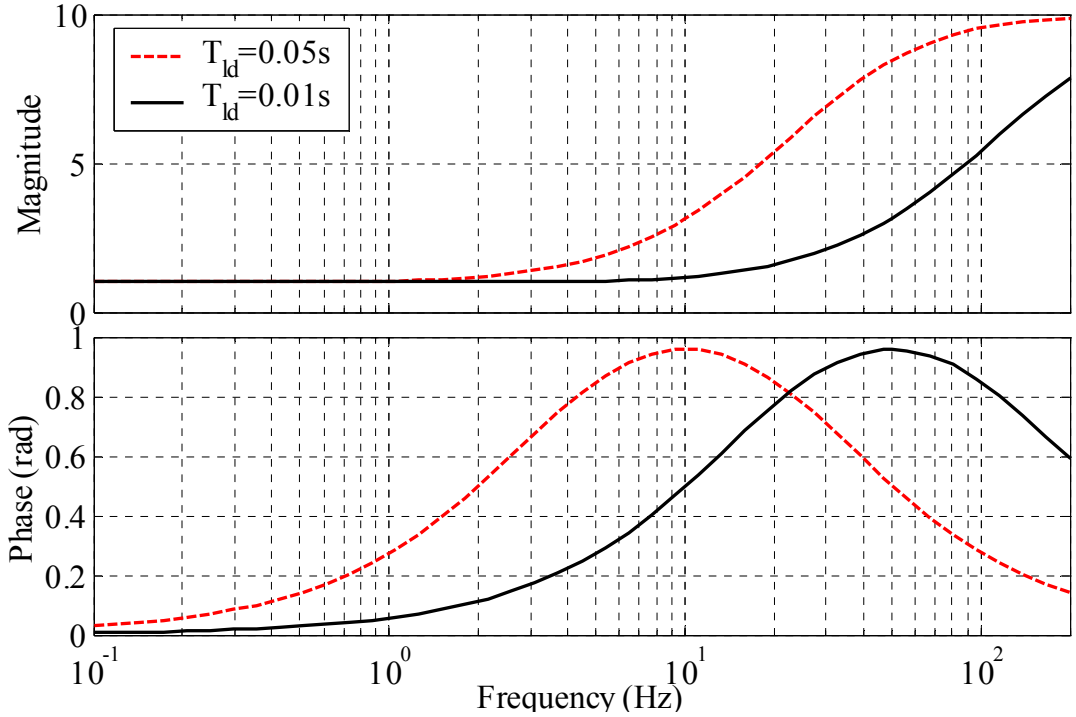

Figure 2.9 Frequency responses of phase-lead networks (0.1-200 Hz)

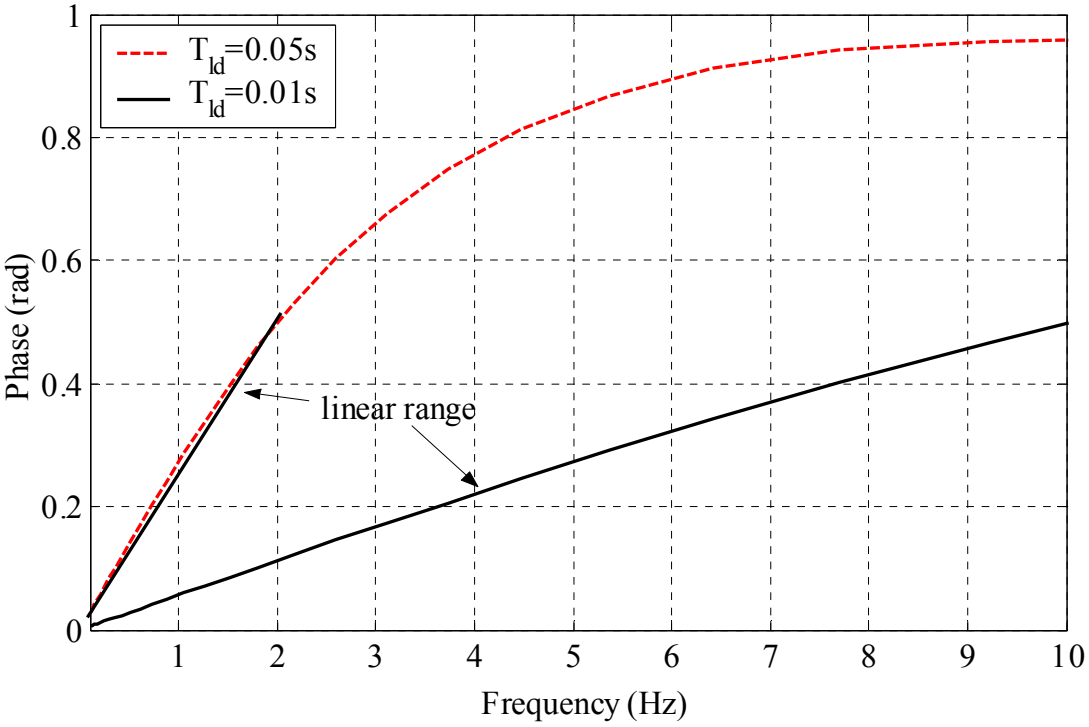

Figure 2.10 Frequency responses of phase-lead networks (0-10 Hz)

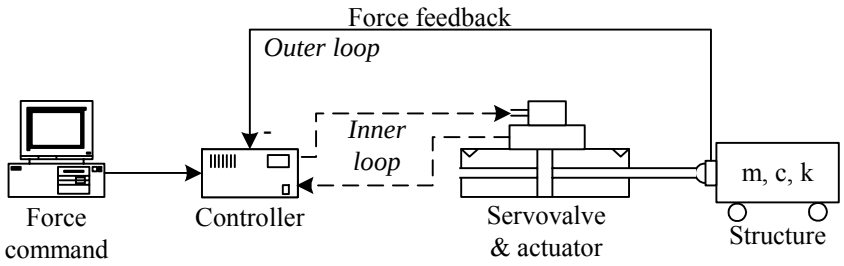

Figure 3.1 A schematic of a testing system in force control

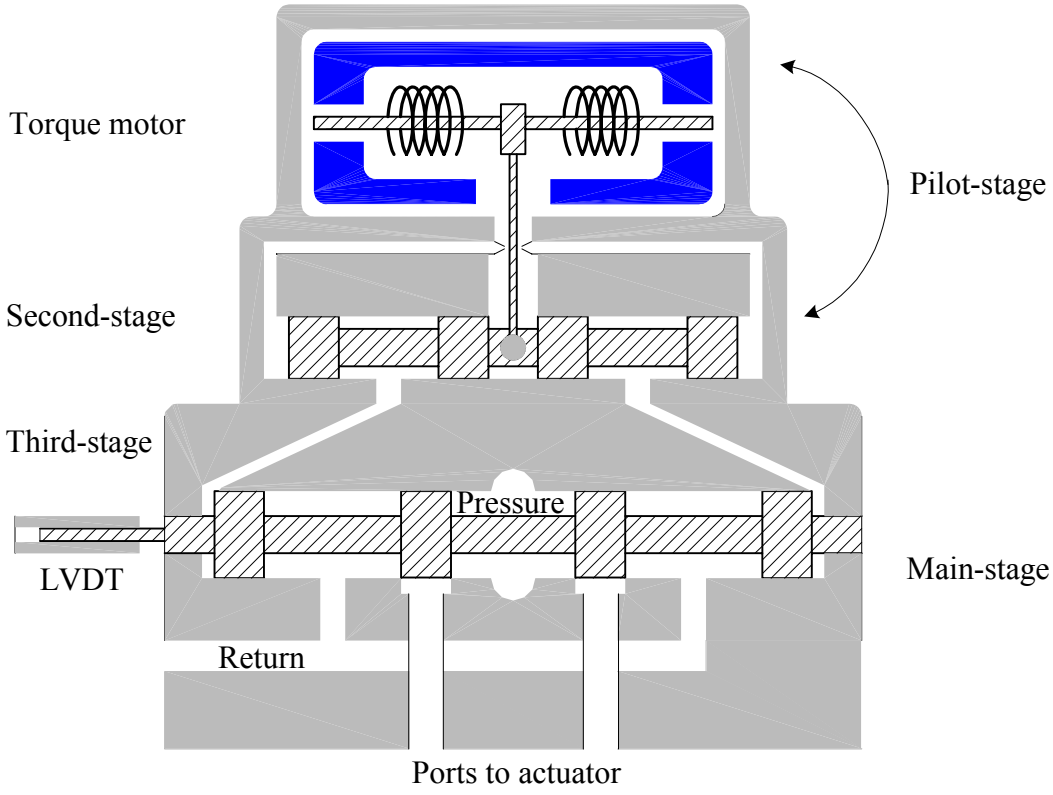

Figure 3.2 A schematic of a three-stage servovalve

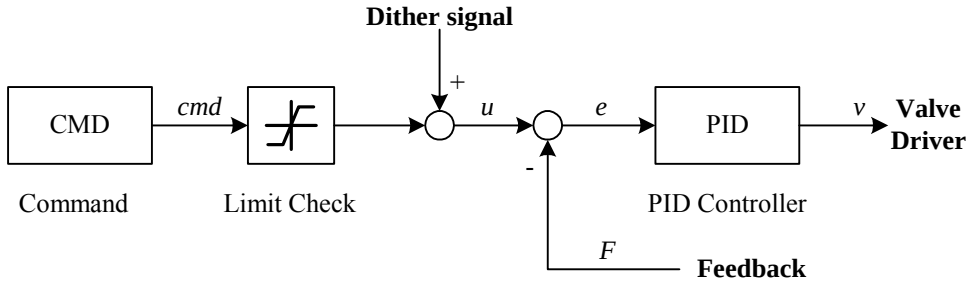

Figure 3.3 A block diagram of a servovalve controller

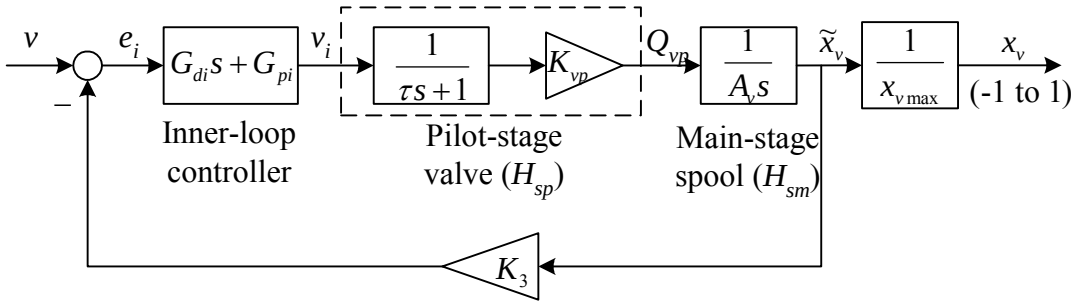

Figure 3.4 A block diagram of a three-stage servovalve (H_s)

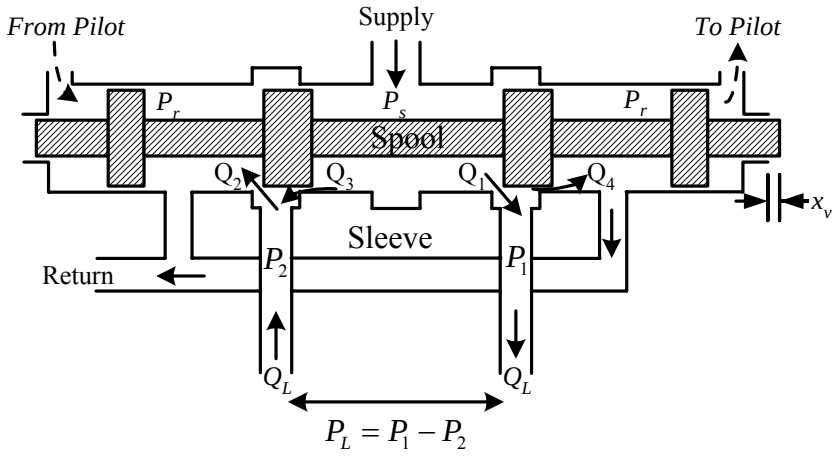

Figure 3.5 A schematic of a main stage spool

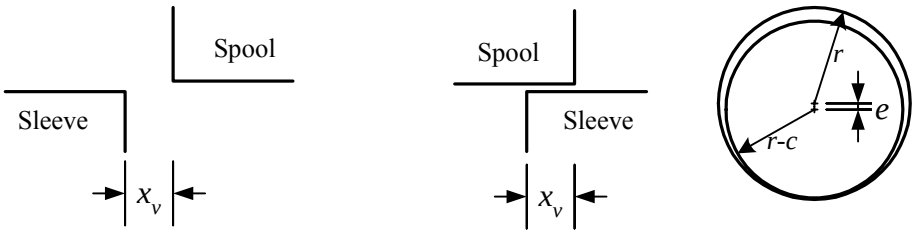

Figure 3.6 (a) load flow orifice; (b) leakage flow orifice

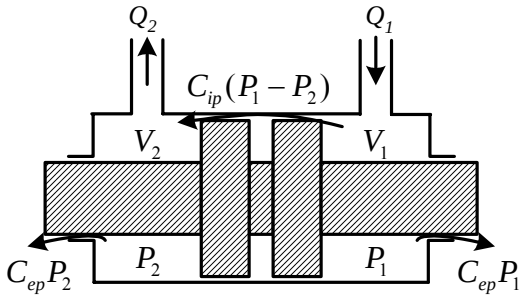

Figure 3.7 A schematic of an actuator piston

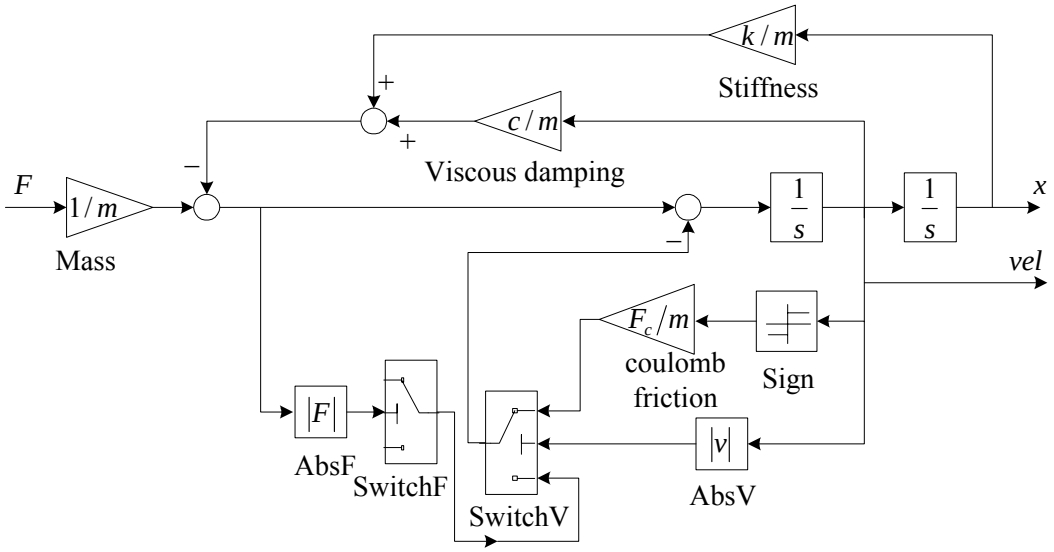

Figure 3.8 A block diagram model of the test structure

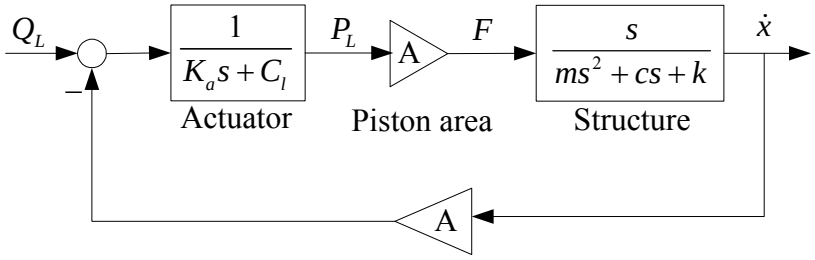

Figure 3.9 The interaction between piston (structure) velocity and actuator dynamics

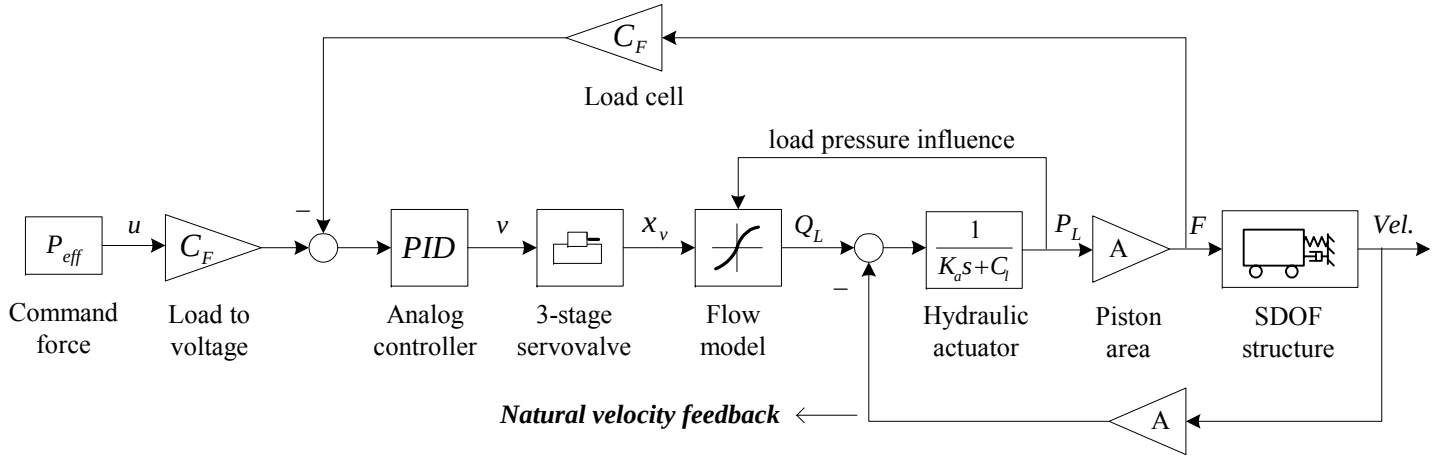

Figure 3.10 A block diagram of a testing system in force control

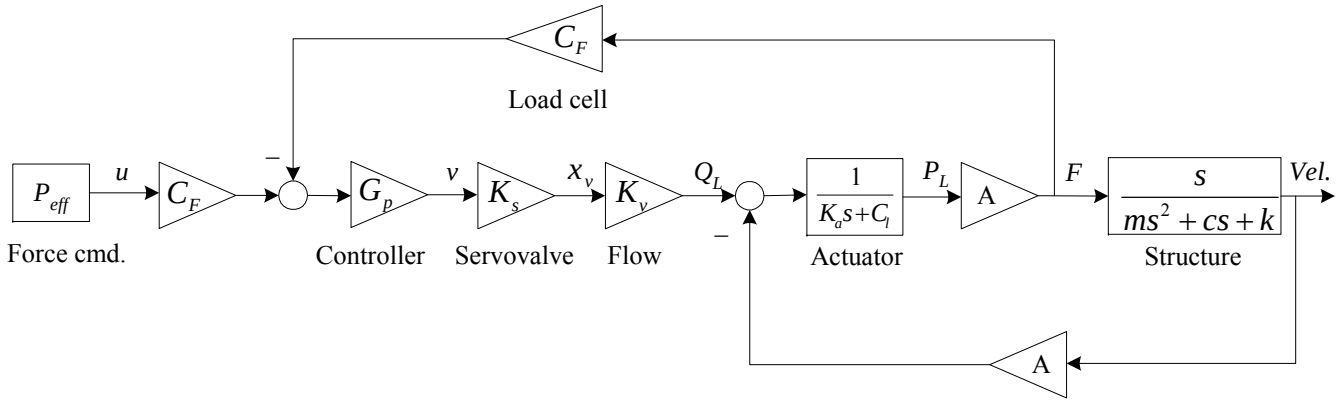

Figure 3.11 A simplified linearized block diagram of a testing system in force control

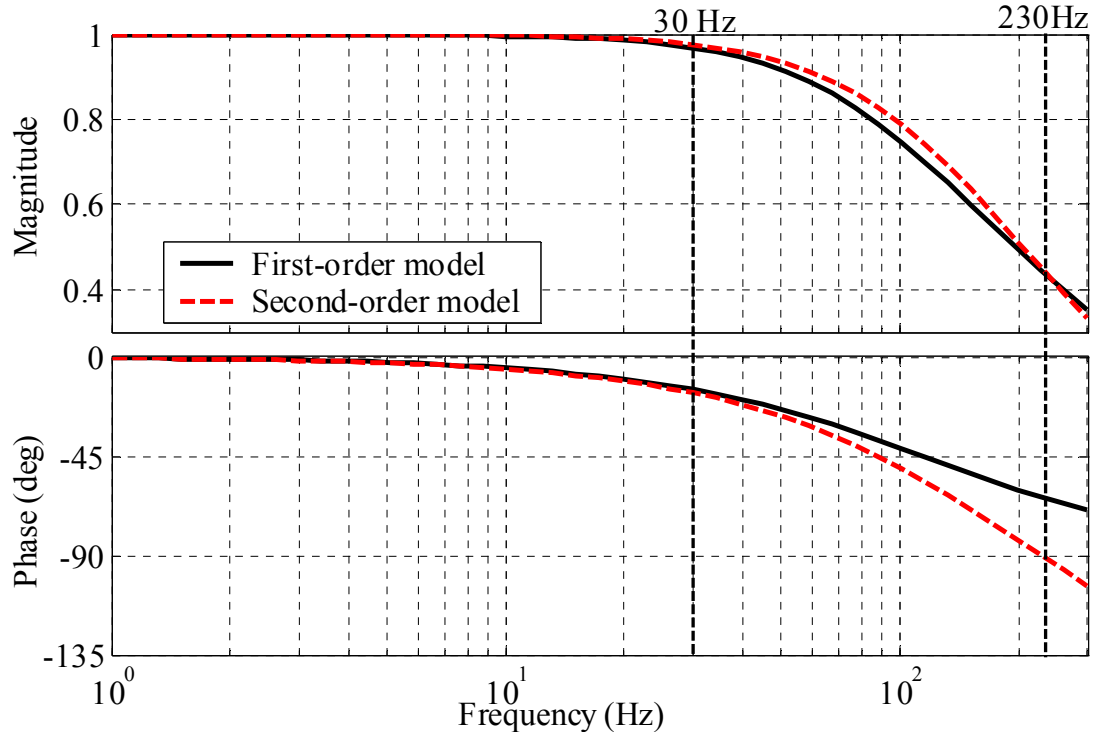

Figure 4.1 Comparison of the frequency response of the first-order and the second-order model for the pilot-stage valve

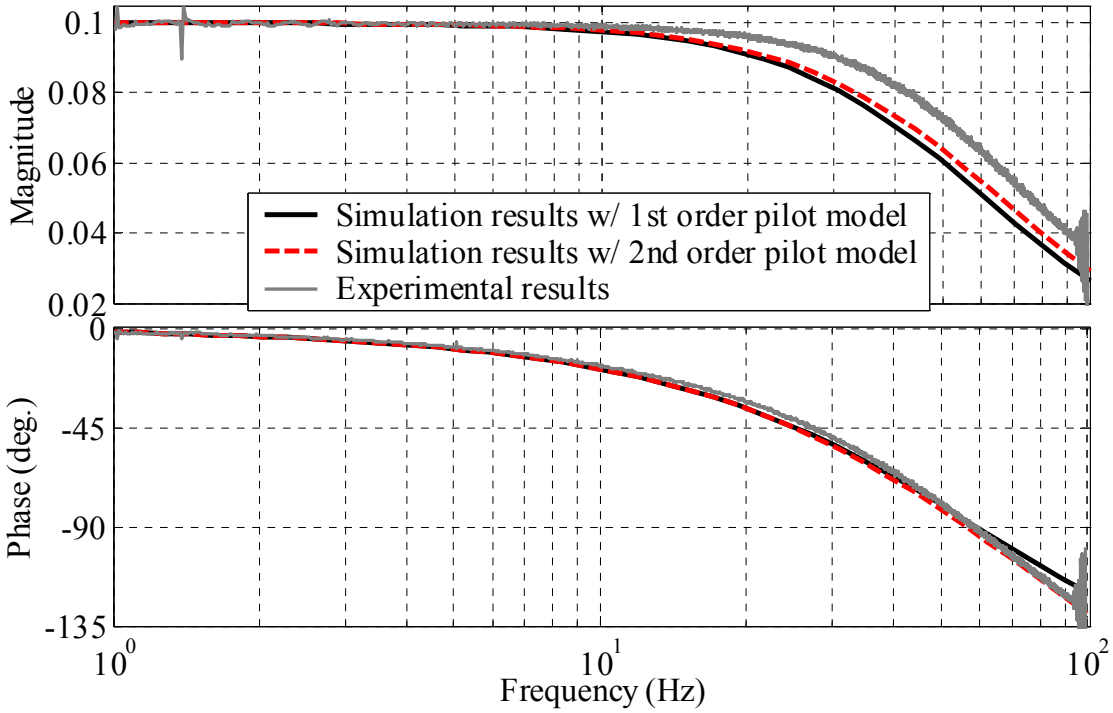

Figure 4.2 The frequency response of the three-stage servovalve

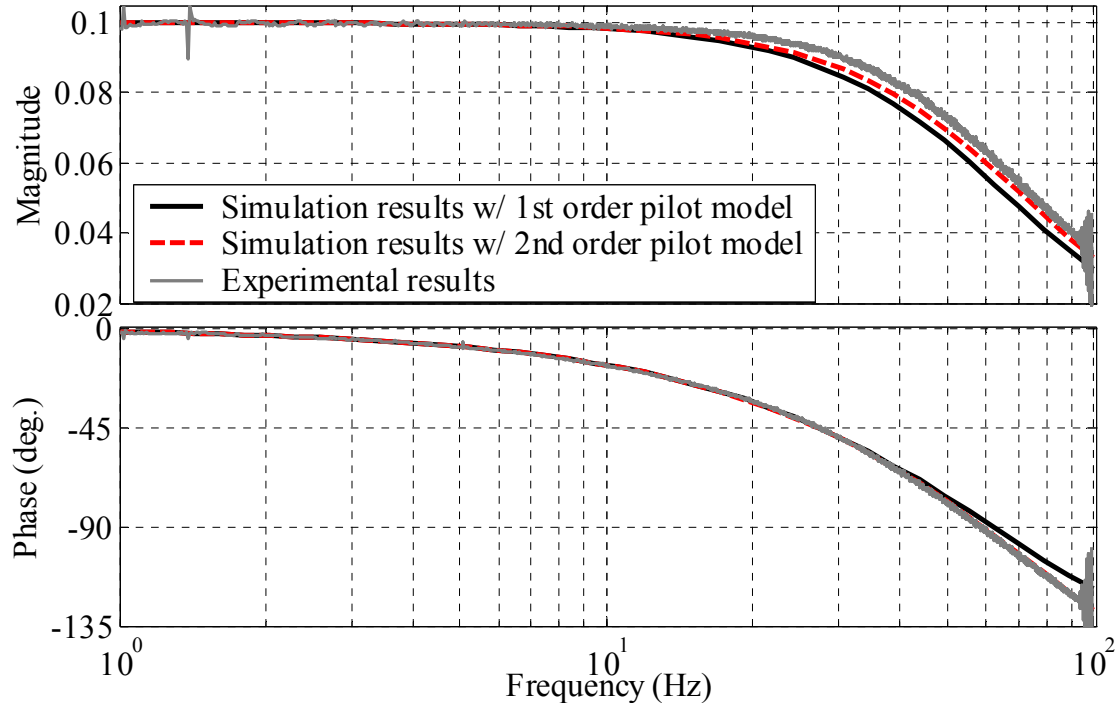

Figure 4.3 The frequency response of three-stage servovalve model with a 110% pilot-stage flow gain in simulation

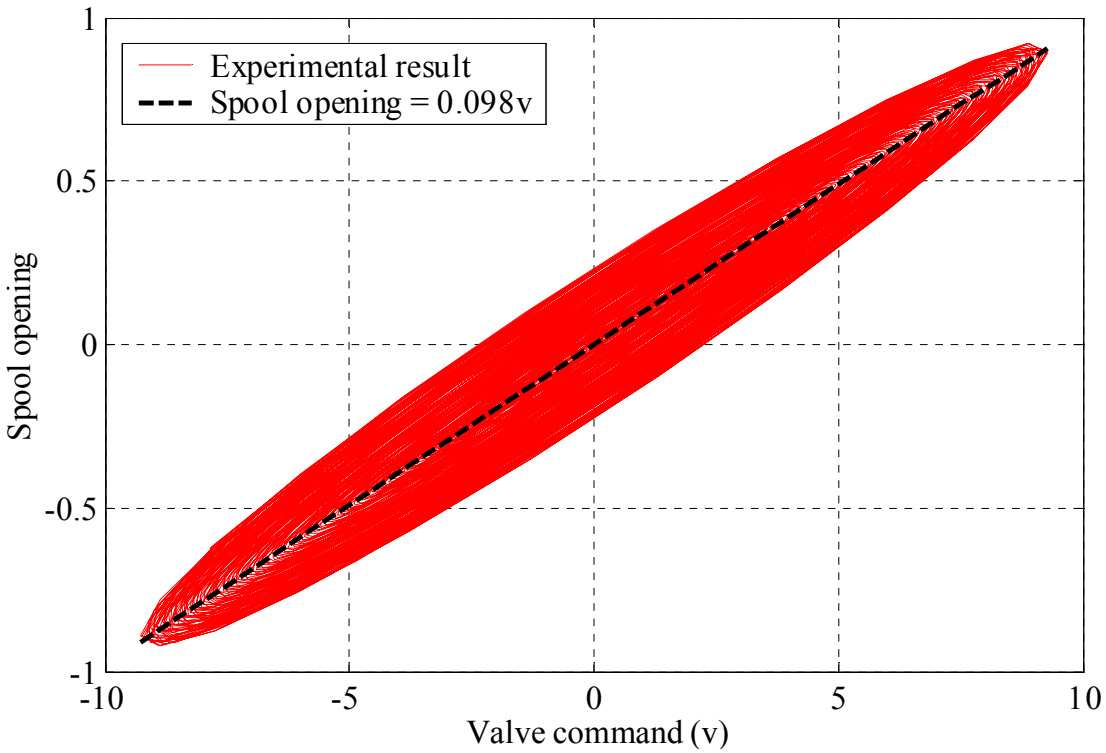

Figure 4.4 Measured spool positions vs. valve commands

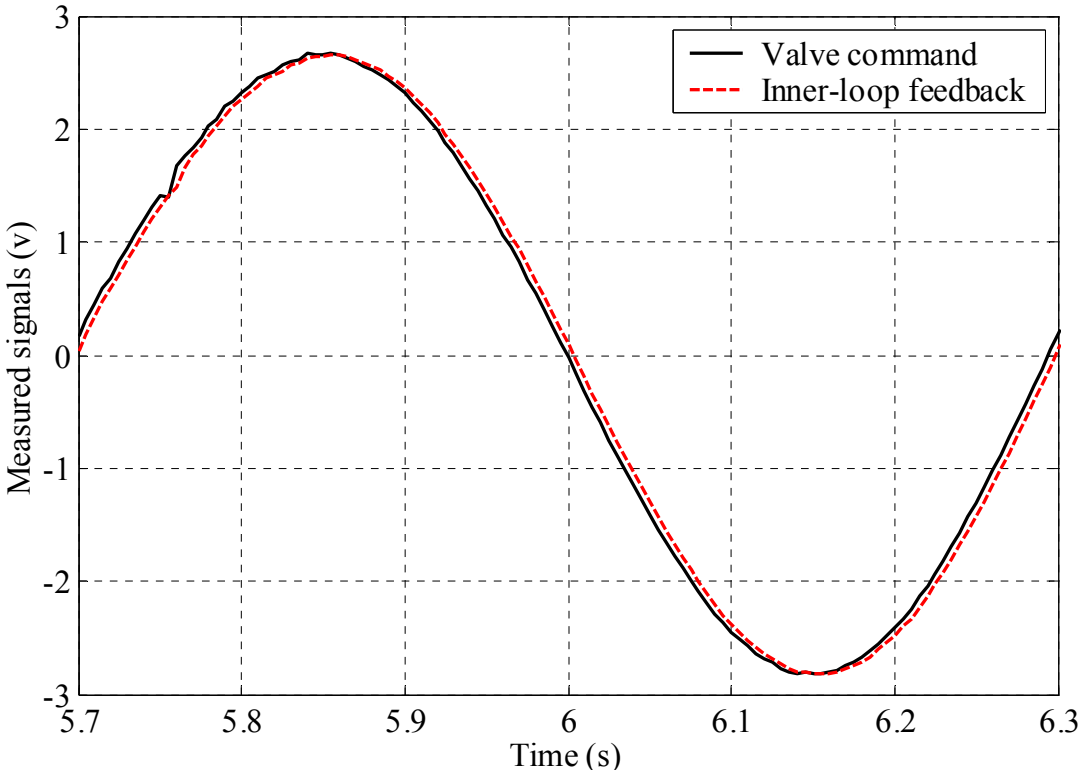

Figure 4.5 Servovalve response delay

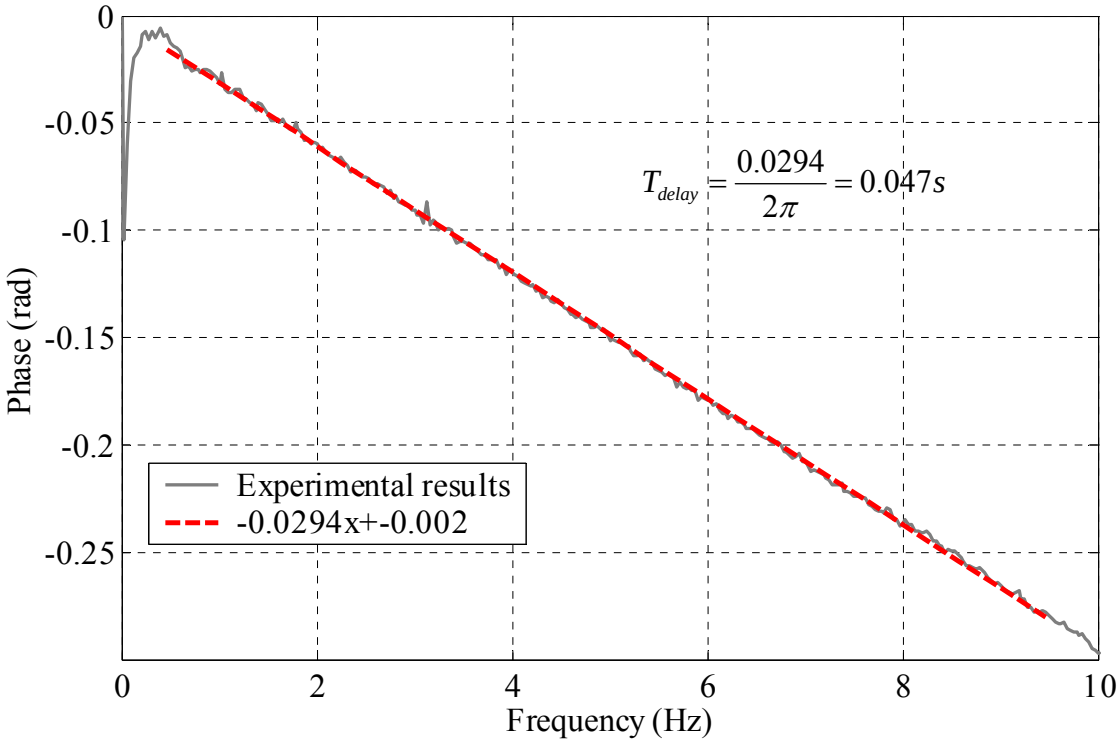

Figure 4.6 Servovalve response delay (frequency domain)

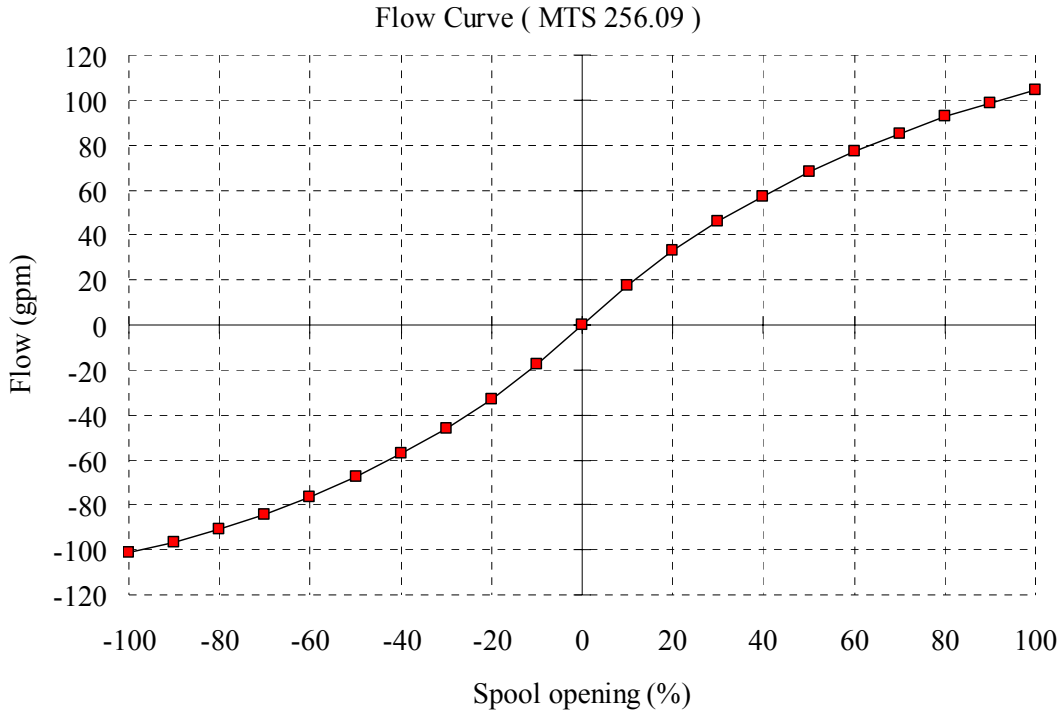

Figure 4.7 A typical flow vs. spool opening curve (regenerated with MTS testing data)

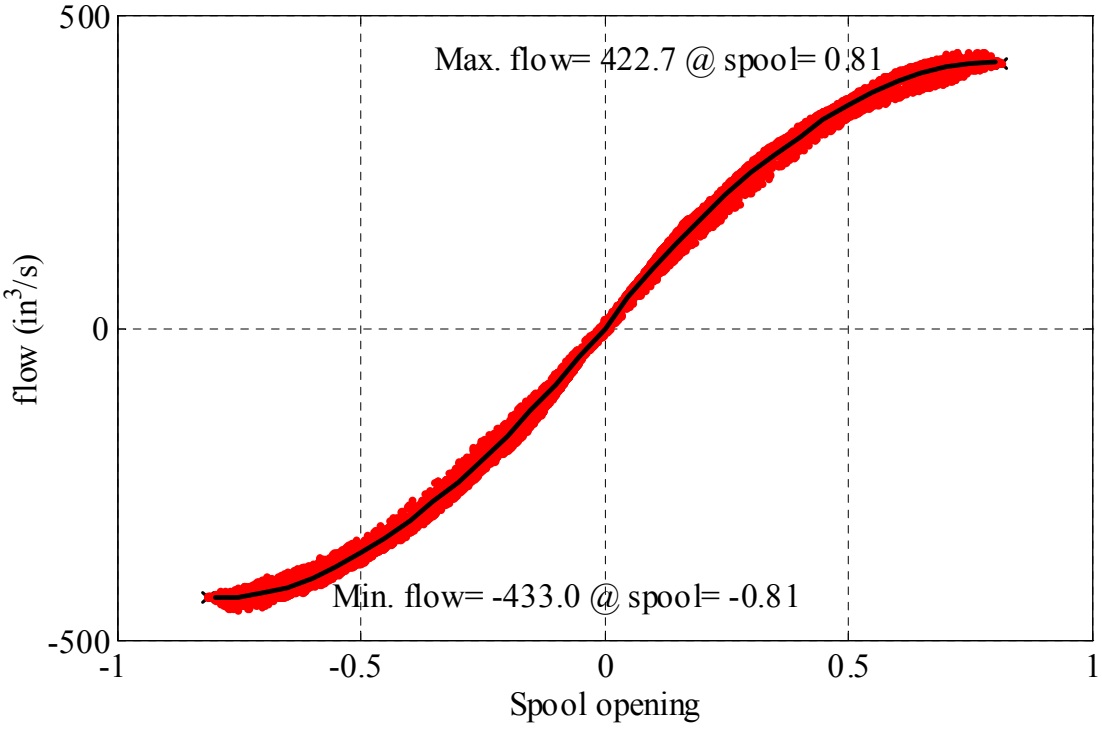

Figure 4.8 A measured flow vs. spool opening curve (no-load flow)

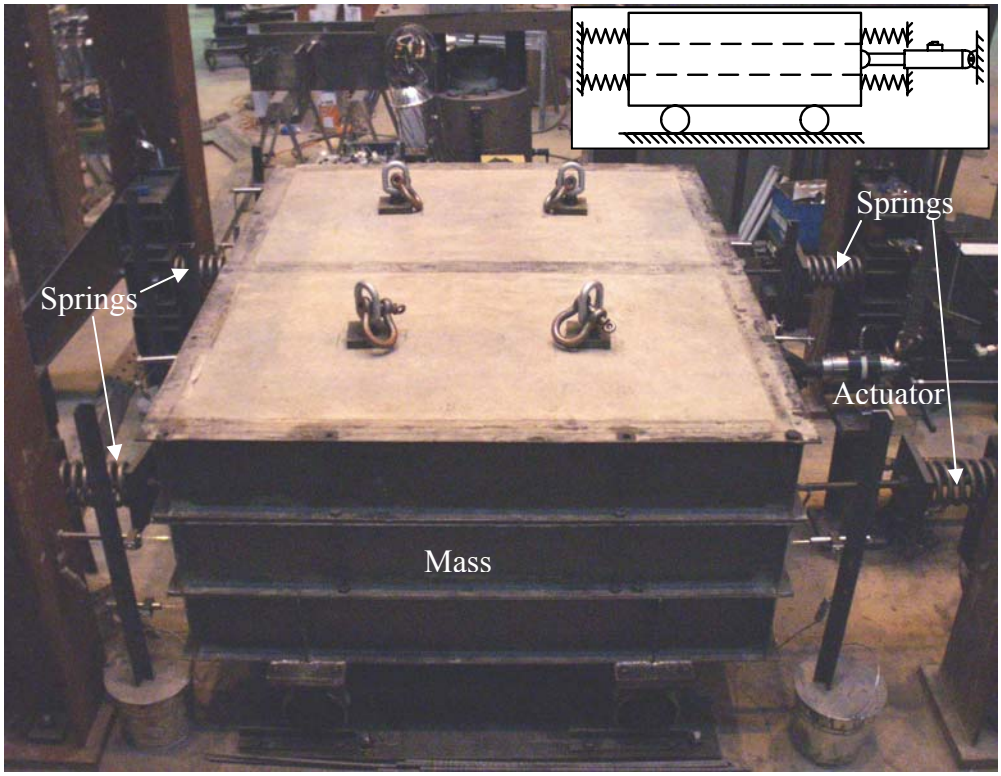

Figure 4.9 The SDOF mass-spring-damper test structure

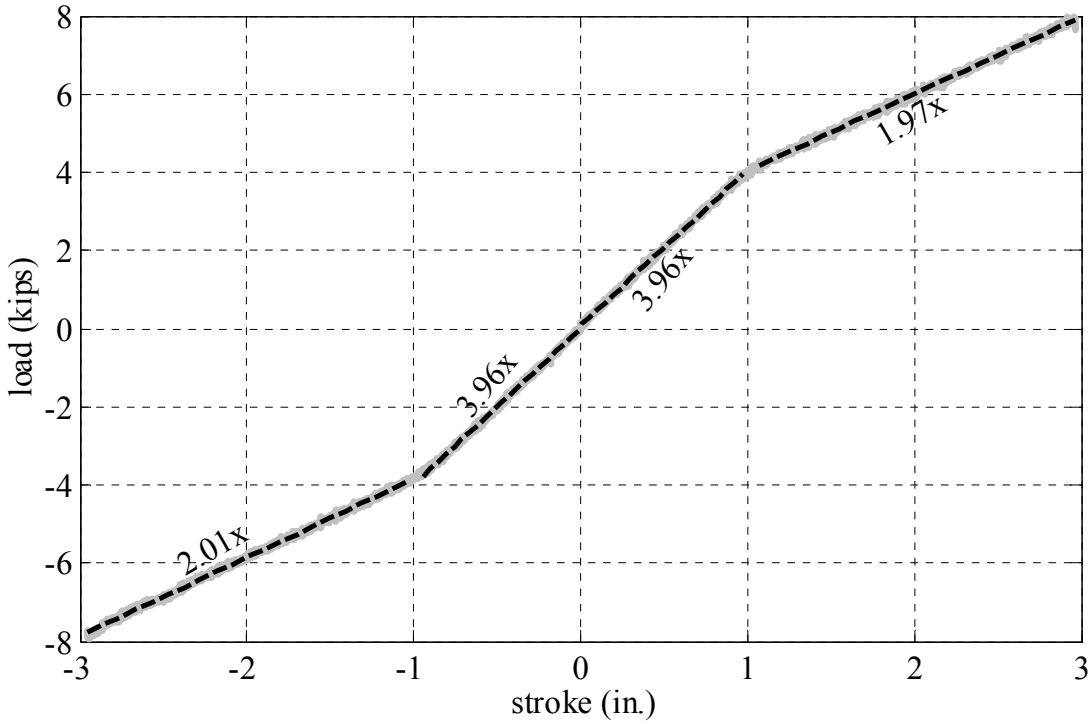

Figure 4.10 A measured force-displacement curve

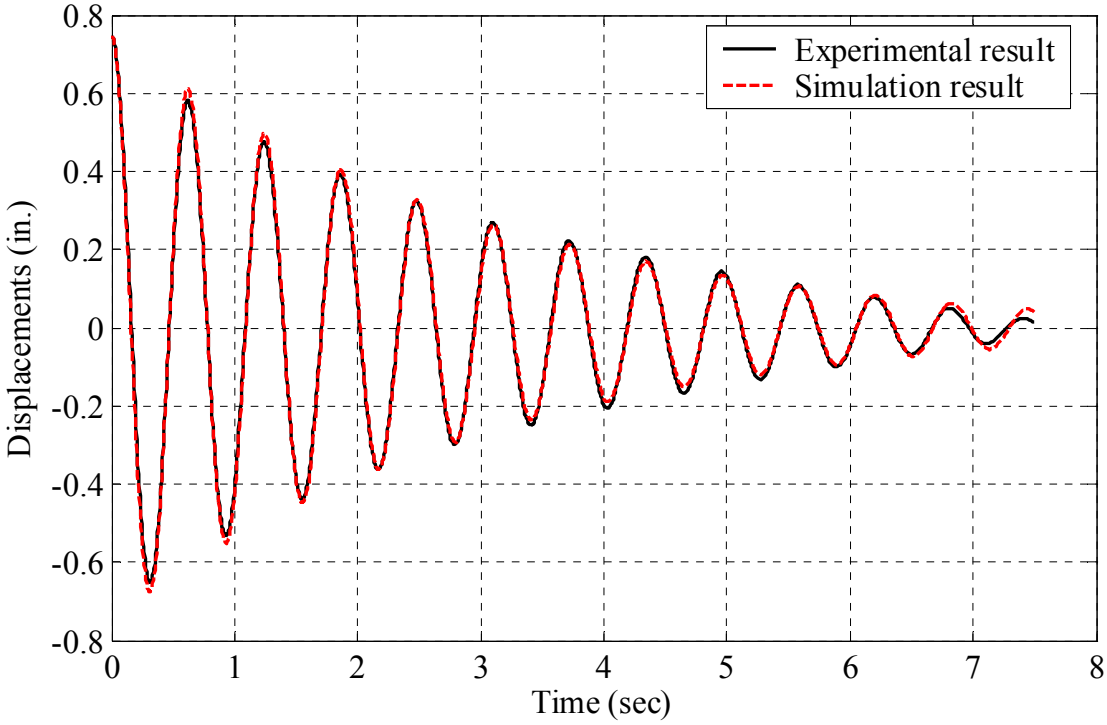

Figure 4.11 A free vibration test with the viscous damper

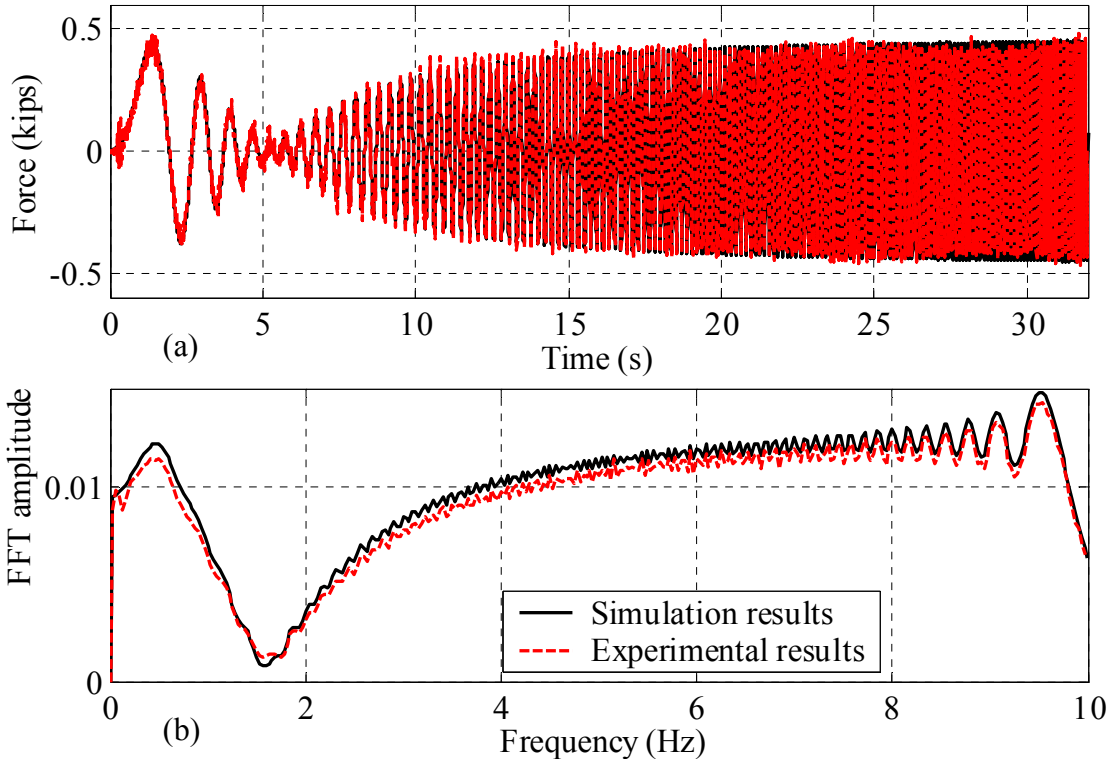

Figure 4.12 Responses of a force-controlled testing system to a 0.5-kip sinesweep input

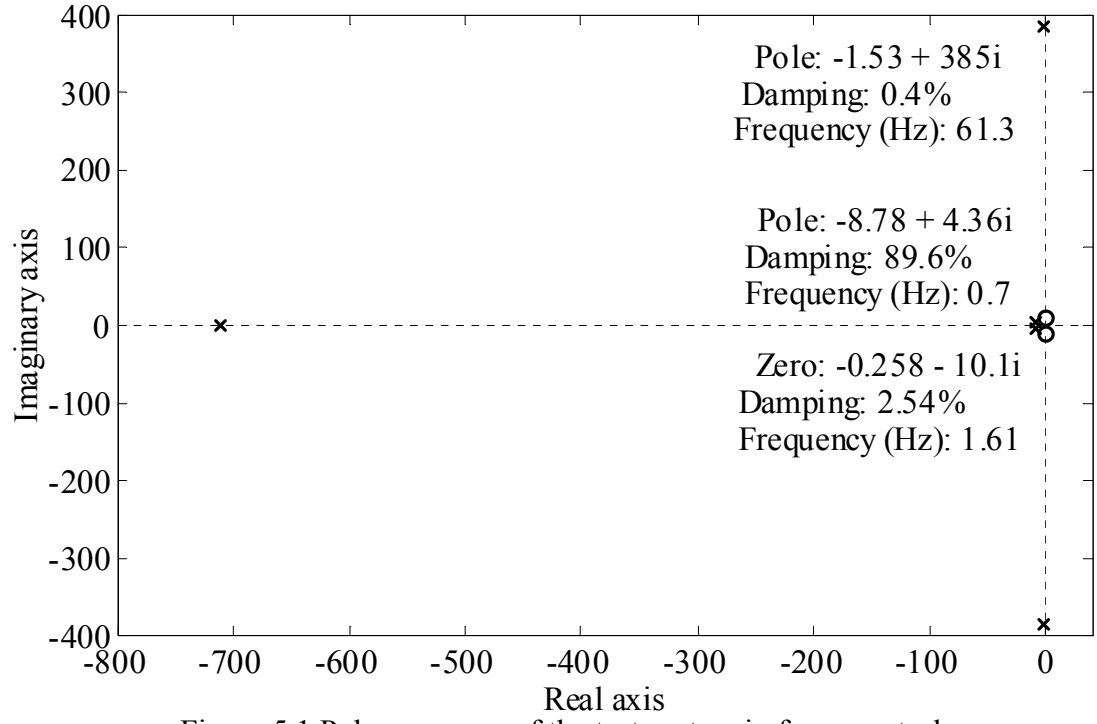

Figure 5.1 Pole-zero map of the test system in force control

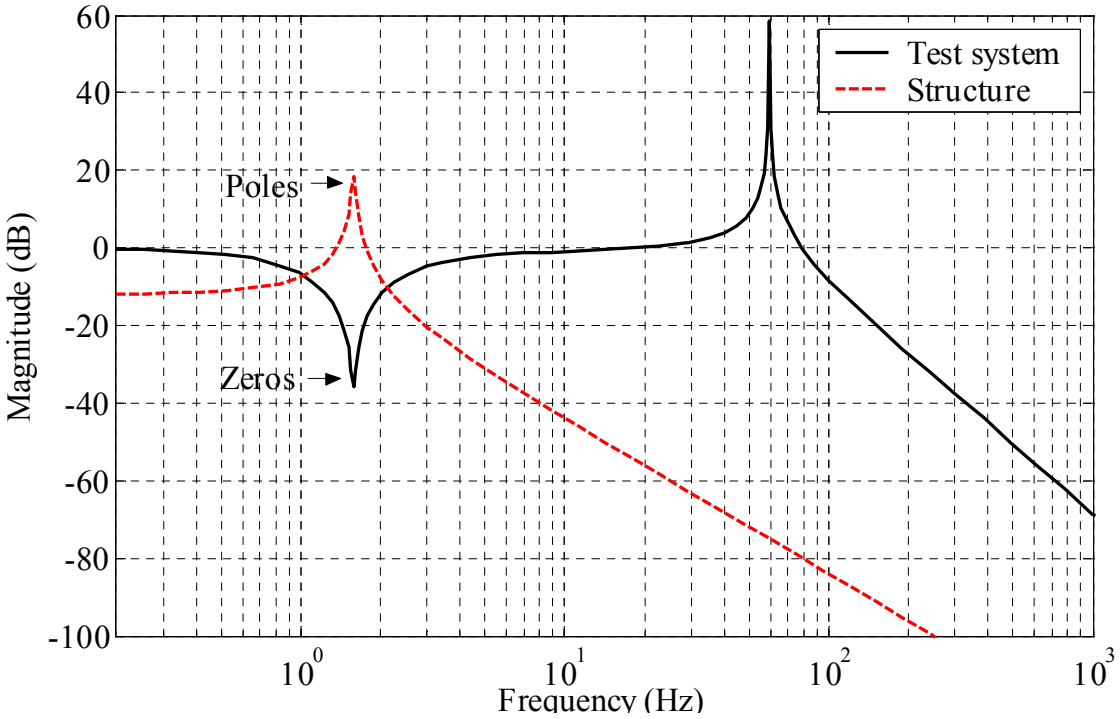

Figure 5.2 Frequency response of a test system in force control

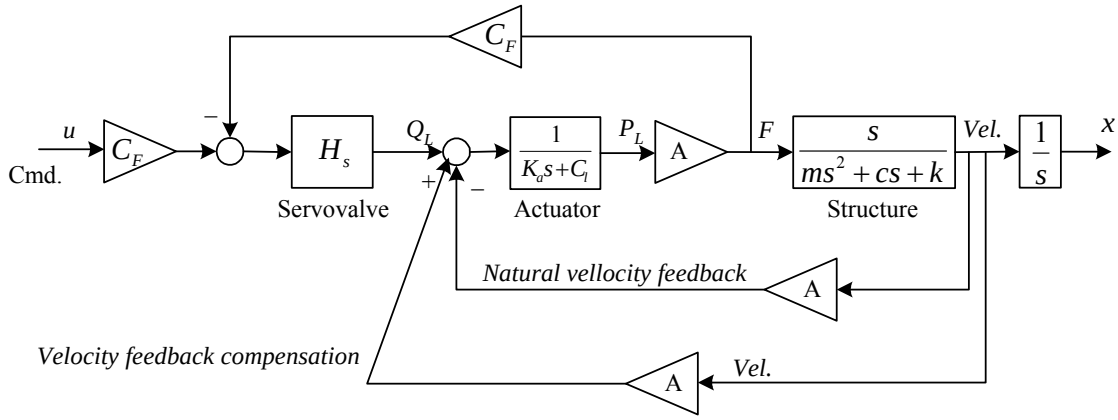

Figure 5.3 The direct velocity feedback compensation

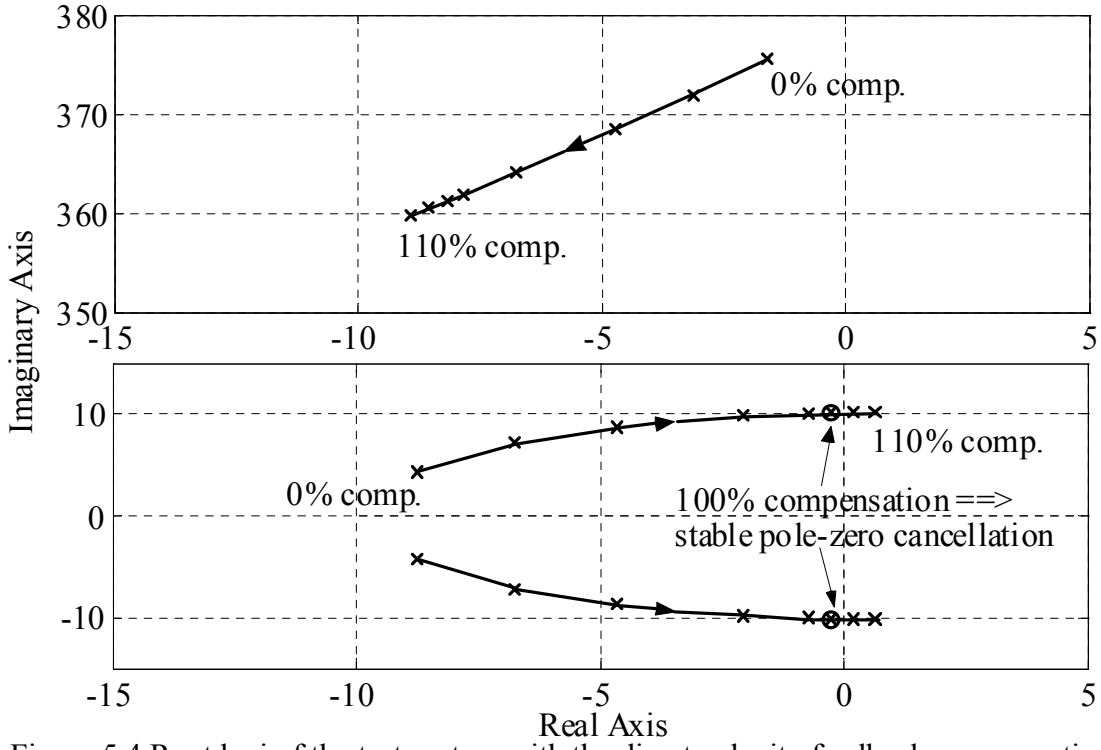

Figure 5.4 Root loci of the test system with the direct velocity feedback compensation

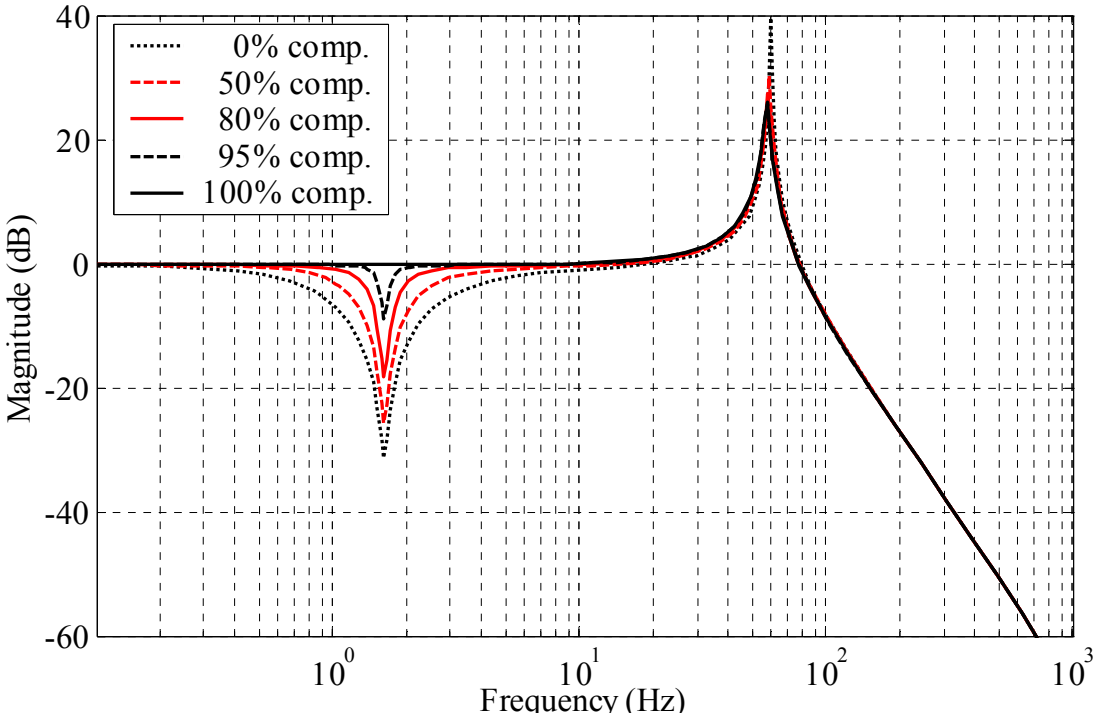

Figure 5.5 Frequency responses of force-controlled systems with various velocity feedback compensations

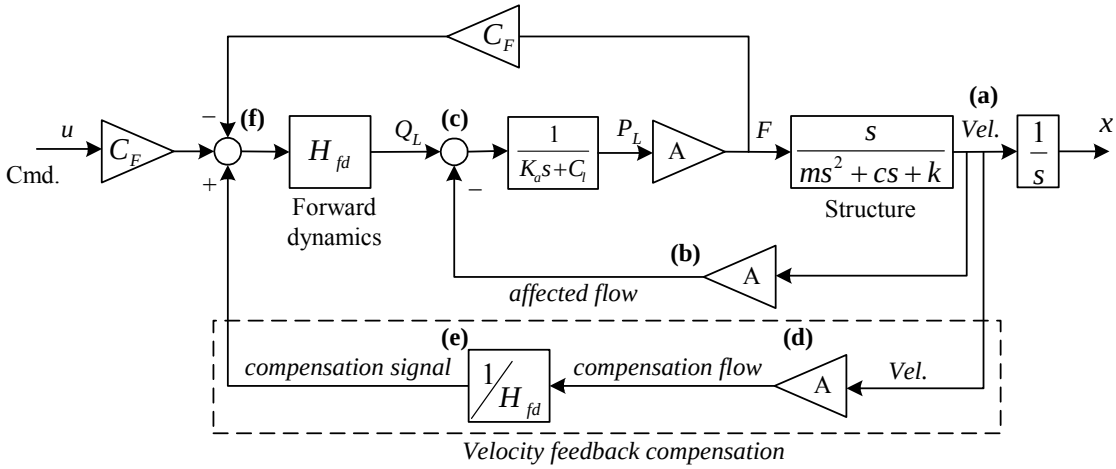

Figure 5.6 A schematic of velocity feedback compensation

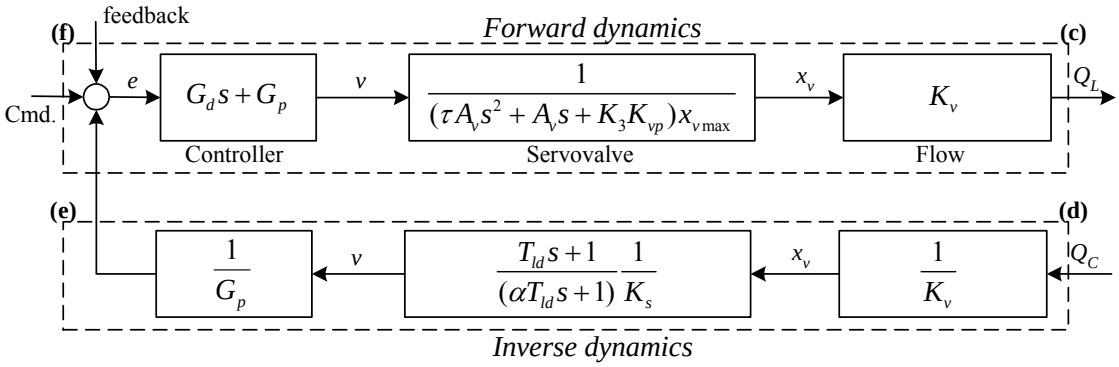

Figure 5.7 Linear velocity feedback compensation design

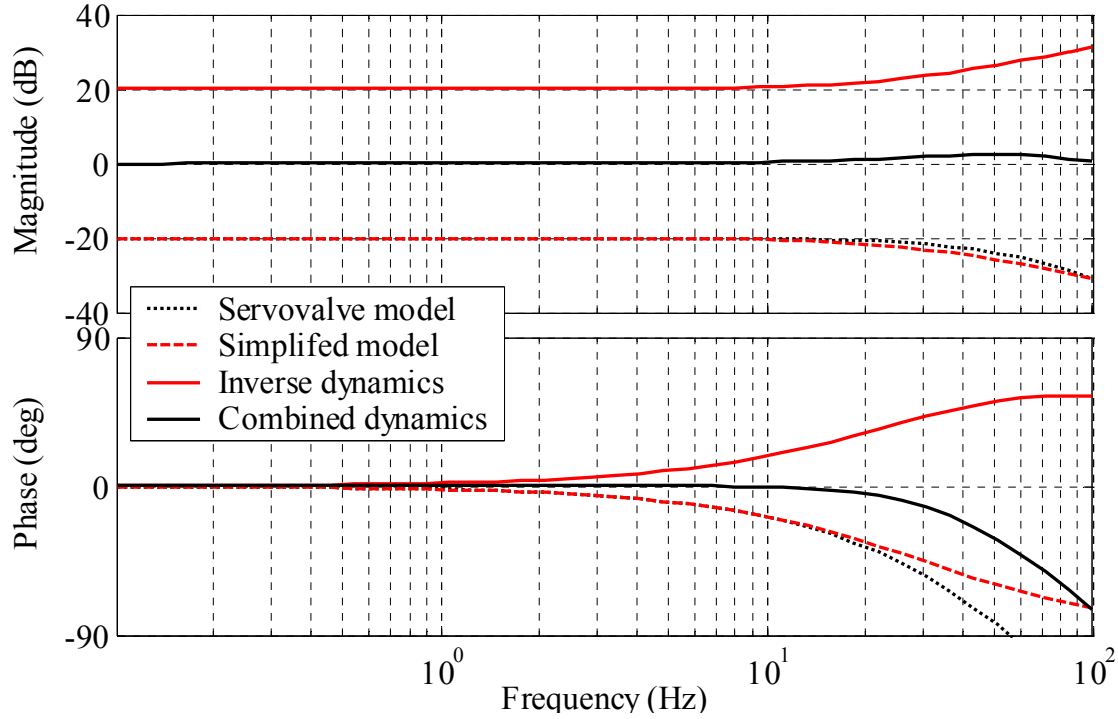

Figure 5.8 Frequency response of the servovalve dynamics and inverse dynamics

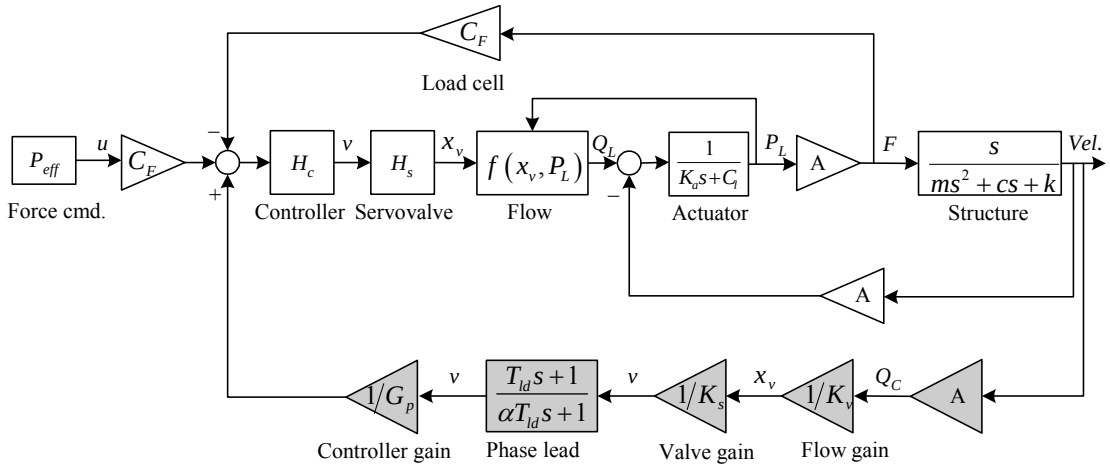

Figure 5.9 The test system with linearized velocity feedback compensation

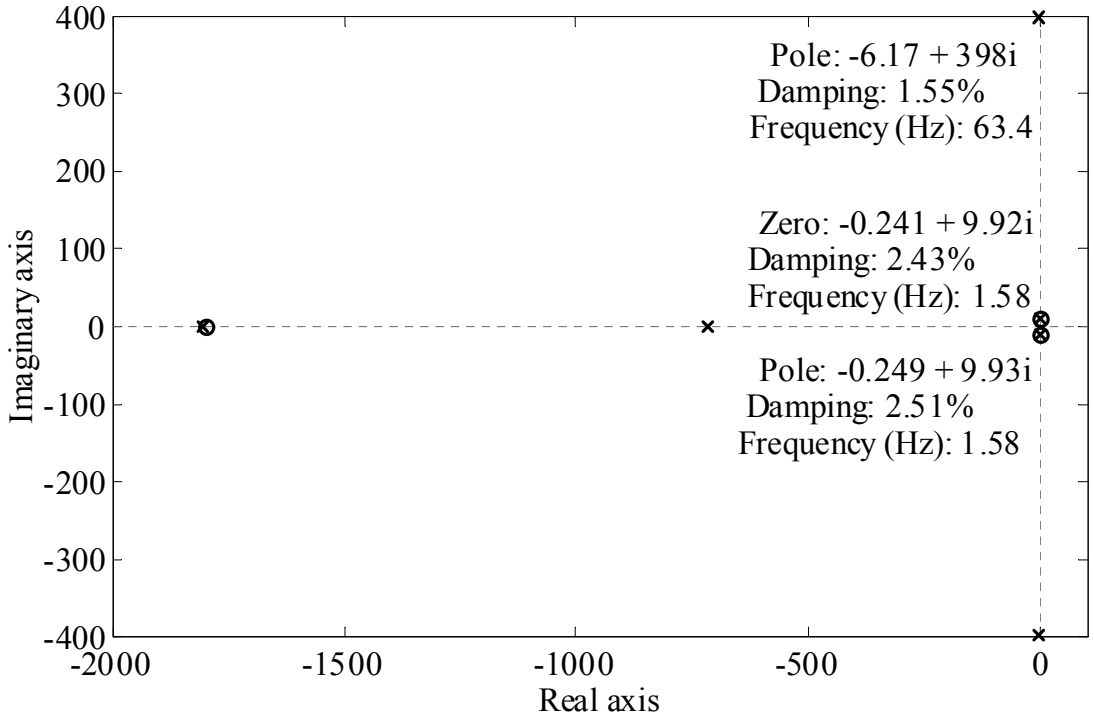

Figure 5.10 Pole-zero map of the linearized system with linearized velocity feedback compensation (from command to force)

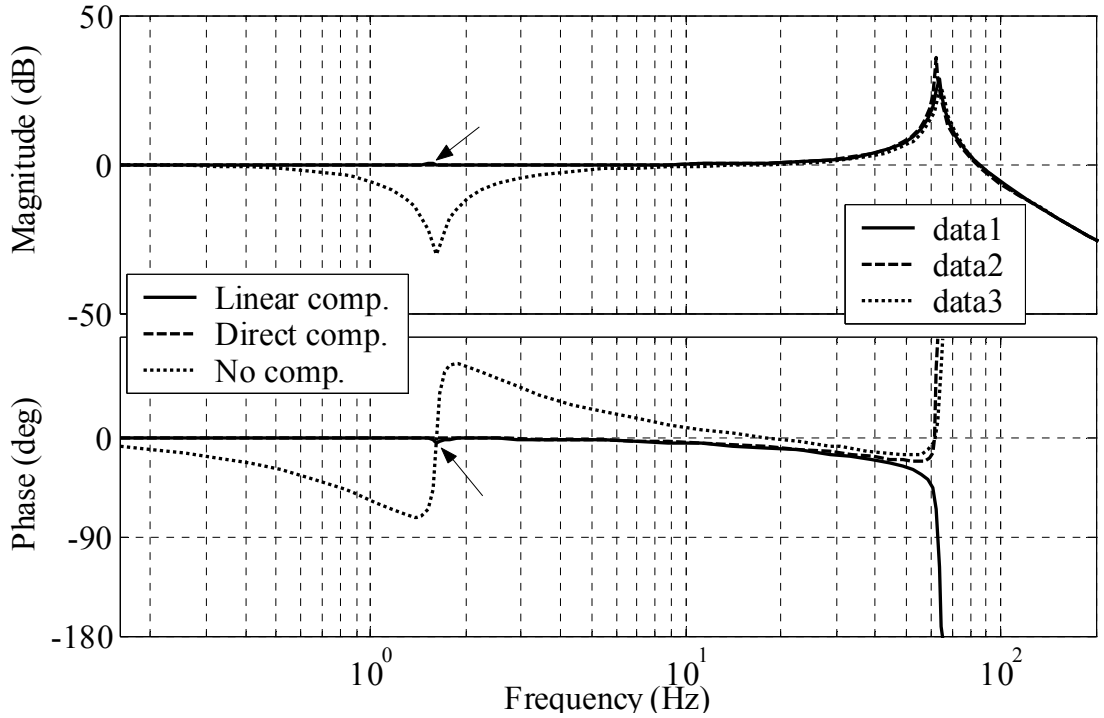

Figure 5.11 Frequency response of the system with linear velocity feedback compensation

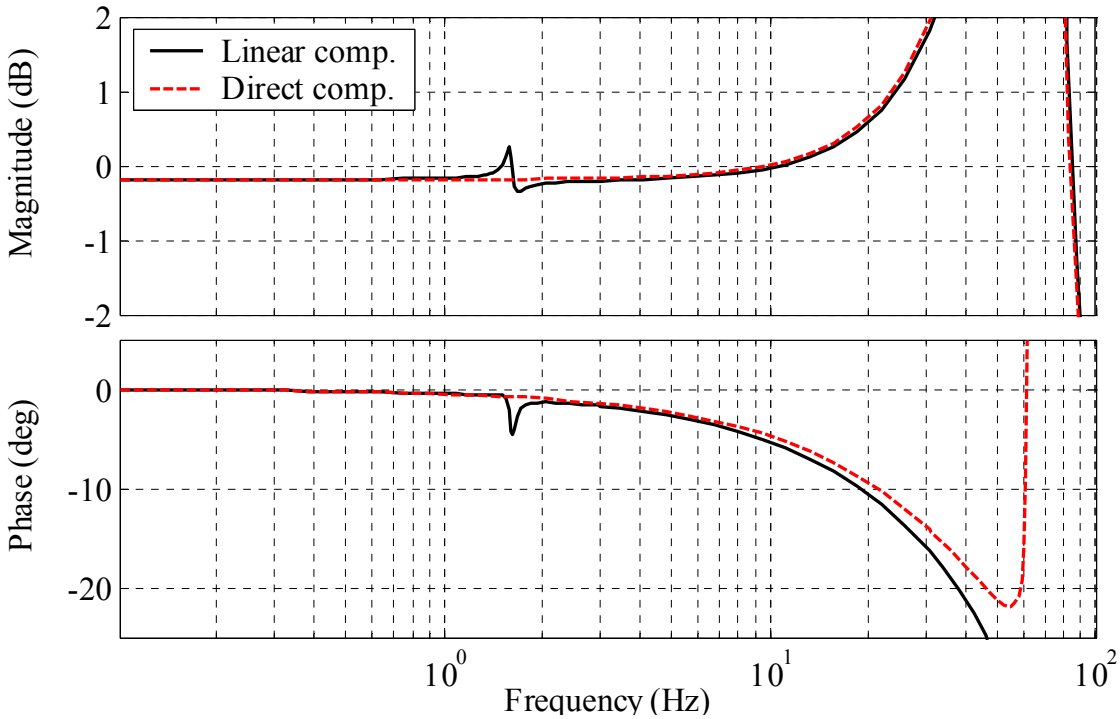

Figure 5.12 Detailed frequency response of the system with linear velocity feedback compensation

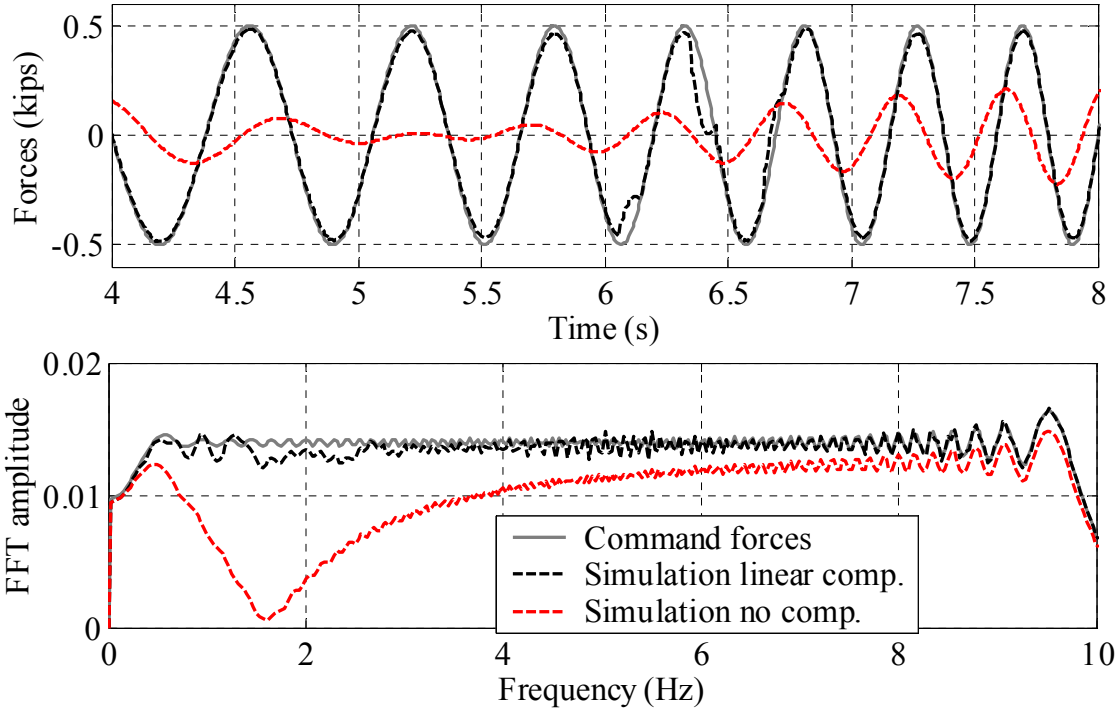

Figure 5.13 Response of the test system with linear velocity feedback compensation subjected to 0.5-kip sine wave sweep (0-10 Hz)

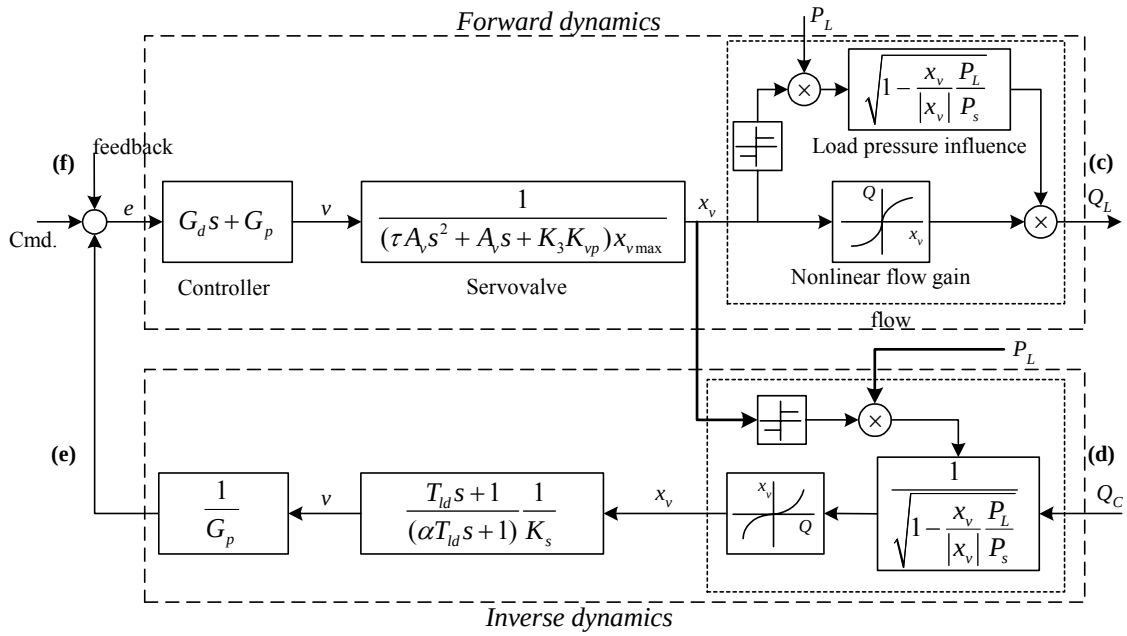

Figure 5.14 Nonlinear velocity feedback compensation design

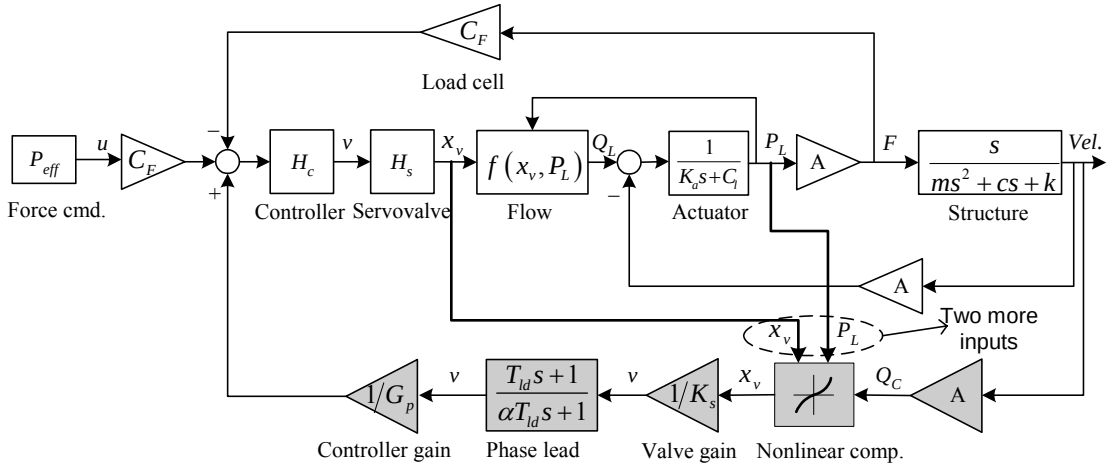

Figure 5.15 Test system with nonlinear velocity feedback compensation

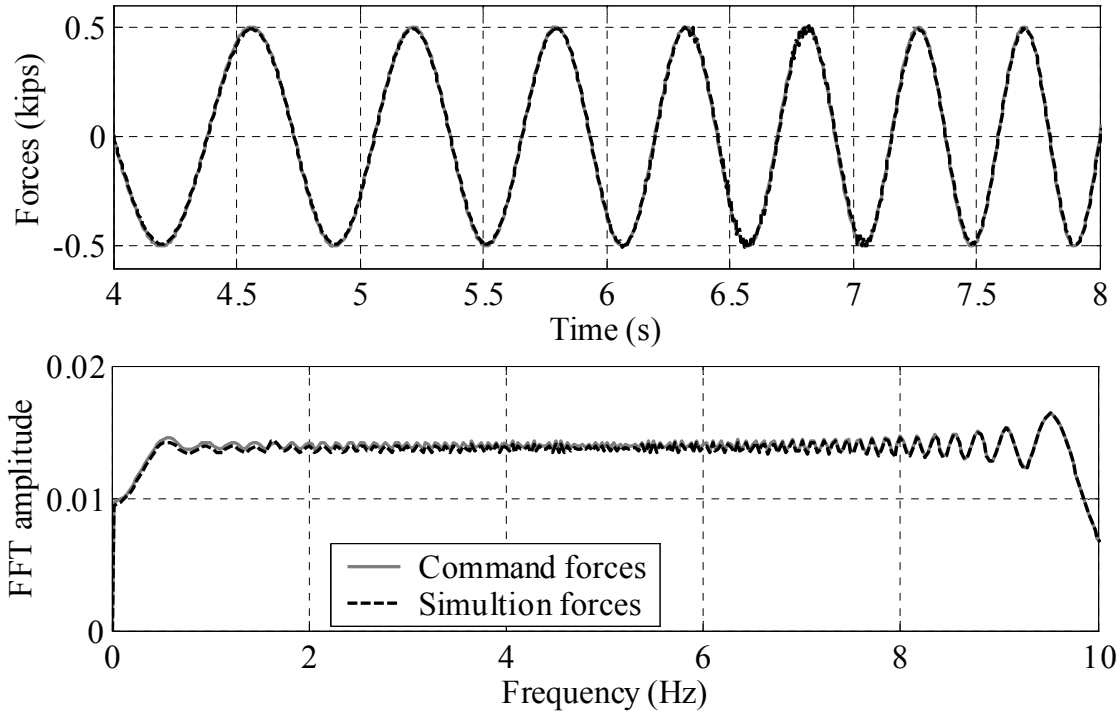

Figure 5.16 Response of the test system with nonlinear velocity feedback compensation subjected to 0.5-kip sine wave sweep (0-10 Hz)

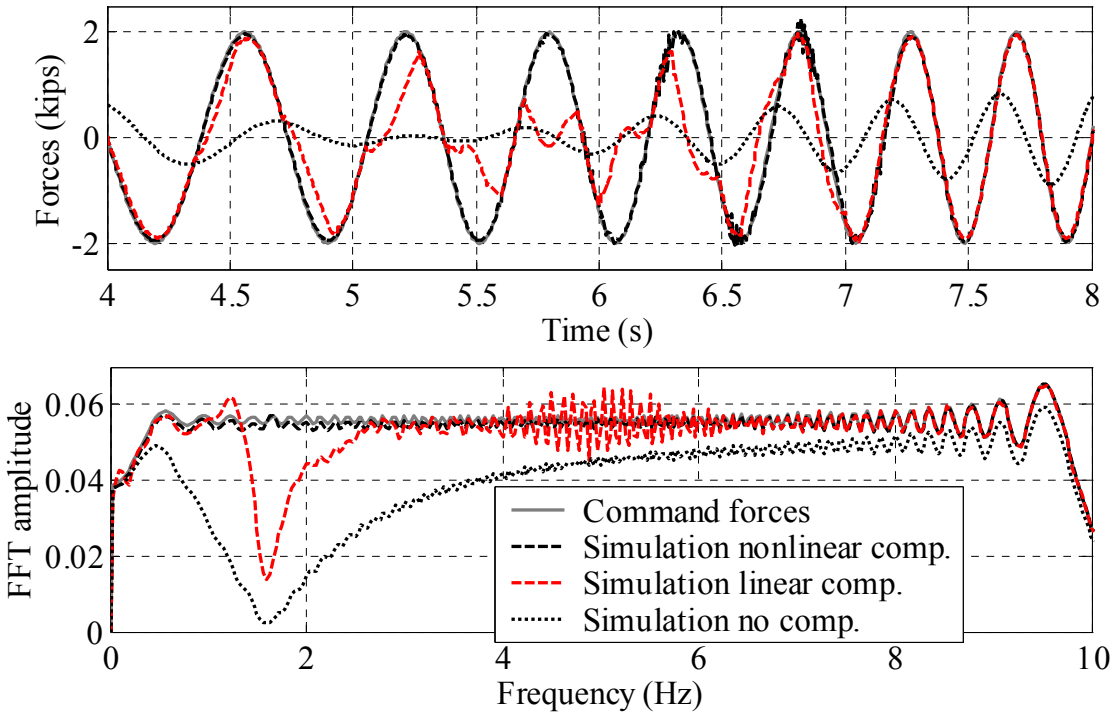

Figure 5.17 Response of the test system with linear and nonlinear velocity feedback compensation subjected to 2.0-kip sine wave sweep (0-10 Hz)

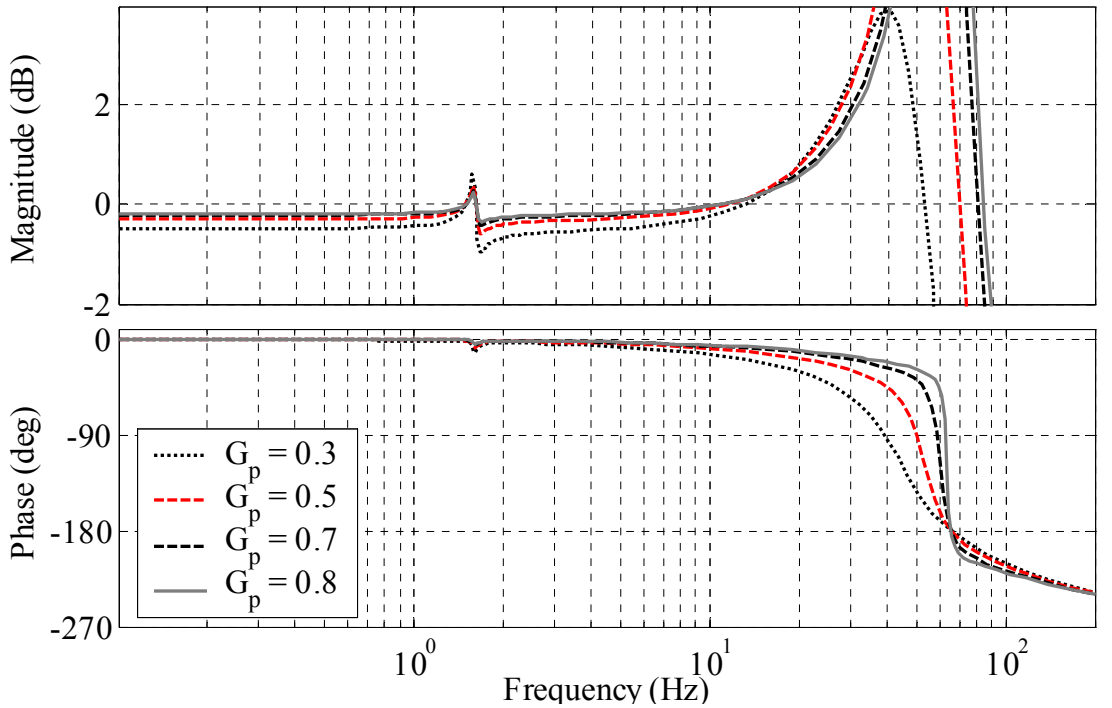

Figure 5.18 Comparison of the frequency responses of the linearly compensated systems with different controller P gain (from command to force)

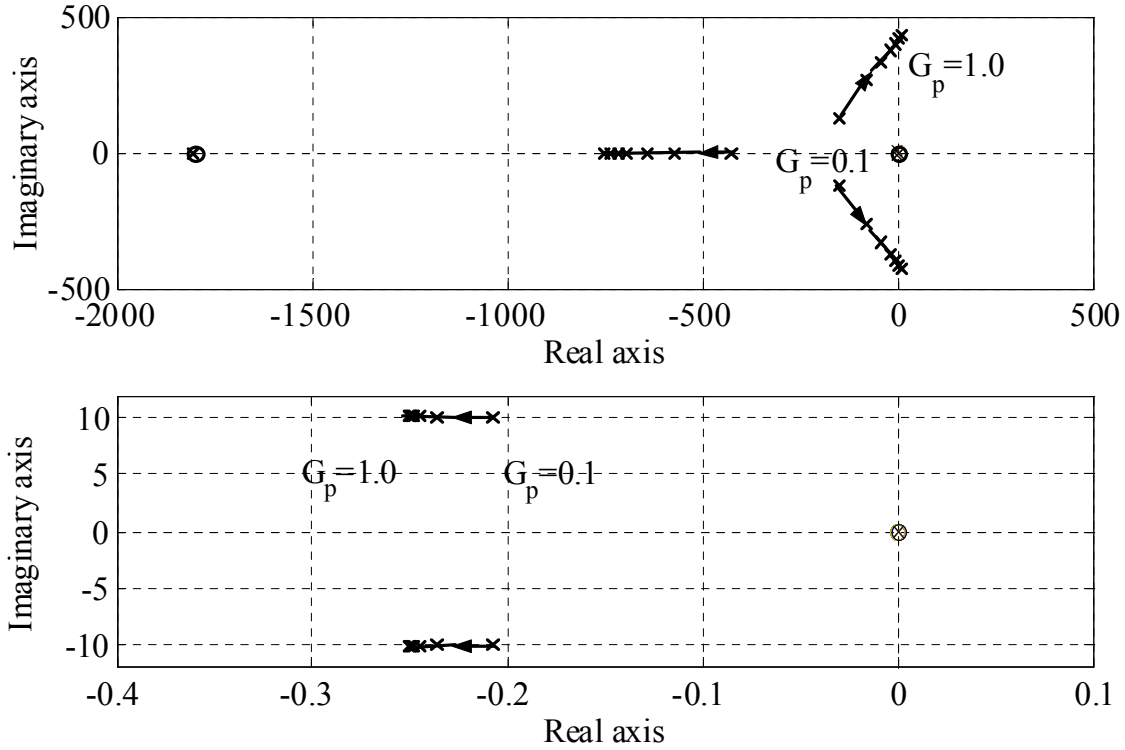

Figure 5.19 Root loci of the linearly compensated systems with respect to controller P gain (from command to displacement)

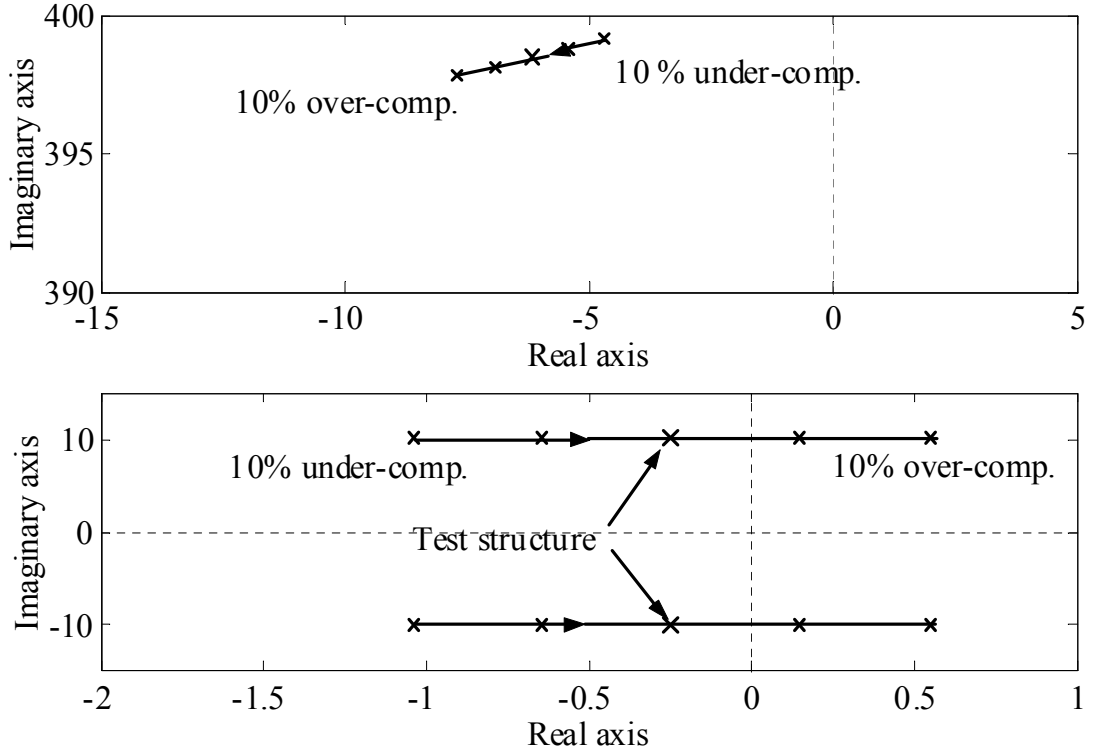

Figure 5.20 Root loci of the linearly compensated systems with respect to percentage compensation (from command to displacement)

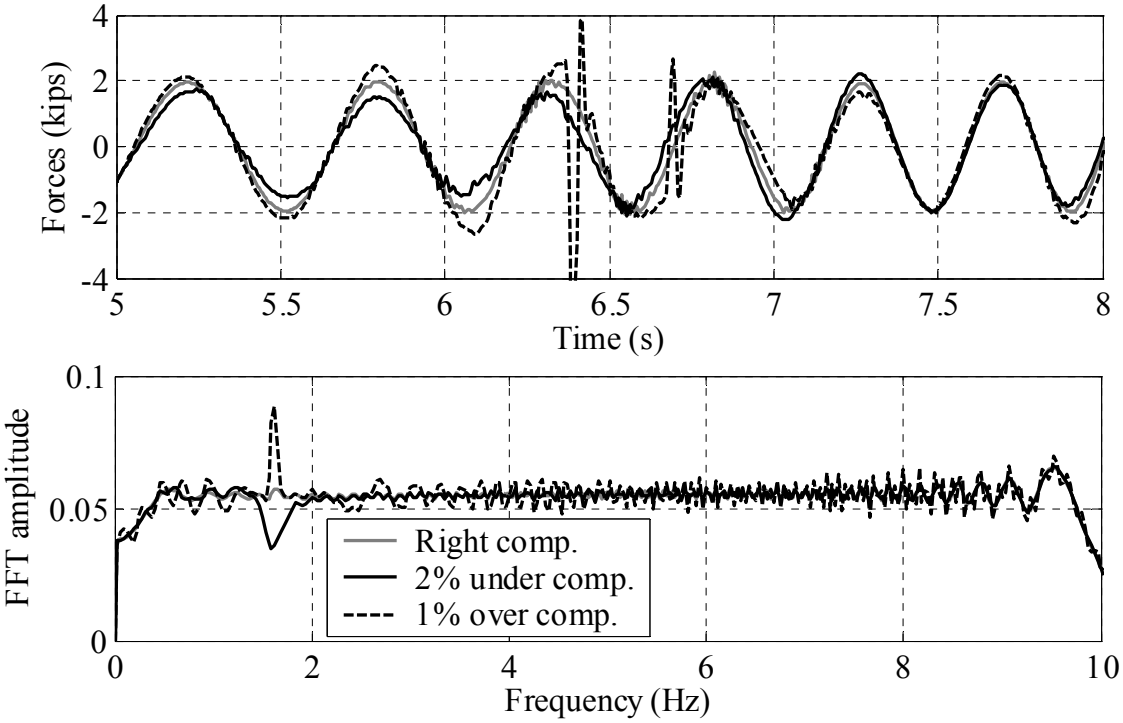

Figure 5.21 Response of the test system with nonlinear velocity feedback compensation subjected to 2.0-kip sine wave sweep (0-10 Hz)

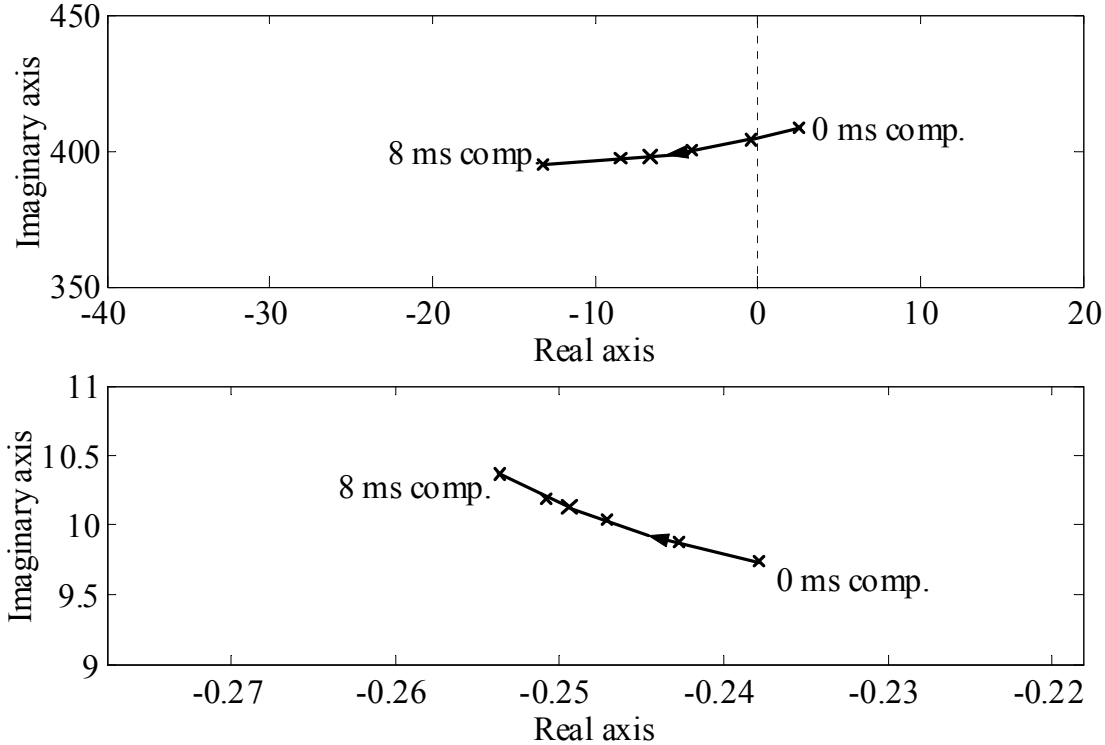

Figure 5.22 Root loci of the linearly compensated systems with respect to delay compensation (from command to displacement)

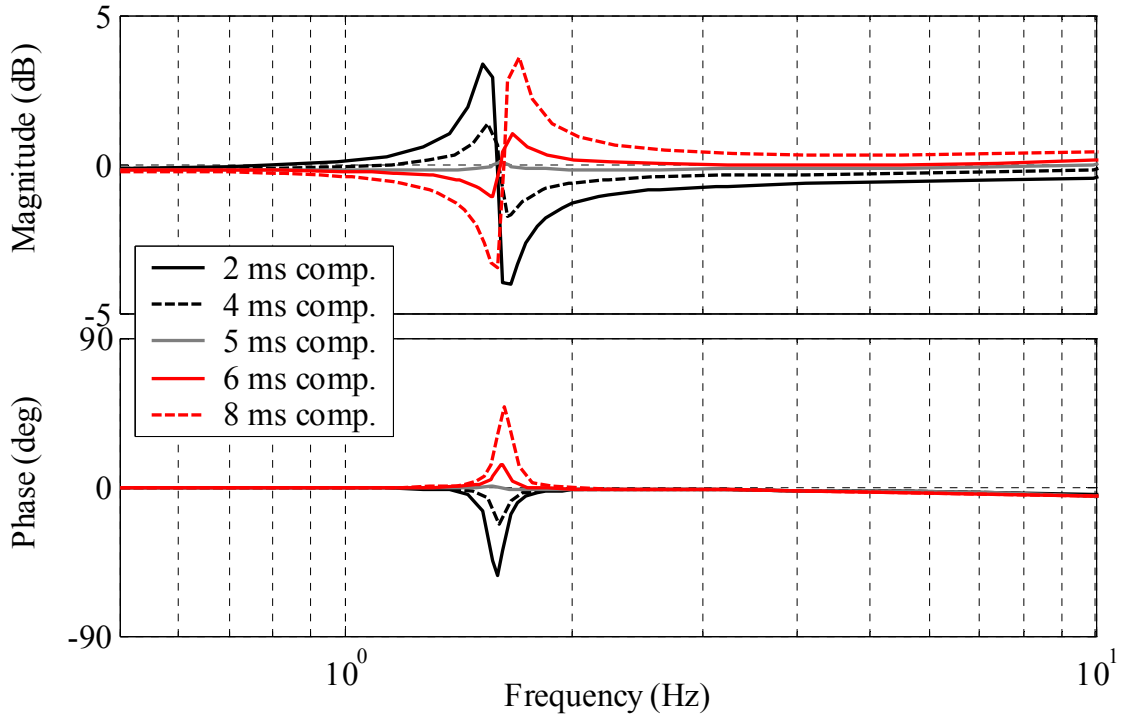

Figure 5.23 Frequency response of the linearly compensated systems with various delay compensations (from command to force)

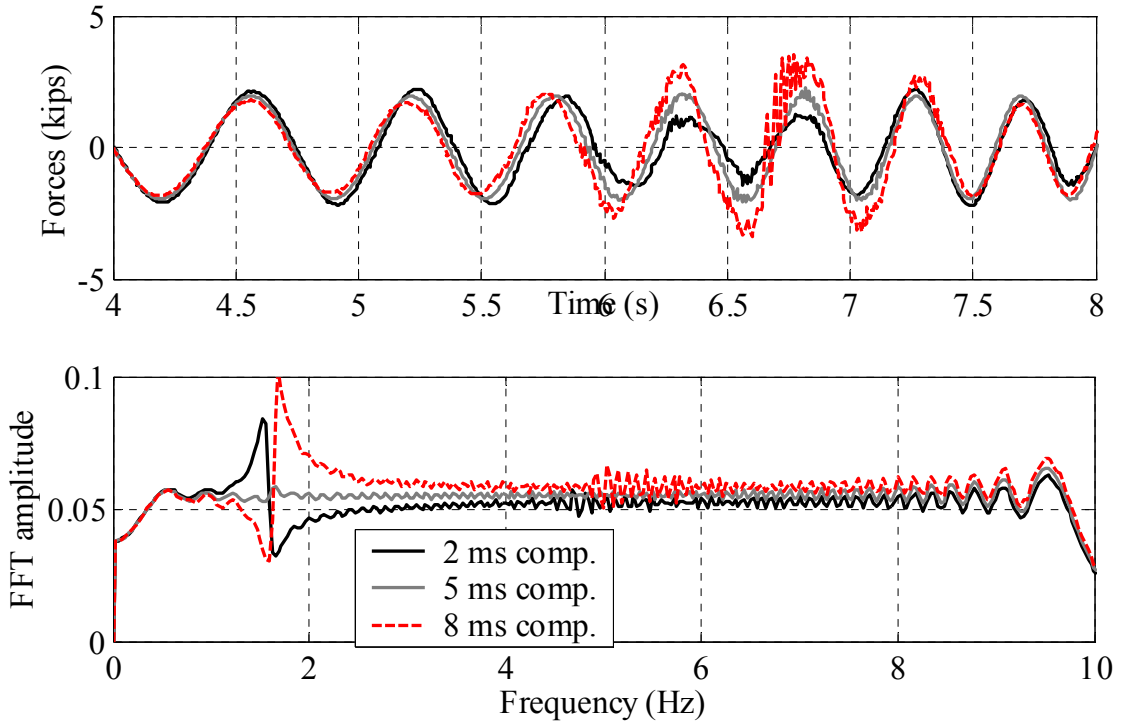

Figure 5.24 Response of the test system with nonlinear velocity feedback compensation (w/ various delay compensations) subjected to 2.0-kip sine wave sweep

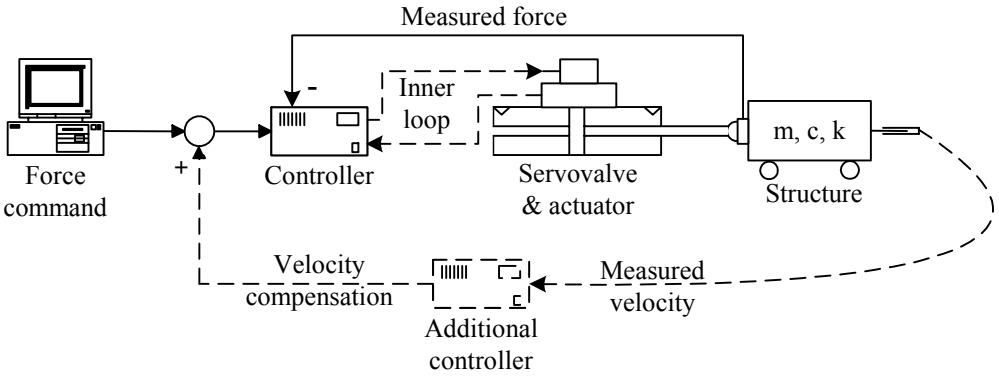

Figure 6.1 Schematic of the test system with velocity feedback compensation

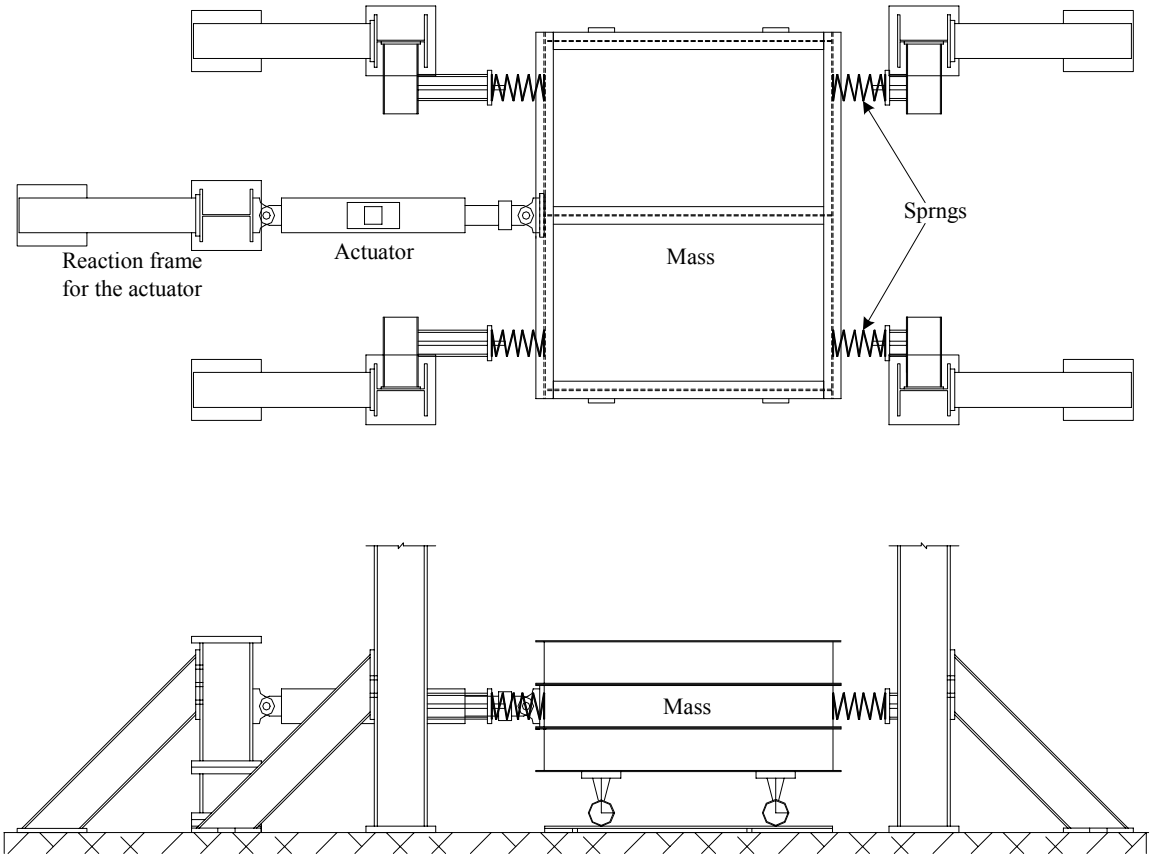

Figure 6.2 Schematic of the SDOF structural model with the actuator

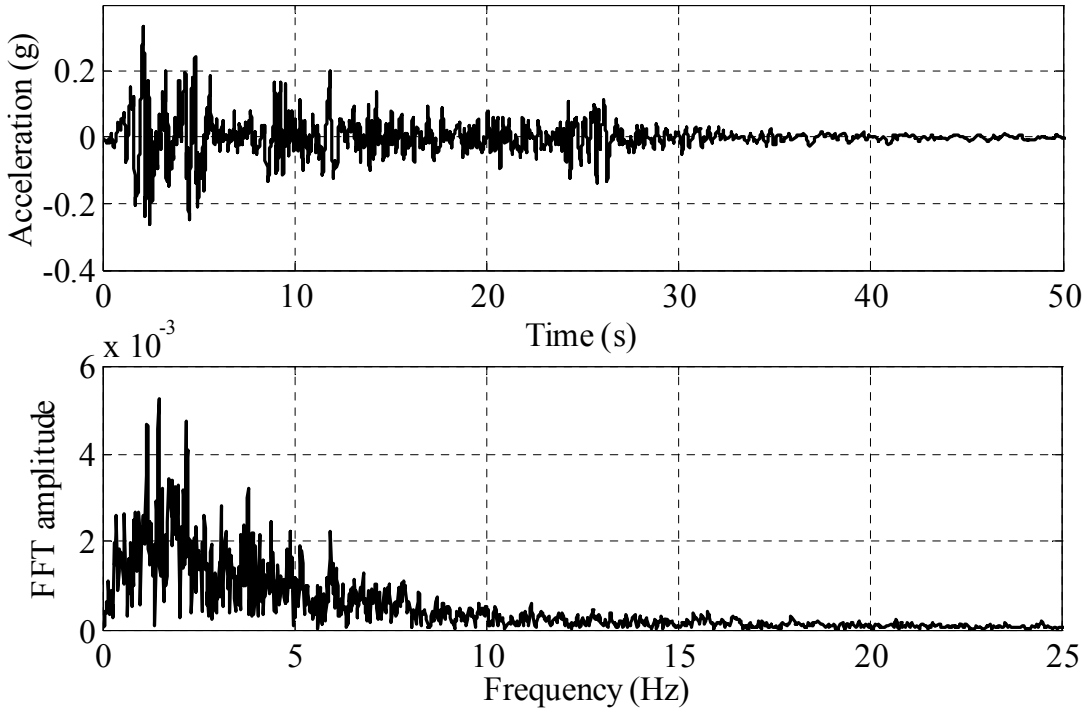

Figure 6.3 The 1940 Imperial Valley earthquake recorded at El Centro (N-S)

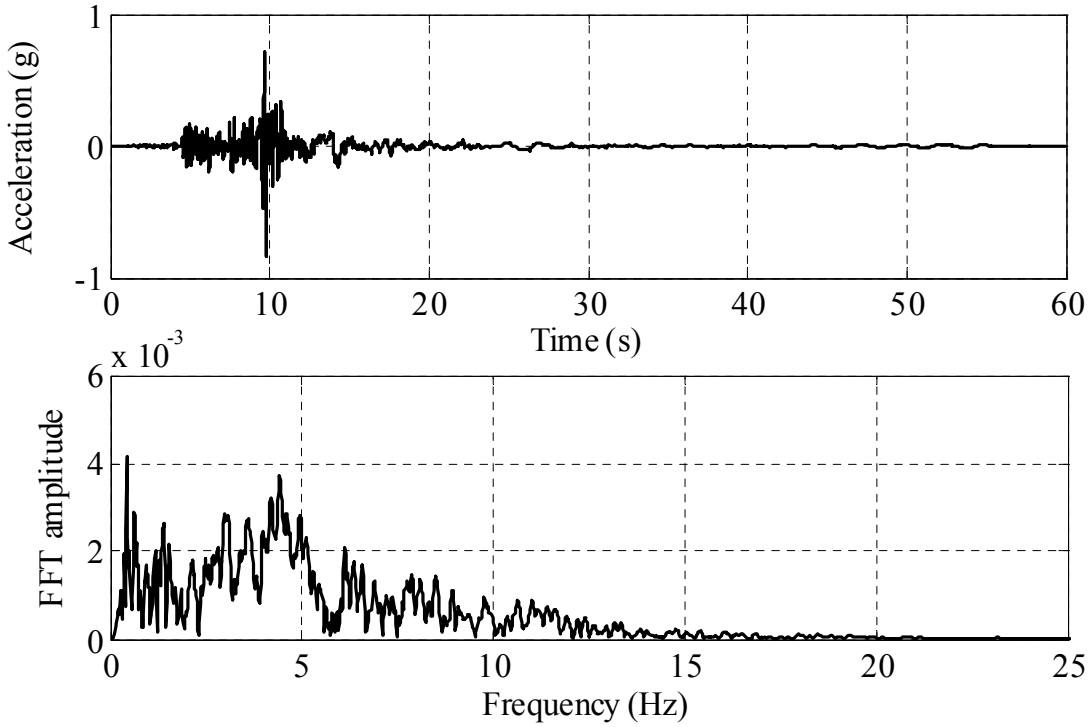

Figure 6.4 The 1994 Northridge earthquake recorded at Santa Monica City Hall (N-S)

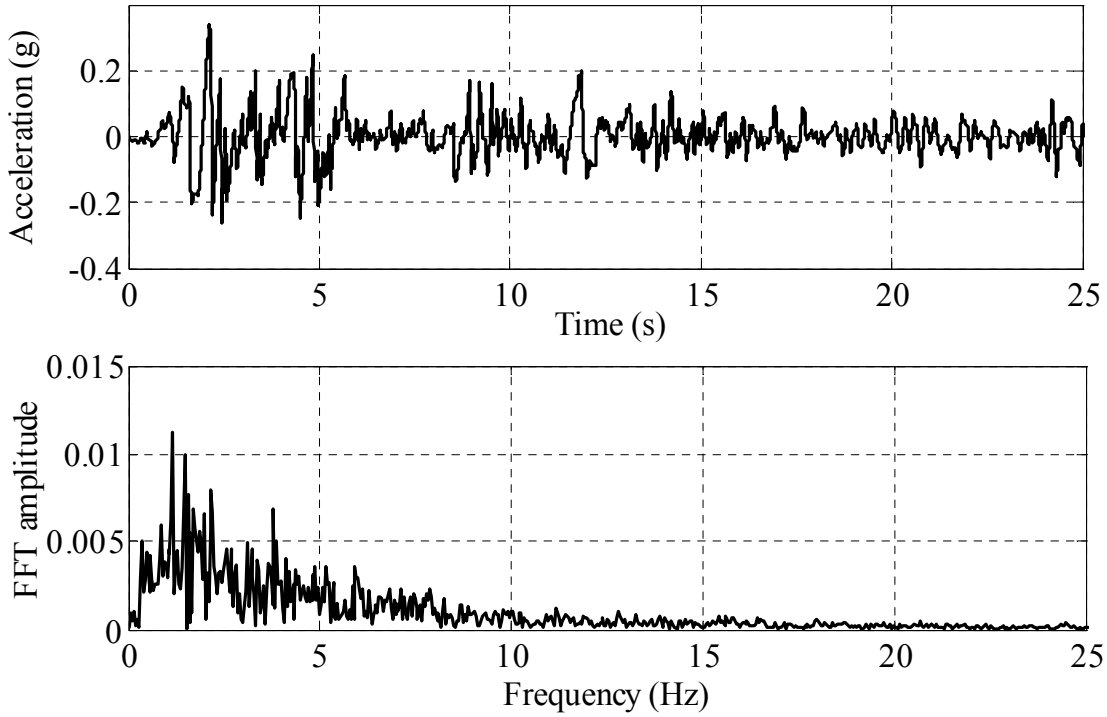

Figure 6.5 First 25 seconds of 1940 El Centro ground acceleration record

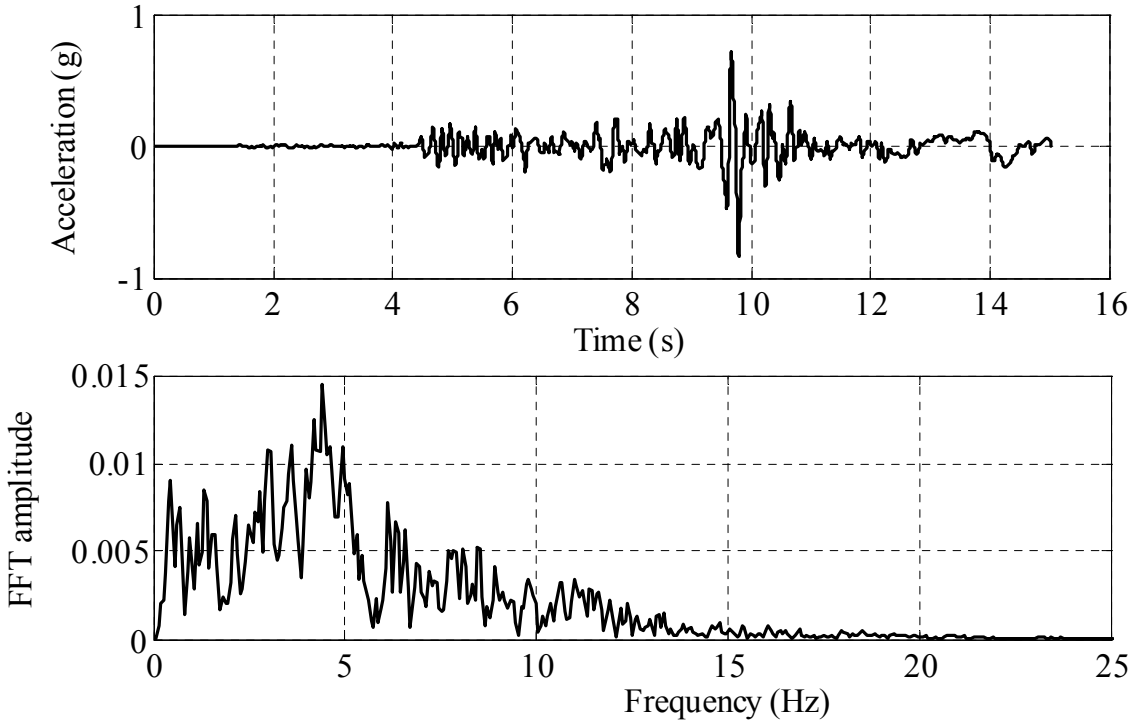

Figure 6.6 First 15 seconds of 1994 Northridge earthquake ground acceleration record

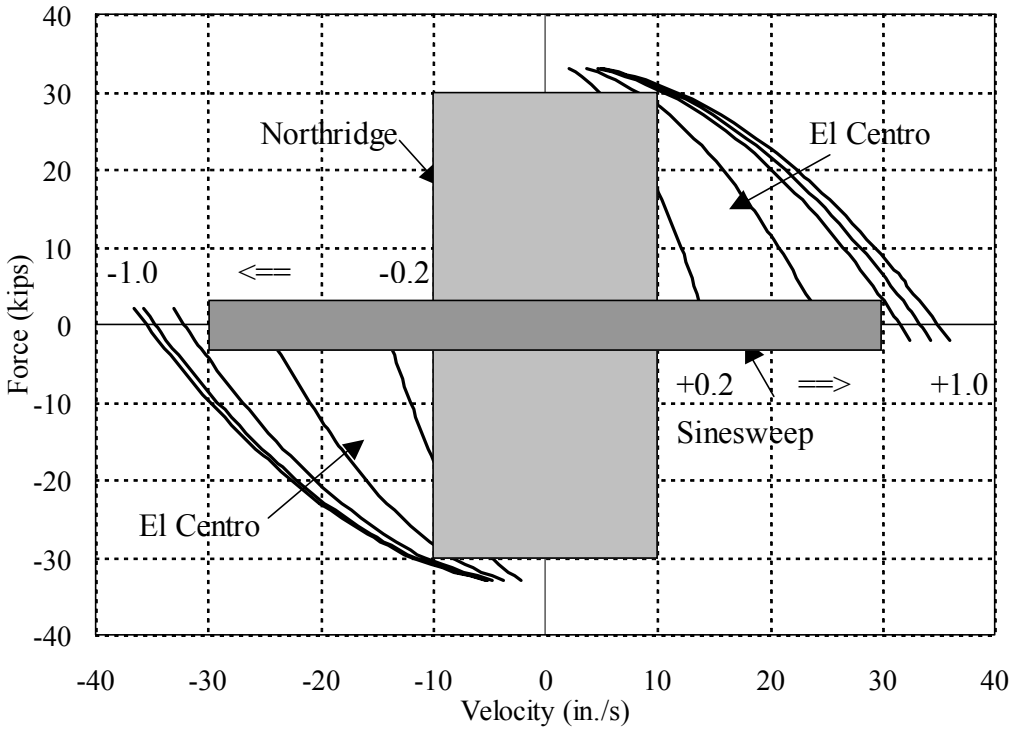

Figure 6.7 Force velocity curve for 35 kip actuator and 90 gpm servovalve with the choice of the ground accelerations

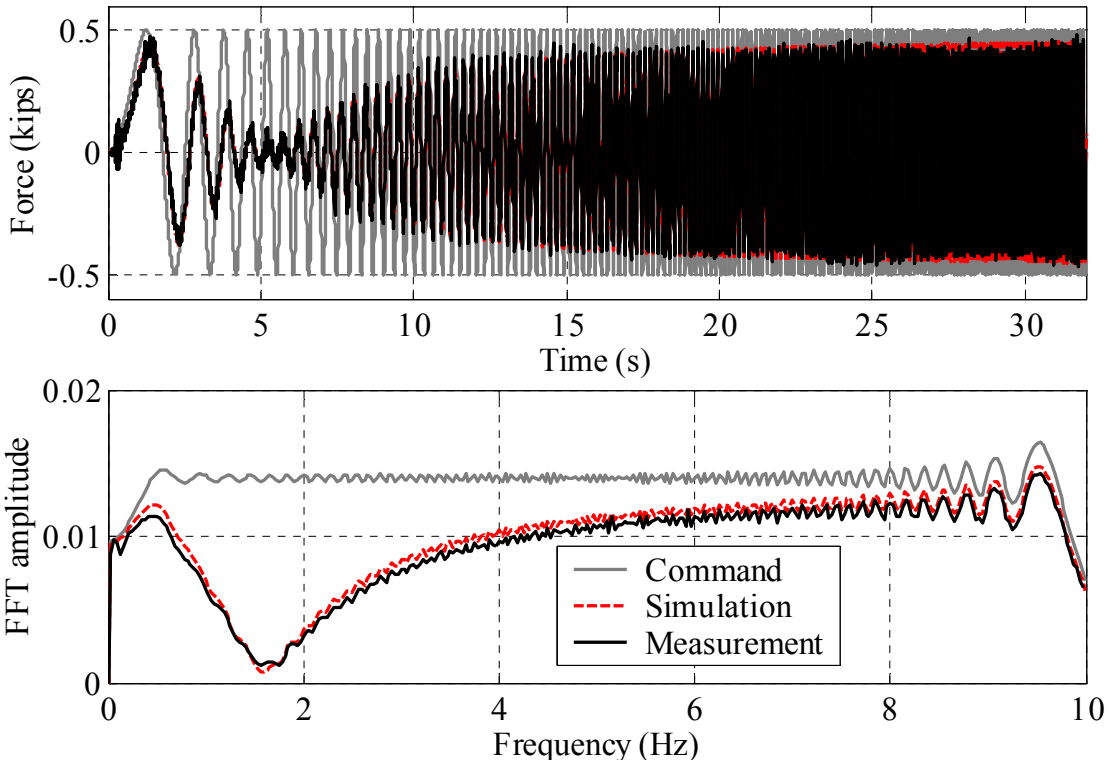

Figure 6.8 System responses with direct implementation of EFT using a 0.5k sinesweep input (force)

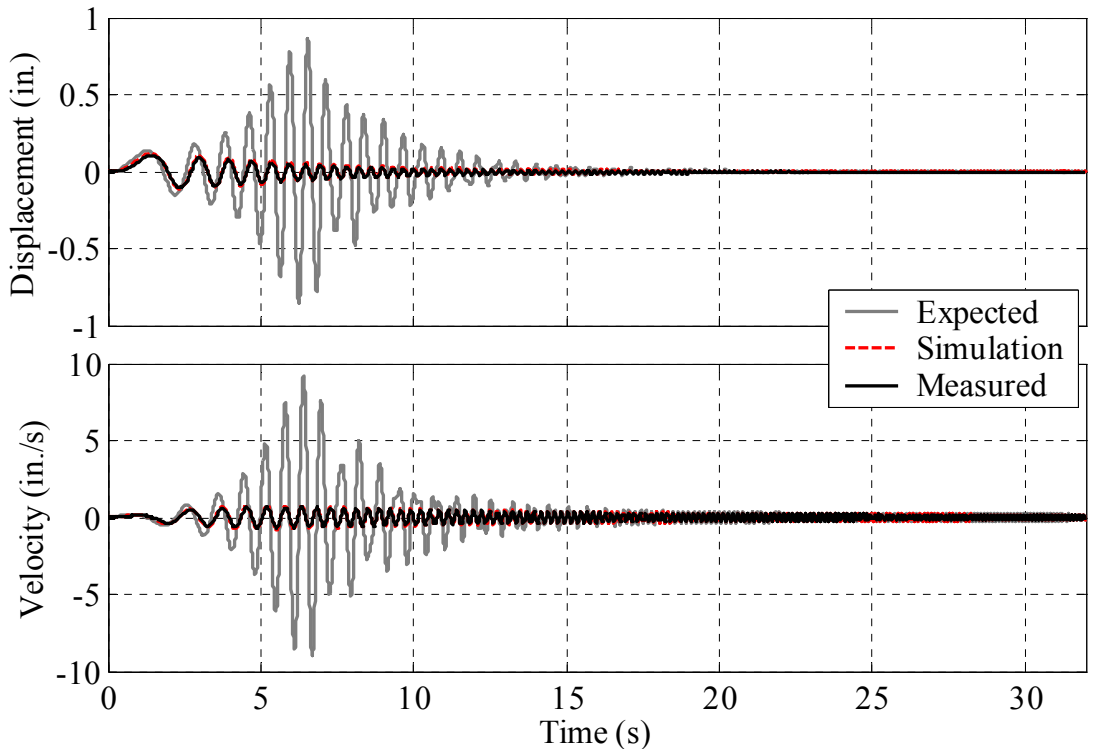

Figure 6.9 Structural responses with direct implementation of EFT using a 0.5k sinesweep input (displacement and velocity)

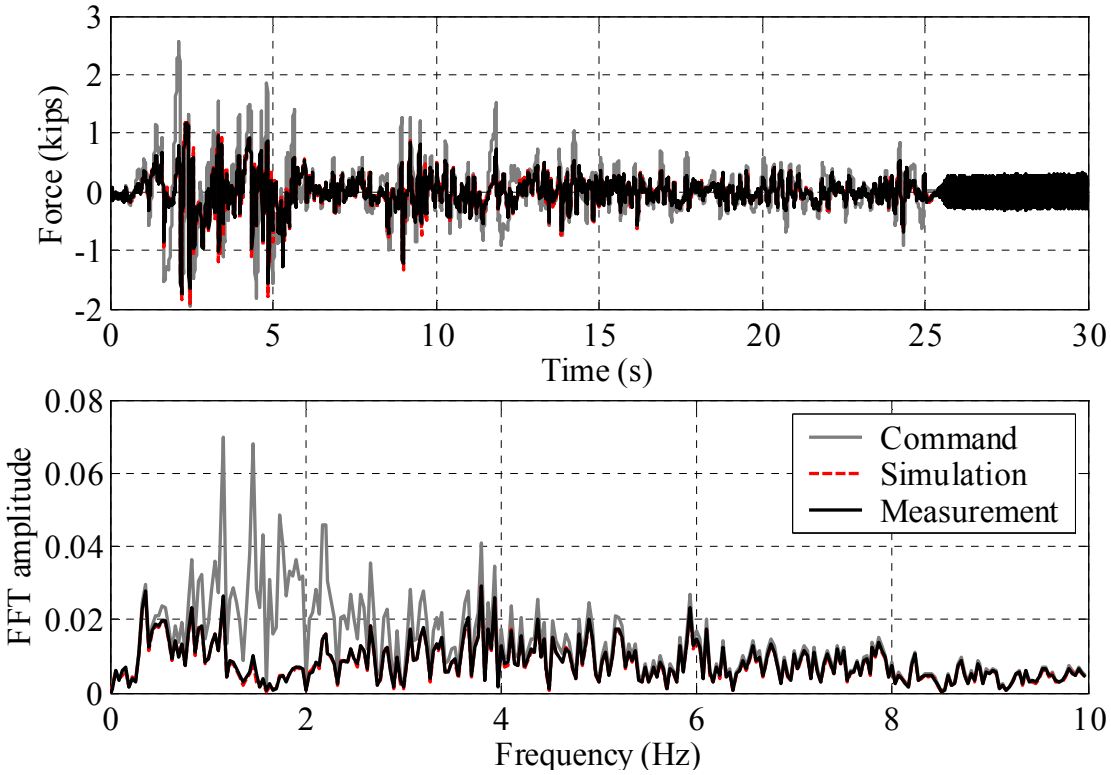

Figure 6.10 System responses with direct implementation of EFT using the El Centro earthquake ground acceleration, 0.17g (force)

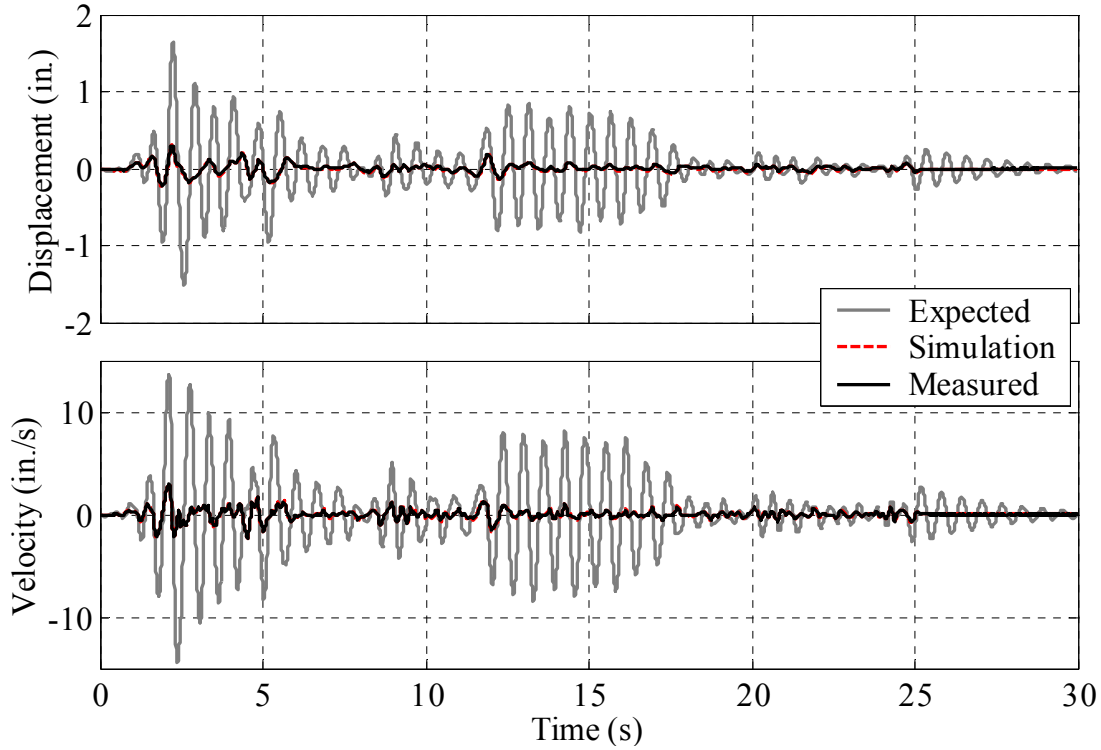

Figure 6.11 Structural responses with direct implementation of EFT using the El Centro earthquake ground acceleration, 0.17g (displacement and velocity)

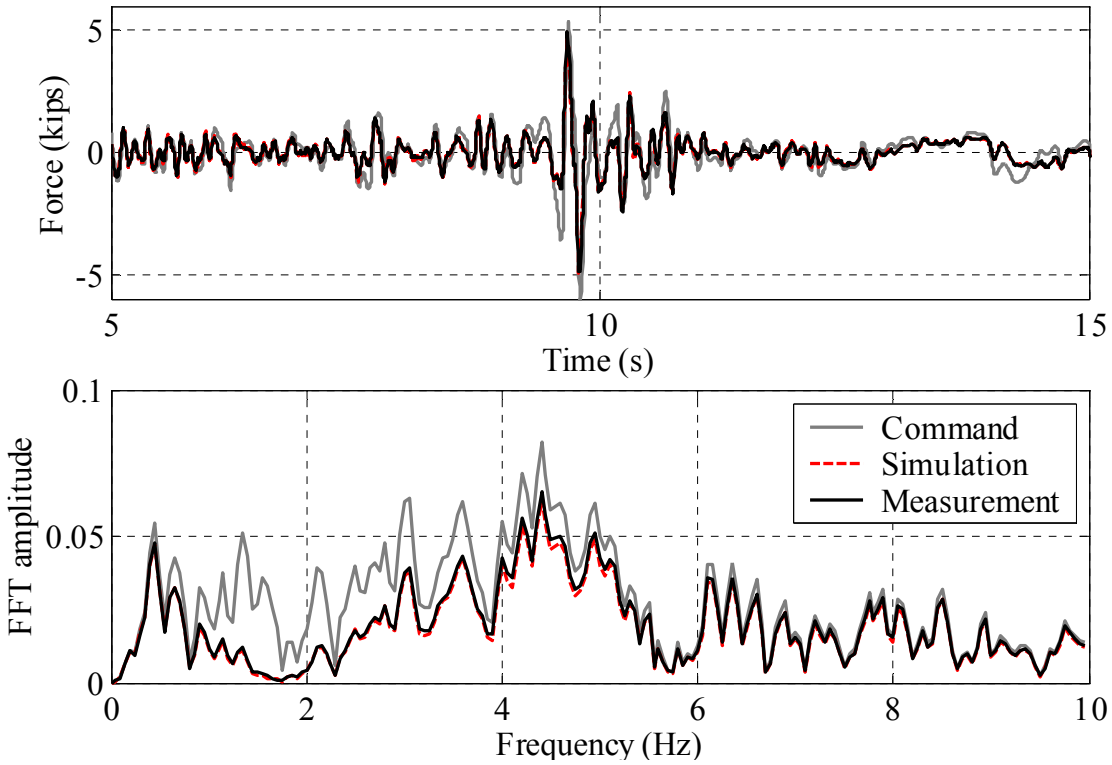

Figure 6.12 System responses with direct implementation of EFT using the Northridge earthquake ground acceleration, 0.42g (force)

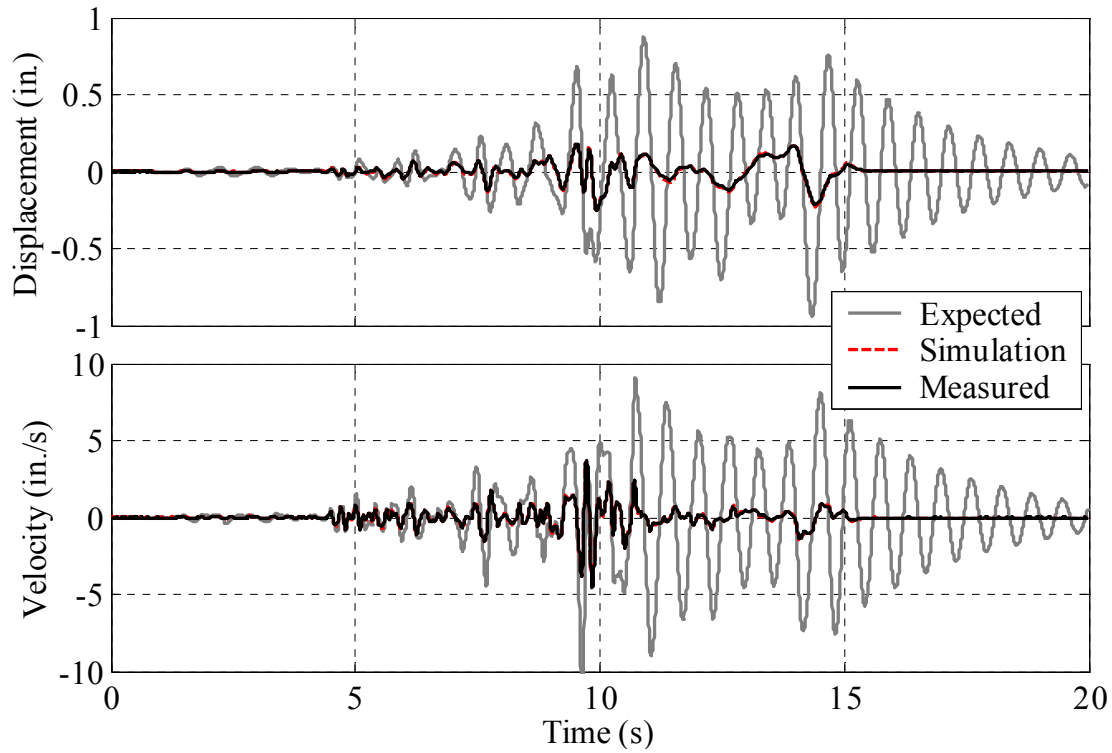

Figure 6.13 Structural responses with direct implementation of EFT using the Northridge earthquake ground acceleration, 0.42g (displacement and velocity)

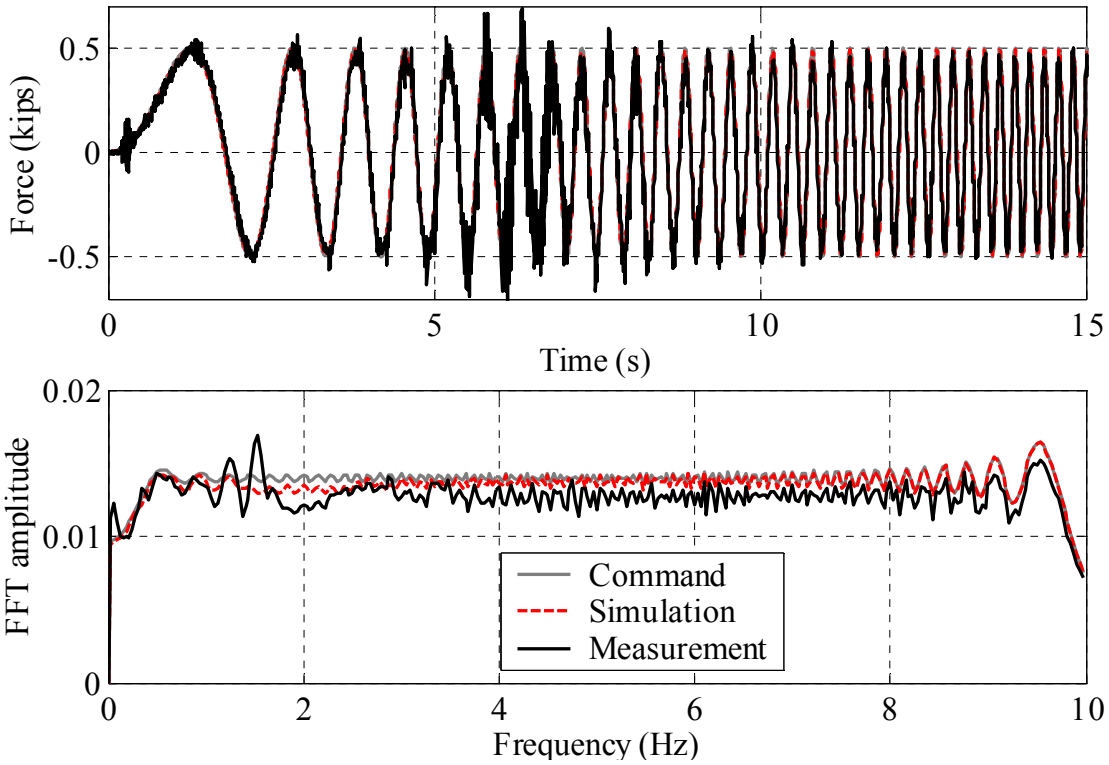

Figure 6.14 System responses with digital linear velocity feedback compensation using a 0.5k sinesweep input (force)

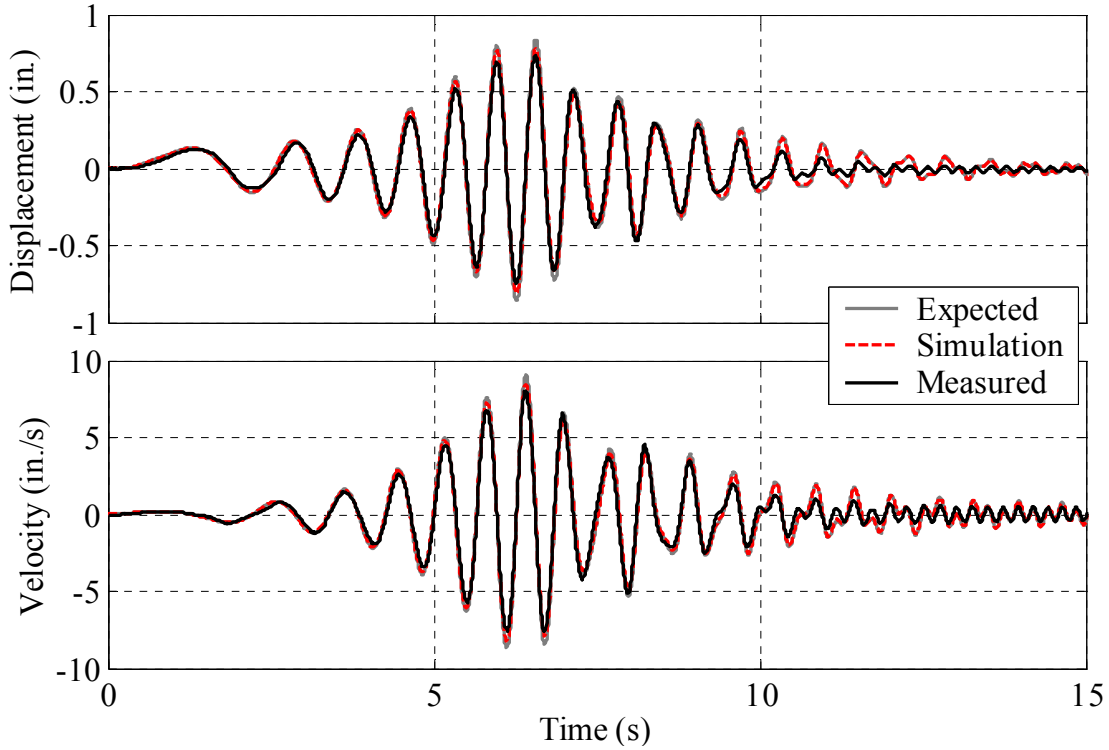

Figure 6.15 Structural responses with digital linear velocity feedback compensation using a 0.5k sinesweep input (displacement and velocity)

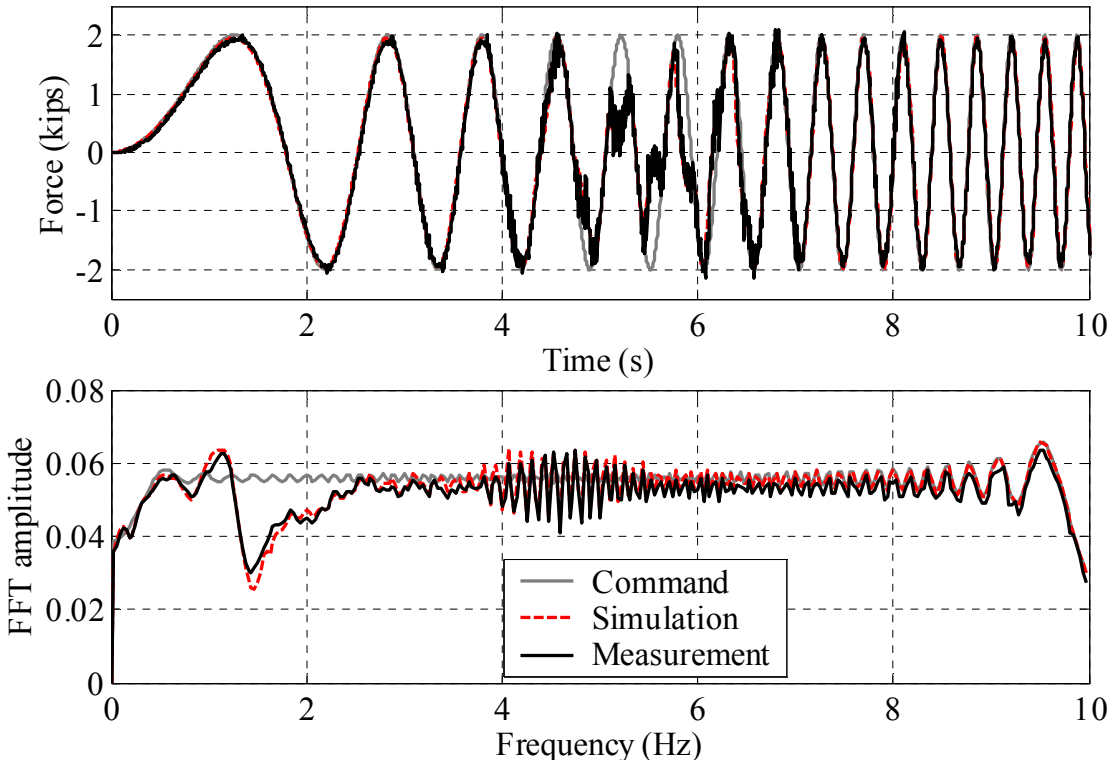

Figure 6.16 System responses with digital linear velocity feedback compensation using a 2.0k sinesweep input (force)

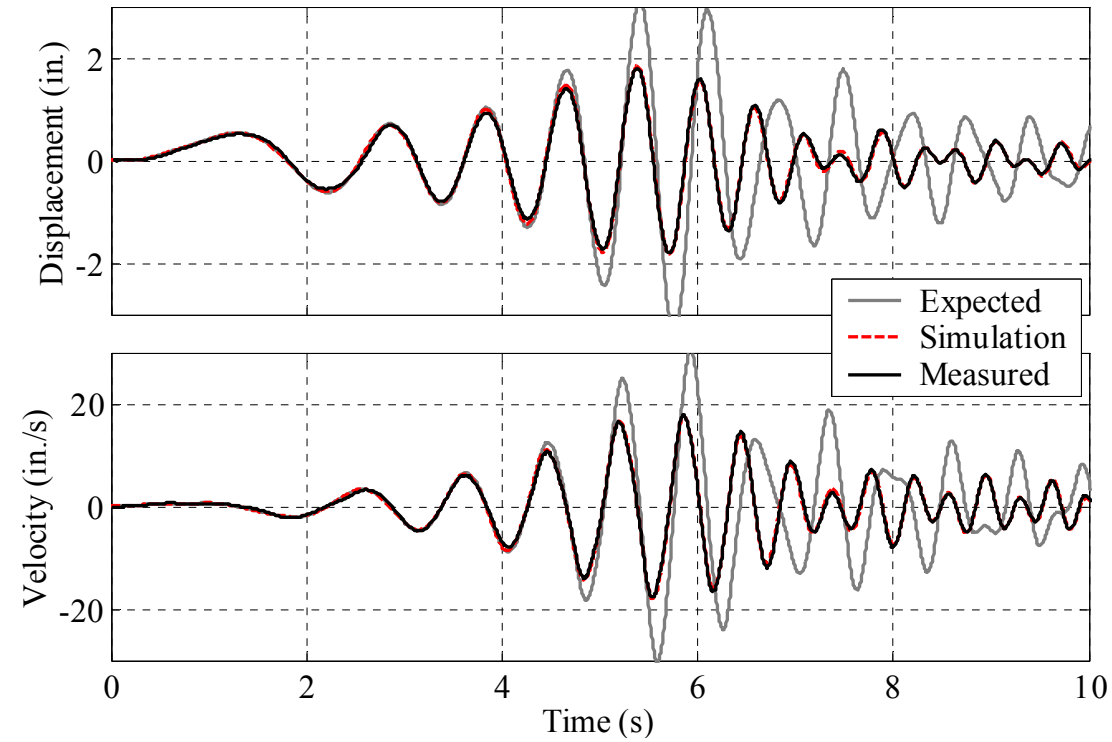

Figure 6.17 Structural responses with digital linear velocity feedback compensation using a 2.0k sinesweep input (displacement and velocity)

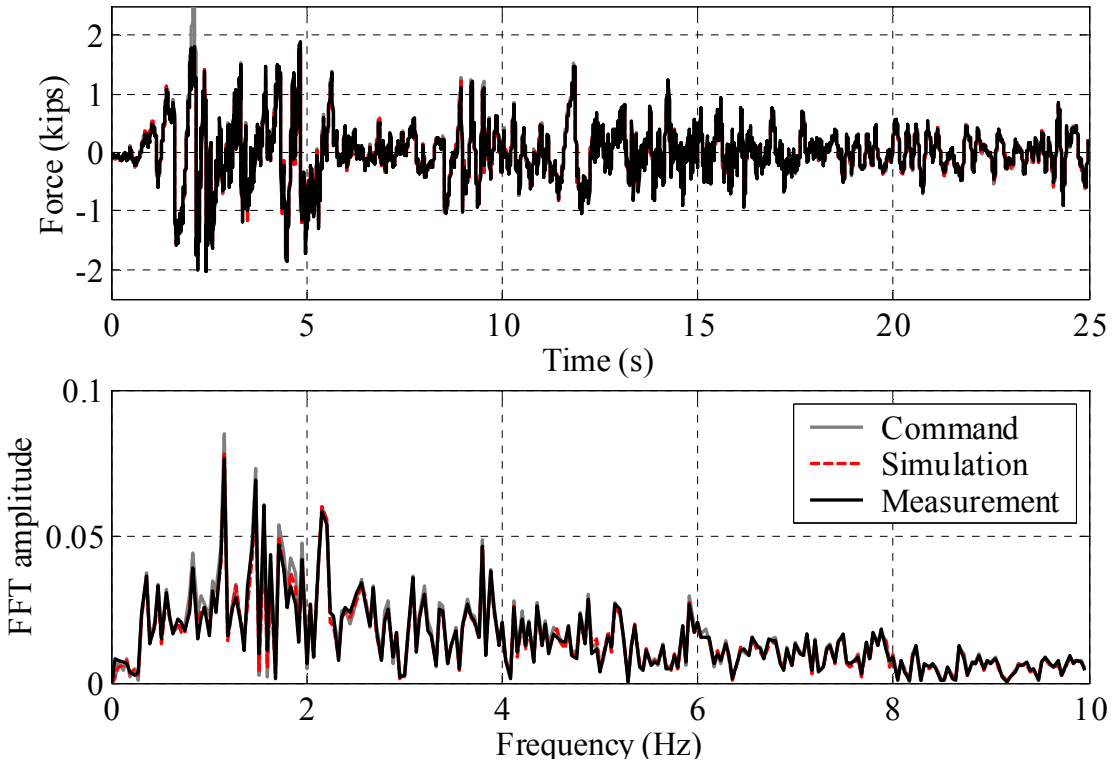

Figure 6.18 System responses with linear velocity feedback compensation using the El Centro earthquake ground acceleration, 0.17g (force)

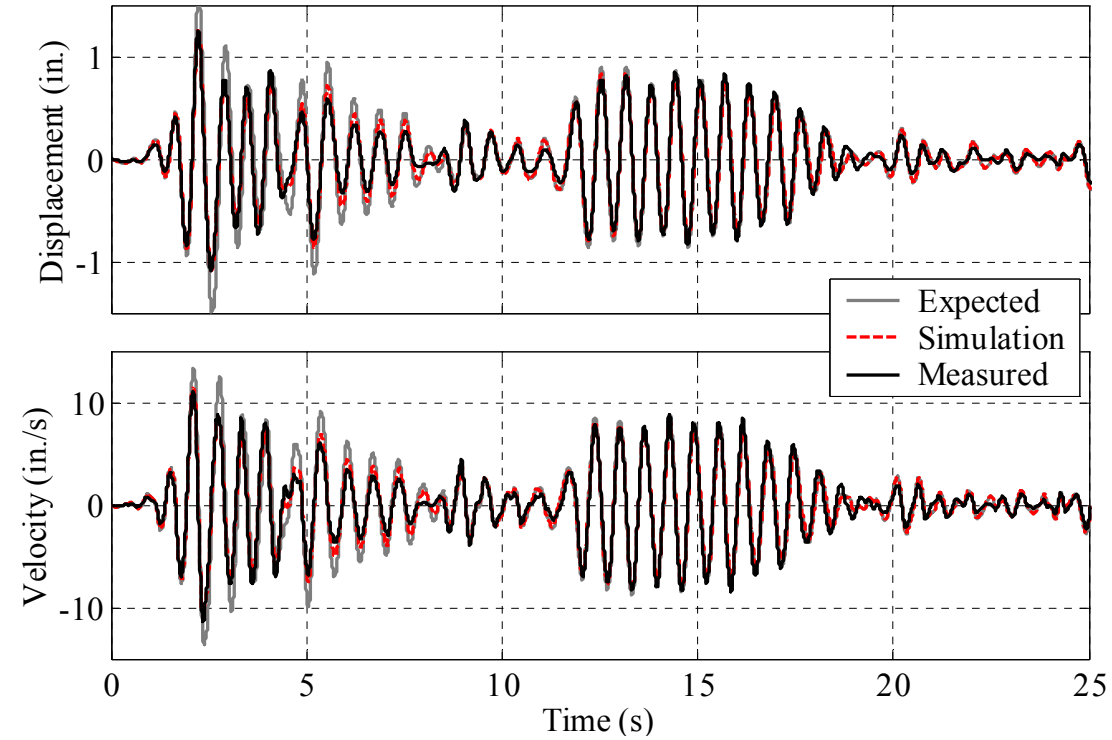

Figure 6.19 Structural responses with linear velocity feedback compensation using the El Centro earthquake ground acceleration, 0.17g (displacement and velocity)

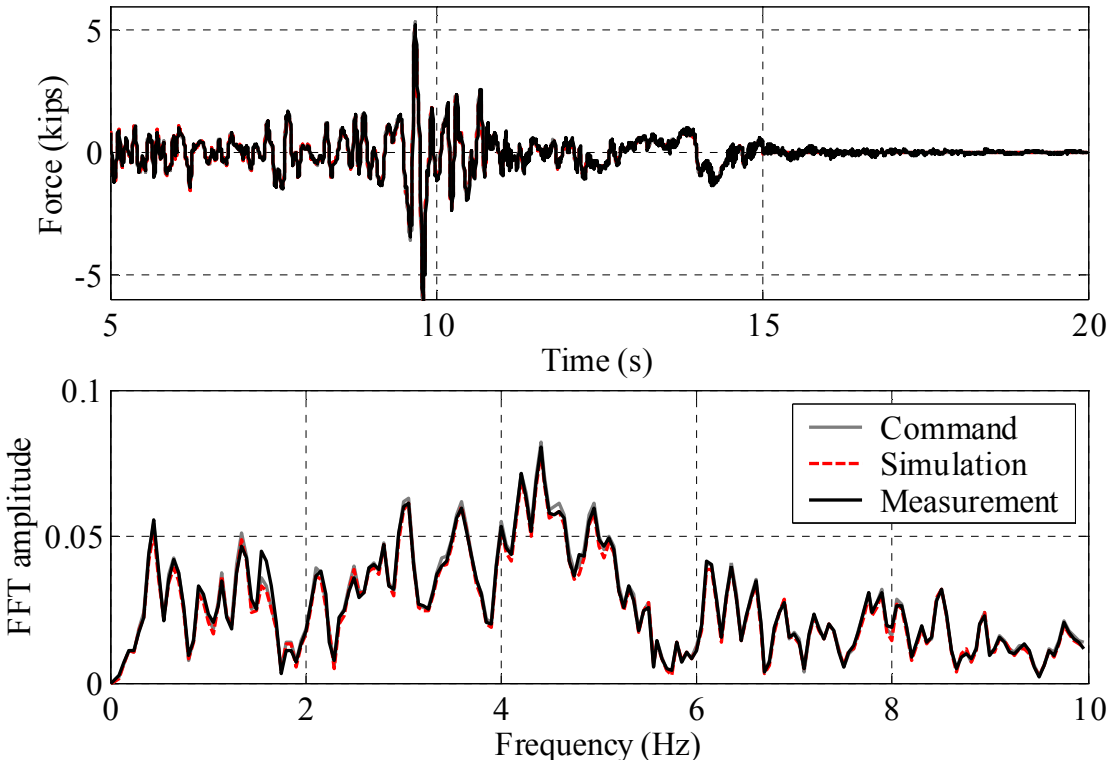

Figure 6.20 System responses with linear velocity feedback compensation using the Northridge earthquake ground acceleration, 0.42g (force)

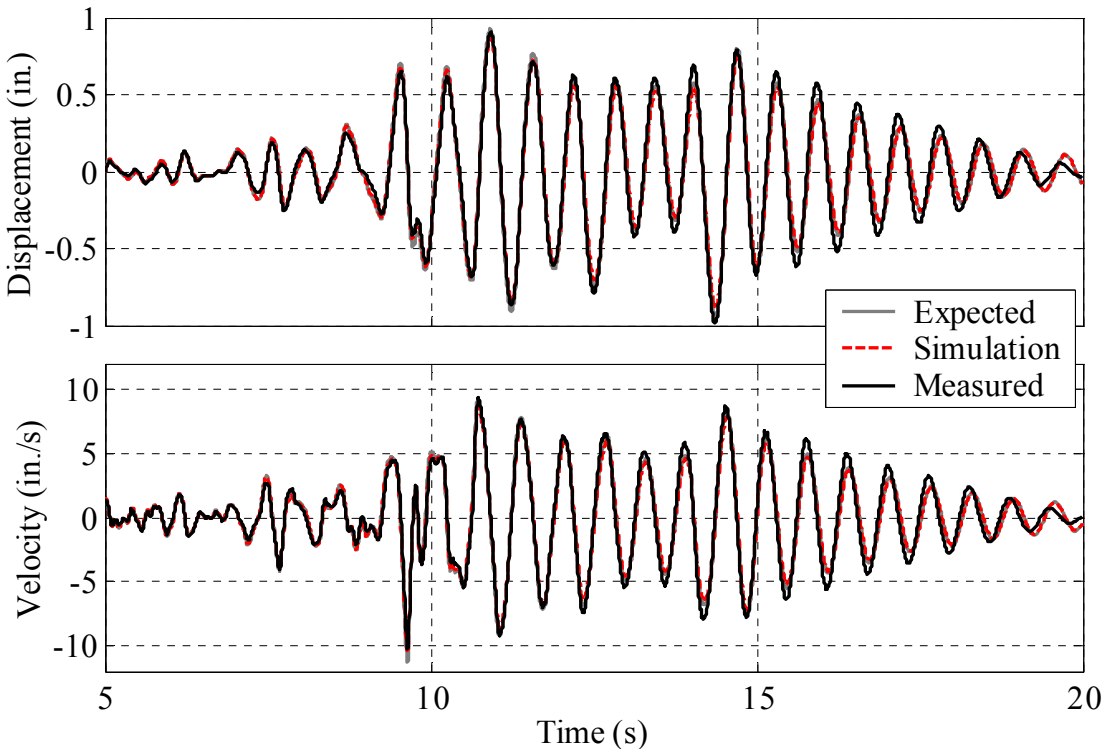

Figure 6.21 Structural responses with linear velocity feedback compensation using the Northridge earthquake ground acceleration, 0.42g (displacement and velocity)

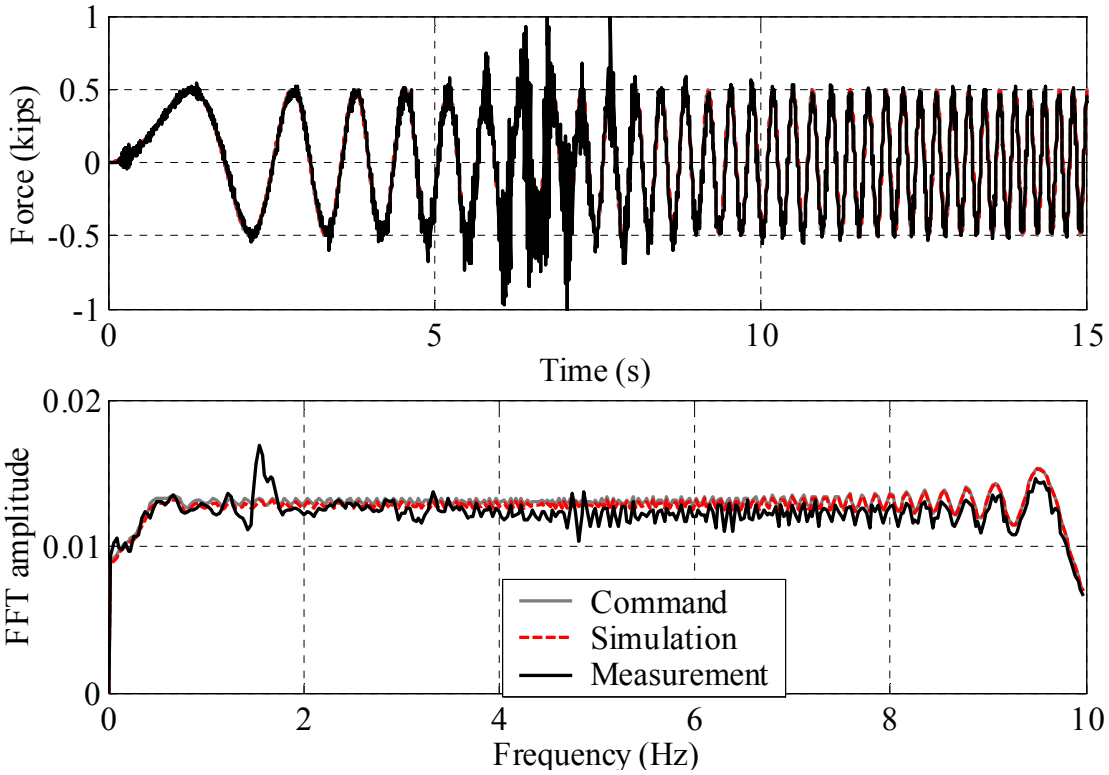

Figure 6.22 System responses with nonlinear velocity feedback compensation using a 0.5k sinesweep input (force)

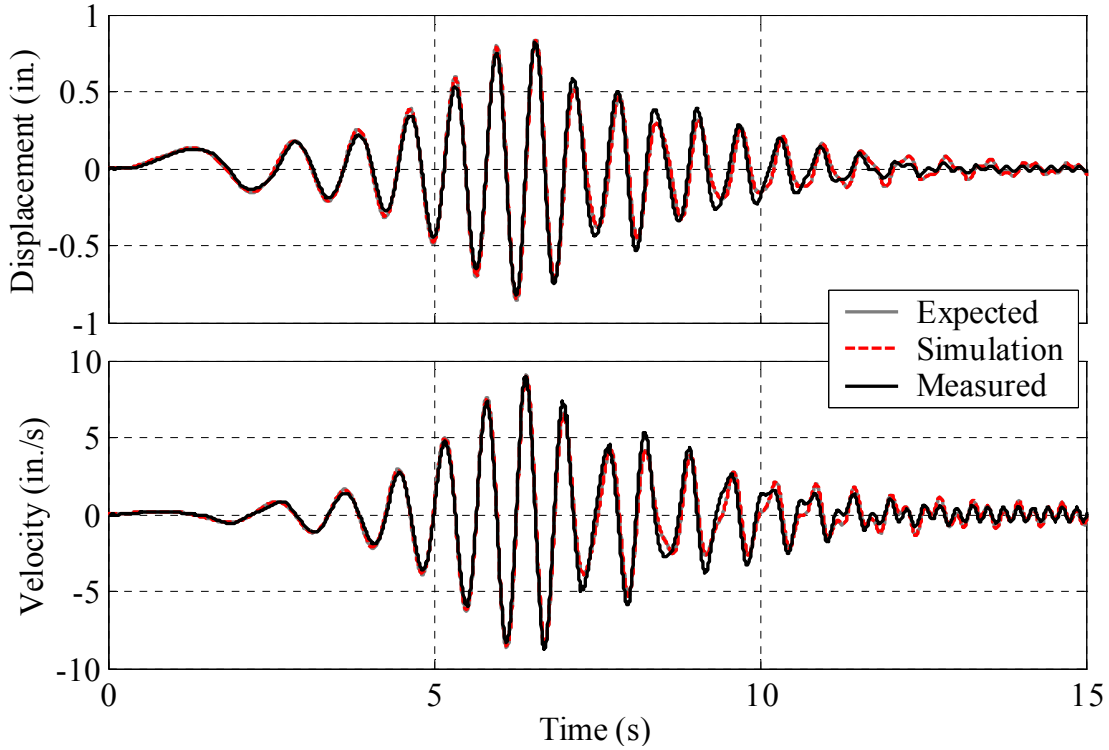

Figure 6.23 Structural responses with nonlinear velocity feedback compensation using a 0.5k sinesweep input (displacement and velocity)

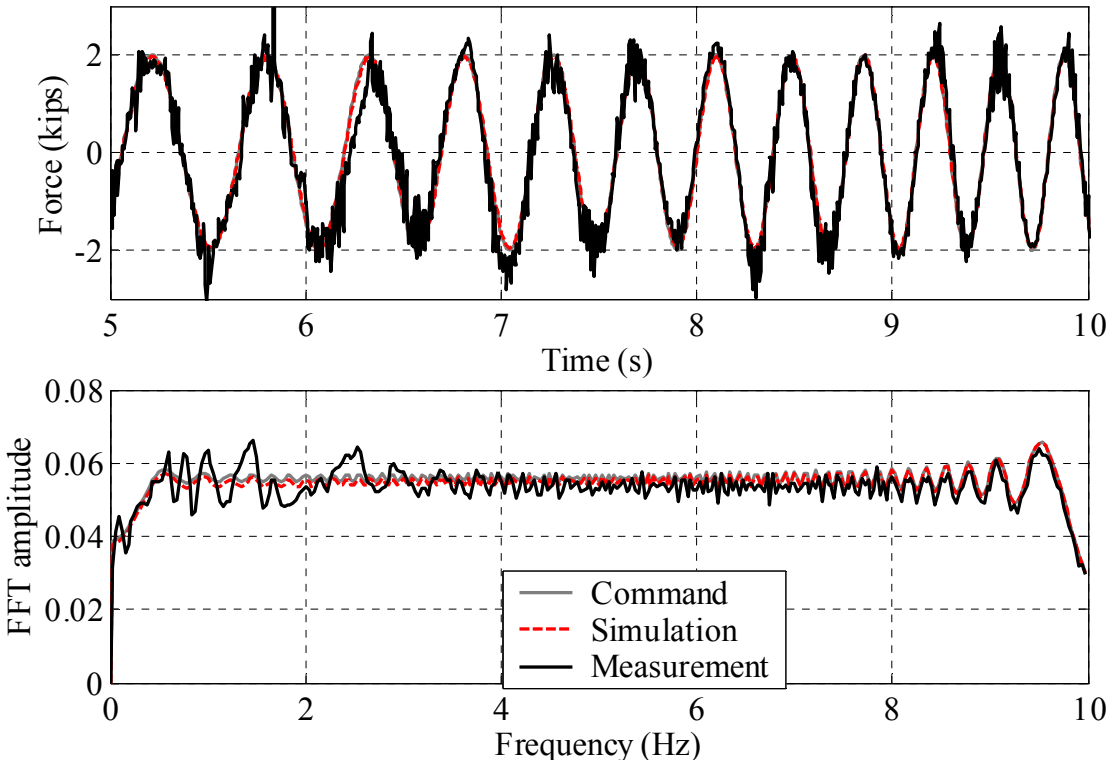

Figure 6.24 System responses with nonlinear velocity feedback compensation using a 2.0k sinesweep input (force)

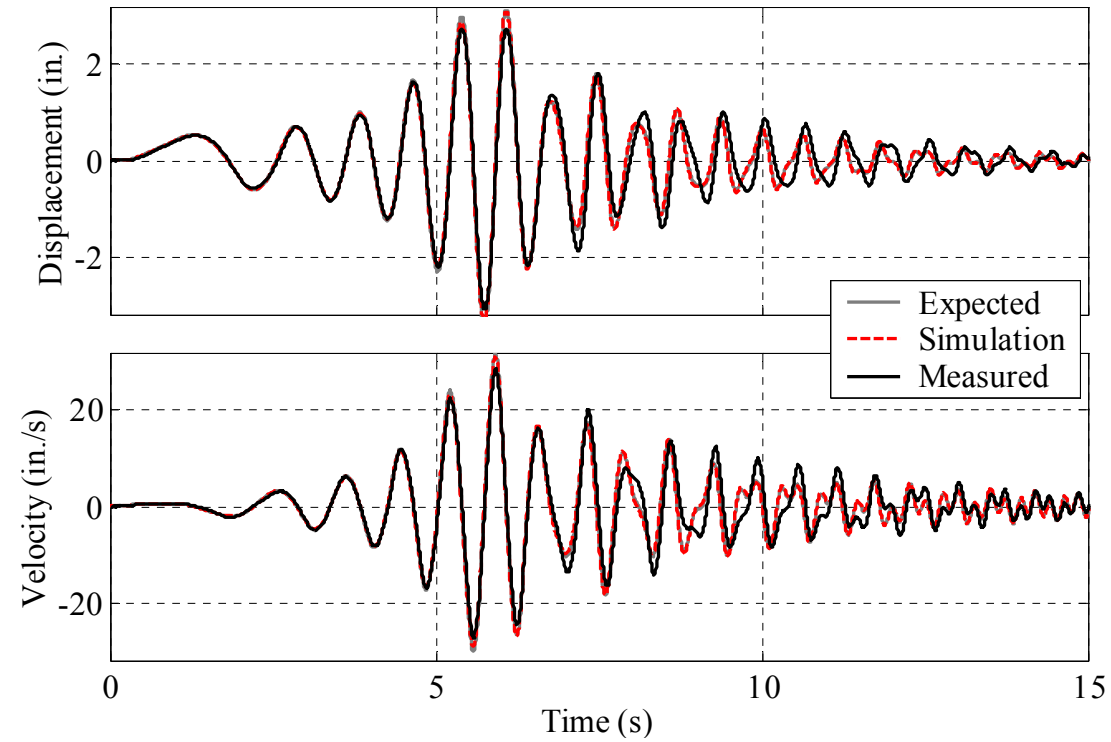

Figure 6.25 Structural responses with nonlinear velocity feedback compensation using a 2.0k sinesweep input (displacement and velocity)

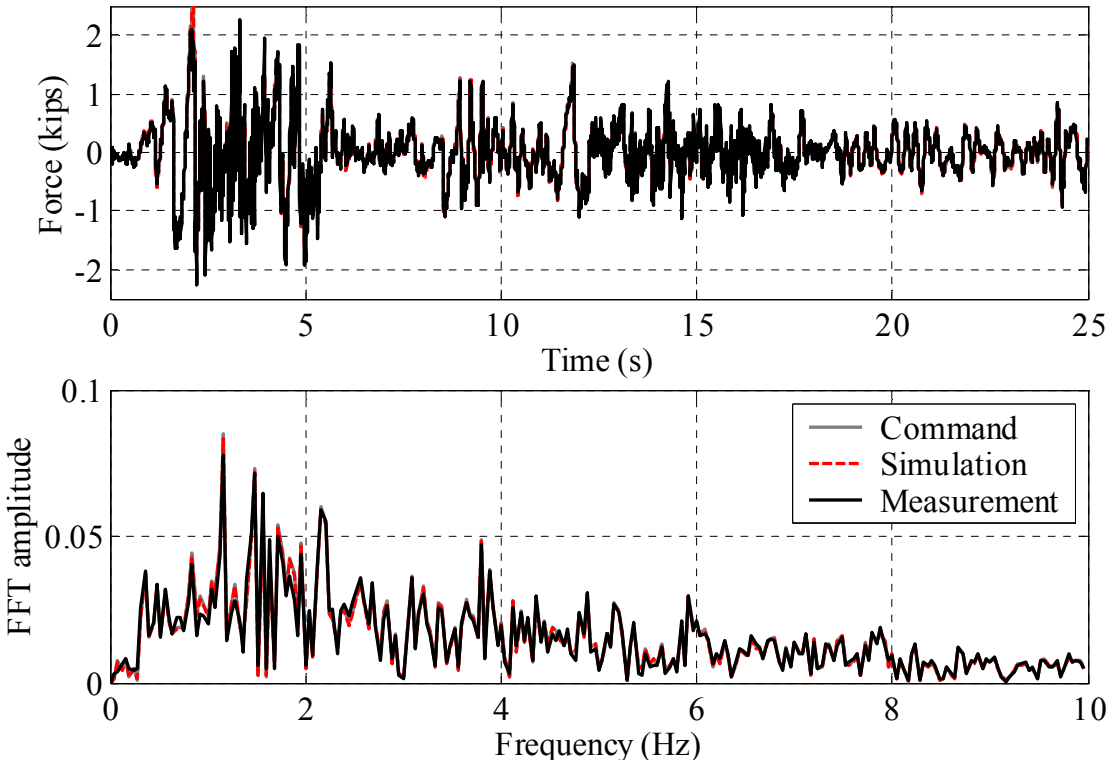

Figure 6.26 System responses with nonlinear velocity feedback compensation using the El Centro earthquake ground acceleration, 0.17g (force)

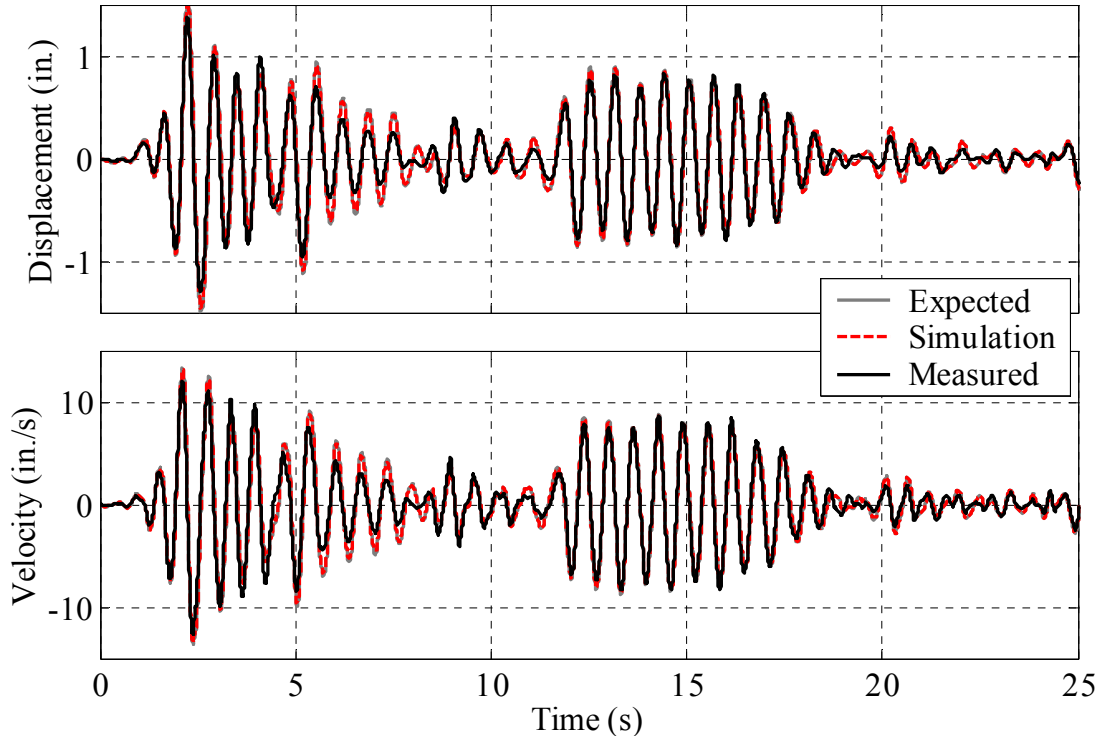

Figure 6.27 Structural responses with nonlinear velocity feedback compensation using the El Centro earthquake ground acceleration, 0.17g (displacement and velocity)

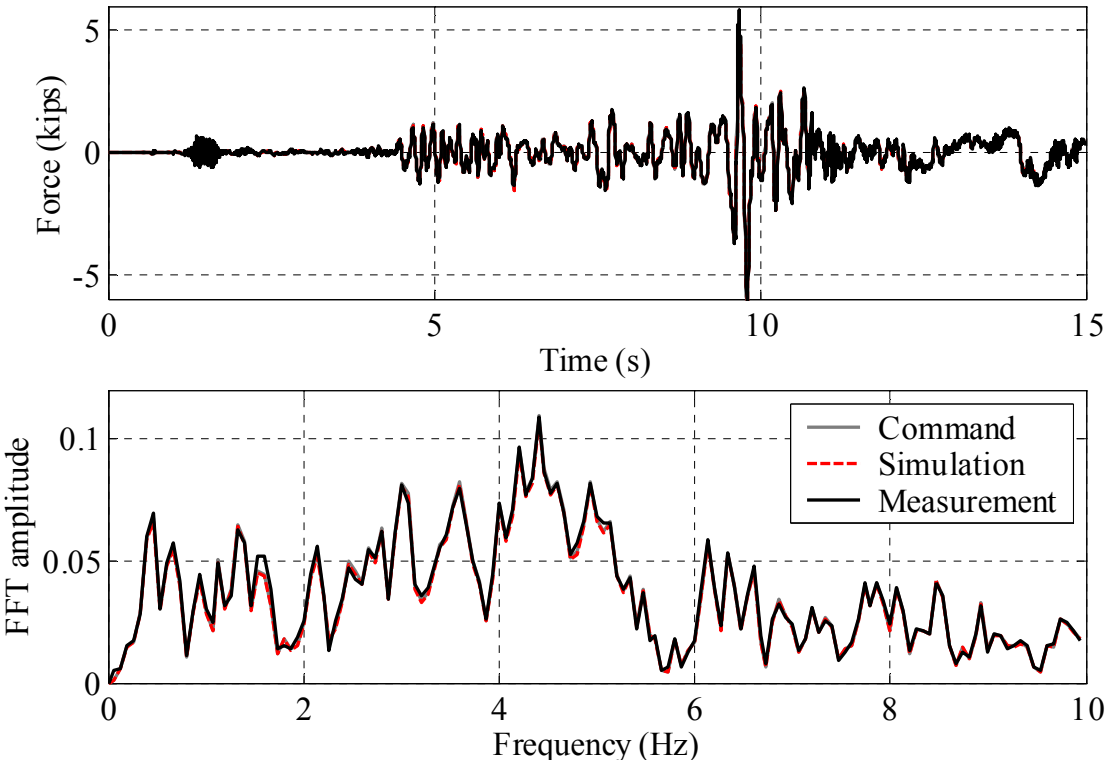

Figure 6.28 System responses with nonlinear velocity feedback compensation using the Northridge earthquake ground acceleration, 0.42g (force)

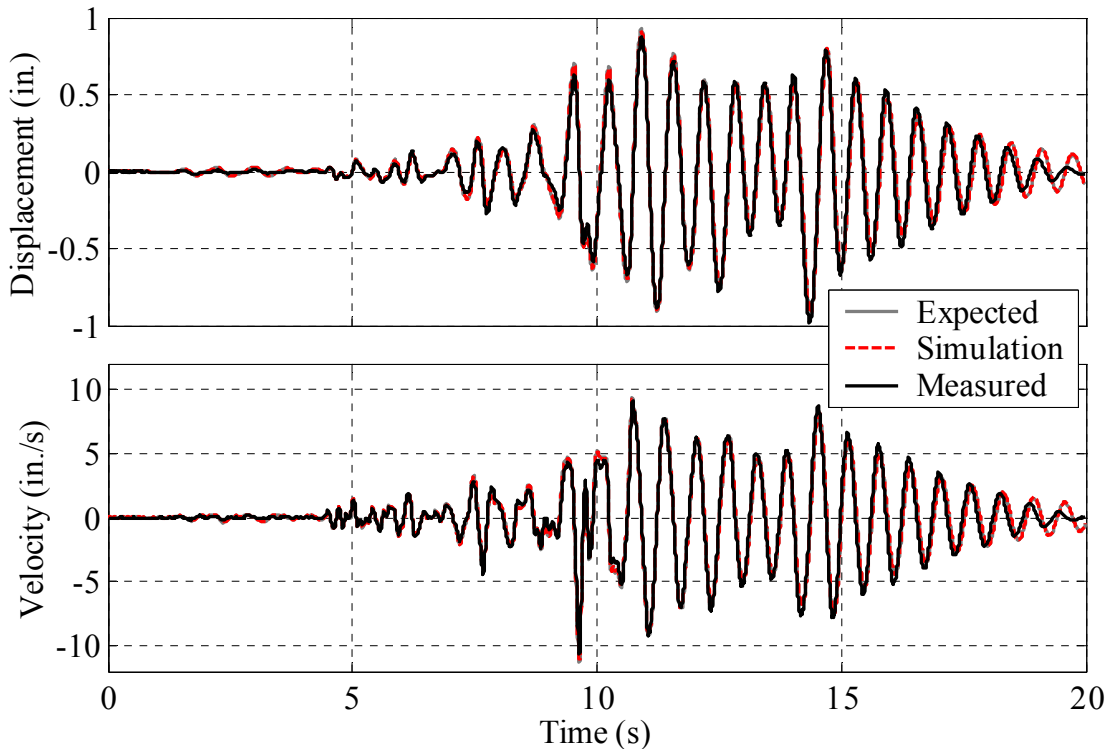

Figure 6.29 Structural responses with nonlinear velocity feedback compensation using the Northridge earthquake ground acceleration, 0.42g (displacement and velocity)

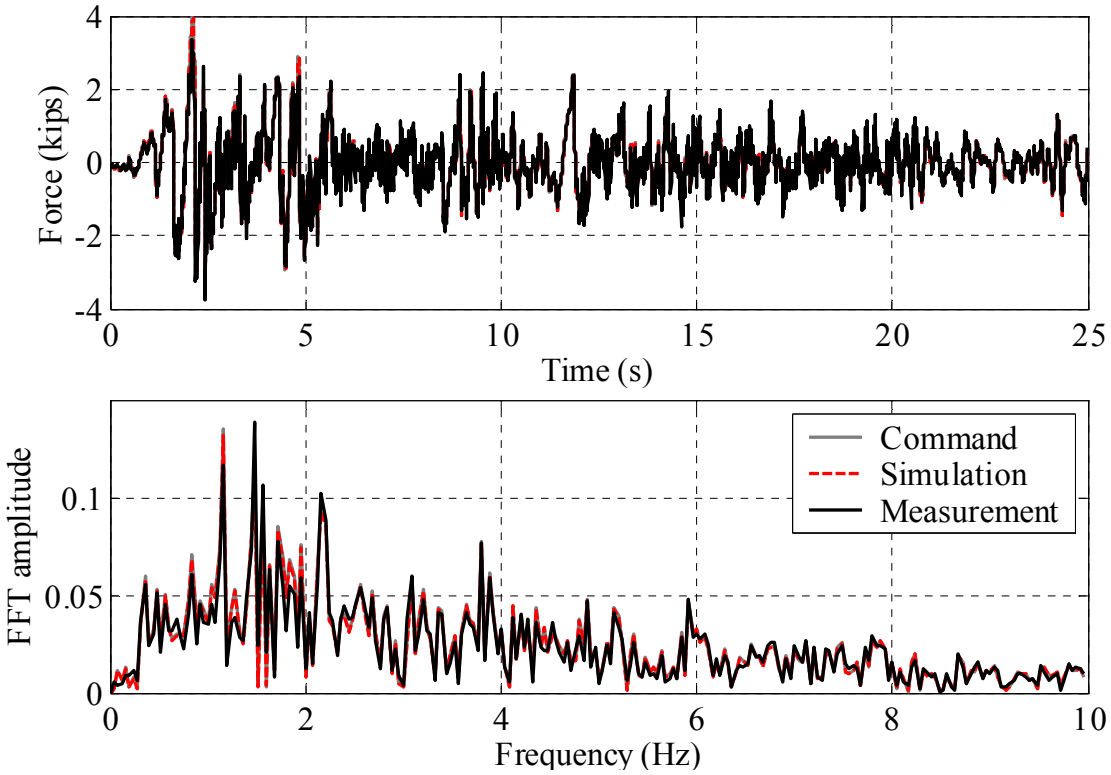

Figure 6.30 System responses with nonlinear velocity feedback compensation using the El Centro earthquake ground acceleration, 0.27g (force)

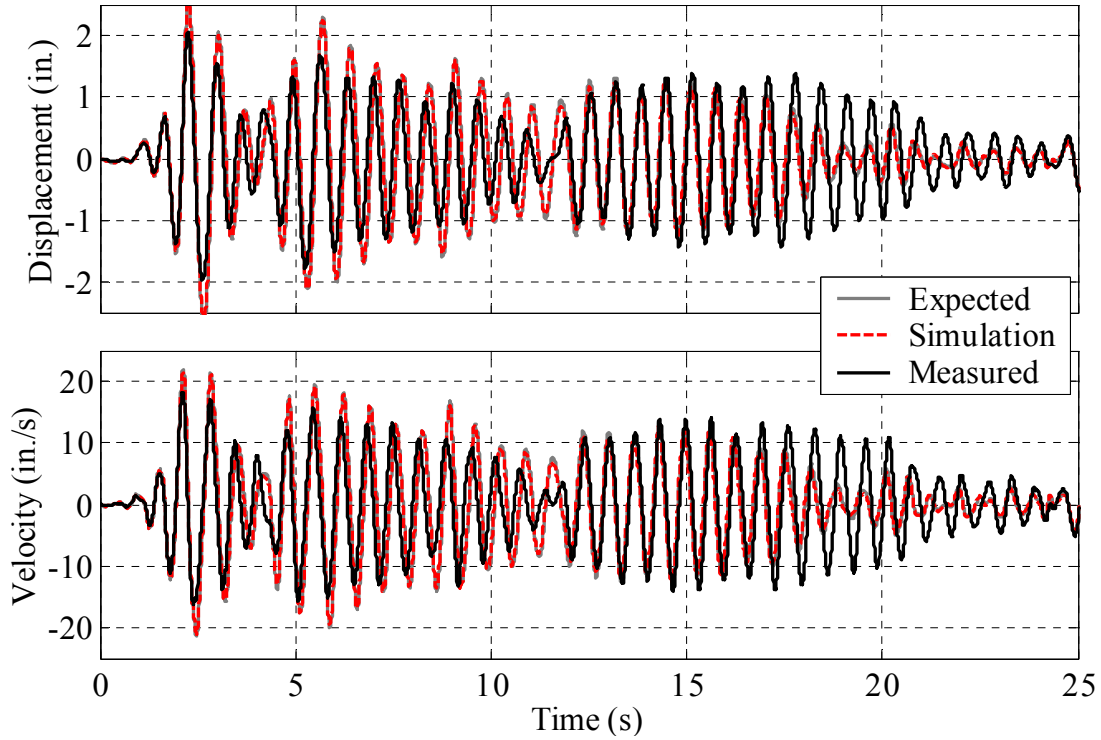

Figure 6.31 Structural responses with nonlinear velocity feedback compensation using the El Centro earthquake ground acceleration, 0.27g (displacement and velocity)

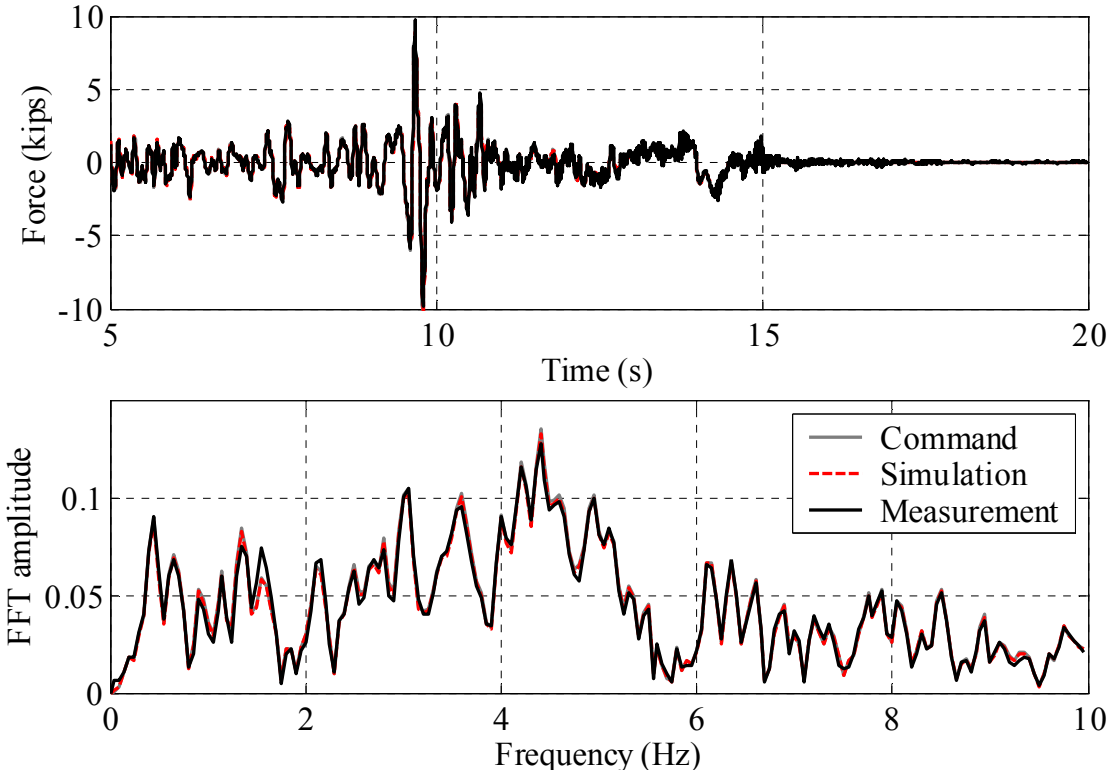

Figure 6.32 System responses with nonlinear velocity feedback compensation using the Northridge earthquake ground acceleration, 0.67g (force)

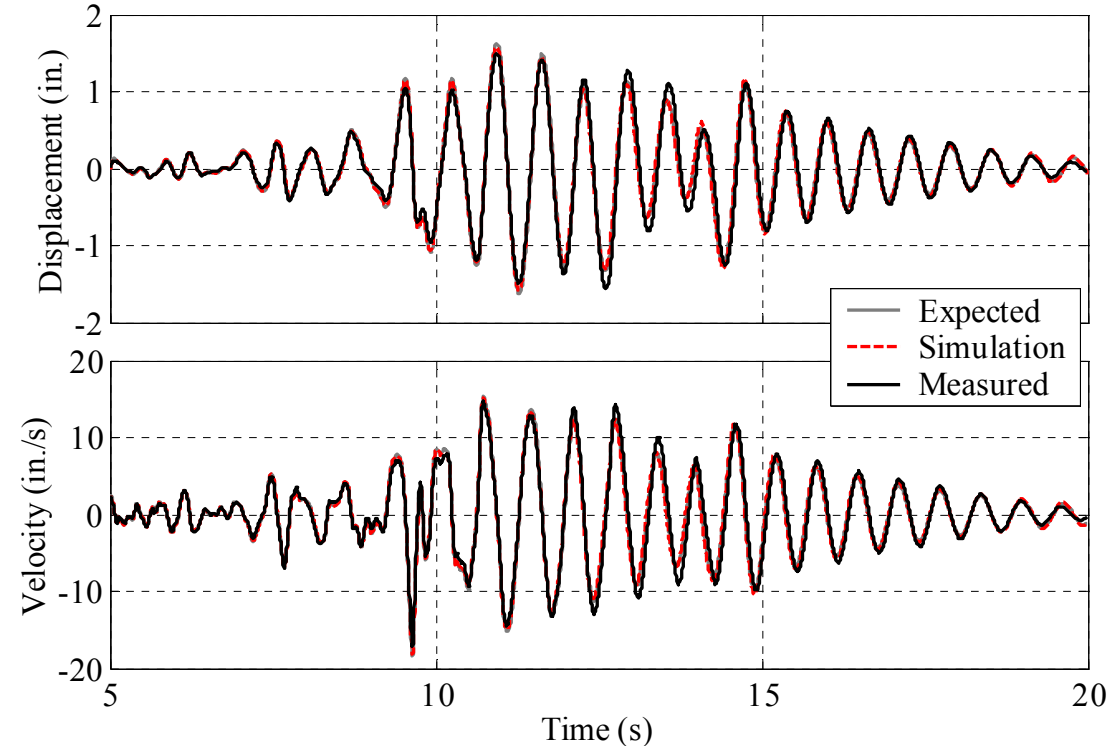

Figure 6.33 Structural responses with nonlinear velocity feedback compensation using the Northridge earthquake ground acceleration, 0.67g (displacement and velocity)

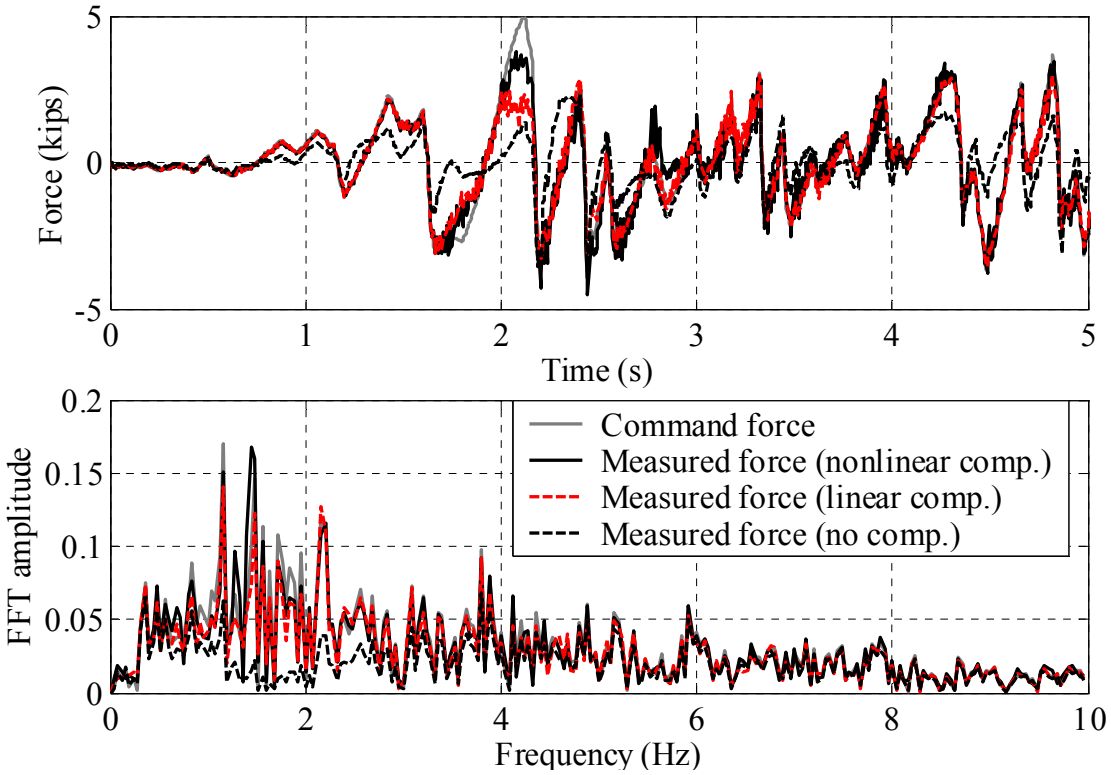

Figure 6.34 Comparison of system responses using the El Centro earthquake ground acceleration, 0.34g (force)

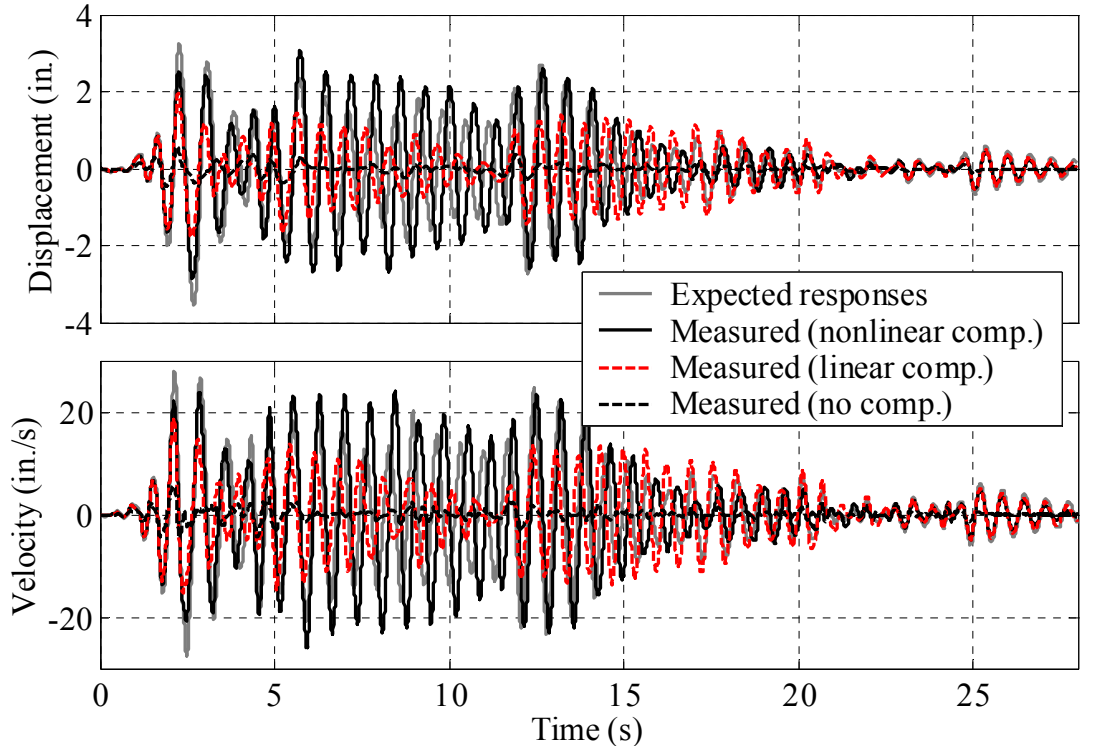

Figure 6.35 Comparison of structural responses using the El Centro earthquake ground acceleration, 0.34g (displacement and velocity)

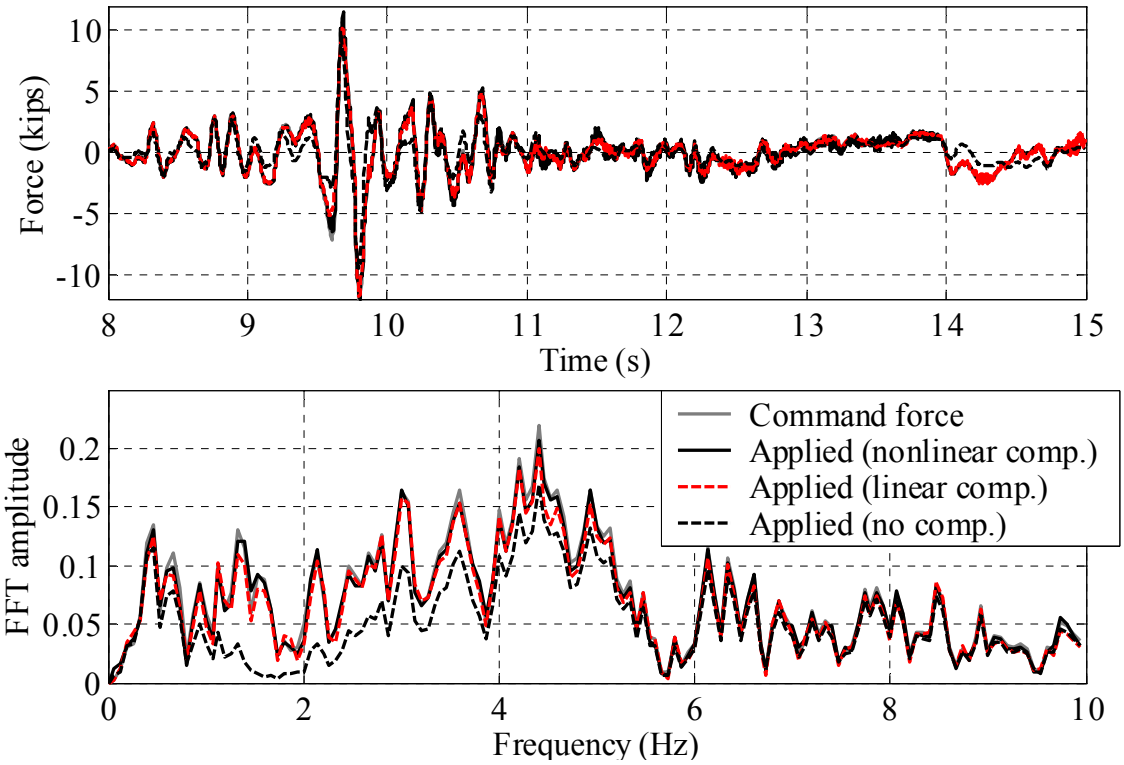

Figure 6.36 Comparison of system responses using the Northridge earthquake ground acceleration, 0.84g (force)

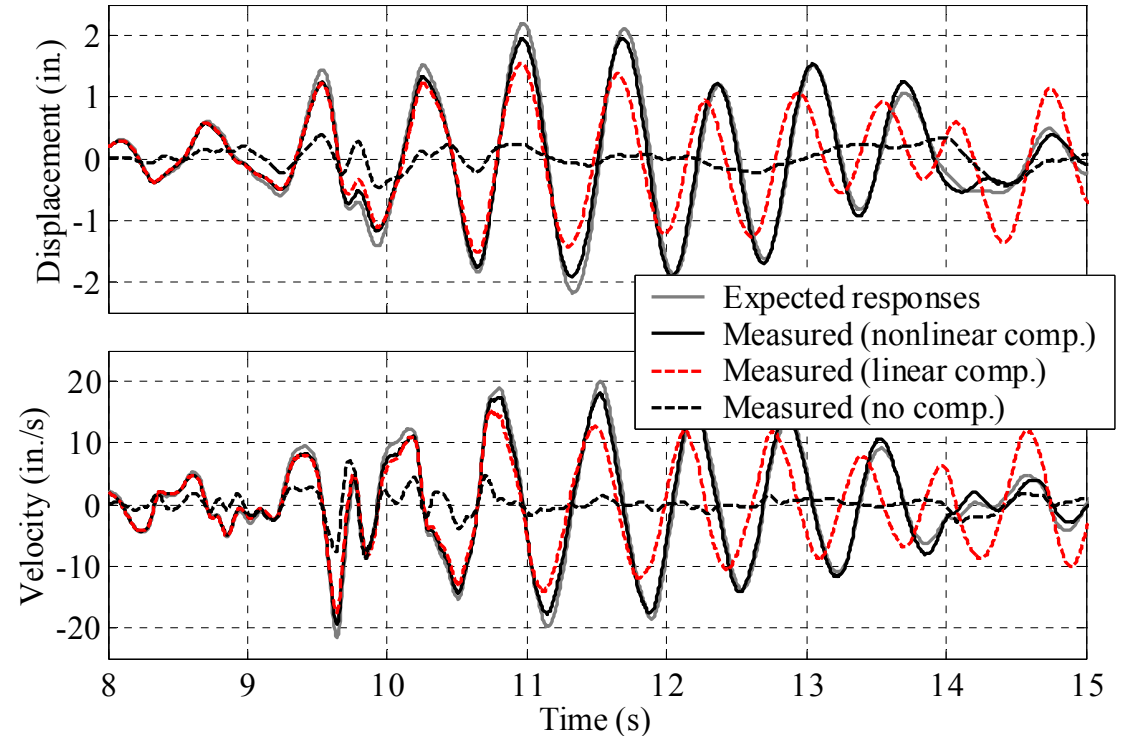

Figure 6.37 Comparison of structural responses using the Northridge earthquake ground acceleration, 0.84g (displacement and velocity)

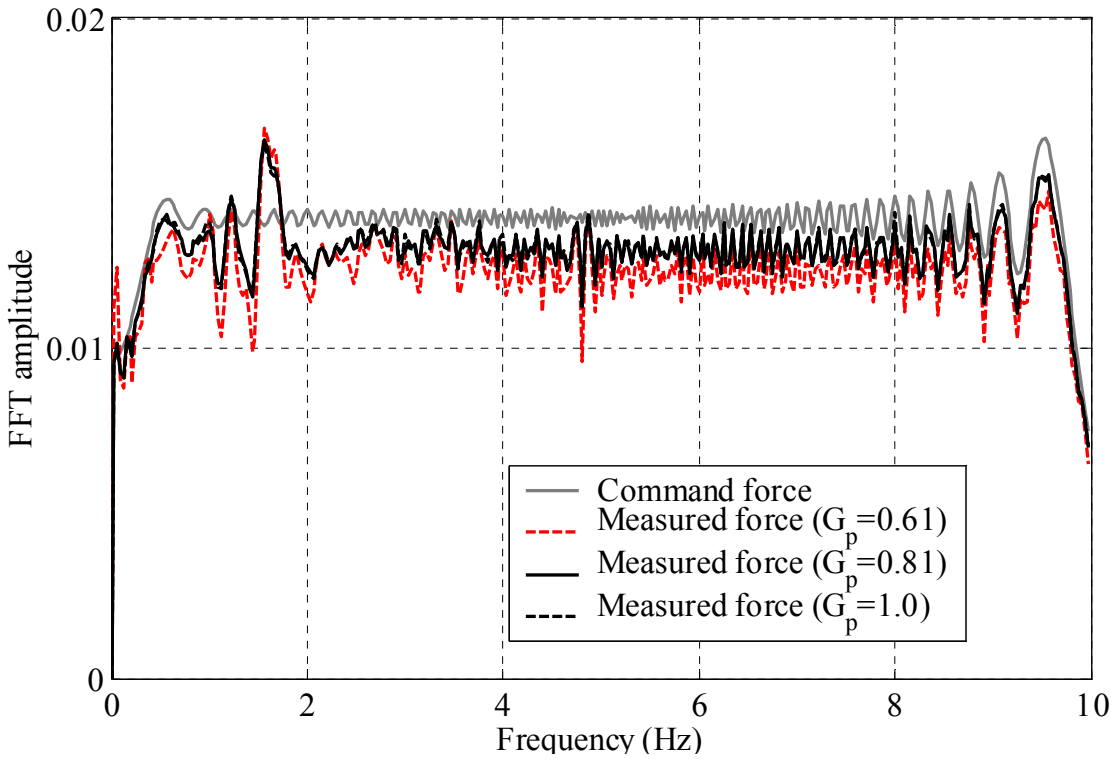

Figure 6.38 Comparison of system responses with linear velocity feedback compensation using a 0.5k sinesweep input (Controller P gain)

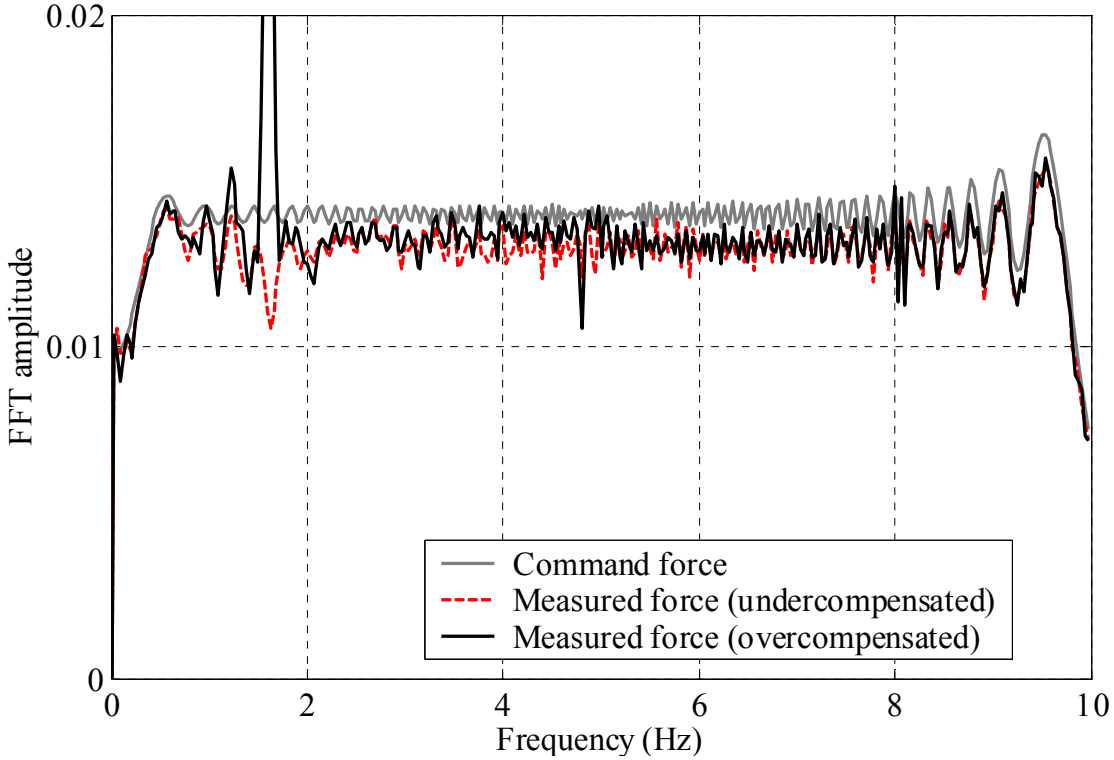

Figure 6.39 Comparison of system responses with linear velocity feedback compensation using a 0.5k sinesweep input (Flow gain)

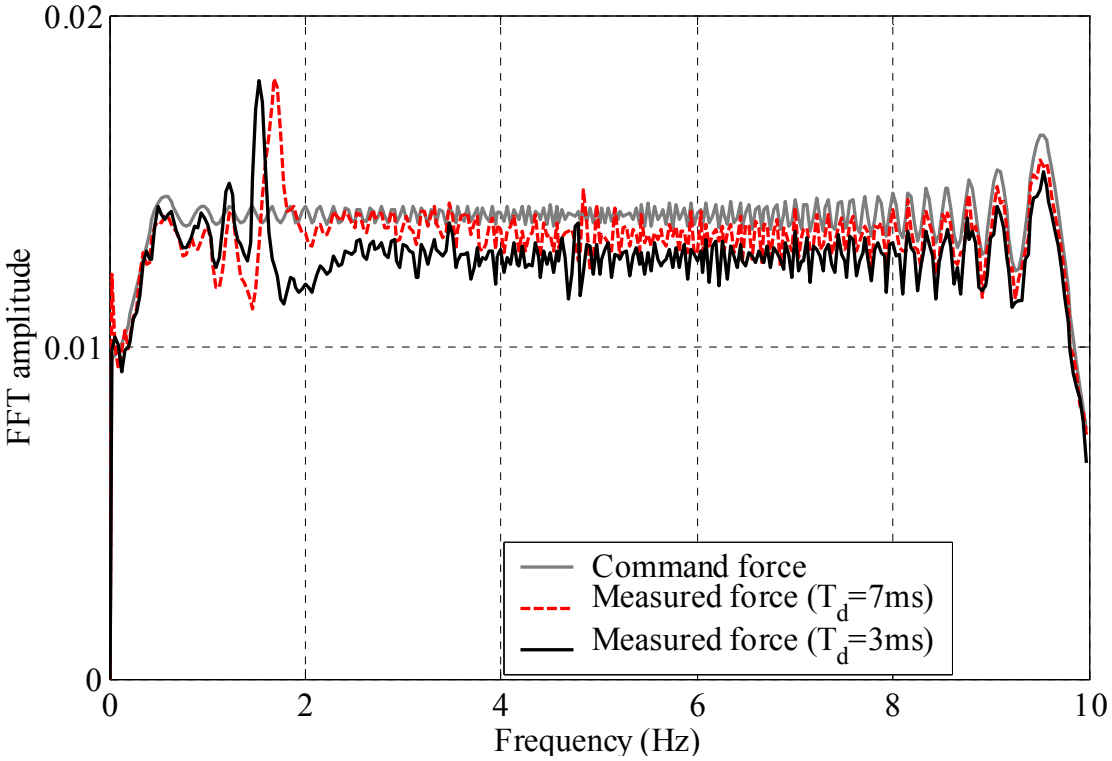

Figure 6.40 Comparison of system responses with linear velocity feedback compensation using a 0.5k sinesweep input (Delay compensation)

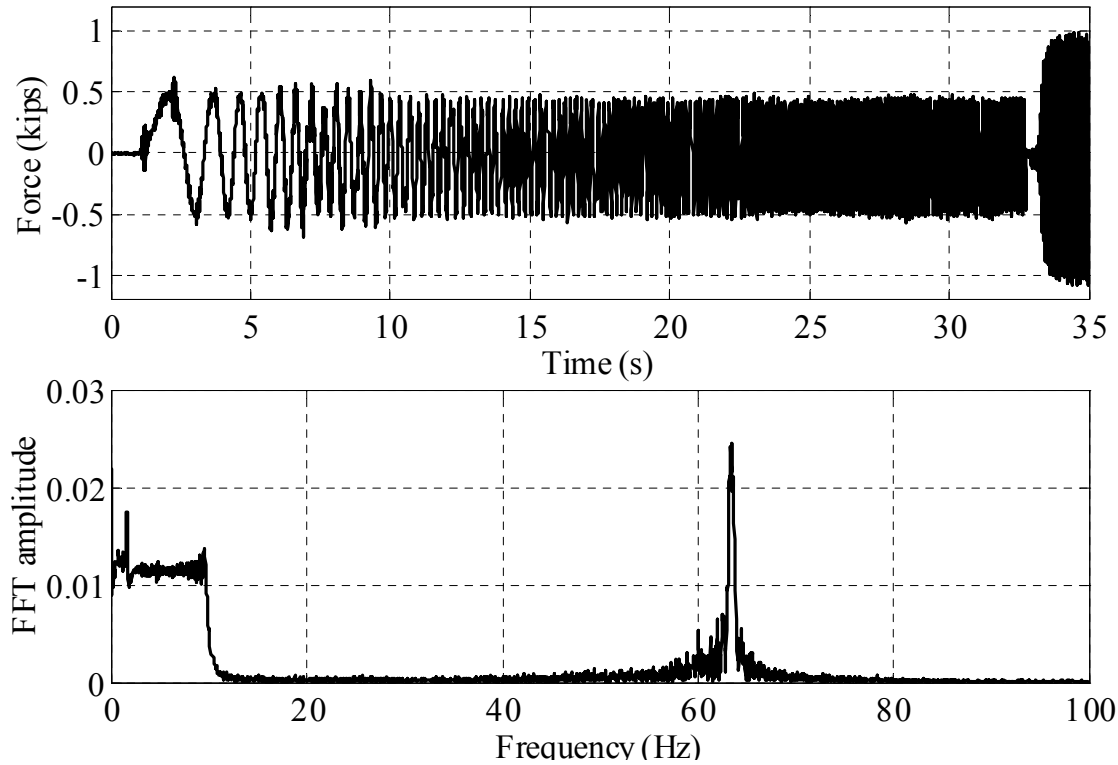

Figure 6.41 An example of high-frequency vibration of the test system

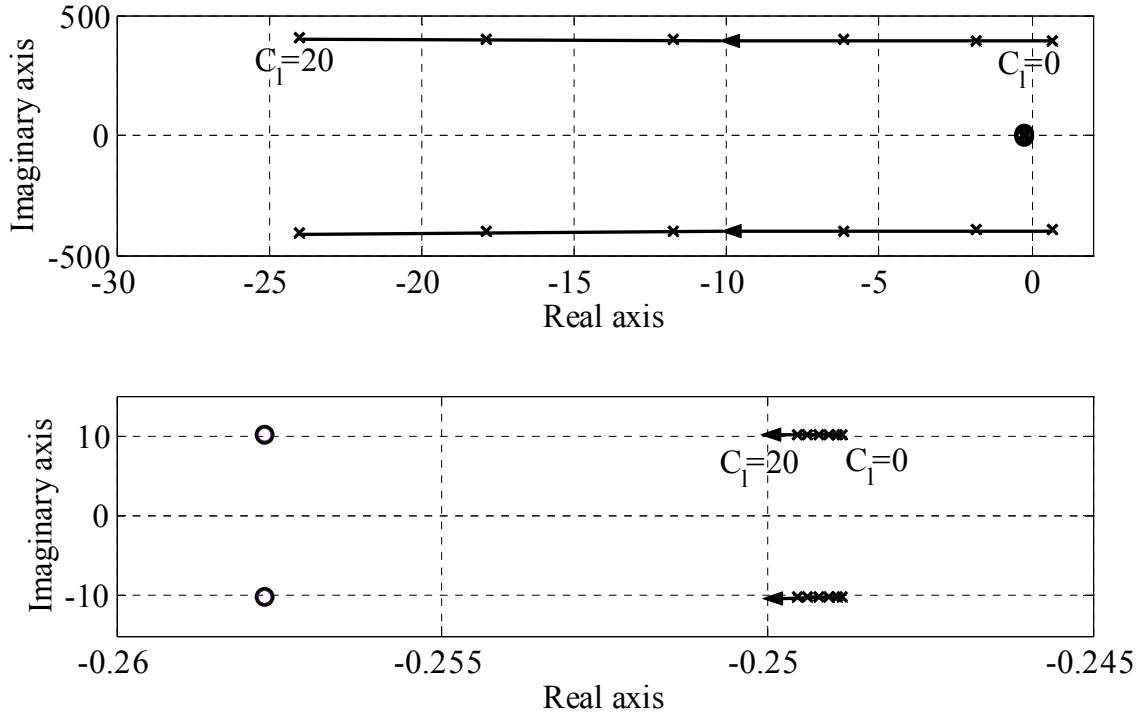

Figure 7.1 Root locus of the linearly compensated systems with respect to proportional leakage C_l (from command to force)

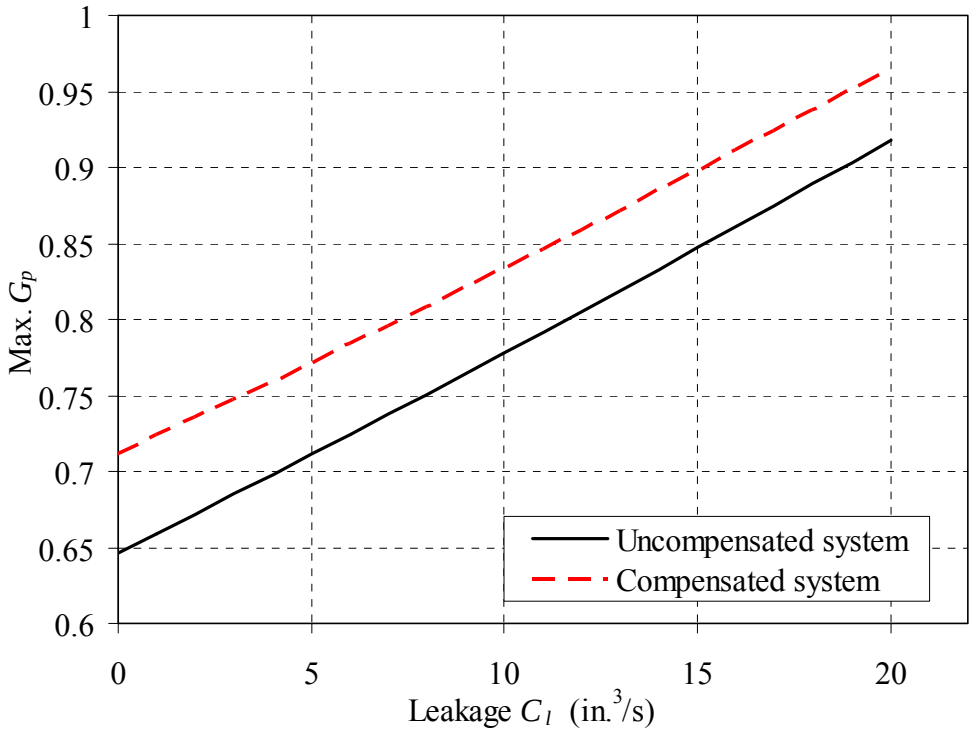

Figure 7.2 Maximum controller P gain vs. the proportional leakage C_l

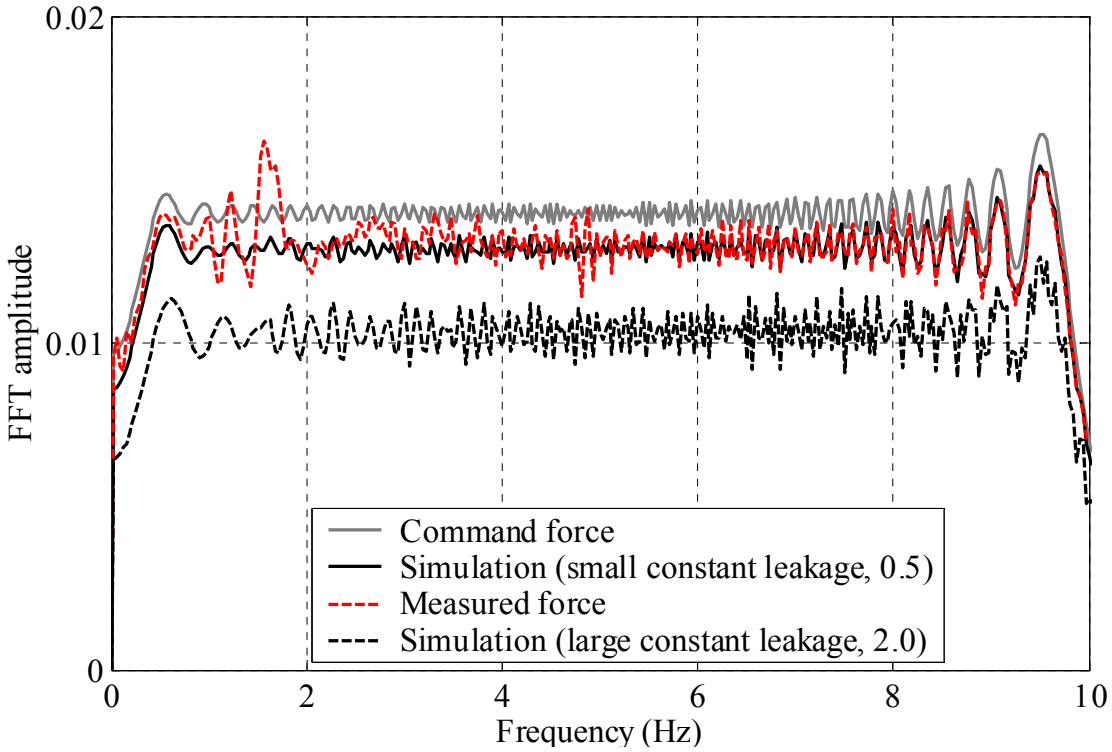

Figure 7.3 Comparison of system response with various constant leakages to a 0.5k sinesweep input

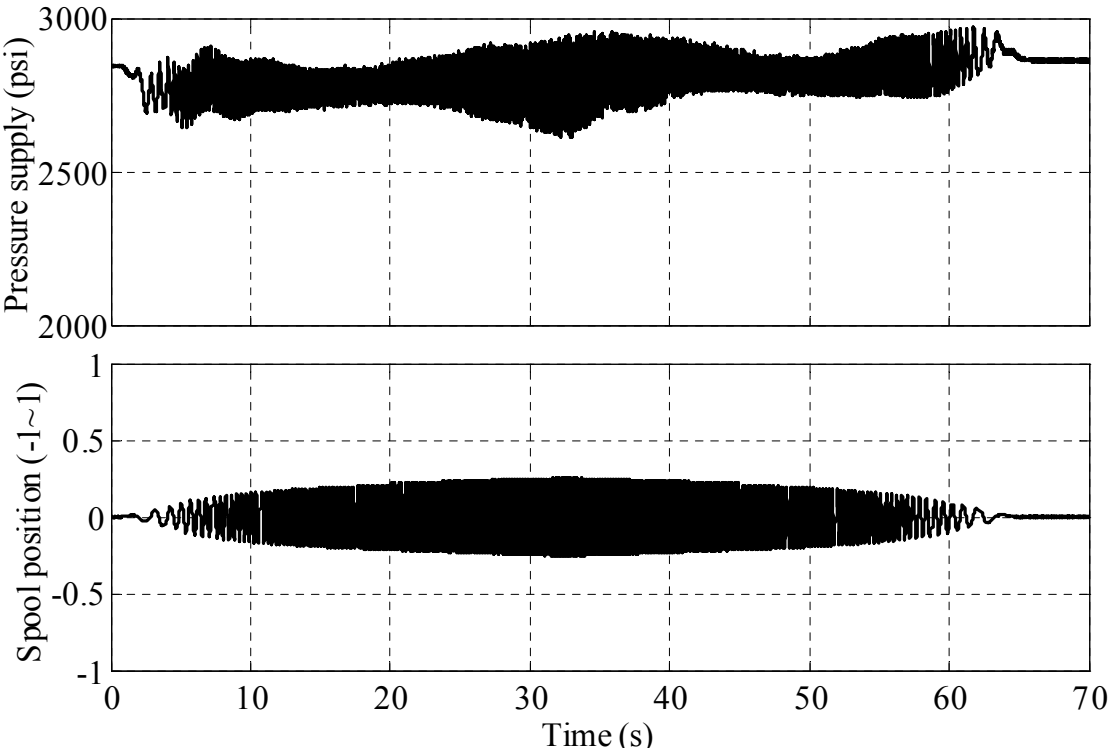

Figure 7.4 Supply pressure variation with small hydraulic power requirement

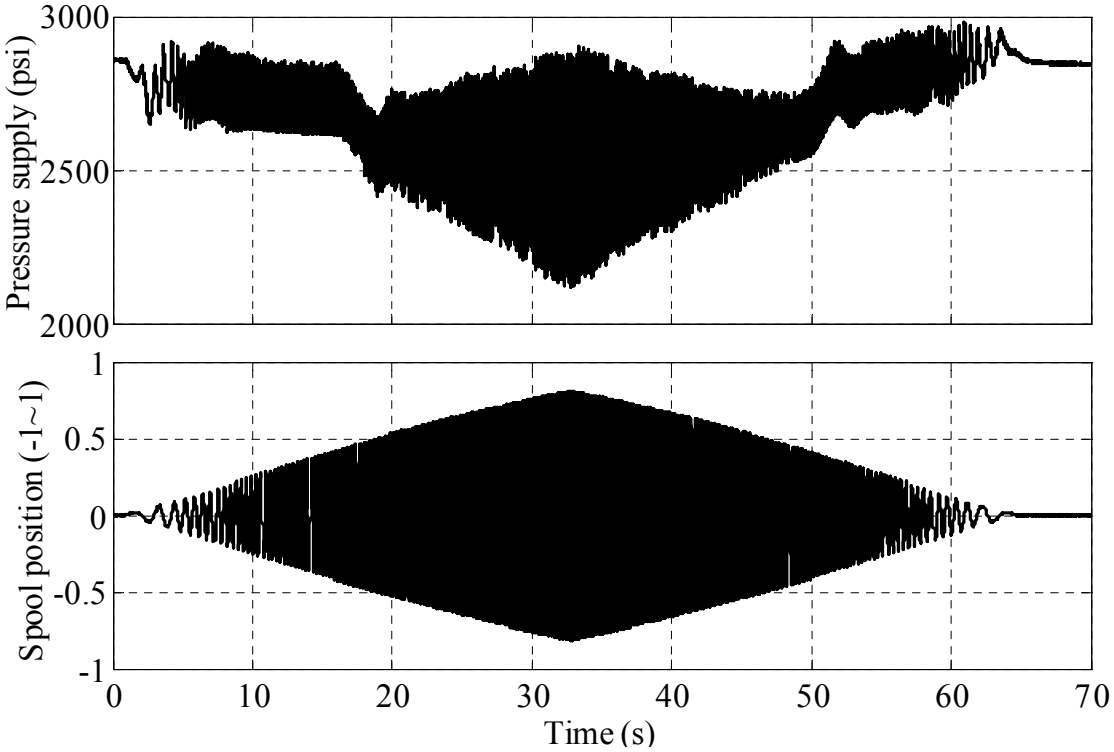

Figure 7.5 Supply pressure variation with large hydraulic power requirement

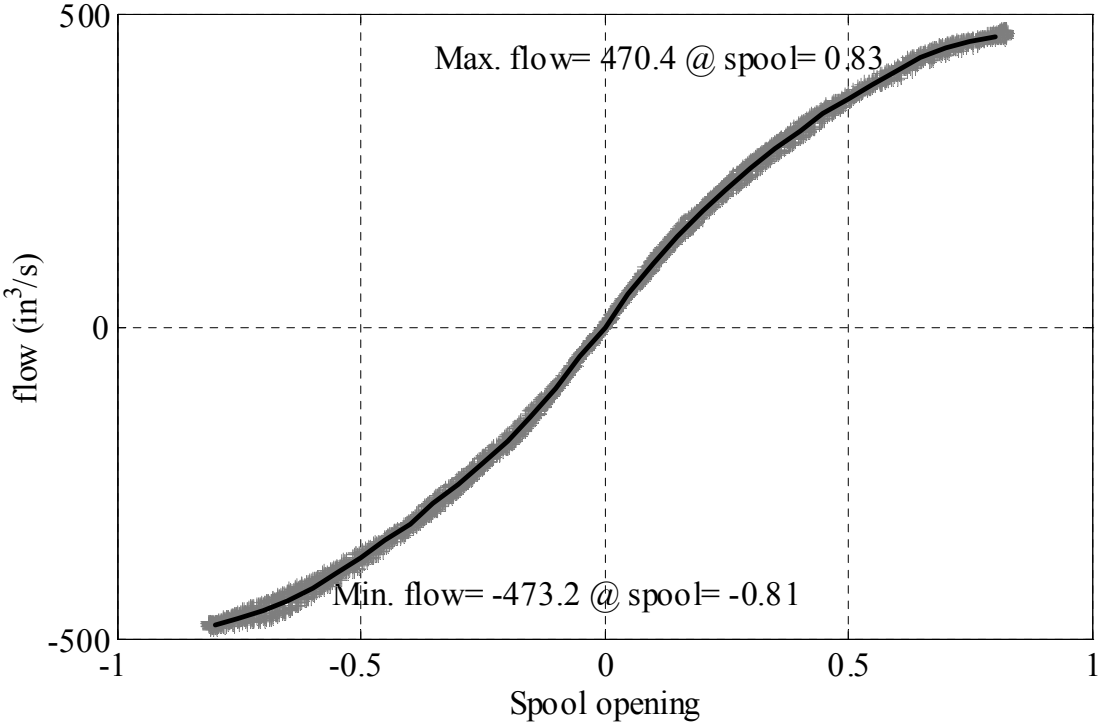

Figure 7.6 Nonlinear flow property of the servovalve with a ¼-gallon accumulator

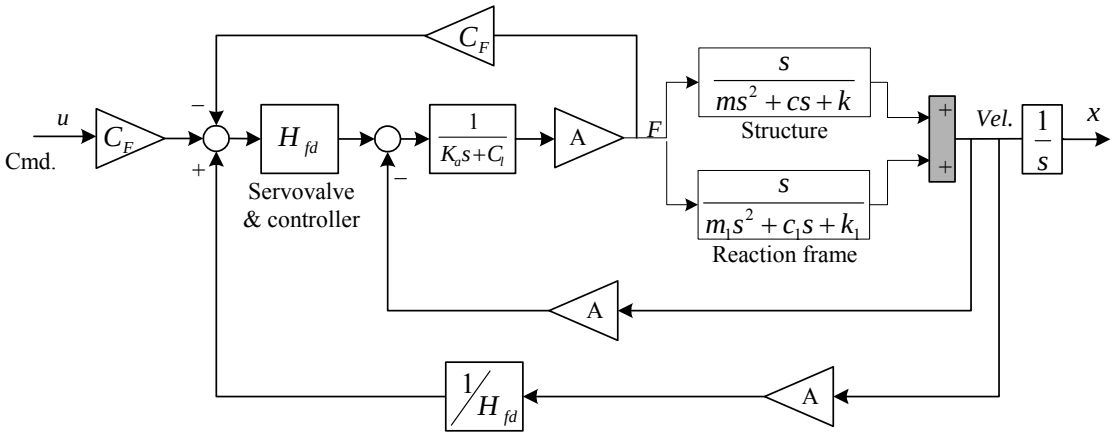

Figure 7.7 Simulation model for the study of the effect of reaction frames

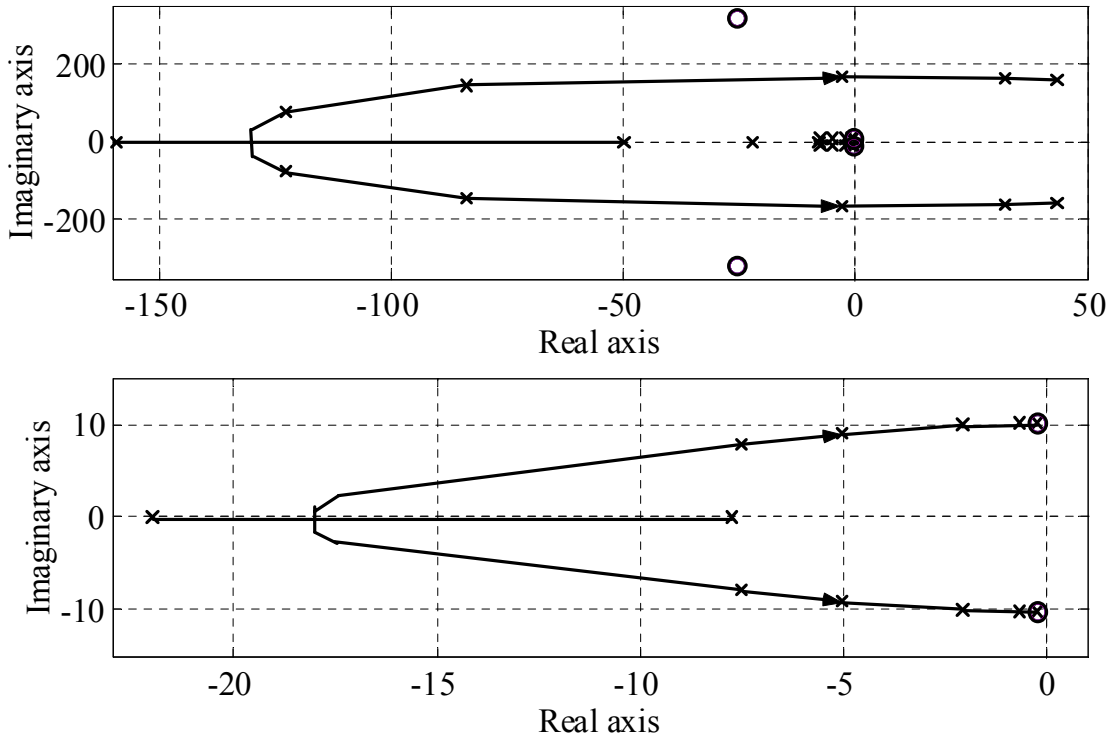

Figure 7.8 Root locus of the linearly compensated system with flexible reaction frame (m/100 + 10k) compensation for piston velocity (from command to force)

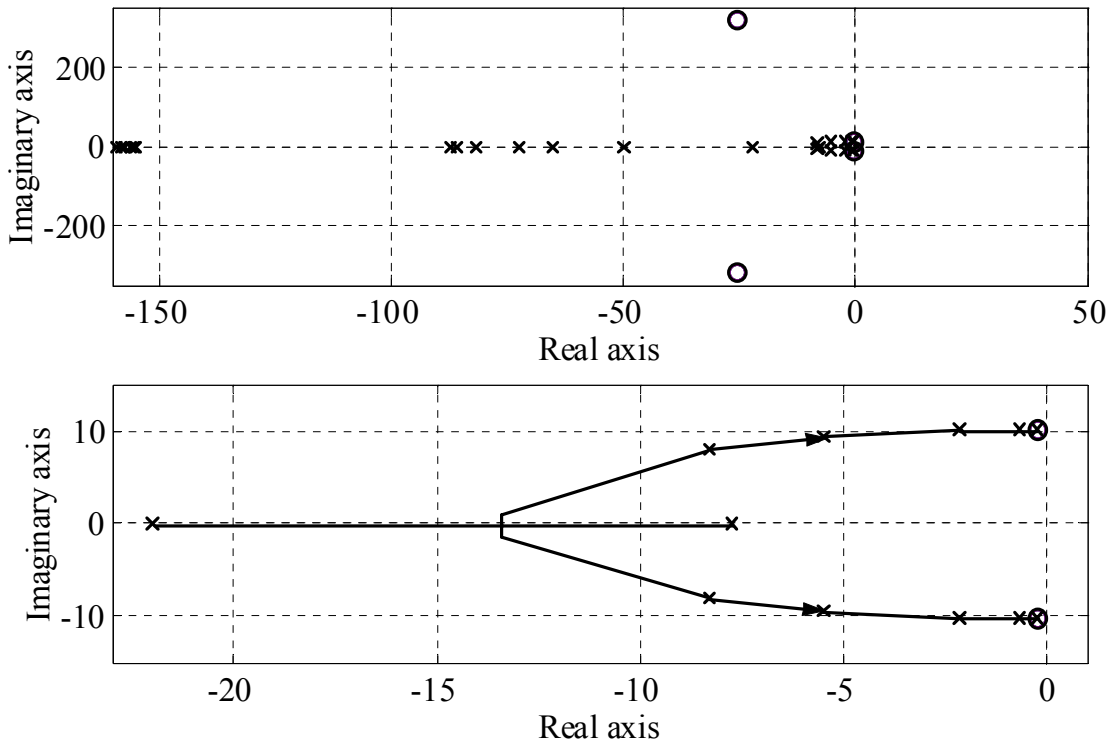

Figure 7.9 Root locus of the linearly compensated system with flexible reaction frame (m/100 + 10k) compensation for structure velocity (from command to force)

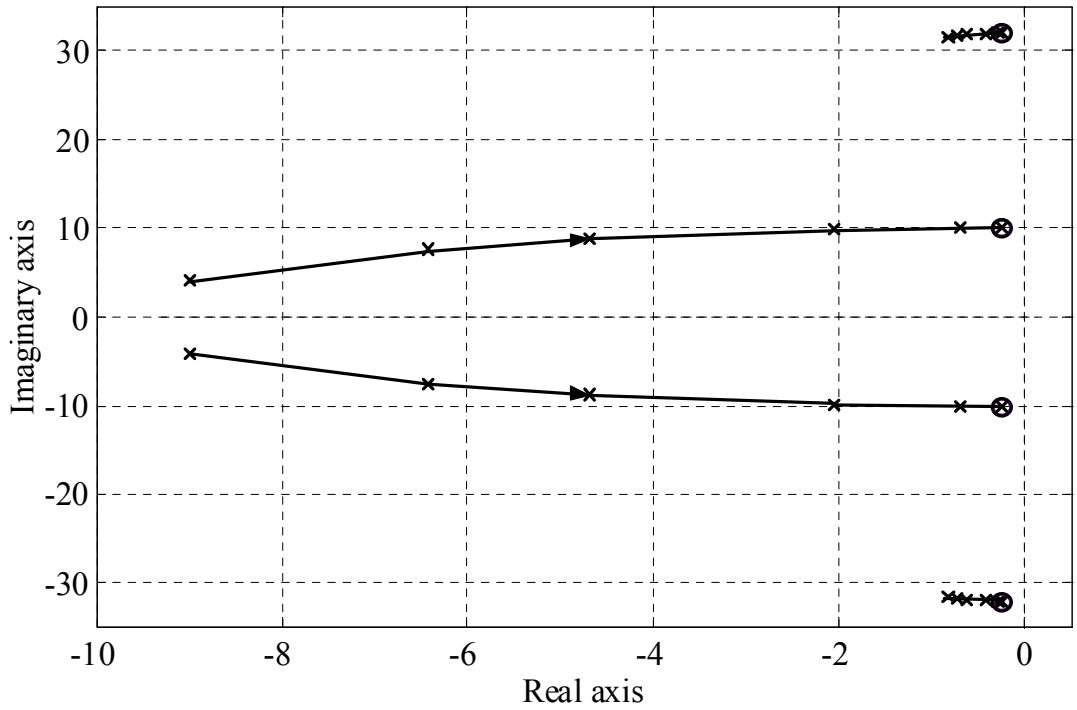

Figure 7.10 Root locus of the linearly compensated system with heavy, stiff reaction frame (10m + 100k) compensation for piston velocity (from command to force)

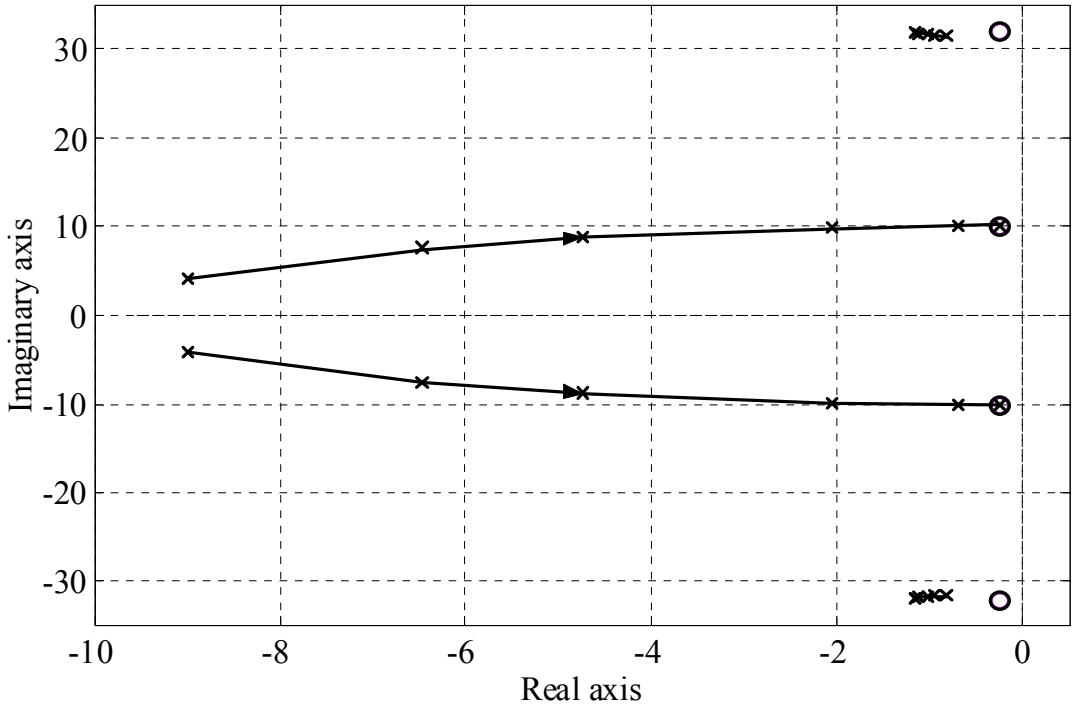

Figure 7.11 Root locus of the linearly compensated system with heavy, stiff reaction frame (10m + 100k) compensation for structure velocity (from command to force)

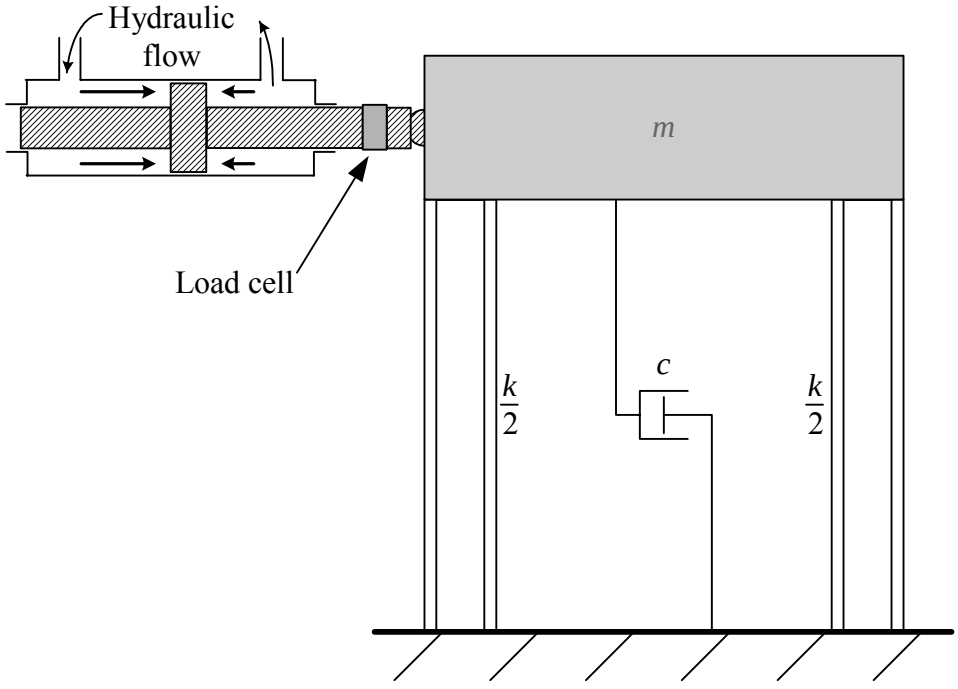

Figure 7.12 A schematic of a test structure with an actuator

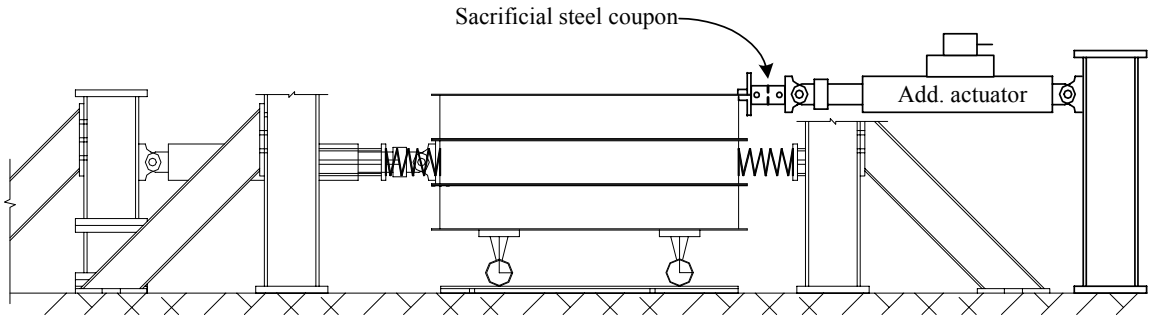

Figure 7.13 A free vibration test setup (with additional actuator)

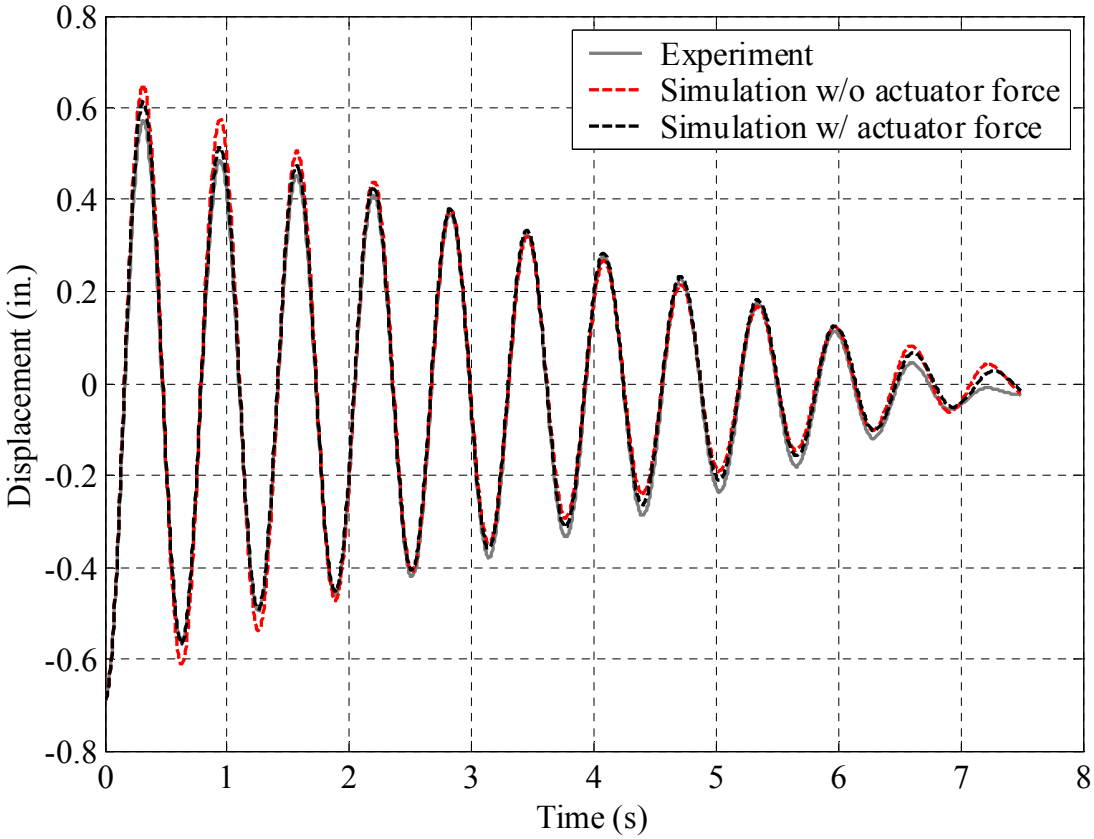

Figure 7.14 Free vibration test and simulation with actuator attached (correctly compensated)

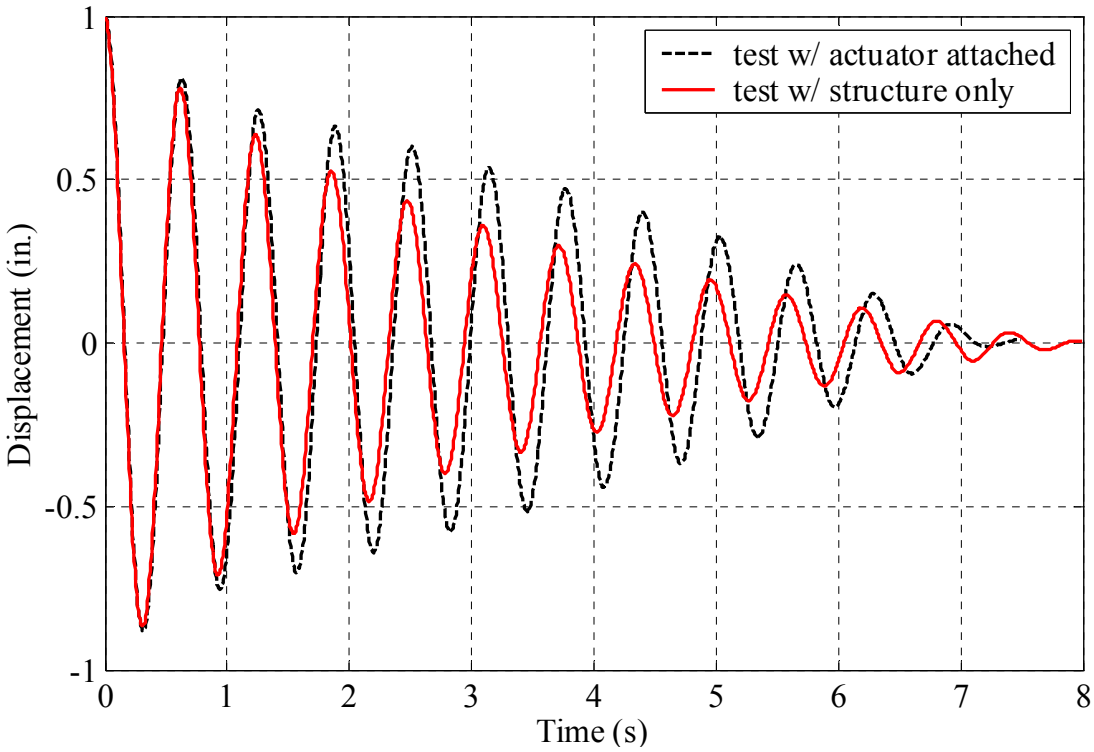

Figure 7.15 Normalized free vibration tests of the SDOF structure

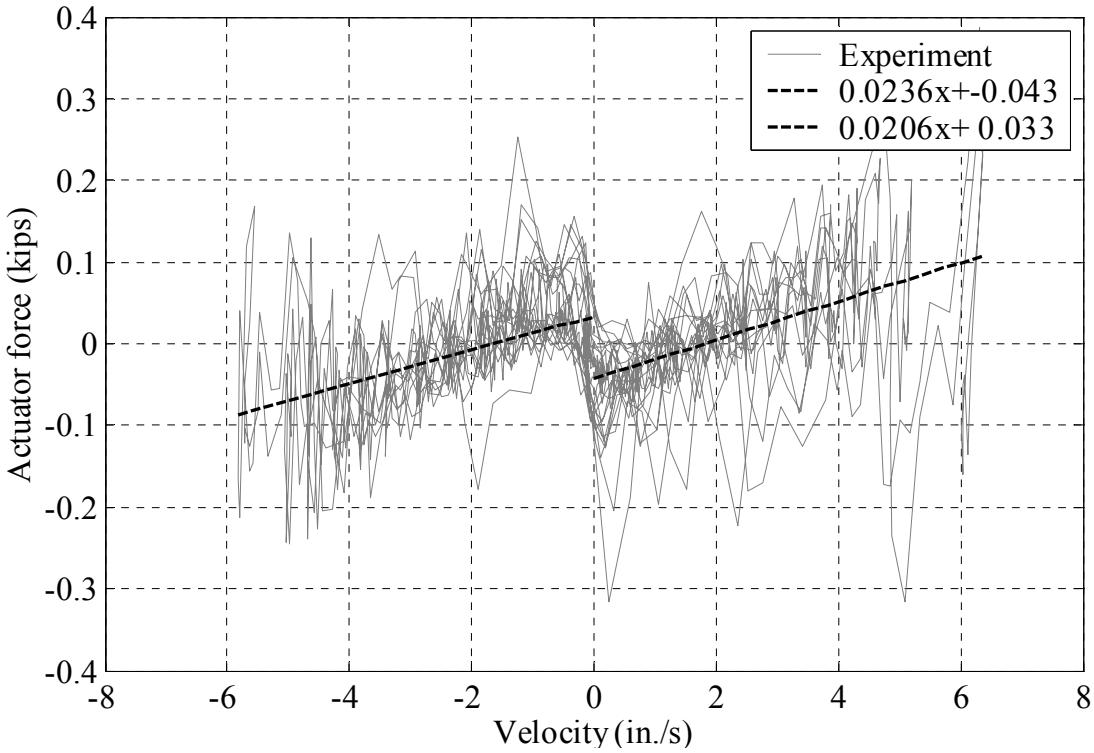

Figure 7.16 Actuator force input vs. structure velocity during the free vibration test with the actuator attached and correctly compensated

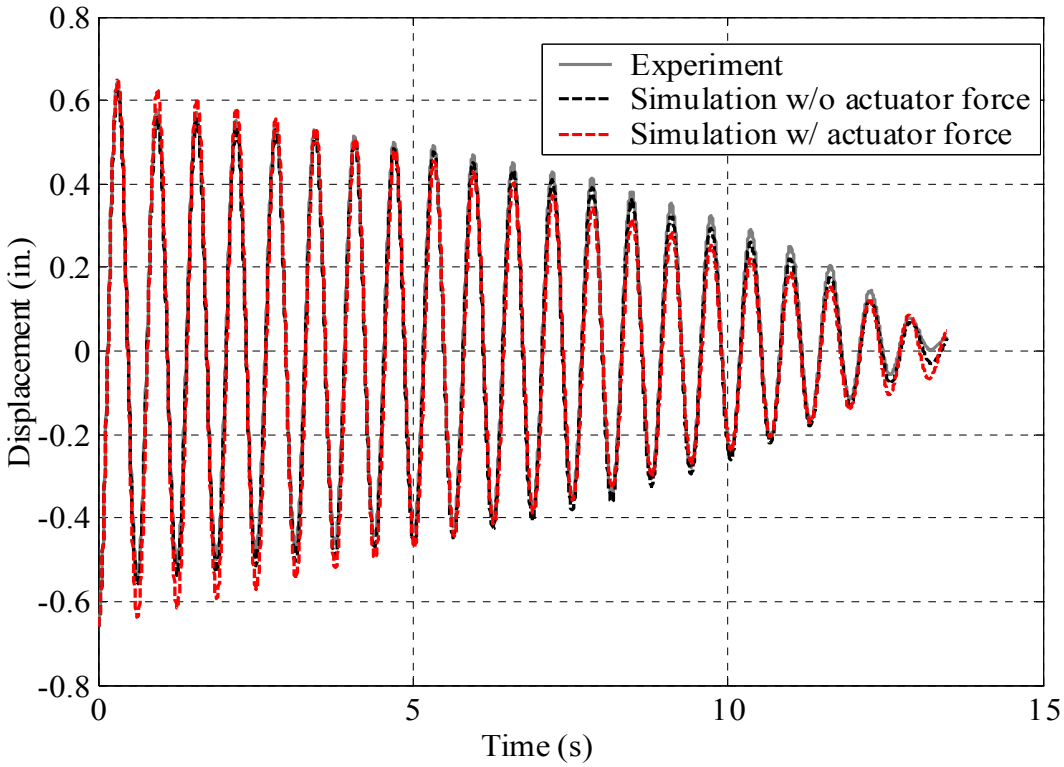

Figure 7.17 Free vibration test and simulation with actuator over-compensated

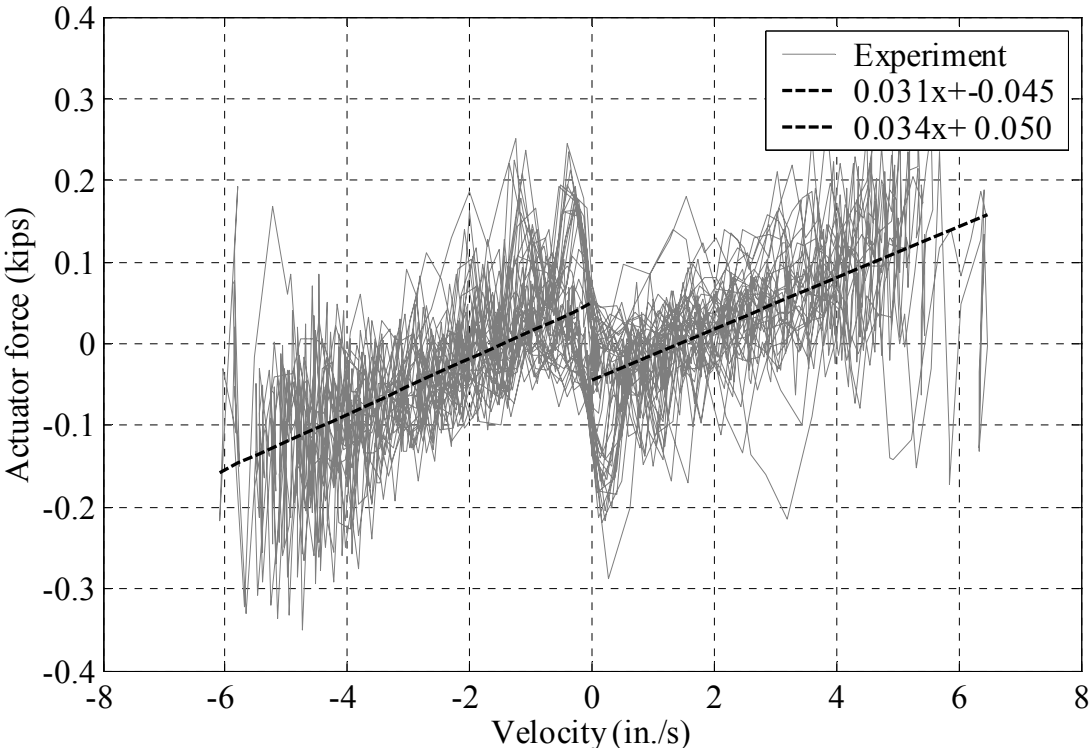

Figure 7.18 Actuator force input vs. structure velocity during the free vibration test with the actuator attached and over-compensated

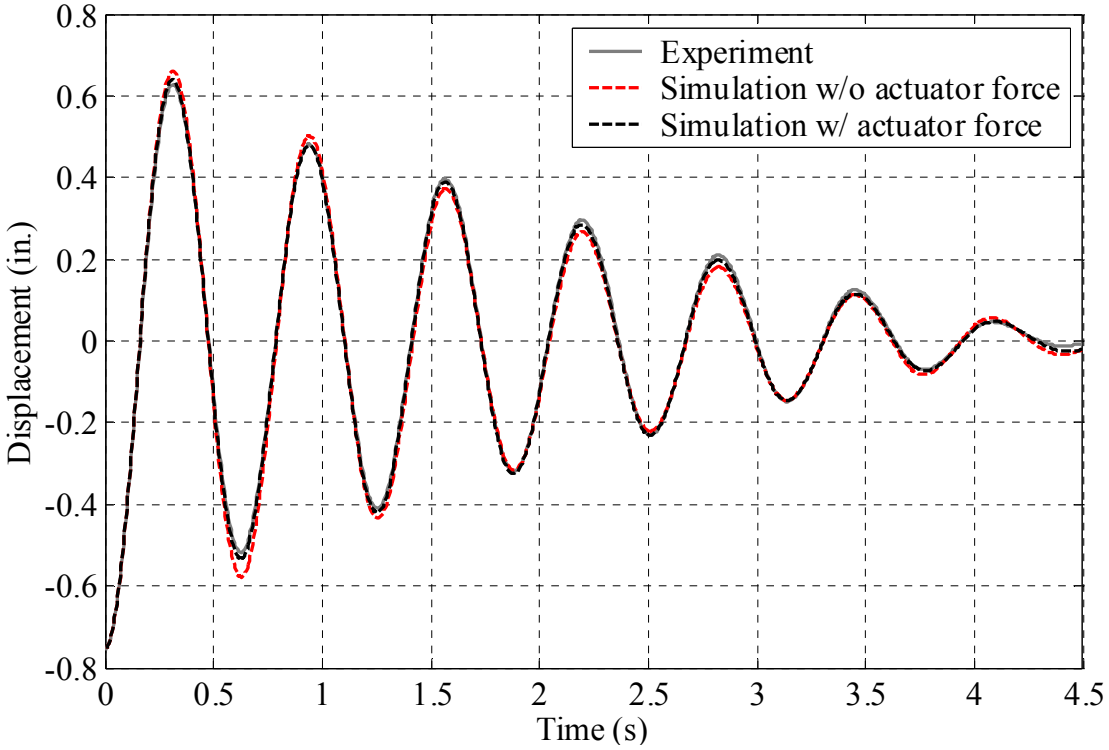

Figure 7.19 Free vibration test and simulation with actuator under-compensated

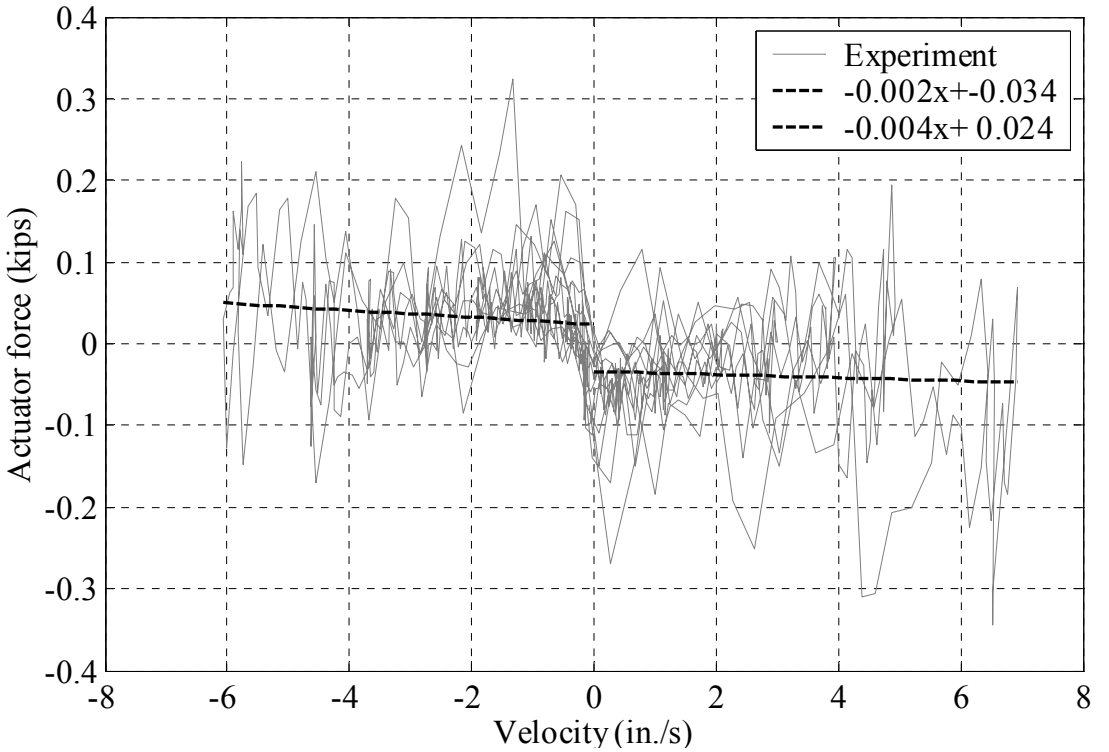

Figure 7.20 Actuator force input vs. structure velocity during the free vibration test with the actuator attached and under-compensated

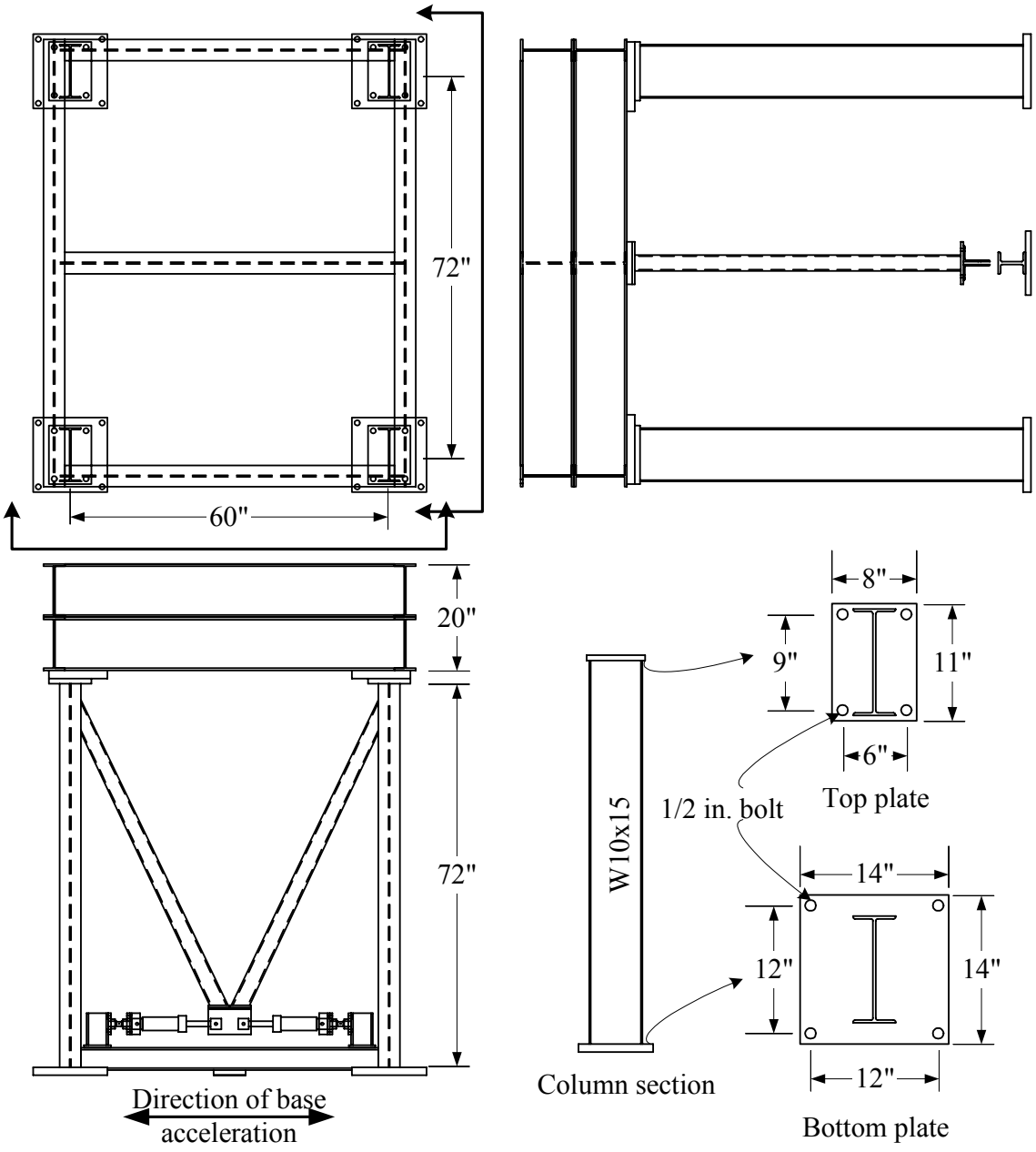

Figure 8.1 Single-story test specimen

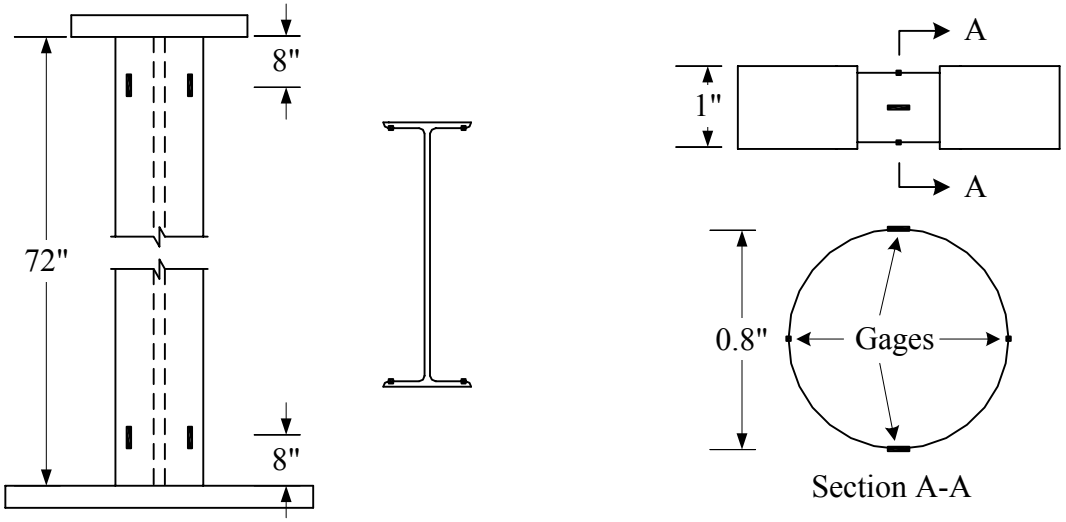

Figure 8.2 Location of strain gages (a) column (b) load cell for damper force measurements

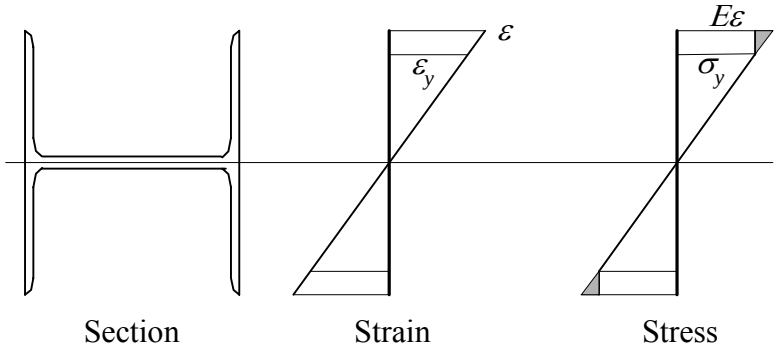

Figure 8.3 The strain and stress distribution across a column section (section not in scale)

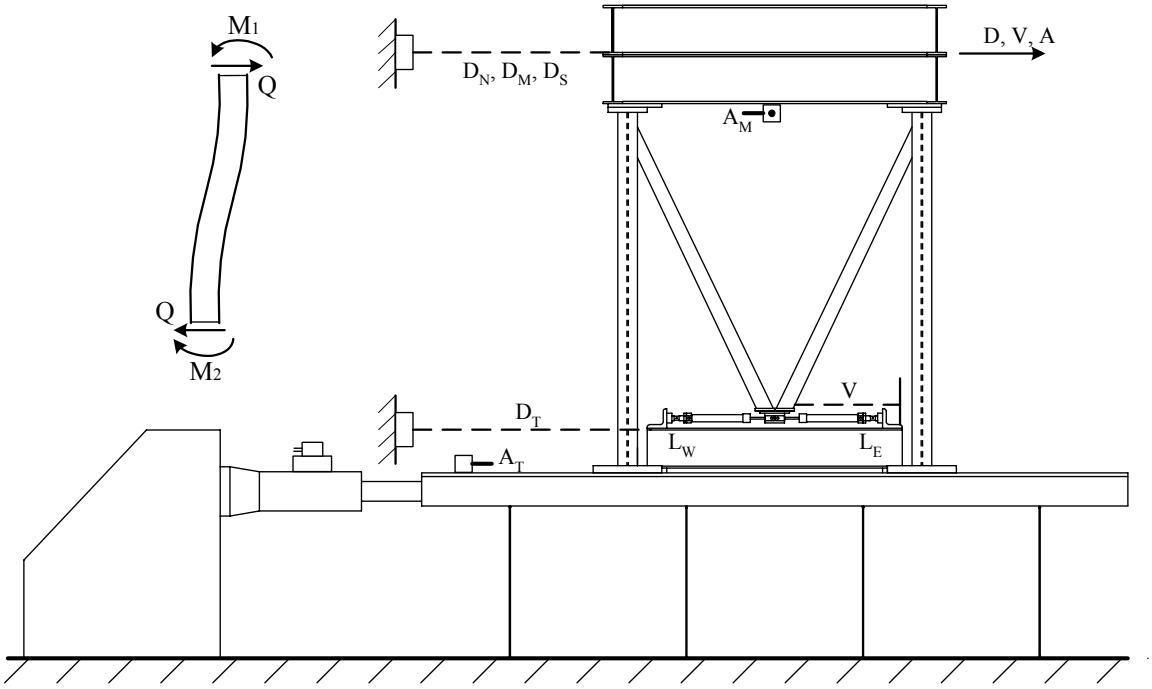

Figure 8.4 Schematic of structure on shake table

Figure 8.5 Structure on shake table

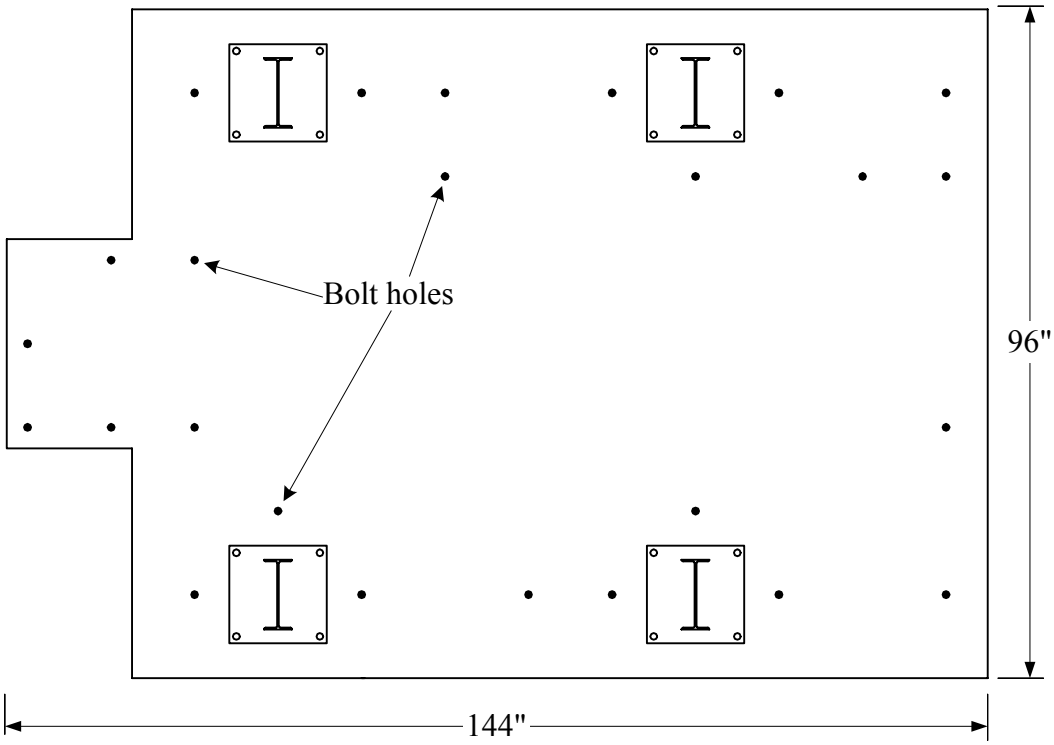

Figure 8.6 Base plate and anchorage pattern for the test structure on shake table

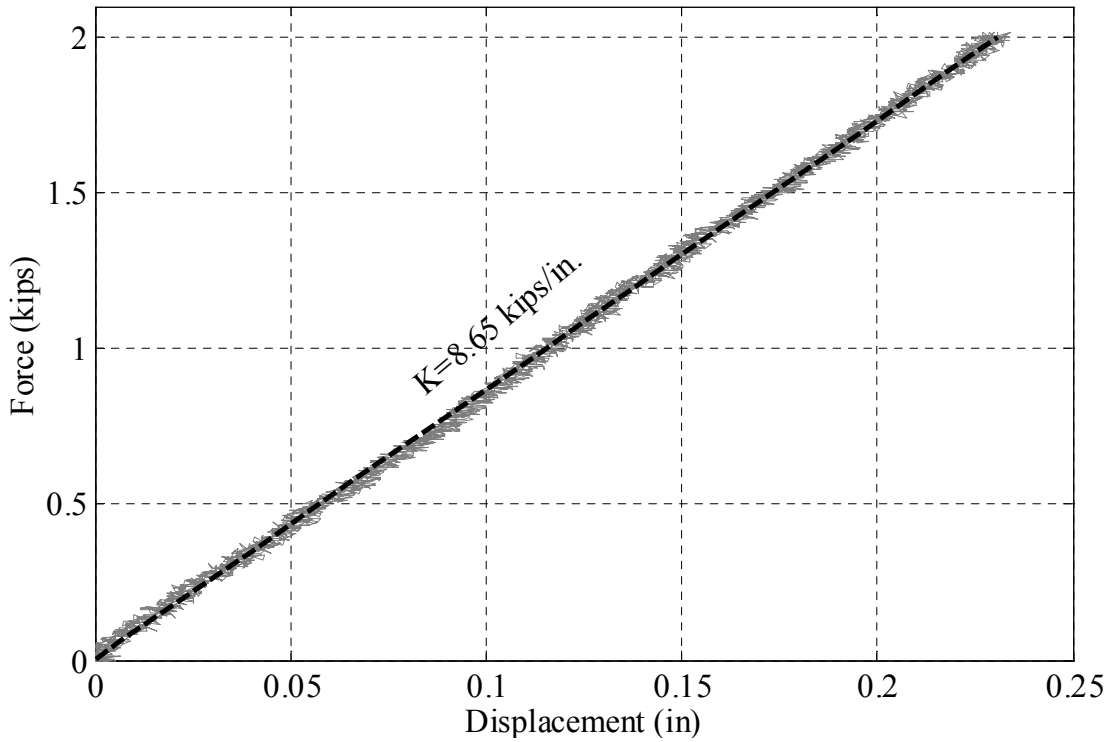

Figure 8.7 Static loading test of structure on shake table

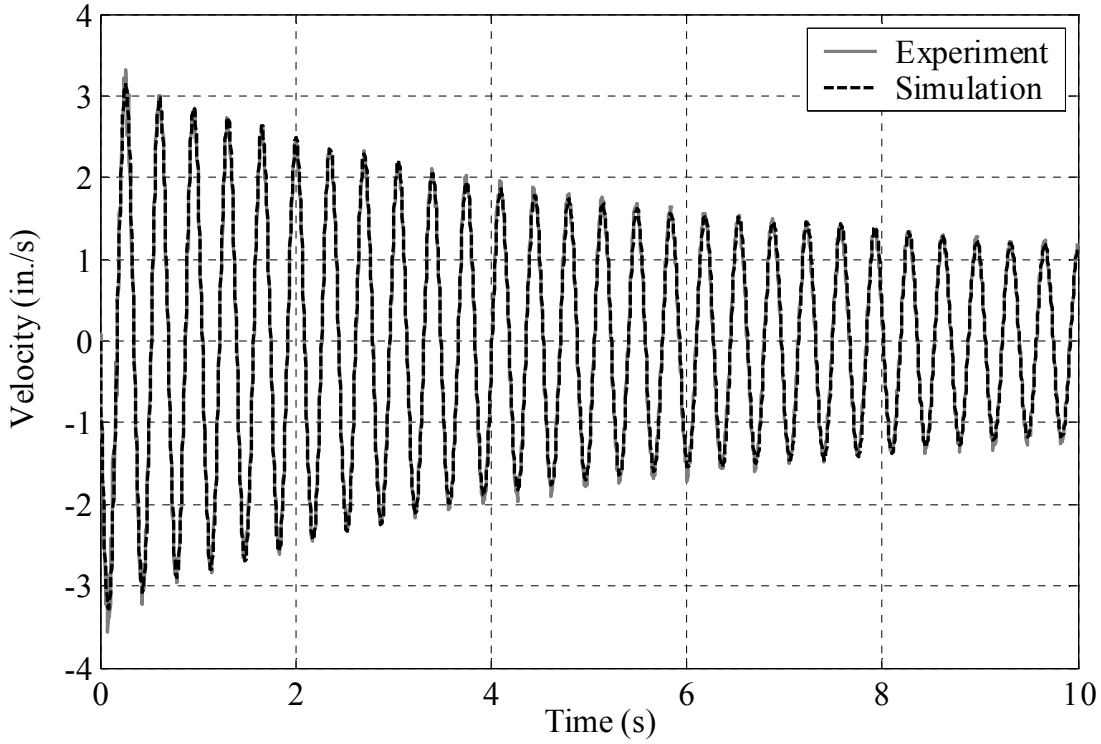

Figure 8.8 Free vibration test of structure on shake table (without dampers)

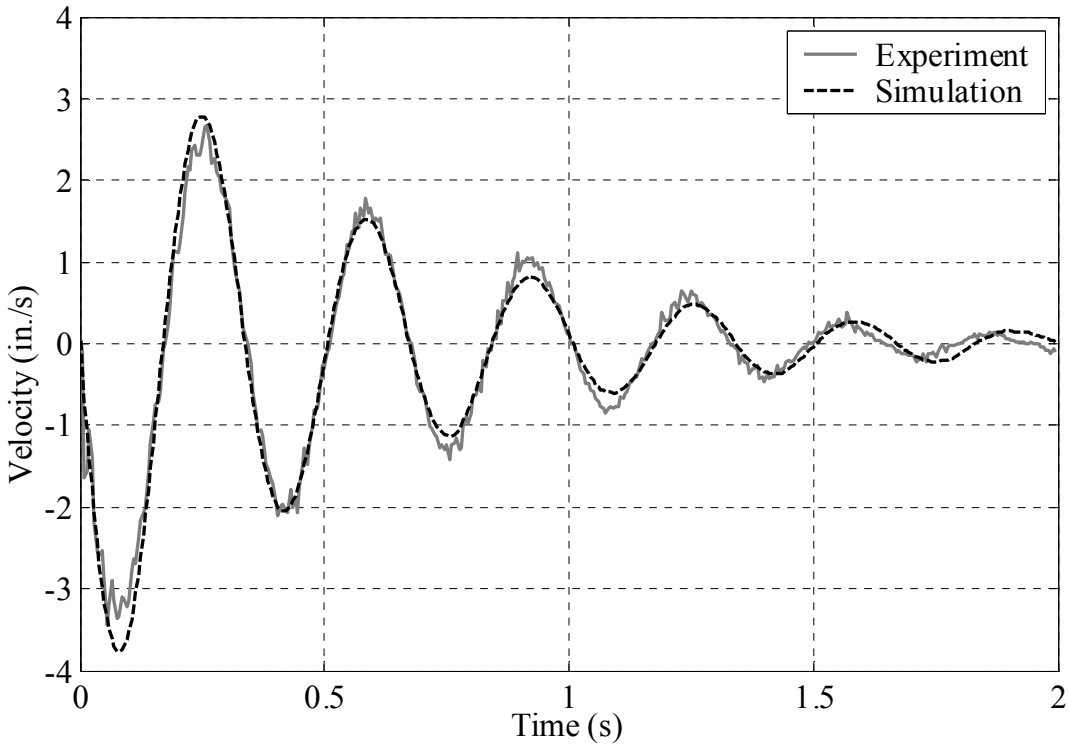

Figure 8.9 Free vibration test of structure on shake table (with dampers)

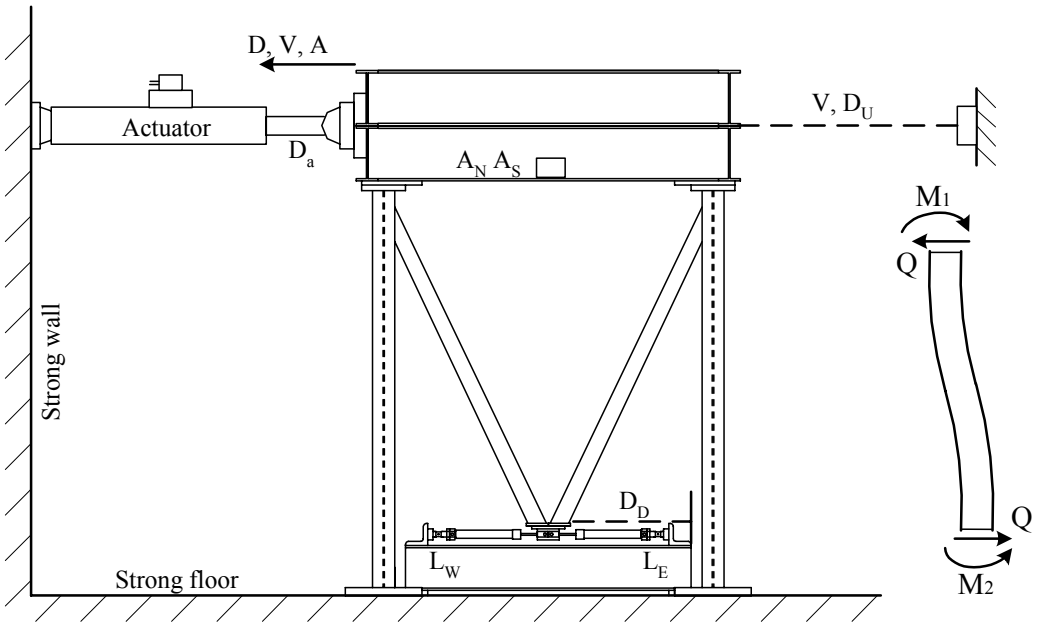

Figure 8.10 Schematic of structure for EFT test

Figure 8.11 Structure for EFT test

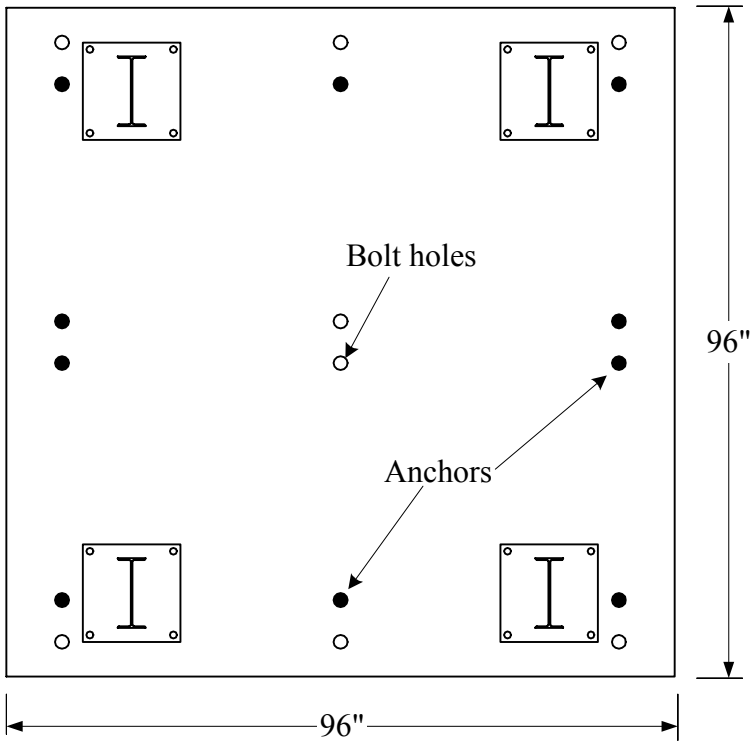

Figure 8.12 Base plate and anchorage pattern for test structure for EFT test

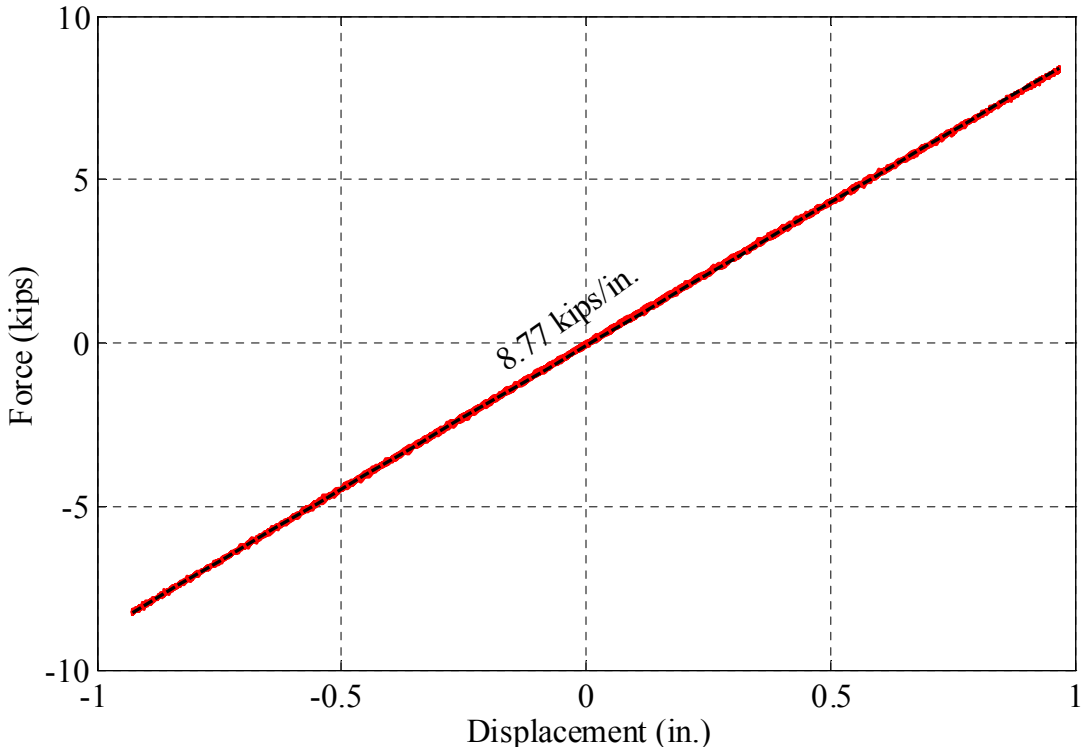

Figure 8.13 Static loading test of structure for EFT test

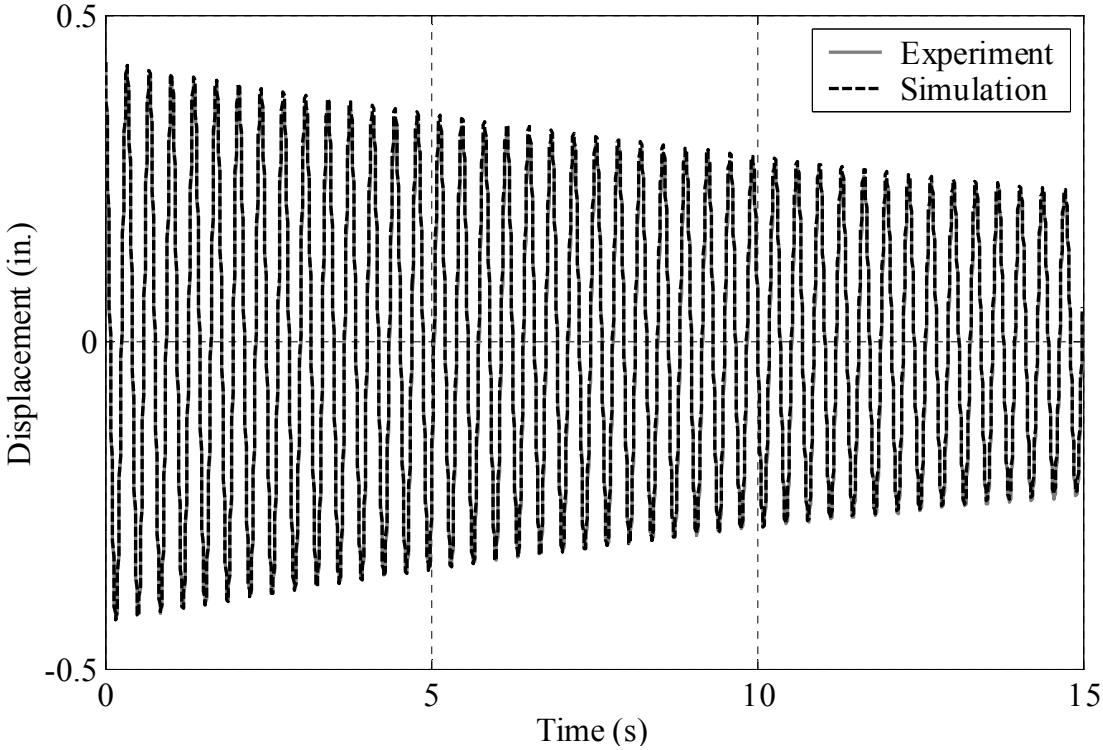

Figure 8.14 Free vibration test of structure for EFT test (without dampers)

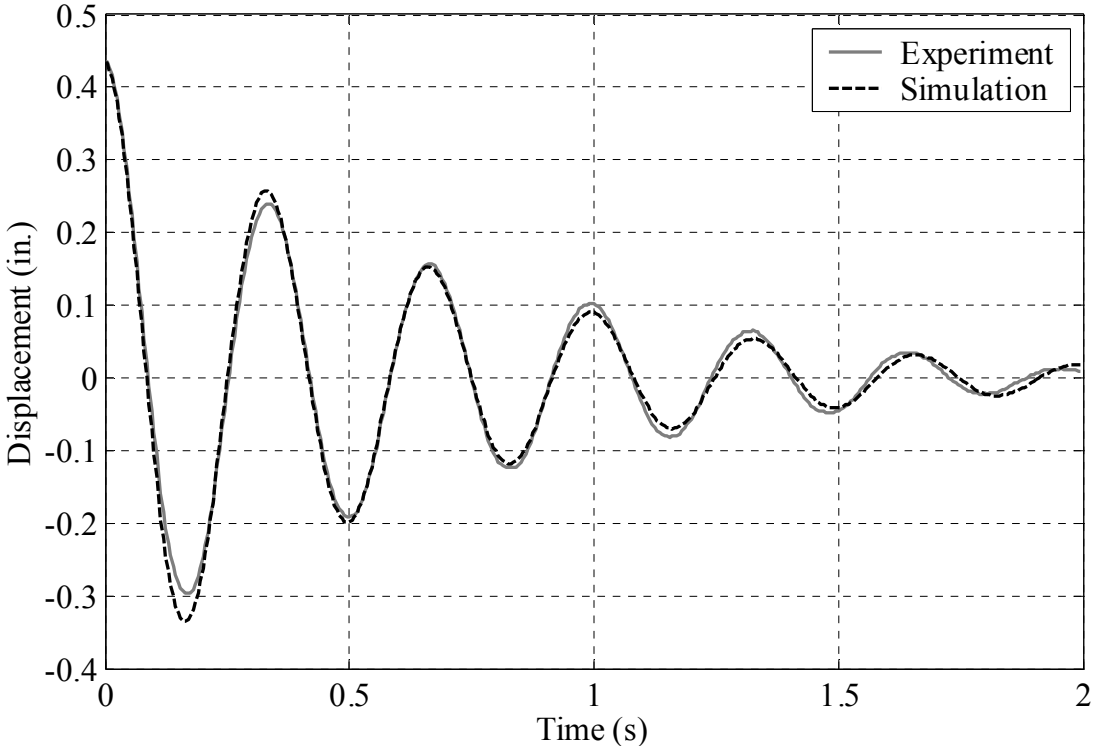

Figure 8.15 Free vibration test of structure for EFT test (with dampers)

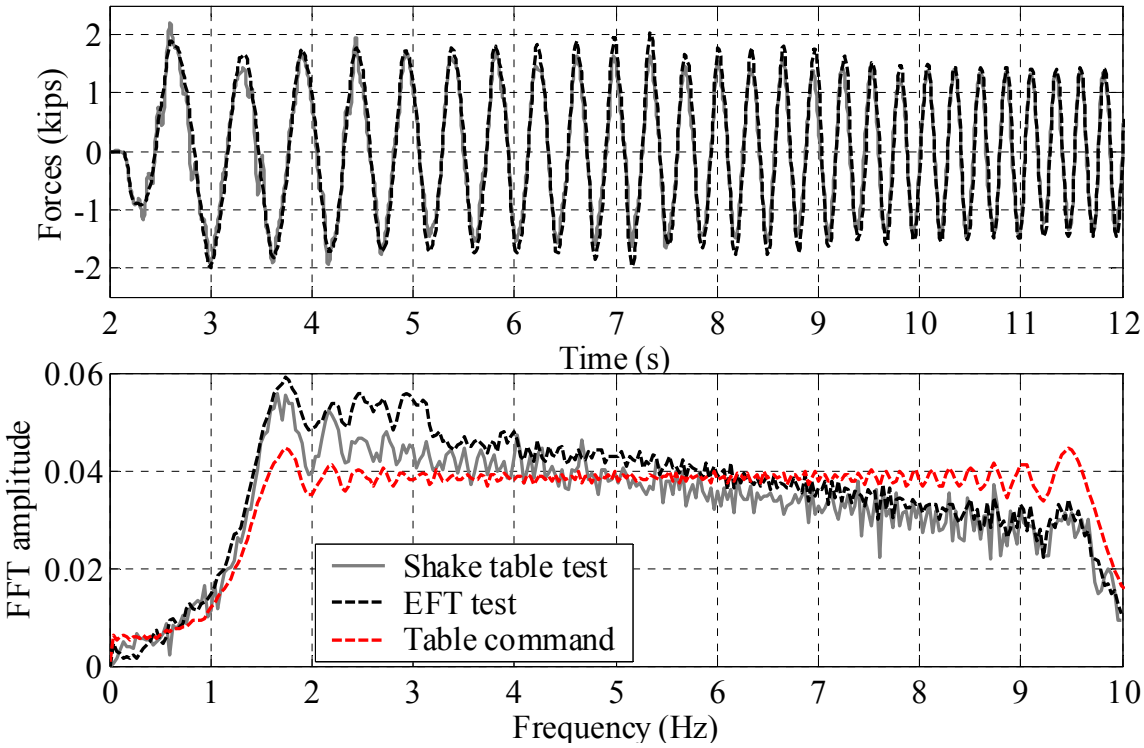

Figure 8.16 Comparison of effective forces from shake table test (mass × measured table acceleration) and measured forces form EFT test (0.13g sinesweep 1-10Hz)

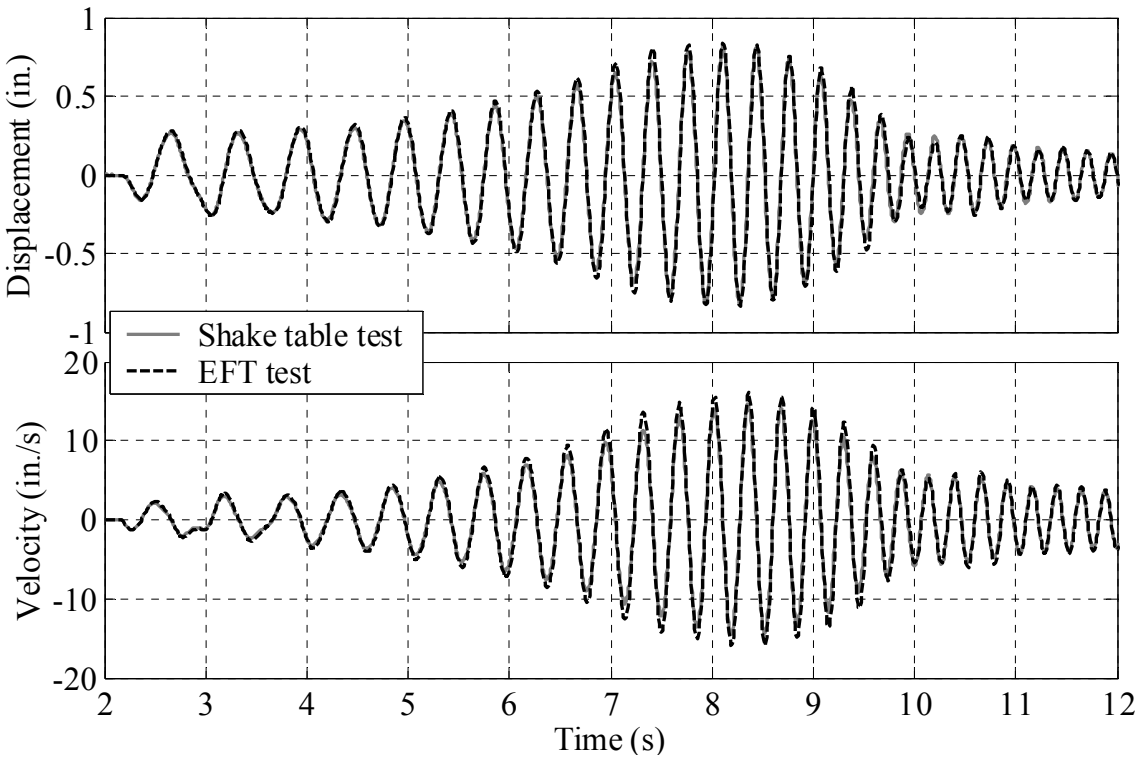

Figure 8.17 Comparison of global structural responses of tests with dampers (0.13g sinesweep 1-10Hz)

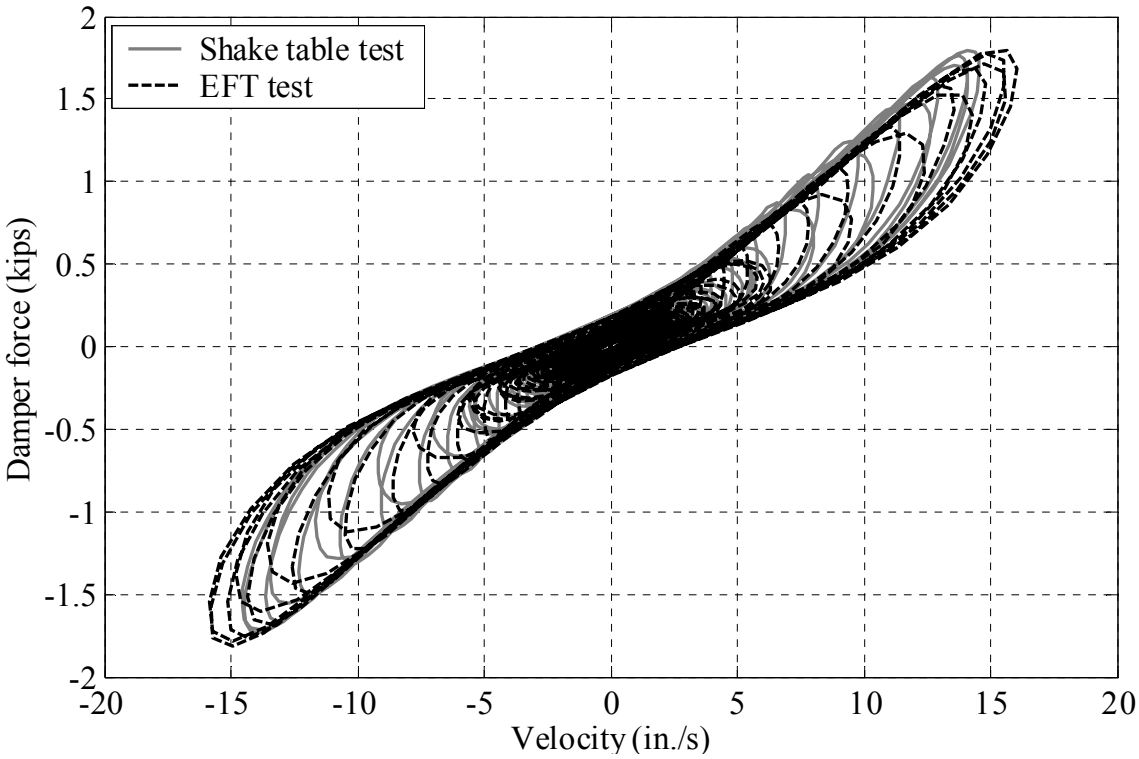

Figure 8.18 Damper performances in tests with 0.13g sinesweep (1-10Hz)

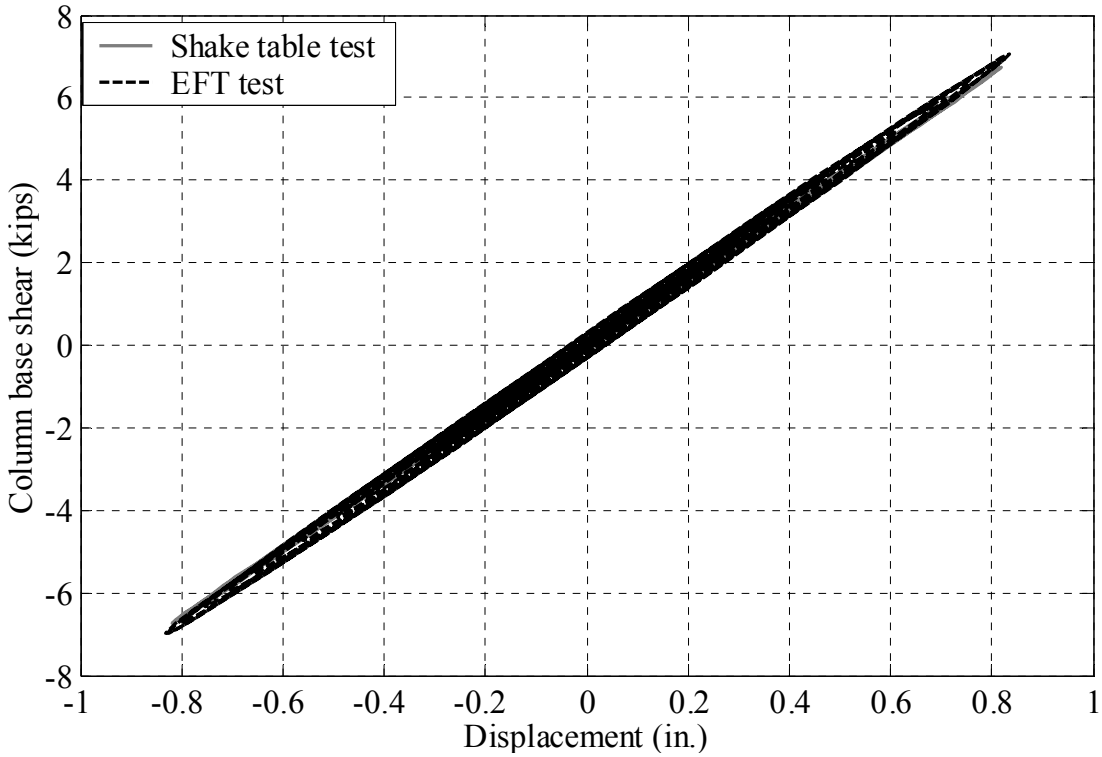

Figure 8.19 Column behavior in tests with 0.13g sinesweep (1-10Hz)

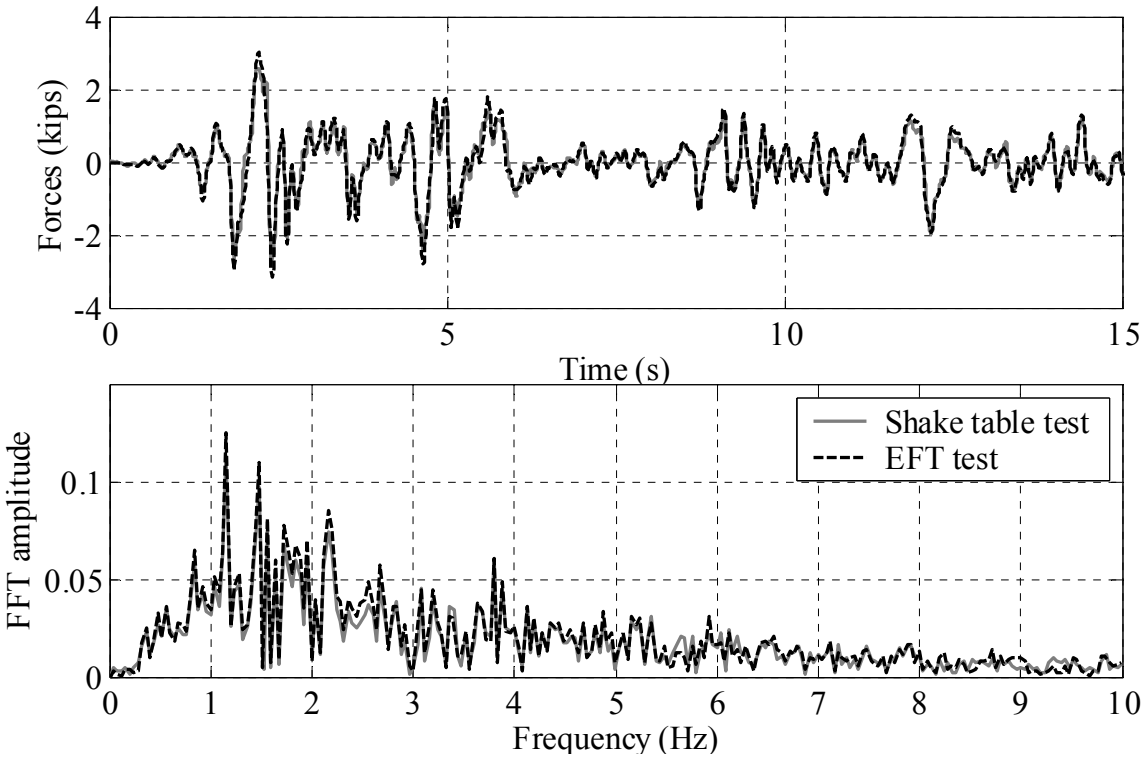

Figure 8.20 Comparison of effective forces from shake table test (mass × measured table acceleration) and measured forces from EFT test (0.29g El Centro)

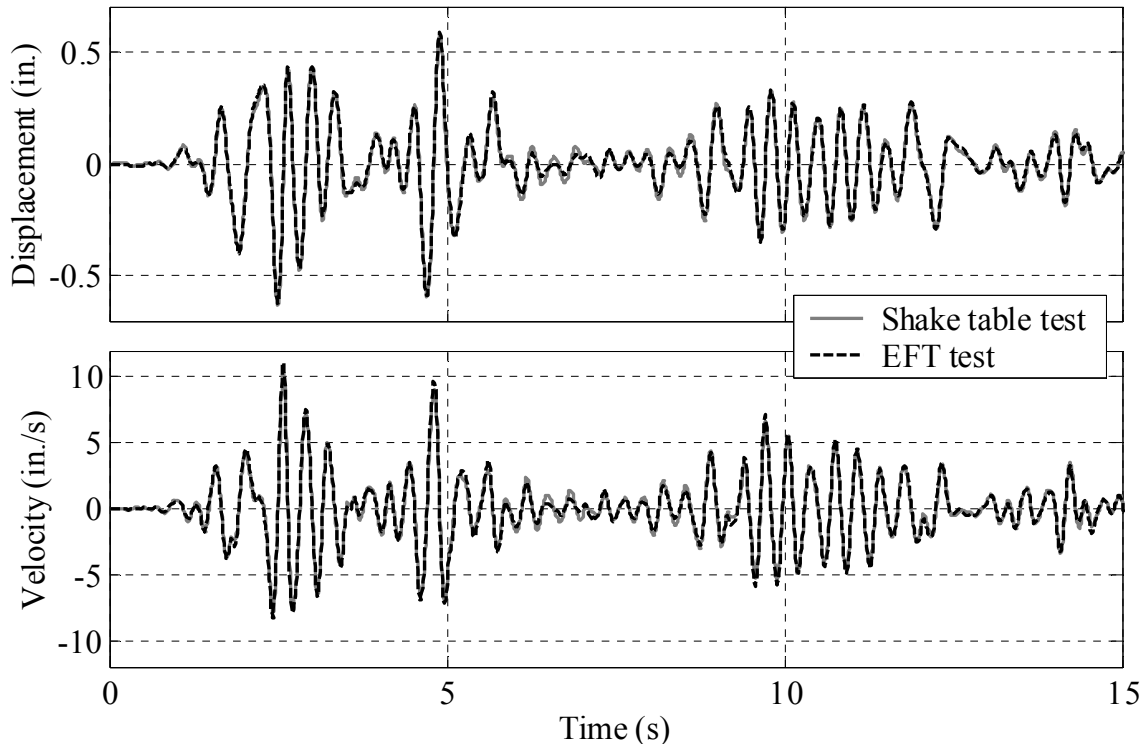

Figure 8.21 Comparison of global structural responses in tests with dampers (0.29g El Centro)

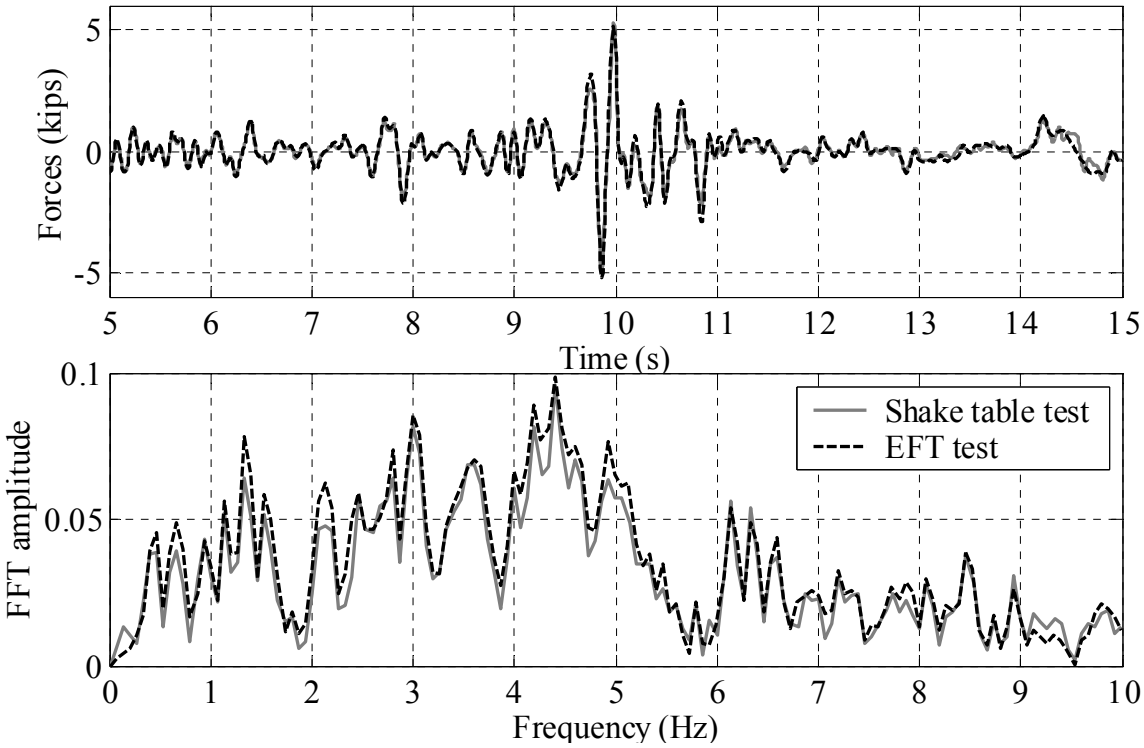

Figure 8.22 Comparison of effective forces from shake table test (mass × measured table acceleration) and measured forces from EFT test (0.55g Northridge)

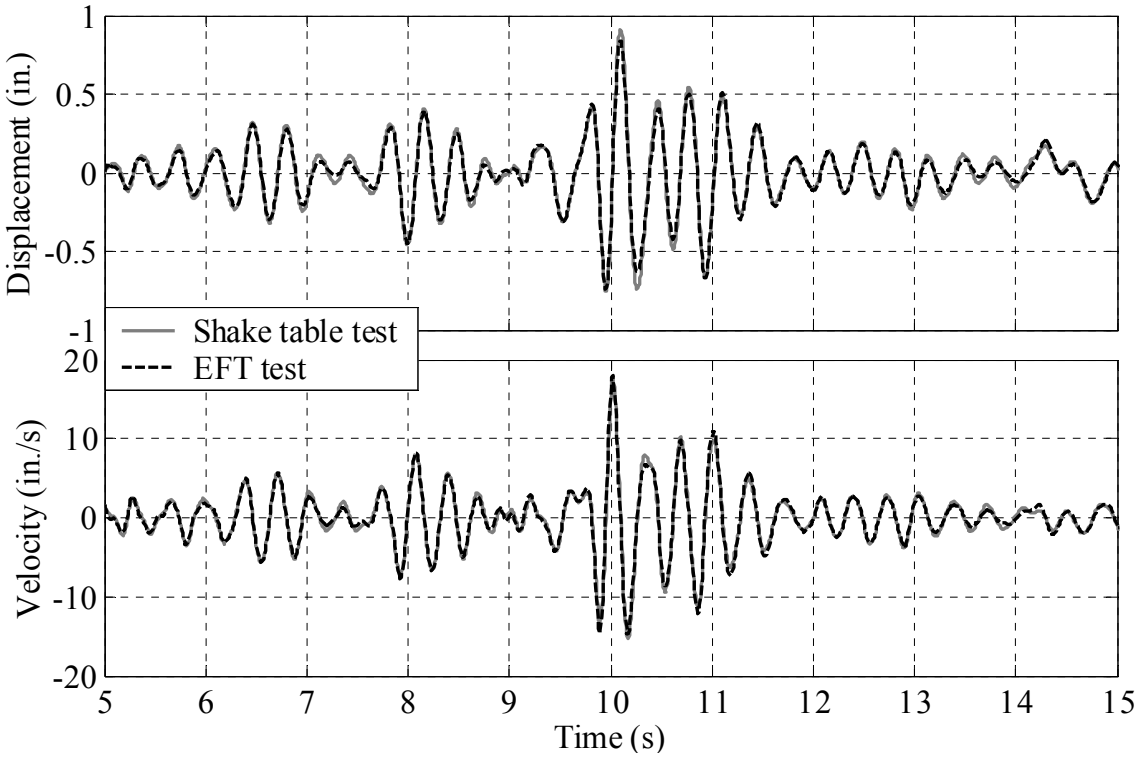

Figure 8.23 Comparison of global structural responses in tests with dampers (0.55g Northridge)

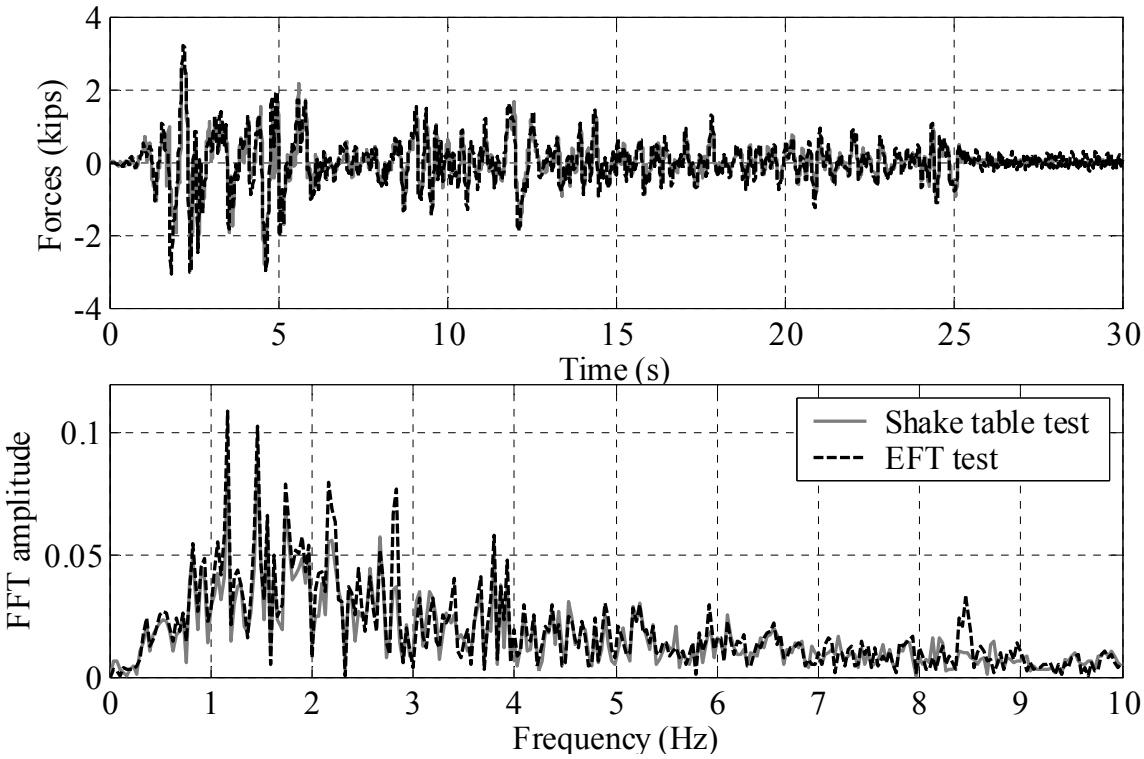

Figure 8.24 Comparison of effective forces from shake table test (mass × measured table acceleration) and measured forces in EFT test without dampers (0.30g El Centro)

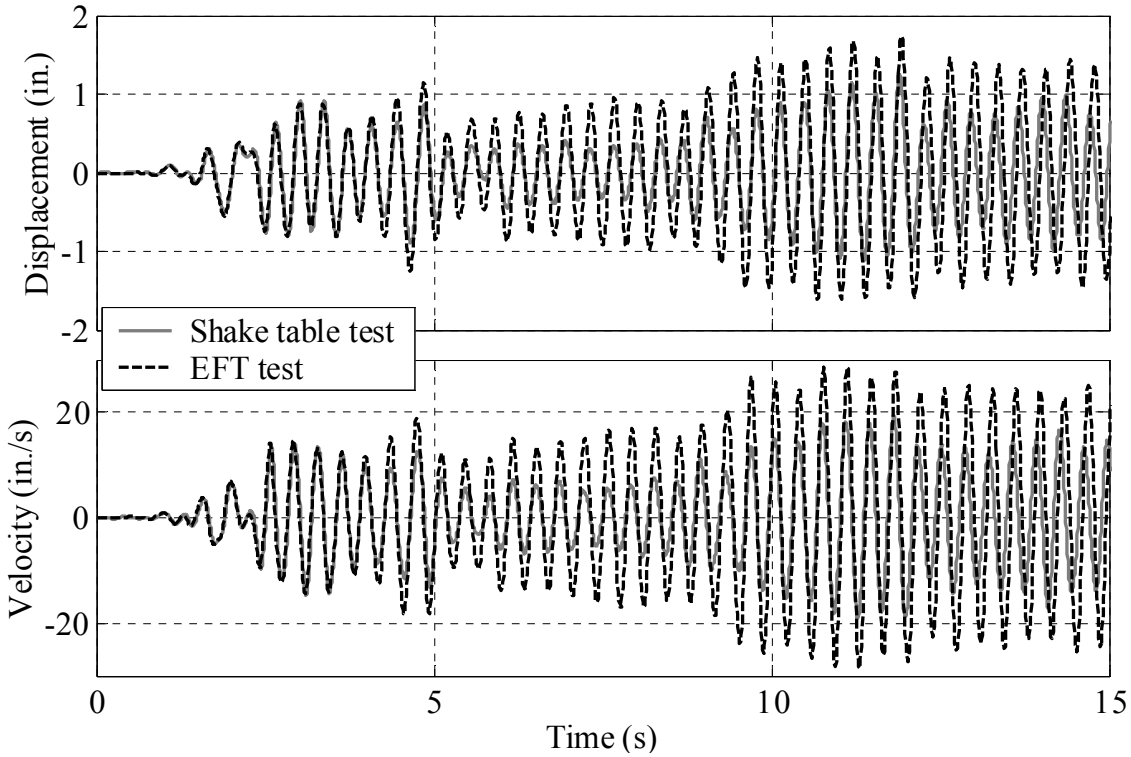

Figure 8.25 Comparison of global structural responses in tests without dampers (0.30g El Centro)

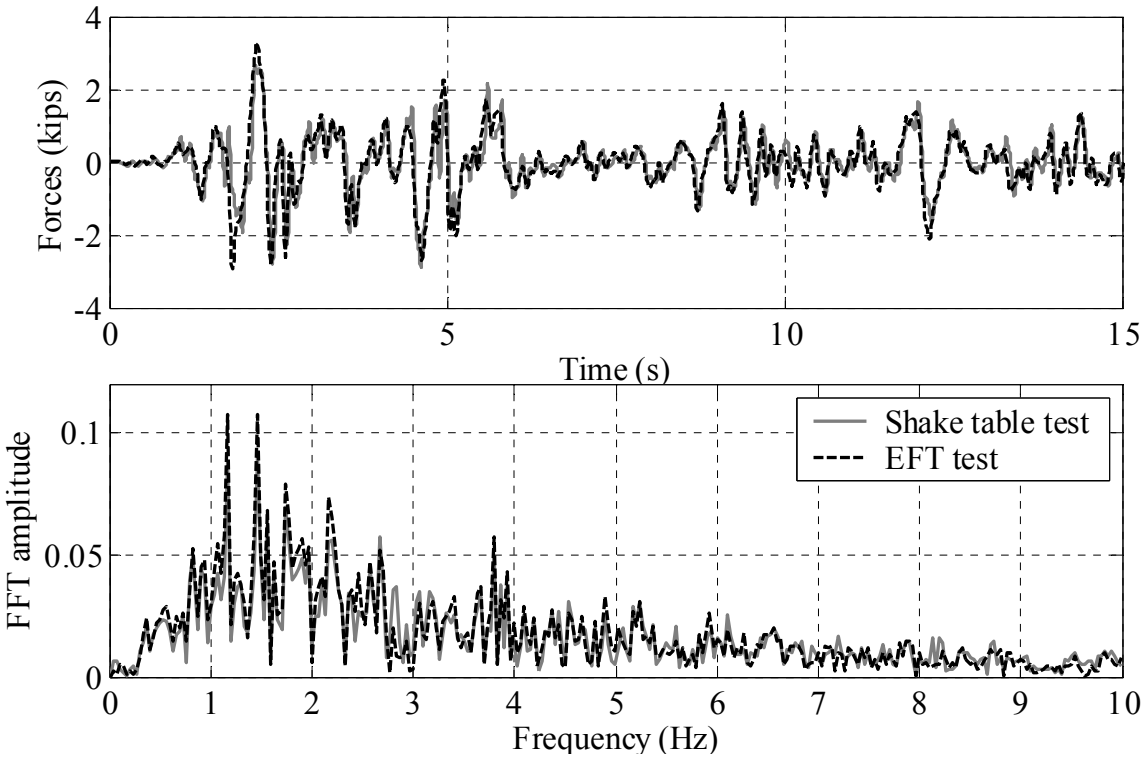

Figure 8.26 Comparison of effective forces from shake table test (mass × measured table acceleration) and measured forces form EFT test with 93% correction (0.30g El Centro)

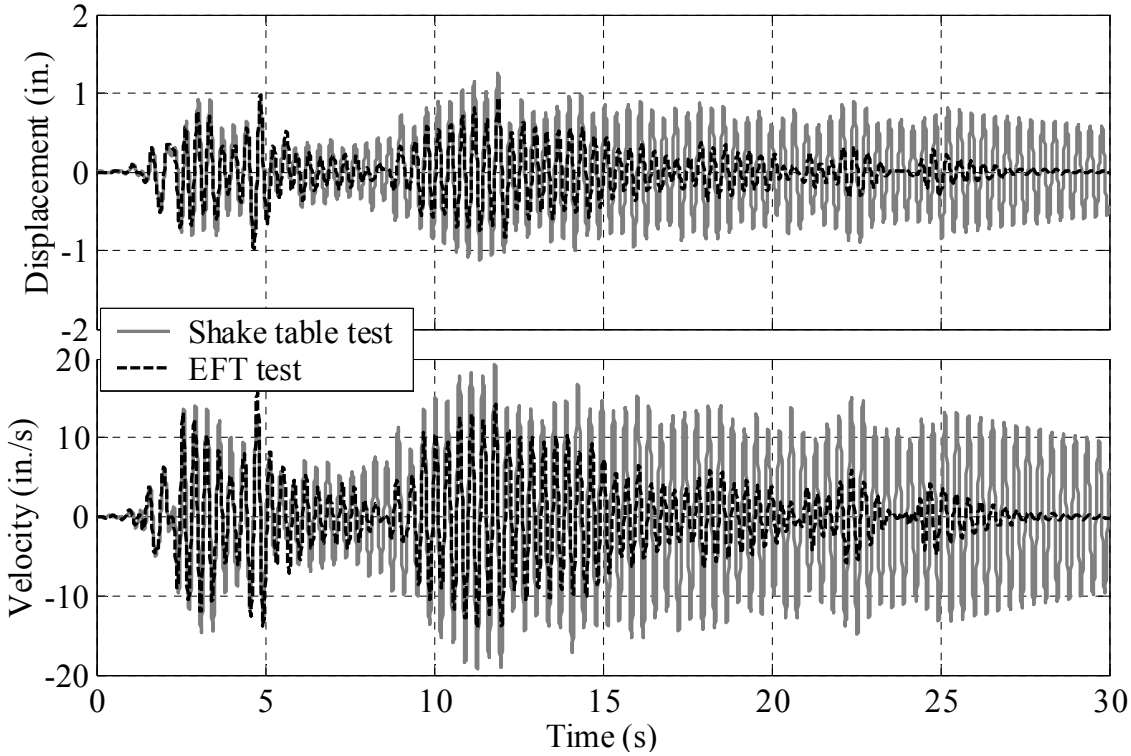

Figure 8.27 Comparison of global structural responses (EFT test with 93% correction) (0.30g El Centro)

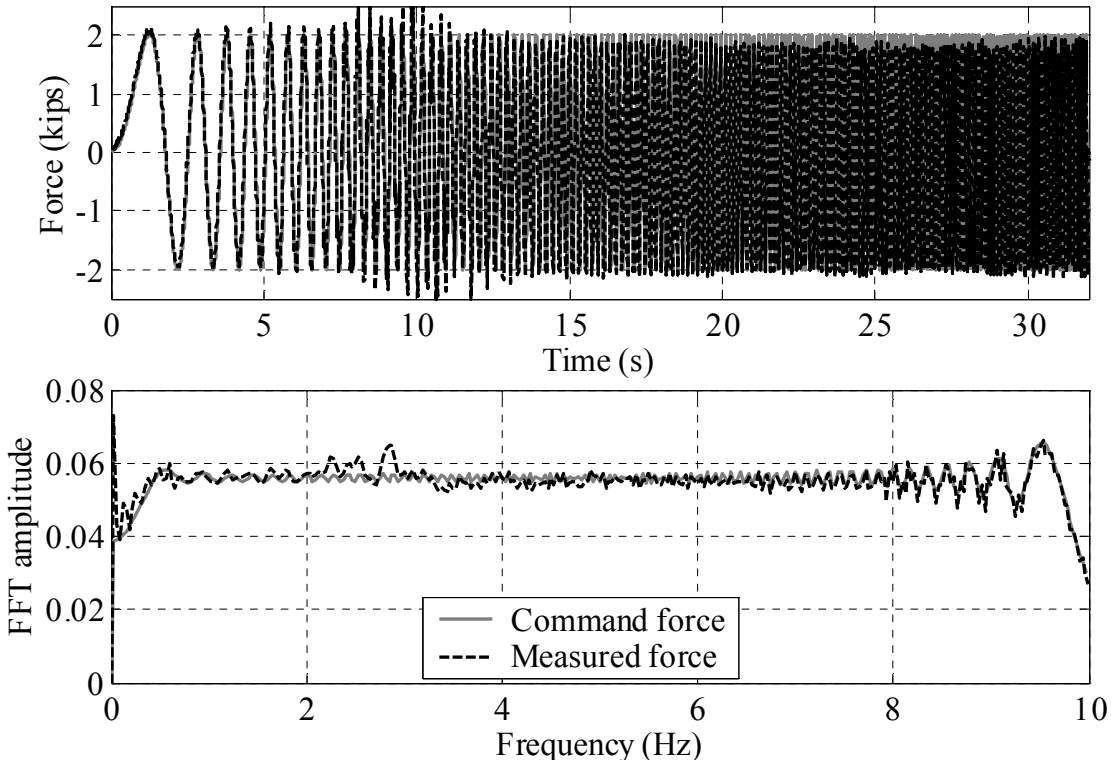

Figure 8.28 Comparison of forces from EFT test with one damper (2k sinesweep)

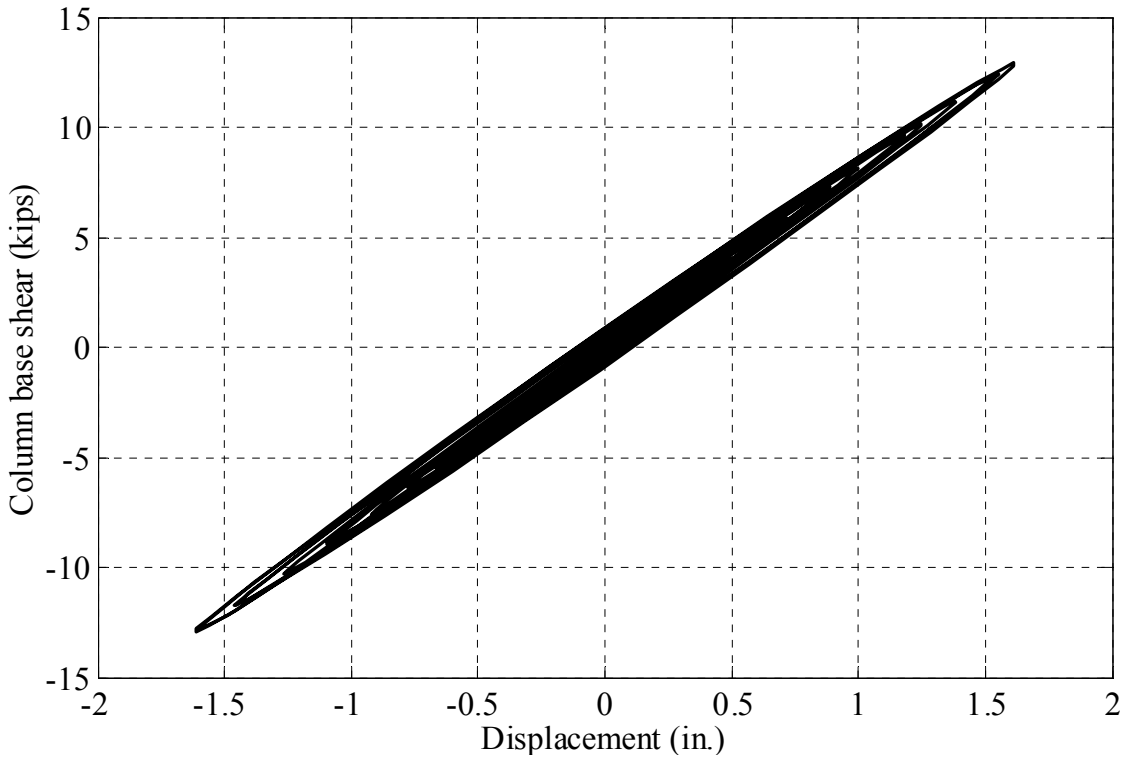

Figure 8.29 Column base shear vs. story drift in EFT test with one damper (2k sinesweep)

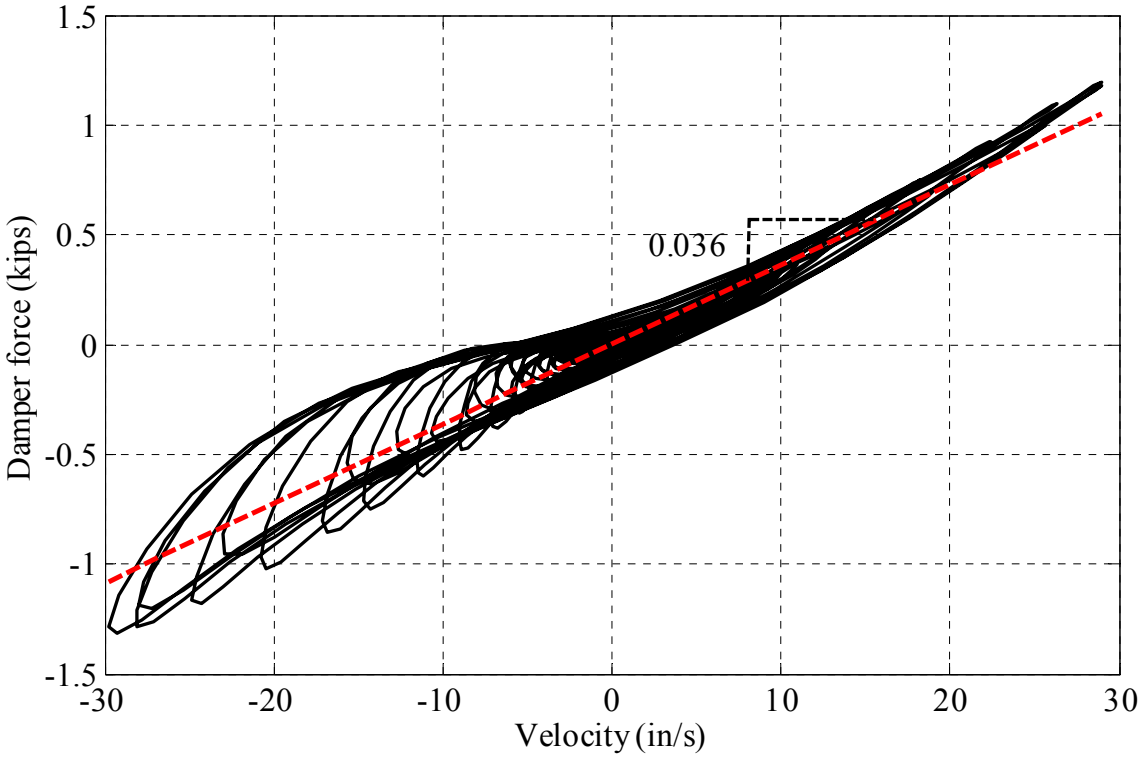

Figure 8.30 Damper force vs. velocity in EFT test with one damper (2k sinesweep)

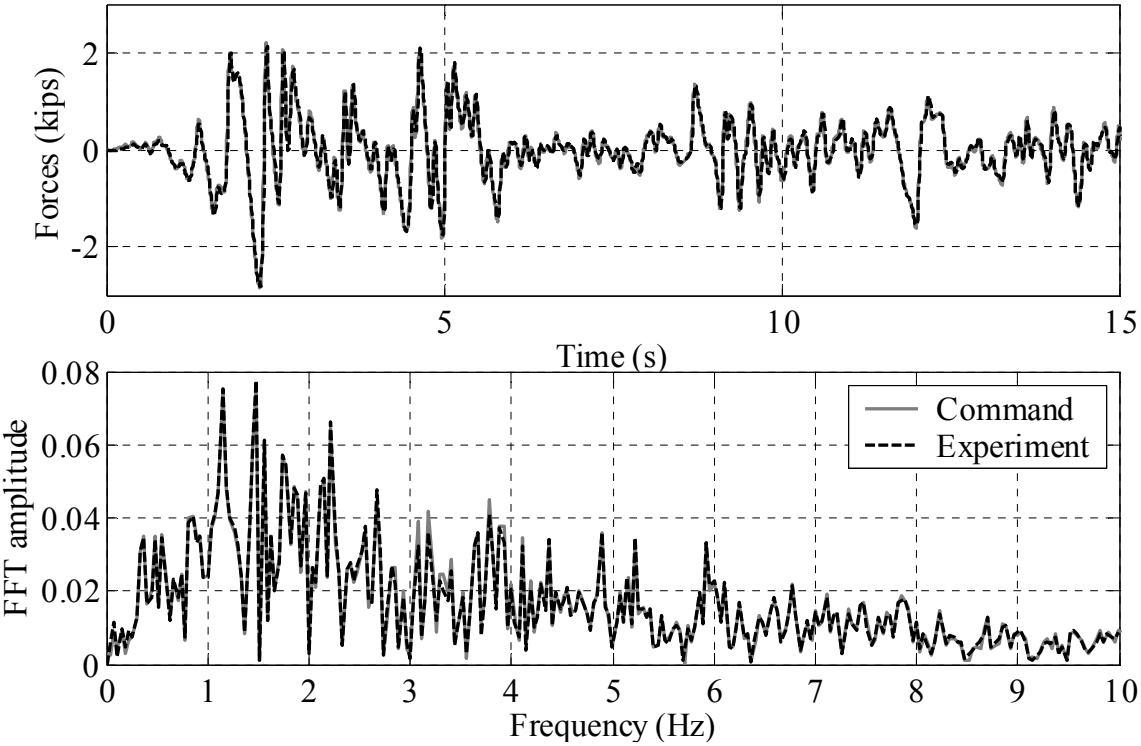

Figure 8.31 Comparison of forces from EFT test with one damper (0.29g El Centro)

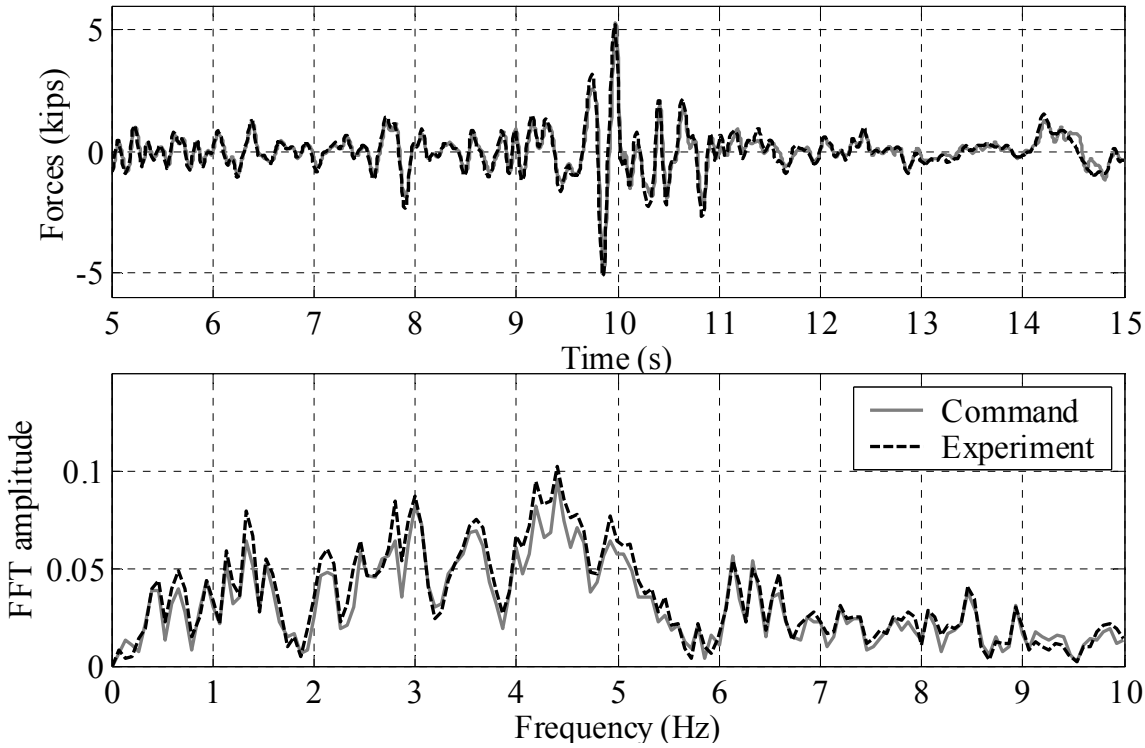

Figure 8.32 Comparison of forces from EFT test with one damper (0.55g Northridge)

APPENDIX 1

A TEST SYSTEM IN DISPLACEMENT CONTROL

To validate the system model developed in Chapter 3 and parameters identified in Chapter 4, the test system was switched to displacement control and analyzed. Figure A1.1 illustrates a block diagram for the system, in which the servovalve/actuator, the structure, and the interaction between them are the same as those of the force-controlled system while the system control is based on the actuator piston displacement instead of the actuator force. The system was tested with a 0.5-inch sinesweep input, and the measured displacement is compared with the displacement command in Fig. A1.2 along with the simulation results. The close match between the simulation and experimental results indicates great accuracy of the models and parameters.

It is of interest to see the effect of the natural velocity feedback and velocity feedback compensation on the displacement-controlled system. The transfer function (G_{xu}) from the command to the displacement output for the system can be derived as

$$G_{xu}(s) = \frac{AK_vC_FK_{vp}G_p}{[(K_as + C_l)(ms^2 + cs + k) + A^2s](\tau A_v s^2 + A_v s + K_3K_{vp})x_{v\max} + AK_vC_FK_{vp}G_p}. \qquad \text{(A1.1)}$$

The system does not have a second-order term corresponding to the structure in the numerator, indicating that the system does not have problems in tracking displacement commands around the natural frequency of the test structure. On the other hand, the transfer function from the command (u) to the applied force (F) is

$$G_{Fu}(s) = \frac{AK_vC_FK_{vp}G_p(ms^2 + cs + k)}{[(K_as + C_l)(ms^2 + cs + k) + A^2s](\tau A_v s^2 + A_v s + K_3K_{vp})x_{v\max} + AK_vC_FK_{vp}G_p}. \qquad \text{(A1.2)}$$

The numerator of G_{Fu} includes the denominator of the test structure, such that the poles of the structure are the zeros of the transfer function. Hence, similar to the force-controlled system, the natural velocity feedback limits the ability of the actuator to apply forces around the natural frequency of the test structure. The inability is demonstrated by a dip at the natural frequency of the test structure in the frequency response of the system shown in Fig. A1.3.

Unlike force-controlled systems, the natural velocity feedback destabilizes the overall system in displacement control. When the displacement command has significant frequency content near the natural frequency of the structure (i.e., the test structure is in resonance), little force is needed for the actuator to follow the displacement command. The natural velocity feedback loop causes the actuator to reduce the force applied to the structure accordingly. In this case, an attempt to compensate for the velocity feedback might destabilize the overall system.

To validate the statement, the system with the natural velocity feedback compensated in a similar way to that discussed in Section 5.2 (direct compensation) was investigated. With a complete compensation, the transfer function G_{Fu} becomes

$$G_{Fu}(s) = \frac{AK_vC_FK_{vp}G_p(ms^2 + cs + k)}{(ms^2 + cs + k)(K_as + C_l)(\tau A_v s^2 + A_v s + K_3K_{vp})x_{v\max} + AK_vC_FK_{vp}G_p}, \quad \text{(A1.3)}$$

and the transfer function G_{xu} becomes

$$G_{xu}(s) = \frac{AK_vC_FK_{vp}G_p}{(ms^2 + cs + k)(K_as + C_l)(\tau A_v s^2 + A_v s + K_3K_{vp})x_{v\max} + AK_vC_FK_{vp}G_p}. \quad \text{(A1.4)}$$

The velocity feedback compensation does not change the zeros of G_{Fu}, indicating that the actuator cannot apply forces at the natural frequency of the structure even with the

velocity feedback compensation. Correspondingly, conjugate zeros at the natural frequency of the structure remain in the compensated system in Fig. A1.4.

An analysis of the denominators of Eqs. (A1.3) and (A1.4) also indicates that the compensated system has two conjugate poles at 17.8 Hz near the imaginary axis as shown in Fig. A1.4. It can be shown that the slightly damped vibration corresponds to the so-called oil-column resonance. The root locus of the system (G_{Fu}) shows that the velocity compensation drives this vibration mode into the unstable region (right-hand side of the *s*-plane). Hence, complete velocity feedback compensation may not be applicable to a system in displacement control.

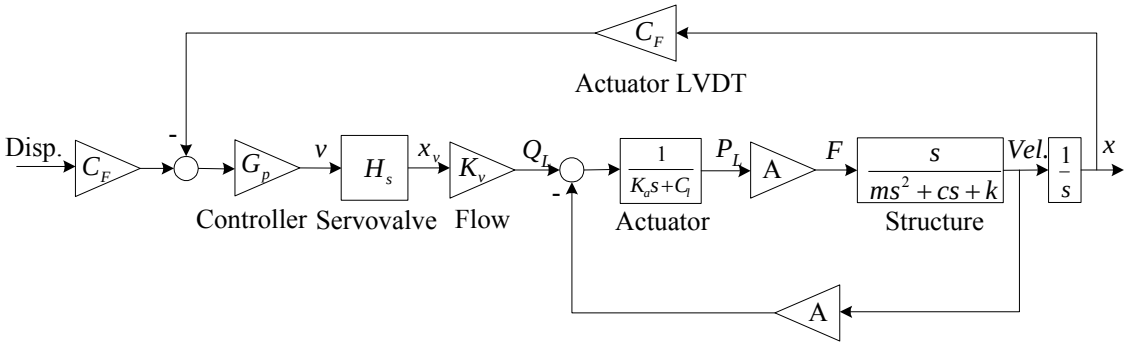

Figure A1.1 Linearized block diagram of test system in displacement control

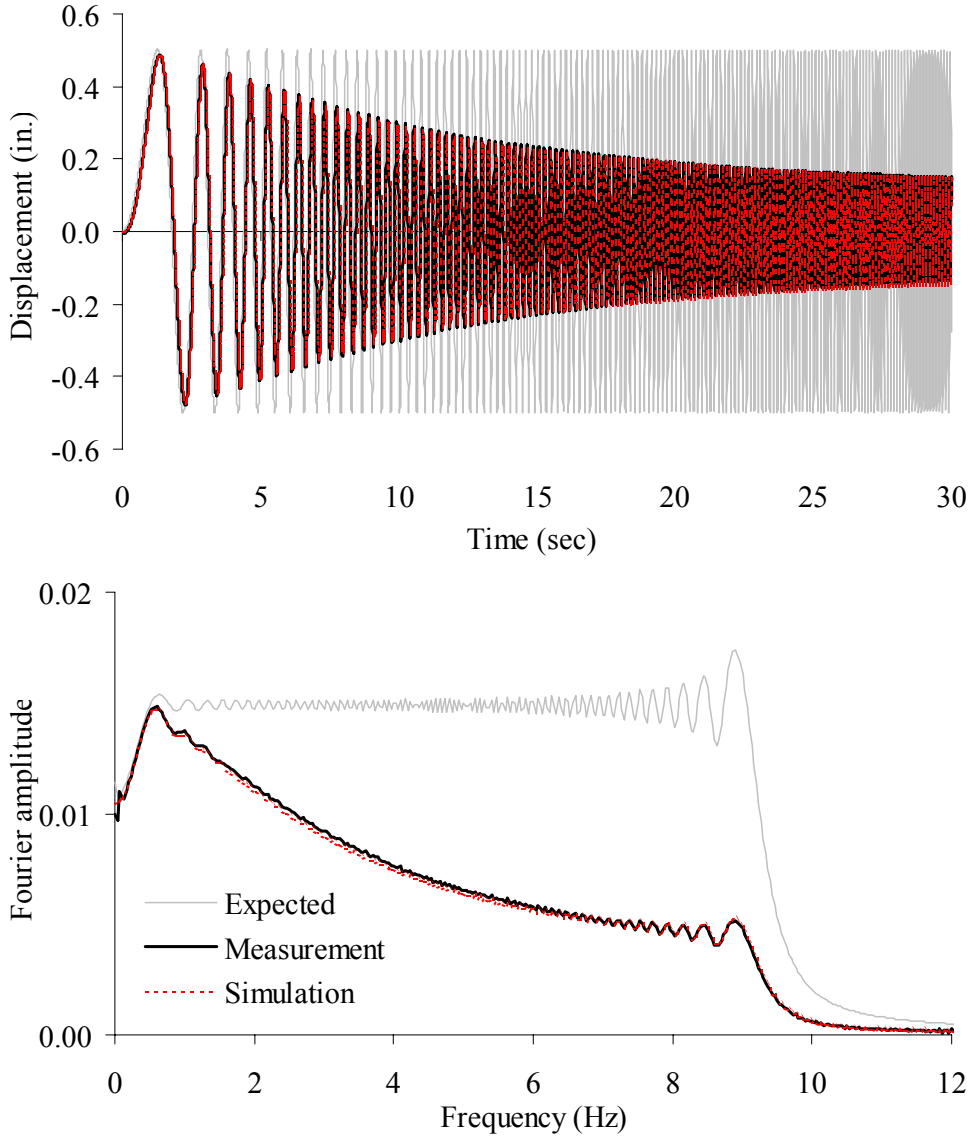

Figure A1.2 Responses of a displacement-controlled system subjected to a 0.5-inch sinesweep input (0-10 Hz)

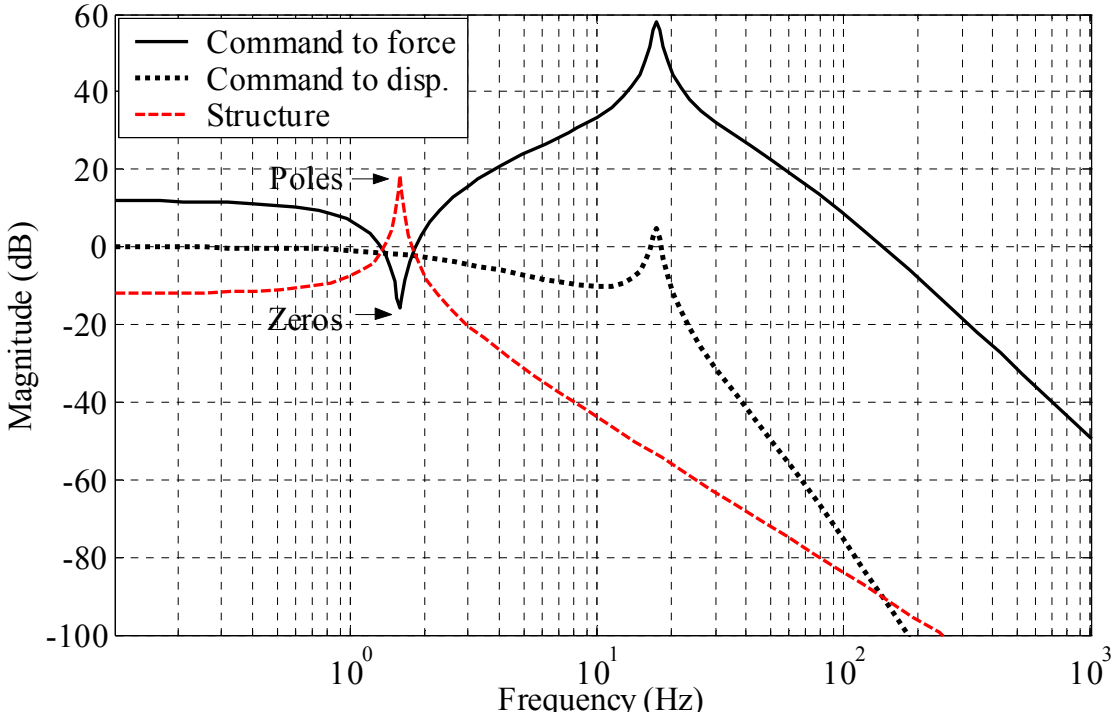

Figure A1.3 Frequency response of the test system in displacement control

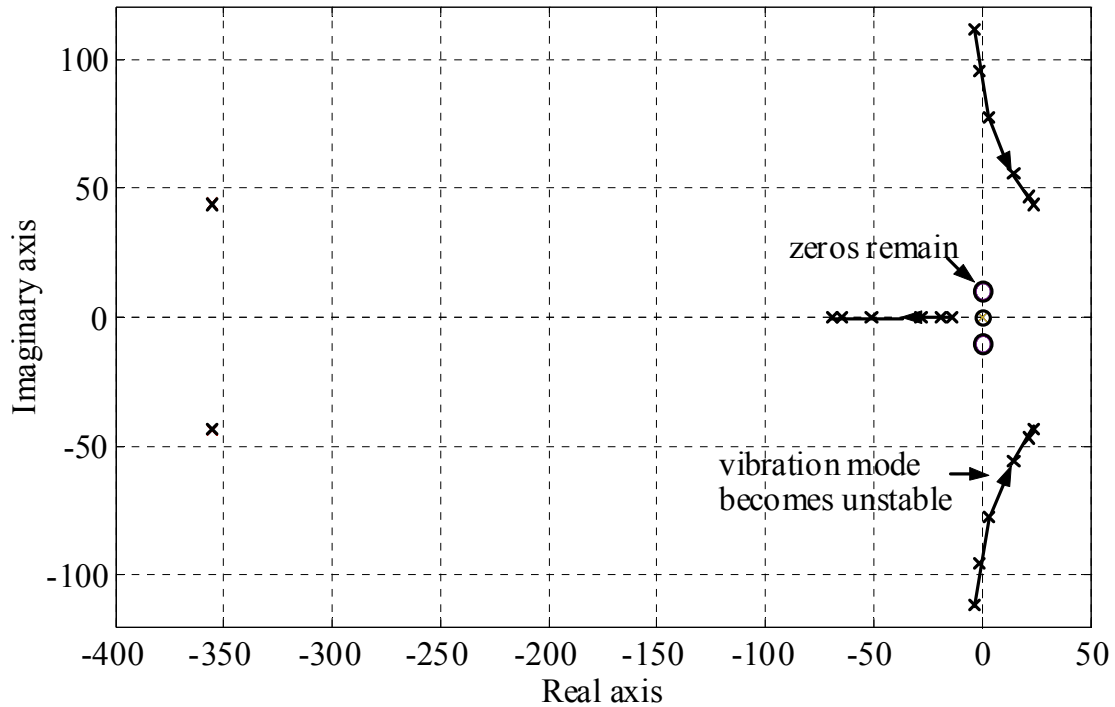

Figure A1.4 Root locus of the displacement-controlled system with respect to percentage ideal velocity feedback compensation (command to force)

APPENDIX 2

NONLINEAR NO-LOAD FLOW GAIN

A typical flow vs. spool opening curve with a pressure drop of 1000 psi across the servovalve and zero load pressure is shown in Fig. 4.8. It can be seen that the flow gain (i.e. the slope of the curve), decreases with an increase in spool opening. Because the no-load flow gain is defined by $K_v = \left(C_d w x_{v\max} \sqrt{1/\rho}\right)\sqrt{P_s}$, and w, $x_{v\max}$, and ρ are fixed quantities, the nonlinearity was attributed to a nonlinear discharge coefficient (C_d).

Theoretical solutions for discharge coefficients are impossible to obtain due to the complex nature of the orifice flow. Experimental results for a submerged orifice (Fig. 2.3) under constant pressure drop across the orifice were chosen to approximate the servovalve orifice flow. As can be seen from Fig. 2.4, the discharge coefficient is a function of the Reynolds number, which in turn is dependent of the orifice geometry and the flow characteristics.

An estimation of the range of Reynolds number is necessary to determine the discharge coefficient for the servovalve orifice in this study. Because the orifices are sharp-edged orifices, it is appropriate to estimate the flow velocity through the orifice by

$$u = \frac{Q_L}{A_{vs}} = \frac{Q_L}{w\tilde{x}_v}. \tag{A2.1}$$

In addition, the spool opening $\tilde{x}_v$ was chosen as the characteristic length of the orifice because the characteristic length is often related to the area of the orifice. Hence,

$$d = \tilde{x}_v. \tag{A2.2}$$

Substituting Eqs. (A2.1) and (A2.2) into Eq. (2.11) yields

$$R = \frac{Q_L}{w\nu}. \tag{A2.3}$$

where w is the area gradient of the main-stage valve spool and ν is the kinematic viscosity of the fluid.

The area gradient of the spool w was estimated using the initial flow gain under a 1000 psi pressure drop across the servovalve. The flow gain was defined in Eq. (3.24) as,

$$K_v = \left.\frac{Q_L}{\tilde{x}_v}\right|_{\tilde{x}_v \to 0} = C_d w \sqrt{\frac{1}{\rho} P_s}\ . \tag{A2.4}$$

Therefore,

$$w = \frac{K_v}{C_d \sqrt{P_s/\rho}} = \frac{(1.6\text{gpm} \times 3.85)/(0.11 \times 0.01)}{0.61\sqrt{1000\text{psi}/0.8 \times 10^{-4}}} \approx 2.6in. \tag{A2.5}$$

In the above calculation, the flow gain had units of in.^{3}/s/in., the pressure supply was the pressure difference across the valve. A discharge coefficient of 0.61 was used because it can be a good approximation for any sharp-edged orifice (Merritt 1967).

It was assumed that the initial flow gain was valid up to 10% spool opening, which corresponds to a flow of 26 gpm (100 in.^{3}/s) under a 3000 psi pressure drop. In addition, a flow rate of 120 gpm (462 in.^{3}/s) was the maximum that could be obtained with the servo-system in this study as shown in the identified flow curve in Chapter 4. Therefore, the flow through the servovalve orifice was estimated between

$$100in.^3/s < Q_L < 462in.^3/s\ . \tag{A2.6}$$

Using Eqs. (A2.5) and (A2.6) in Eq. (A2.3), the range of the Reynolds number was estimated using Eq. (A2.3) as: $665 < R_e < 3064$. Based on Fig. 2.4, the discharge

coefficient was estimated between

$$0.74 > C_d > 0.65. \tag{A2.7}$$

Because the discharge coefficient was larger than the assumed average value (0.61), an upgraded average value of the discharge coefficient (0.7) was plugged into Eq. (A2.5) to estimate the area gradient. The new value, 2.27 in., was very close to the actual spool perimeter obtained from the servovalve manufacturer. Following the same procedure shown above, the range of Reynolds number was determined as

$$760 < R_e < 3509, \tag{A2.8}$$

which slightly changed the range of discharge coefficient shown in Eq. (A2.7).

Therefore, the discharge coefficient of the servovalve orifice decreases with an increase in servovalve flow. The reduced discharge coefficient results in a decreased servovalve flow gain for an increase in spool opening. In addition, the flow property of a servovalve can be affected by other uncertainties in the system, such as the hydraulic supply pressure drop as the hydraulic demand (consumption) increases. Therefore, it is not practical to derive a closed-form solution of the discharge coefficients as a function of spool opening, and the actual servovalve flow property (the no-load flow gain) must be determined experimentally.

APPENDIX 3

A PROCEDURE FOR THE IMPLEMENTATION OF EFT

To implement the effective force testing method, in addition to a servo-hydraulic controlled actuator and a data acquisition system, the following hardware is required: a velocity transducer for velocity feedback compensation (cable extension type), a unit buffer (analog circuit) for powering the velocity signal, a Digital Signal Processor (DSP) and its host computer. This section presents a typical procedure for testing structures using the EFT method. Note that the discussion shown below includes some quantities based on experiences gained in this study.

The implementation of the velocity feedback compensation requires the identification of the forward dynamics of the servovalve and its controller, which contains three major components: the PID control with a zero I gain described by,

$$H_c = \frac{1}{G_d s + G_p}, \tag{A3.1}$$

where G_p and G_d are the proportional and derivative gain of controller, respectively; the second-order servovalve dynamics by,

$$H_s = \frac{K_{vp}}{\tau A_v s^2 + A_v s + K_3 K_{vp}} \frac{1}{x_{v\max}}, \tag{A3.2}$$

where τ is the equivalent time constant of the pilot-stage valve, K_{vp} is the pilot-stage valve flow gain, A_v is the main-stage spool area, K_3 is the sensitivity factor of the internal LVDT, and $x_{v\max}$ is the maximum spool stroke; and the nonlinear servovalve flow property stated by

$$Q_L = K_v x_v \sqrt{1 - \frac{x_v}{|x_v|}\frac{P_L}{P_s}} \tag{A3.3}$$

where K_v is the no-load flow gain of the servovalve, x_v is the spool opening of the servovalve, P_L is the load pressure ($P_L A$ is approximately the force applied to the structure, and A is the actuator piston area), and P_s is the supply pressure.

Match Test and Equipment Capacity

Equipment capacity includes the load capacity of an actuator and the flow capacity of its servovalve. The load capacity of an actuator can be found in its product specification (e.g., 35 kips for the MTS 244.23 actuator), or estimated by 90% of the supply pressure times the actuator piston area. The servovalve flow capacity can be estimated as $Q_{\text{rated}}\sqrt{0.9P_s/P_{\text{srated}}}$, where Q_{rated} is the rated flow of the servovalve at a pressure drop of P_{srated} across the servovalve (e.g., 90 gpm for the MTS 256.09 three-stage servovalve under 1000 psi) and P_s is the supply pressure (roughly 3000 psi in this study). The calculated flow capacity is limited by other factors in the hydraulic system, such as the capacity of the pump and service manifold, and the diameter of hydraulic supply hoses. Accurate flow capacity of a servovalve can be obtained as presented later.

During an EFT test, the maximum structural velocity should be smaller than 80% of the servovalve flow capacity divided by the actuator piston area, and the maximum effective force should be smaller than 50% of the actuator load capacity. If the maximum force likely happens at the same moment as the maximum velocity (i.e., the effective force input has significant content near the resonant frequency of the test structure), the maximum spool opening should be smaller than 60%. Refer to Spink (2002) for an actuator/servovalve sizing technique.

Identify Structural Properties

Static loading tests and free vibration tests can be used for structure identification. Note that the effective force command is directly related to the structure mass, and errors in the estimation would affect the force applied to the structure and potentially the nonlinear structural behavior. In addition, the stability of the test system is related to the structural damping. Testing of a structure with a minimum of 2% critical damping using EFT can be conducted with reasonable confidence. The identified structural properties can be used to estimate the peak structural responses for the capacity check of equipment and sensors.

Identify Servovalve Dynamics

To invert the servovalve dynamics for the velocity feedback compensation, the valve gain (K_s) and the response delay (T_d) are required. The second-order servovalve model shown by Eq. (A3.2) requires many valve parameters such as valve spool area and the maximum spool stroke. If the parameters were not available, a measured frequency response could be used to estimate the parameters for an equivalent second-order model,

$$H_s = \frac{K_s}{\frac{1}{\omega_v^2}s^2 + \frac{2\zeta_v}{\omega_v}s + 1}. \tag{A3.4}$$

A test was conducted to generate a frequency response plot, in which the actuator was in displacement control, and the actuator piston was kept in its neutral position (the hydraulic supply to the main-stage valve was turned off). The proportional gain of the servovalve controller was set to unity and the derivative gain set to zero, such that the valve command signal could be controlled without additional equipment. A small amplitude (20% spool opening) sinesweep input (0-100 Hz in 100 seconds) was chosen

as the command signal.

Matlab® function *fft(x)* was used to calculate the Fourier transform (FFT) of the measured input and output signals. For a series of samples x with a length N and a sample frequency h (Hz), function *fft*(x) results in a series of complex numbers with the same length. The first half of the transformed data corresponds to frequencies from zero to $h/2$ with an interval of h/N. The magnitude response of the system can be constructed by plotting the ratio of the magnitude of the FFT of the output signal to the magnitude of the FFT of the input signal against the frequency; the phase response of the system can be constructed by plotting the phase difference between the two transformed signals against the frequency.

Figure A3.1 presents a measured frequency response of the servovalve. The amplitude corresponding to the asymptotical line of the magnitude response gave a valve gain (K_s) of 0.1. The frequency corresponding to the 90°-phase point indicated an equivalent natural frequency (ω_v) of 58 Hz. The corresponding amplitude is 63%, indicating an equivalent damping (ζ_v) of 80% ($1/(2\times 0.63)$). The frequency response of the identified second-order model was compared with the experimental results and that of Eq. (A3.2) in Fig. A3.1. Although a better match is evident with the identified system across the whole frequency range (0-100 Hz), it can be shown that Eq. (A3.2) better fit the experimental frequency response at low frequencies (0-20 Hz). The time delay was usually underestimated using $2\zeta_v/(2\pi\omega_v)$ (e.g., 4.4 ms in this case), because pilot-stage valve flow gain may reduce with an increase in hydraulic demand (spool opening). Nevertheless, the obtained delay time can be a good approximation, and the obtained

servovalve model can be used in the system stability analysis.

Identify Servovalve Flow Property

With an estimated pressure supply (0.9 P_s), the initial flow gain (K_v) was estimated based on the related initial flow gain, which is usually documented in the product specification. The nonlinear flow curve was identified experimentally using a series of tests with sinusoidal commands, in which the actuator was in displacement control. The structure was detached form the actuator such that the pressure difference across the actuator piston (load pressure) was negligible. The spool opening was obtained directly by measuring the inner-loop feedback while the corresponding flow was calculated by the piston velocity multiplied by the piston area. The piston velocity was calculated using the central difference method from the measured piston displacement.

Although the frequency of the sinusoidal displacement command can be determined through trial and error, the following discussion provides a guideline for selecting the frequency such that the valve command can be controllable. A block diagram of a linearized model of the test system with the actuator running in the air is presented in Fig. A3.2. The transfer function of the system from command (u) to DC error (e) is

$$G_{eu} = \frac{As}{As + C_F G_p K_s K_v}. \tag{A3.5}$$

As can be seen, the error (valve command) increases with an increase in the input frequency. A frequency, at which the error is 90% of the command was chosen as the frequency of the sinusoidal command. Hence, the frequency ω was obtained by solving

$$\left|G_{eu}\right| = \frac{A\omega}{\sqrt{\left(A\omega\right)^2 + \left(C_F G_p K_s K_v\right)^2}} = 0.9. \tag{A3.6}$$

The frequency was calculated as 5.2 Hz with the previously obtained initial flow gain (1003 in^3/s). On the other hand, the servovalve flow gain decreases as the spool opening increases; hence, the slope of the line connecting the origin and the related flow point (600 in^3/s) was used to re-calculate the frequency. The estimation resulted in a frequency of 3.1 Hz, and 3 Hz was used in the tests.

Tests with 90% (4.5 in.), 80% (4 in.), 60% (3 in.), 40% (2 in.), and 20% (1 in.) full stroke were conducted, and the flow curve up to 80% spool opening were obtained as the average of these individual curves. The result of the identification process is shown in Table A3.1, in which linear extrapolation was used to generate the points beyond the 80% spool opening.

Determine the Maximum Controller P Gain

A large P gain improves the overall performance of the test system, while it may render the system into unstable region. The maximum controller P gain was obtained through by analyzing the system stability as shown below (Mathematica® 4.0 was used).

Linearized system model:

$$Gs[s\_] = \frac{Kvp}{\tau\, Av\, s^2 + Av\, s + Kvp\, K3}\,\frac{1}{xv2}$$

$$G1[s\_] = CF\, Gp\, Gs[s]\, Kv$$

$$Ga[s\_] = \frac{A\,(m\,s^2 + c\,s + k)}{(Ka\,s + Cl)\,(m\,s^2 + c\,s + k) + A^2\,s}$$

$$Gload = \frac{G1[s]\,Ga[s]}{1 + G1[s]\,Ga[s]}$$

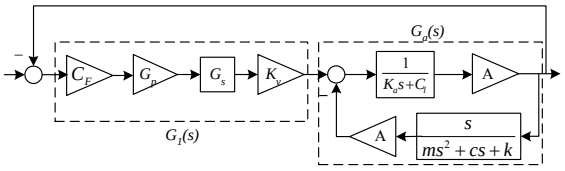

Coefficient of characteristic function:

```
a5 = Coefficient[Denominator[Simplify[Gload]], s, 5]
a4 = Coefficient[Denominator[Simplify[Gload]], s, 4]
a3 = Coefficient[Denominator[Simplify[Gload]], s, 3]
a2 = Coefficient[Denominator[Simplify[Gload]], s, 2]
a1 = Coefficient[Denominator[Simplify[Gload]], s, 1]
a0 = Coefficient[Denominator[Simplify[Gload]], s, 0]
```

s^5	a_5	a_3	a_1
s^4	a_4	a_2	a_0
s^3	b_1	b_2	0
s^2	c_1	c_2	
s^1	d_1		

Routh's stability array

$$Av\, Ka\, m\, xv2\, \tau$$

$$Av\, Ka\, m\, xv2 + Av\, c\, Ka\, xv2\, \tau + Av\, Cl\, m\, xv2\, \tau$$

$$Av\, c\, Ka\, xv2 + Av\, Cl\, m\, xv2 + K3\, Ka\, Kvp\, m\, xv2 + A^2\, Av\, xv2\, \tau + Av\, c\, Cl\, xv2\, \tau + Av\, k\, Ka\, xv2\, \tau$$

$$A\, CF\, Gp\, Kv\, Kvp\, m + A^2\, Av\, xv2 + Av\, c\, Cl\, xv2 + Av\, k\, Ka\, xv2 + c\, K3\, Ka\, Kvp\, xv2 + Cl\, K3\, Kvp\, m\, xv2 + Av\, Cl\, k\, xv2\, \tau$$

```
A c CF Gp Kv Kvp + Av Cl k xv2 + A^2 K3 Kvp xv2 + c Cl K3 Kvp xv2 + k K3 Ka Kvp xv2
A CF Gp k Kv Kvp + Cl k K3 Kvp xv2
```

System parameters:

```
CF = 0.25; Kv = 1003; Ka = 0.3182; A = 12.73; Ks = 0.1; Cl = 5.5;
τ = .0014; Kvp = 0.644; Av = 0.3044; K3 = 90.91; xv2 = 0.11; m = 0.0399; c = 0.027; k = 3.9518;
```

Determine maximum controller P gain (G_p)

```
b1 = Expand[(a4 a3 - a5 a2) / a4]
b2 = Expand[(a4 a1 - a5 a0) / a4];
Solve[b1 == 0, Gp]
{{Gp → 0.781878}}
c1 = Expand[(b1 a2 - b2 a4)]
c2 = a0;
Solve[c1 == 0, Gp]
{{Gp → -0.0226048}, {Gp → 0.717729}}
d1 = Expand[c1 b2 - b1 c2]
Solve[d1 == 0, Gp]
{{Gp → -21.4791}, {Gp → -0.0232171}, {Gp → 0.711336}}
```

Therefore, the controller P gain (G_p) needs to be smaller than 0.71. Note that the theoretical limit was calculated based on a 5.5 in.^{3}/s/ksi leakage. A larger controller P gain might be applicable if the system leakage were greater than the assumed value.

Tests with Small Amplitude Sinesweep Input

Small amplitude tests with linearized velocity feedback compensation before real tests were conducted to find out if the identified parameters were accurate. If the P gain were too large, a high frequency vibration would be excited even with zero command. If the flow curve underestimates the real flow property of the servovalve, a large amplitude spike would result at the natural frequency of the test structure or the system might become unstable with vibration at the resonant frequency of the structure. On the other hand, tests based on an underestimated flow curve would have a sharp amplitude drop at the natural frequency of the structure. With insufficient delay compensation, a peak before a valley appeared in the FFT of the measured force while a peak after a valley appeared in the frequency domain when the delay was overcompensated. In addition, if

the test results indicated that the measured force was below the command across the whole frequency range (due to constant leakage), a factor greater than unity could be applied to the effective force command to compensate for the effect.

Table A3.1 Identified flow property of servovalve

spool	4.5 in.	4.0 in.	3.0 in.	2.0 in.	1.0 in.	Average
-1.0						-536.17
-0.9						-508.20
-0.8	-480.23					-480.23
-0.7	-451.58	-452.95				-452.26
-0.6	-421.14	-418.66				-419.90
-0.5	-377.87	-378.40	-374.90			-377.05
-0.4	-324.33	-324.78	-323.40			-324.17
-0.3	-258.76	-260.20	-262.71	-262.04		-260.93
-0.2	-185.68	-186.82	-187.78	-192.67		-188.24
-0.1	-98.81	-99.43	-100.05	-102.97	-103.62	-100.98
0.0	0.00	0.00	0.00	0.00	0.00	0.00
0.1	100.17	100.68	101.20	103.87	105.28	102.24
0.2	185.17	185.85	186.45	191.19		187.16
0.3	258.73	260.02	262.02	261.00		260.44
0.4	321.32	322.19	319.87			321.13
0.5	372.72	372.50	364.29			369.83
0.6	412.53	409.88				411.20
0.7	441.91	440.00				440.96
0.8	468.31					468.31
0.9						495.67
1.0						523.02

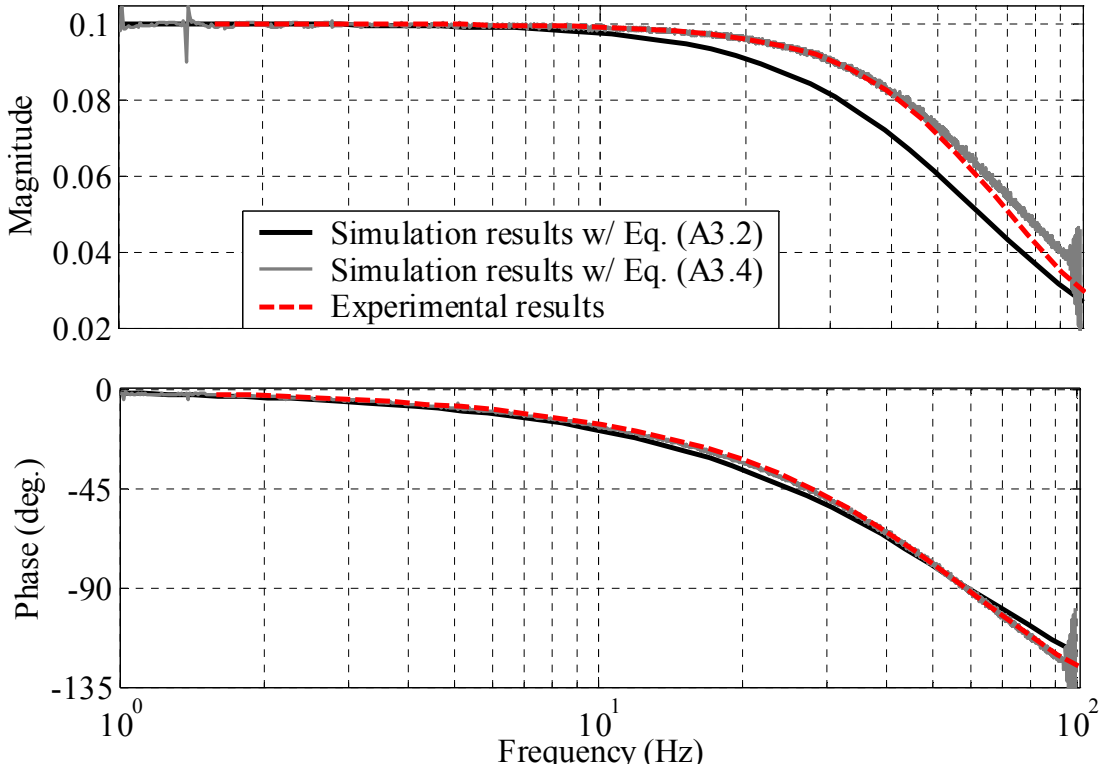

Figure A3.1 Frequency response of the estimated second-order servovalve model

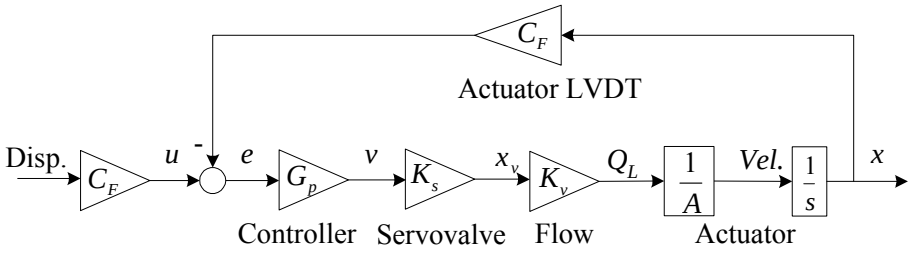

Figure A3.2 Test system with actuator running in the air

APPENDIX 4

DETAILS OF THE SIMPLIFED SDOF STRUCTURE

The SDOF structure consisted of a cart (mass) and four springs, two on each side of the mass. The cart consisted of three rectangular steel frames filled with reinforced concrete and bolted on the top of four caster wheels as shown in Fig. A4.1. Springs were type UM-1000 from Belts Spring Company, San Leandro, CA with a nominal stiffness of 1 kip/in. and 6-inch travel length. The connection between the springs and the reaction frames is shown in Fig. A4.2. The springs were precompressed by 1 in. The precompression was enacted as follows: starting from the null position of the actuator piston, the actuator was commanded to have positive 1 inch offset (the cart was pulled back by 1 inch). The connections of the springs on the opposite side were adjusted such that the springs touched the mass. Then the actuator was commanded to have negative 1 inch offset, and the connections of the springs at the actuator side were adjust such that that the springs touched the mass. Finally, when the actuator went back to its null position, all springs were compressed by 1 inch. A maximum cart (mass) displacement of 4 in. was set in the servovalve controller to avoid damage of the springs due to extensive deformation.

Load was applied to the SDOF model with a 35 kip actuator controlled by a 90 gpm three-stage servovalve. The actuator reacted against a loading frame bolted to the laboratory strong floor. The connections of the actuator swivel heads with the mass and the reaction frame are shown in Fig. A4.3. Finally, the configuration of the "additional leakage passage" discussed in Section 6.6.1 is illustrated by dashed lines in Fig. A4.4.

Figure A4.1 Three steel frames filled with concrete atop four caster wheels

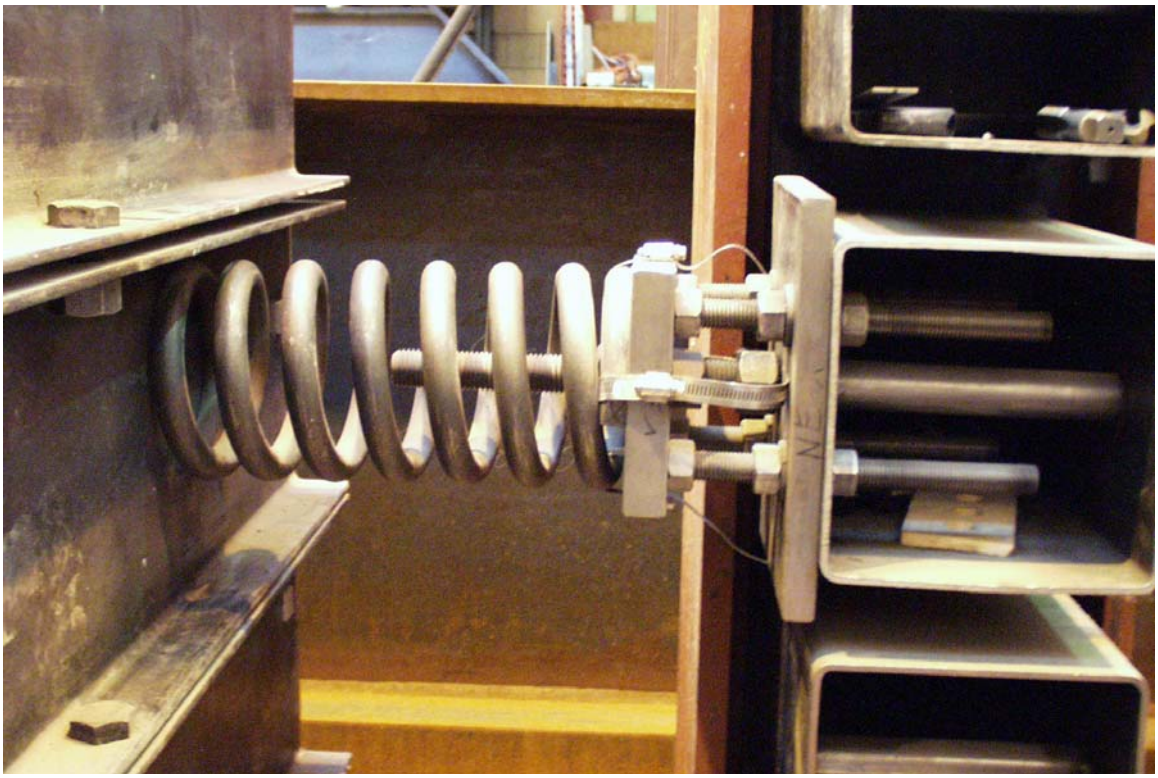

Figure A4.2 A detailed spring connection

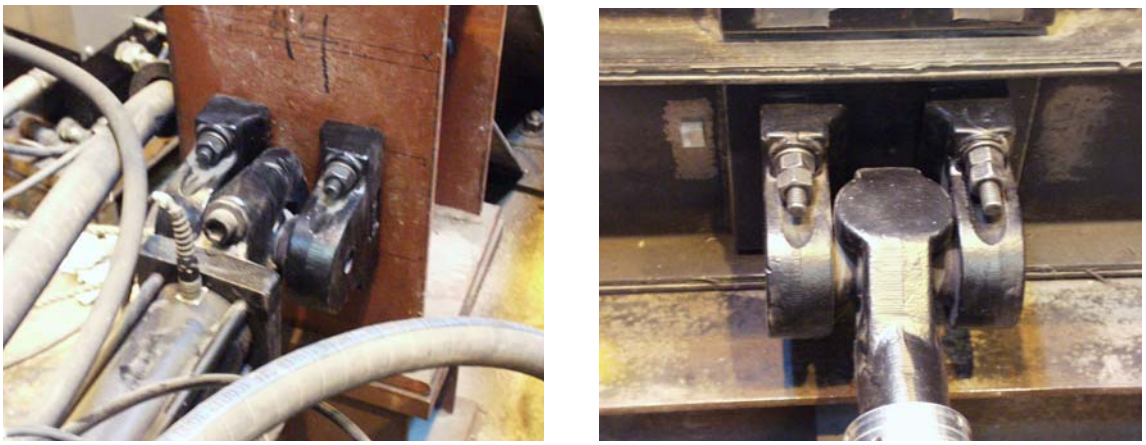

Figure A4.3 Connection of the actuator

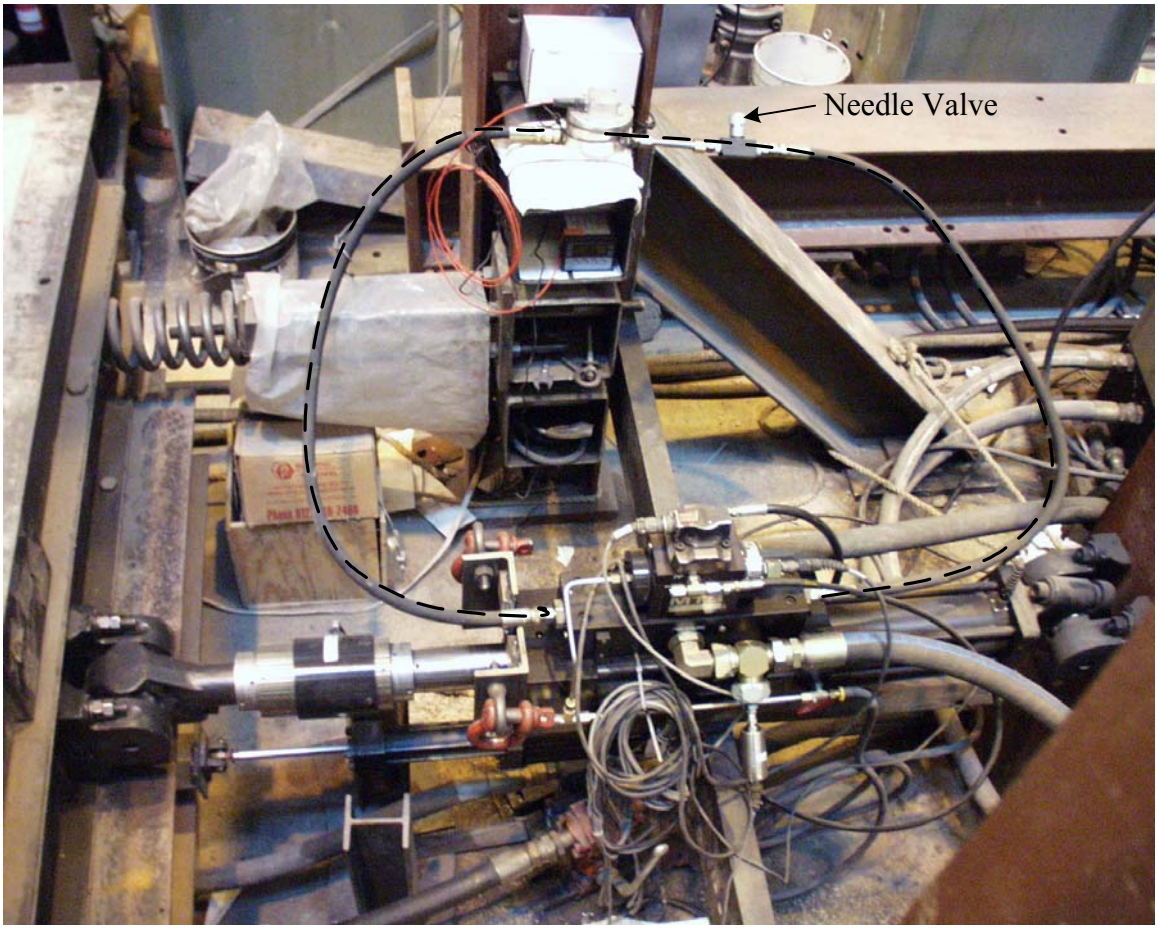

Figure A4.4 Connection of the additional leakage passage

APPENDIX 5

SAMPLE EFFECTIVE FORCE DATA FILE

The data file for the signal generation at the University of Minnesota has the following structure:

Line #1	# sinesweep …	Notes. A '#' in the beginning is needed
Line #2	5001	Total data points
Line #3	0.002	Time step
Line #4		
Line #5		
Line #6		
Line #7		Blank lines are necessary,
Line #8		and data should start from line #11
Line #9		
Line #10		
Line #11	0	Start command data
Line #12	3.92699E-06	
Line #13	1.5708E-05	
Line #14	3.53429E-05	
Line #15	6.28319E-05	
…	…	
…	…	
Line #5009	-0.248674673	
Line #5010	-0.125329338	
Line #5011	0	End of command data

APPENDIX 6

DIGITAL VELOCITY COMPENSATION IN C LANGUAGE

The digital implementation of the nonlinear velocity feedback compensation is shown below in C language. The sample C program includes all necessary functions and commands for a real-time operation of the Digital Signal Processor (DSP). The italic lines are related to the velocity feedback compensation algorithm, while the normal lines are functions and commands defined by the manufacturer for the operation of the DSP.

```
/*****************************************
*  FILE:  eft_nonlinear.c
*
*  RELATED FILES:  brtenv.h, eft_nonlinear.h
*
*  DESCRIPTION:
*    DSP implementation of nonlinear velocity feedback compensation
*
*  INPUT:
*    effective force command (v), velocity (v), spool position (v), and load (v)
*
*  OUTPUT:
*    compensated command (v)
*
*  (C) 2001-2003 Jian Zhao, University of Minnesota
*****************************************/
#include <brtenv.h>                     /* basic real-time environment */
#include <math.h>
#include "eft_nonlinear.h"              /* variable and constant definition */

void isr_t1();
void lead_coeffcients_transferfunction();   /* phase lead network coefficients */
double lead();                          /* adjust phase */
double lookup();                        /* nonlinear flow property */

void main()
{
  init();                               /* initialize hardware system */
```

```
  msg_info_set(MSG_SM_RTLIB, 0, "System (EFT) started.");

// define constants
  Tl = Tl_DEF/(1-ALPHA);          /* lead time constant */
  Ks = 0.1;                       /* valve gain */
  Gp = 1.0012;                    /* controller P gain */
  A = 12.73;                      /* piston area */
  CF = 0.25;                          /* sensitivity factor (load) */
  Ps = 2.65;                          /* pressure supply */
  Kfix = 1/Ks/Gp;                     /* correction gain (temporary) */

// reset virables
  In_prev = 0.0;                      /* the first input to the phase lead */
  Out_prev = 0.0;                     /* the first output of the phase lead */
  ii = 0;                             /* counter */
  adc_1 = 0.0;                        /* input #1 command */
  adc_2 = 0.0;                        /* input #2 velocity */
  adc_3 = 0.0;                        /* input #3 spool */
  adc_4 = 0.0;                        /* input #4 load */
  adc_1_i = 0.0;                      /* initial offset input #1 command */
  adc_2_i = 0.0;                      /* initial offset input #2 velocity */
  adc_3_i = 0.0;                      /* initial offset input #3 spool */
  adc_4_i = 0.0;                      /* initial offset input #4 load */

  dac_1 = 0.0;                        /* output #1 command */

  RTLIB_TIC_INIT();                   /* enable execution time measurement */
  RTLIB_SRT_START(DT, isr_t1);        /* enable sampling clock timer */

  while(1)
  {                                   /* background process */
   while (msg_last_error_number() == DS1102_NO_ERROR)
   {
    RTLIB_BACKGROUND_SERVICE() ;
   } /* while NO_ERROR */

   RTLIB_SRT_DISABLE();               /* disable sampling clock timer */

   while (msg_last_error_number() != DS1102_NO_ERROR)
   {
    RTLIB_BACKGROUND_SERVICE() ;
   } /* while ERROR */

   RTLIB_SRT_ENABLE();
  } /* while(1) */
```

```
} /* main() */

/*---------------------------------------------------------------------
* timer1 interrupt service routine
*---------------------------------------------------------------------*/
void isr_t1()                           /* timer1 interrupt service routine */
{
 ii=ii+1;                               /* count for 10 sec */
 RTLIB_SRT_ISR_BEGIN();                 /* overload check */

 host_service(1,0);
 RTLIB_TIC_START();                     /* start execution time measurement */
 ds1102_ad_start();                     /* start ADC's */
 adc_1 = ds1102_ad(ADC1);               /* command read in */
 adc_2 = ds1102_ad(ADC2);               /* velocity read in */
 adc_3 = ds1102_ad(ADC3);               /* spool opening read in */
 adc_4 = ds1102_ad(ADC4);               /* load pressure read in */

 if (ii > 10/DT)                        /* operation */
 {
  cmd = (adc_1-adc_1_i)*IO_MAX;/* Convert input_1 to command */
  vel = (adc_2-adc_2_i)*IO_MAX/V_SENS;          /* Convert input_2 to velocity */
  spo = (adc_3-adc_3_i)*IO_MAX; /* Convert input_3 to spool position */
  lpres = (adc_4-adc_4_i)*IO_MAX/CF/A; /* Convert input_4 to pressure */

  flow = vel*A;                         /* Compensation flow */

  if (spo > 0.0)                        /* positive spool opening */
  {
     flow = flow/sqrt(1-lpres/Ps);      /* load pressure influence*/
  }
  else                                  /* negative spool opening */
  {
     flow = flow/sqrt(1+lpres/Ps);      /* load pressure influence*/
  }

  In_cur = lookup();                    /* nonlinear flow gain*/

  spool = lead();                       /* adjust phase */

  dac_1 = spool*Kfix+cmd*1.02;          /* generate command */
  dac_1 = dac_1/IO_MAX;                 /* convert it to [-1~1] for output */
 }
 else                                   /* find initial offsets */
 {
```

```
   adc_1_i = adc_1_i+adc_1;
   adc_2_i = adc_2_i+adc_2;
   adc_3_i = adc_3_i+adc_3;
   adc_4_i = adc_4_i+adc_4;
   if (ii > 10/DT-1)
   {
   adc_1_i = adc_1_i/ii;
   adc_2_i = adc_2_i/ii;
   adc_3_i = adc_3_i/ii;
   adc_4_i = adc_4_i/ii;
   } /* end while */
  } /* one step finishes */

  ds1102_da(DAC1,dac_1);                /* output result to DAC1 */
  exec_time = RTLIB_TIC_READ();         /* calculate execution time */
  RTLIB_SRT_ISR_END();                  /* end of interrupt service routine */
}

/*-------------------------------------------------------------------------
* Coeffcients used in phase lead network from transfer function
*-------------------------------------------------------------------------*/
void lead_coeffcients_transferfunction()
{
  C_in = (1-2*Tl/DT)/(1+2*ALPHA*Tl/DT);
  C_out = -(1-2*ALPHA*Tl/DT)/(1+2*ALPHA*Tl/DT);
  C_cur = (1+2*Tl/DT)/(1+2*ALPHA*Tl/DT);
}

/*-------------------------------------------------------------------------
* phase lead network
*-------------------------------------------------------------------------*/
double lead()
{
  double yk1;
  int i;
  lead_coeffcients_transferfunction();

/* lead computation */
  yk1 = C_in*In_prev+C_out*Out_prev+C_cur*In_cur;

/* save previous results */
  In_prev = In_cur;
  Out_prev = yk1;

  return yk1;
```

```
}

/*---------------------------------------------------------------------
* lookup table of nonlinear inverse of flow curve
*---------------------------------------------------------------------*/
double lookup()
{
  double spool;
  int i;

  spool = 0.0;
  for (i = 1; i<MAXPTS; i++)
  {
    if (flow < Xflow[i])
    {
          spool = Yspool[i-1] + (flow-Xflow[i-1])*(Yspool[i]-Yspool[i-1])/(Xflow[i]-
                Xflow[i-1]);
      goto FOUNDOK;
    }
  }
FOUNDOK:
  return spool;
}

/*****************************************
*  FILE:  eft_nonlinear.h
*
*  DESCRIPTION:  Head file for eft_nonlinear.c
*****************************************/
#define DT 5.0e-4                       /* .5 ms simulation step size */
#define IO_MAX 10.0F                    /* maximum I/O voltage */
#define V_SENS 0.195672                 /* sensitivity factor of velocity transducer */
#define MAXPTS 21                       /* maximum data points of the flow curve */

double In_prev;                         /* previous input for phase lead */
double Out_prev;                        /* previous output for phase lead */
double In_cur, Out_cur;                 /* current input and output for phase lead */
double C_in, C_out, C_cur;              /* coefficients used in phase lead */

#define Tl_DEF 0.005                    /* leading time */
#define ALPHA 0.1                       /* leading coef. */
volatile double Tl;                     /* leading time and coef. */
double Kfix;                            /* Fixed feedforward gain */
double Ks;                              /* Servovalve gain */
double Gp;                              /* MTS controller P gain */
```

```
double A;                       /* Actuator piston area */
double Ps;                      /* pressure supply */
double CF;                      /* Actuator load conversion factor */
double cmd;                     /* Command signal read-in */
double vel;                     /* Velocity signal read-in */
double spo;                     /* Current spool opening read-in */
double lpres;                   /* load pressure read-in */
double flow;                    /* flow to be compensated */
double spool;                   /* spool opening in compensation */


/* variables for I/O of the board */
double adc_1, adc_2, adc_3, adc_4;          /* input channels */
double adc_1_i, adc_2_i, adc_3_i, adc_4_i;
double dac_1, dac_2, dac_3, dac_4;          /* output channels */

/* variables for execution time profiling */
double exec_time;                           /* execution time */

/* coefficients of nonlinear flow aeftb01.p0# on 04/28/2003 w/ an accumulator */
    double Xflow[MAXPTS] = {-515.2, -500.2, -480.2, -452.3, -419.9, -377.1, -324.2,
                            -260.9, -188.2, -101.0, 0.0, 102.2, 187.2, 260.4, 321.1,
                            369.8, 411.2, 441.0, 468.3, 488.3, 503.3};
    double Yspool[MAXPTS] = {-1.0, -0.9, -0.8, -0.7, -0.6, -0.5, -0.4, -0.3, -0.2, -0.1, 0.0,
                             0.1, 0.2, 0.3, 0.4, 0.5, 0.6, 0.7, 0.8, 0.9, 1.0};

#define ADC1 1                  /* Input channel 1 */
#define ADC2 2                  /* Input channel 2 */
#define ADC3 3                  /* Input channel 3 */
#define ADC4 4                  /* Input channel 4 */

#define DAC1 1                  /* Output channel 1 */
#define DAC2 2                  /* Output channel 2 */
#define DAC3 3                  /* Output channel 3 */
#define DAC4 4                  /* Output channel 4 */
```

APPENDIX 7

DETAILS OF THE ONE-STORY STEEL STRUCTURE

The one-story structure consisted of a mass and four columns at its corners as shown in Figs. 8.5 and 8.11. The mass consisted of two rectangular steel frames filled with reinforced concrete. The columns were bolted at both ends as shown in Fig. A7.1. A V-shape brace made of tube 3×3×¼ was used to engage two fluid dampers. The connection between the brace and the dampers is shown in Fig. A7.2. The damper forces were monitored using two load cells as shown in Fig. A7.3.

During the shake table study, the velocity transducer was installed close to the dampers as shown in Fig. A7.3 because the velocity at the brace tip was slightly larger (approximately 3%) than that at the story mass due to a slight overturning of the structure. Fig. A7.4 (a) shows two accelerometers in the shake table study mounted on the bottom of the mass, one of which monitored the out of plane response of the structure.

During the EFT study, the structural configuration remained the same, while the instrumentation for global responses is different as shown in Fig. 8.11. Test results indicated that the contribution of the overturning of the structure to the structural response was negligible. Hence, the velocity transducer was installed at the actuator height but at the opposite side of the structure from the actuator as shown in Fig. A7.5. The connection of the actuator with the structure, including a 2-inch thick plate is shown in Fig. A7.6. Two LCA-100-2 accelerometers by Jewell Instruments were used in the EFT test, the mounting of which is shown in Fig. A7.4 (b). Finally, Fig. A7.7 shows the configuration of the ¼ gallon accumulator mentioned in Chapter 7.

Figure A7.1 Column end connections

Figure A7.2 Connection of the dampers

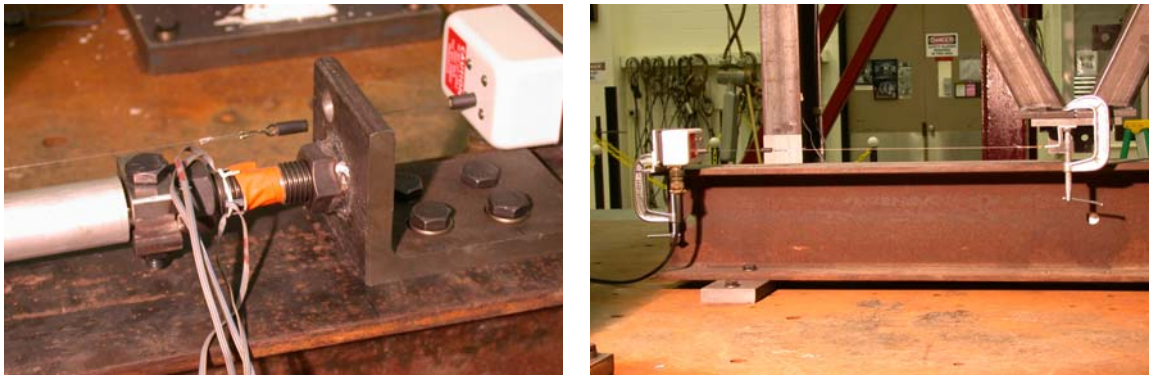

Figure A7.3 Connection of the load cell and velocity transducer (Shake table)

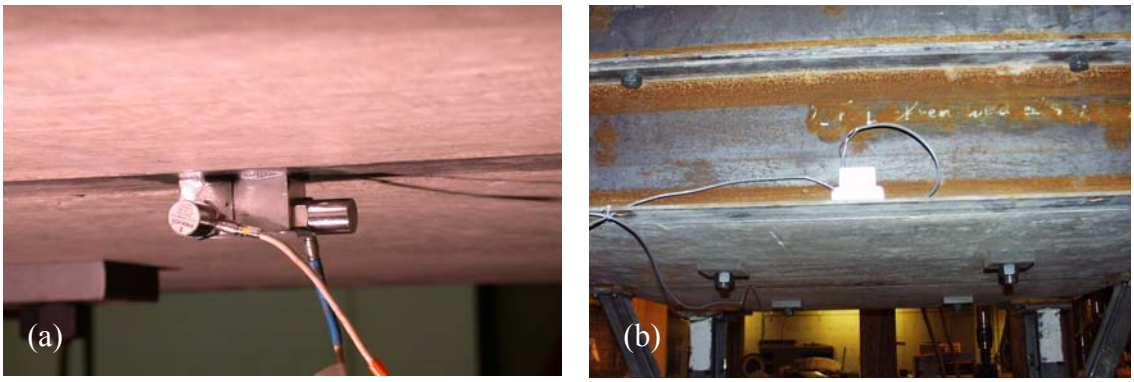

Figure A7.4 Connection of the accelerometers (a) underneath the mass in shake table; (b) On top of the bottom flange of the side W section of the mass in EFT

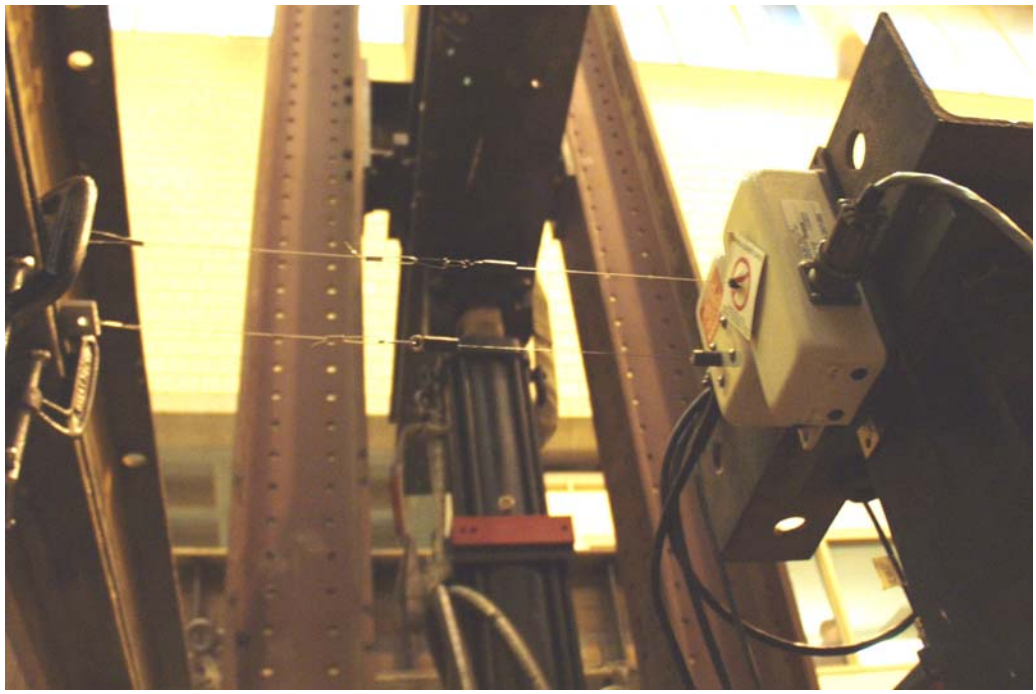
Figure A7.5 Connection of the velocity and displacement transducers from a reaction frame to the test structure (EFT)

Figure A7.6 Connection of the actuator with the structure (EFT)

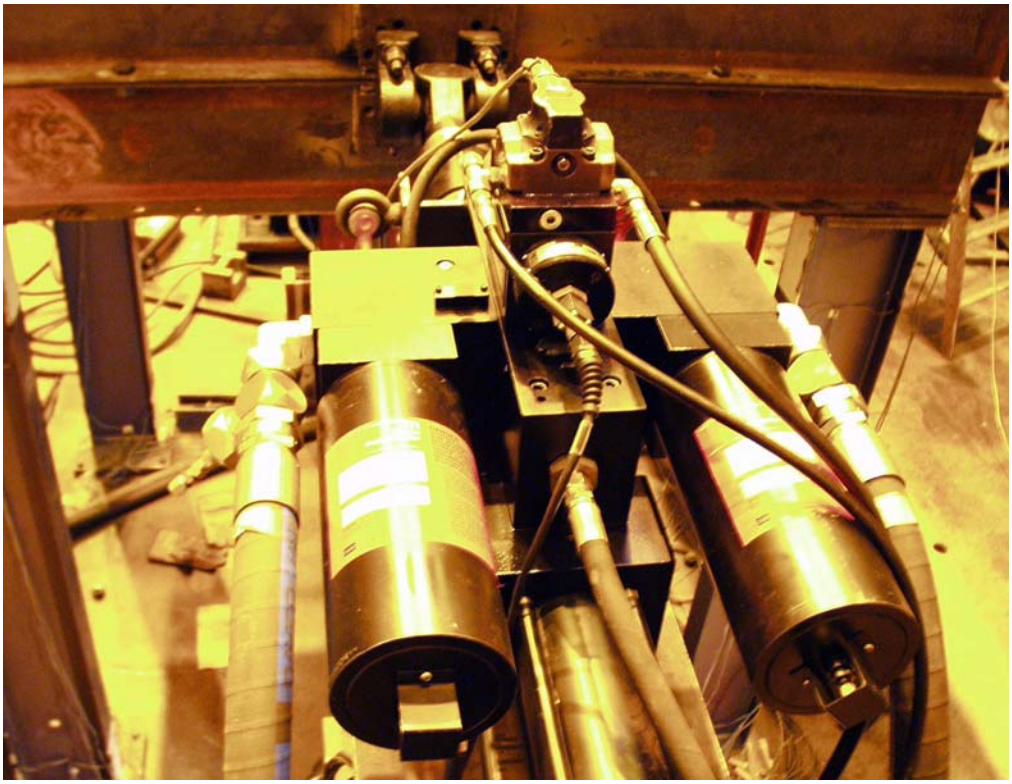

Figure A7.7 Connection of the accumulator (EFT)